Study of the Higgs self coupling in ATLAS detector at LHC. Study of performances of the timing detector for the high luminosity phase of LHC

Océane Perrin

UNIVERSITE CLERMONT AUVERGNE

ECOLE DOCTORALE DES SCIENCES FONDAMENTALES

THESE

présenté pour l'obtention du grade de

DOCTEURE D'UNIVERSITE en Physique

Spécialité: *Particules, Interactions, Univers*

Par **Océane Perrin**

Etude de l'autocouplage du boson de Higgs avec le détecteur ATLAS au LHC. Performances d'un détecteur en temps pour la phase de Haute Luminosité du LHC

Soutenue publiquement devant le jury: le 20 décembre 2023

Président: M. Dominique Pallin	- Directeur de recherche, LPC
Rapporteur et examinateur: Mme Sophie Trincaz-Duvoid	- Professeure à Sorbonne Univ., LPNHE
Rapporteur et examinateur: M. Sébastien Viret	- Chercheur, IP2I Lyon
Examinateur: M. Stefano Manzoni	- Chercheur, CERN
Directeur de thèse: M. Djamel Boumediene	- Directeur de recherche, LPC

Abstract

A bosonic particle with a mass equal to 125GeV was observed in 2012, by ATLAS and CMS collaborations at the Large Hadron Collider (LHC). This particle was associated with the Higgs Boson or BEH boson, predicted fifty years before its discovery by François Englert, Robert Brout and Peter Higgs. This particle validates the BEH mechanism, explaining the origin of the mass of known particles and the electroweak symmetry breaking. Since its discovery, it has become crucial to probe the various properties of the Higgs boson such as the Higgs self-coupling. The success in probing Higgs self-coupling will bring another probe of the standard model and will provide a direct measurement of the Higgs field potential in the vacuum. This measure is performed through a global analysis of the di-Higgs (HH) production at LHC, decaying into various channels. This thesis focuses on the study of the decay of the Higgs boson pair into two light leptons with the same charge (referred to as 2ℓSS) within the context of the Run2 at LHC, providing an integrated luminosity of $139\,\mathrm{fb}^{-1}$ and a centre of mass energy of $\sqrt{s} = 13\,\mathrm{TeV}$. The study based on Monte-Carlo simulations aims to develop a machine learning-based strategy to discriminate the signal (2ℓSS originating from the decay of the Higgs boson pair) from the background (all other processes producing 2ℓSS events). An analysis of background noise estimation and systematic uncertainty estimation is also presented in this work. Finally, although the measurement of the self-coupling can be constrained by Run2, its direct measurement is expected in the High-Luminosity phase of the LHC (HL-LHC). This phase involves a five-fold increase in instantaneous luminosity, requiring an upgrade of the ATLAS detector to ensure performance comparable to Run2 performances, despite the increase of radiation and pile-up effects. As a result, a new high-granularity timing detector (HGTD) will be added. A study on the readout electronics of this future detector is presented in this thesis, determining its performance in the test bench and during irradiation tests.

Résumé

Une particule ayant une masse de 125 GeV a été observée en 2012 grâce au grand collisionneur de hadrons (Large Hadron Collider - LHC) par les collaborations ATLAS et CMS. Cette particule fut associée au boson de Higgs ou boson BEH, dont l'existence fut prédite en 1964 par François Englert, Robert Brout et Peter Higgs. Cette particule permit de valider l'existence du mécanisme BEH, expliquant l'origine de la masse des particules découverte dès lors et de la brisure de symétrie électrofaible. Depuis sa découverte, il est devenu crucial de sonder les différentes propriétés que l'on confère au boson de Higgs. En particulier, l'auto-couplage du boson de Higgs est une des propriétés les plus attendues et une mesure de ce paramètre permettrait d'obtenir une mesure directe du potentiel de Higgs dans le vide. Cette mesure se réalise grâce à la production de di-Higgs au LHC, en exploitant différents canaux de désintégrations. Cette thèse porte sur l'étude de la désintégration de la paire de boson de Higgs en deux leptons légers de même charge (appelé signature ou 2ℓSS), dans le cadre du Run2 du LHC correspondant à une luminosité intégrée de $139\,\text{fb}^{-1}$ et une énergie de centre de masse de $\sqrt{s} = 13\,\text{TeV}$. L'étude utilise des simulations Monte-Carlo et vise à développer une stratégie basée sur le machine learning afin de maximiser la distinction entre le signal (2ℓSS issues de la désintégration de la paire de Higgs) et les bruits de fond (ensemble des processus produisant la signature). Une étude sur l'estimation des bruits de fond ainsi que sur l'estimation des incertitudes systématiques y sont aussi présentées. Enfin, bien que la mesure de l'auto-couplage puisse être contrainte par le Run2, sa mesure directe est attendue pour la phase de haute luminosité du LHC (HL-LHC). Cette phase implique une augmentation de la luminosité instantanée par un facteur 5, nécessitant une actualisation du détecteur ATLAS afin de garantir des performances comparables à celles du Run2, malgré l'augmentation des radiations et de l'effet d'empilement. De ce fait, un nouveau détecteur en temps à haute granularité (HGTD) sera ajouté. Une étude portant sur l'électronique de lecture de ce futur détecteur est présentée dans cette thèse, déterminant les performances en banc de tests ou lors de tests d'irradiations.

Remerciements

Firstly, I would like to thank my supervisor Djamel Boumediene for his guidance and his great support. He offers me wonder-full opportunities to embrace these three years of PhD.

I would like to thank the ATLAS team and the Laboratoire de Physique de Clermont for the opportunity and their welcome. In particular, I express my gratitude to Romain Madar, David Calvet, Laurent Royer, Alexandre Soulier, Geraldine Fettahi and Florence Holop for your help when I met issues.

I am grateful to all students that cross my path, during HGTD shifts, non-permanent meetings or the organization of the scientific days. I spend memorable moments with them.

Je souhaite remercier mes amis: A mes paturges, qui malgré la distance qui nous sépare tous, m'ont apporté un soutien et surtout des fou-rires incroyables, vivement nos futurs courses de déambulateurs. Je remercie aussi les Originales, pour nos soirées restos et les visios, surtout en période de COVID. Et enfin merci à mon amie Enora, pour nos conversations de mamies et merci de m'avoir ramené pendant les soirées oenologies... (PS: je n'aime toujours pas les Simpsons).

Enfin, je voudrais remercier ma famille et plus particulièrement mes parents pour leur soutien continuel. Ils m'ont offert la possibilité de poursuivre et de réaliser mon rêve. Je les remercie plus particulièrement de m'avoir pousser à me réinscrire en 5/2, au moment ou je voulais tout abandonner et d'avoir pris soin de mon chat quand je ne le pouvais pas.

Je souhaite remercier aussi mon conjoint pour avoir été présents dans les moments de stresse, de tristesse et de fatigue, tel un pilier sur lequel j'ai pu me reposer depuis onze ans. Petits doigts entrelacés.

To my boss papi

Plan

List of Figures

List of Tables

Introduction

"I am just a child who has never grown up. I still keep asking these 'how' and 'why' questions"
Stephen Hawking, *The brief history of time*

One of the most interesting questions in our quest to understand the universe was about the constituents of matter. For a long time, matter was composed of four elements: fire, earth, air and water, with two forces, attractive and repulsive allowing the elements to interact. In the 17^{th} century, a corpuscular theory emerged: the matter is composed of clusters of "corpuscles". In the early 1800s, John Dalton postulated that all matter is made up of small, identical and indivisible particles called atoms which cannot be created or destroyed. While later discoveries probed that atoms were not the smallest invisible particles, his idea of a fundamental component and his law of conservation remained and prepared the ground for subatomic physics. In the late 19^{th} century, i.e. in 1886 and 1891, a serie of experiments was performed by E. Goldstein and J.J Thomson respectively. They observed two tiny charged particles, known today as proton and electron. Forty years later, the discovery of the neutron completed the structure of the atom. After the Second World War particle physicists built dedicated supercolliders, such as the Large Hadron Collider (LHC), in order to investigate deeper into the subatomic world. In twenty years, theories and discoveries came one after another, with the emergence of Quantum Field Theory and the electroweak symmetry breaking. In 1975, the Standard Model (SM) was presented in full for the first time and it remains today the main and most powerful theory, able to explain most of the physics phenomena.

In 2012, the ATLAS and CMS collaborations at LHC discovered a new particle consistent with the hypothetical Higgs boson predicted in 1964 as the SM particle associated with the Higgs field theory. This discovery validated the mechanism which confers a mass to each massive particle. Since then, its properties have been deeply probed using proton-proton collision data at LHC. A precise measurement of the coupling properties of the Higgs boson can provide key tests of the Standard Model validity. Among those, the Higgs self-interaction

coupling or Higgs self-coupling λ_{HHH} is one of the most important because it is intrinsically linked to the shape of the Brout-Englert-Higgs mechanism and subsequently to the electroweak symmetry-breaking (EWSB). The value of this parameter is predicted based on the Higgs mass such as λ_{HHH}^{SM}. A measurement of a deviation in this parameter could have important consequences for the understanding of the EWSB and could reveal new physics. The λ_{HHH} measurement can be performed in the Higgs boson pair (HH) production cross section at LHC. This thesis presents the search for HH events produced from gluon-gluon fusion and vector boson fusion mechanism using Run2 data collected between 2015 and 2018 with the ATLAS detector. My work is focused on the HH decaying to two light leptons with the same charge signature.

While the analysis of the Run2 and Run 3 datasets are expected to constrain highly the value of the Higgs self-coupling, its measurement is expected during the High Luminosity phase of the LHC (HL-LHC). In this period, the instantaneous luminosity will be about 7 times larger than the Run2, for this reason, the ATLAS detector needs to be upgraded. To disentangle the primary interaction from the pileup events, the ATLAS collaboration will install an additional sub-detector to exploit the timing information of particles, called the High Granularity Timing Detector (HGTD). My contribution to the development of this sub-detector relies on the test of the front-end electronics prototypes and the participation of the various test beam campaigns.

This thesis is organized into seven chapters. Chapter 1 introduces the theoretical concepts of the Standard model. Chapter 2 discusses the phenomenology and experimental concepts of the Higgs boson. Chapter 3 and 4 present the ATLAS experiment at LHC and its High-luminosity upgrade HGTD. Then, the tests performed on the Front-End electronics and in test beam are presented in chapter 5. Chapter 6 presents the objects used in Monte Carlo simulations. Finally, chapter 7 gives a presentation of the analysis in the light lepton pair with the same charge.

Chapter 1

The Standard Model

This chapter presents an outline of the Standard Model (SM) as well as the theoretical and experimental motivation of the analysis in the Higgs field. The first section describes the fundamental particles of matter and their interactions. The section 1.2 describes the concept of symmetry in fundamental physics. Finally, section 1.3 introduces the Higgs mechanism and the Higgs boson properties.

1.1 The Standard Model of Particle Physics

The Standard Model of particle physics is a scheme that introduces known particles and forces with well-defined calculation rules, agreeing with a multitude of experiments. The Standard Model history started in the early 1960s with the publication of the iconic paper from Steven Weinberg in 1967 [1] which determined the direction of the high-energy physics research. This paper laid the foundations for the unified theory of the electromagnetic and weak interactions of leptons. This theory has been proposed the same year by Abdus Salam [2]. The term 'Standard Model' was coined for the first time in 1975 by Abraham Pais and Sam Treinman, and represents more than 400 years of research in physics.

1.1.1 Elementary particles of matter

The Standard Model of particle physics is the theoretical framework describing how all elementary particles interact with each other. The elementary particles can be divided according to their spins: Fermions and Bosons.

The **fermions** follow the Fermi-Dirac statistics and gather 24 different particles subdivided into quarks, leptons and their corresponding antiparticles as shown in figure 1.1. The prop-

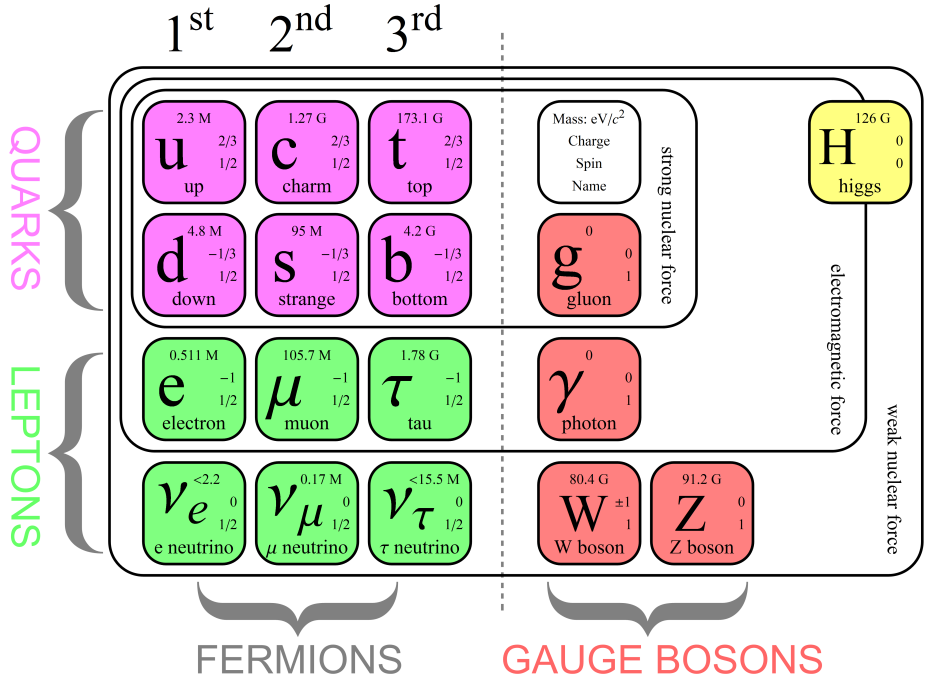

Figure 1.1: Standard Model particles and interactions

erties awarded to the antiparticles are similar to their corresponding particle, except for the charge. The particles are grouped into three generations, each generation is identical to the two others with increasing mass ranges. Quarks are not present in nature as free particles, they exist in an arrangement of quarks called hadrons. Only fermions of the first generation (electrons, up and down quarks) are usually observed, they mainly constitute the surrounding matter. Properties conferred to each particle are summarized in table 1.1.

The **bosons** have an integer spin. The spin-1 bosons carry the different fundamental interactions. The photon (γ) mediates the electromagnetic force, the W and Z bosons carry the weak force, and finally, the gluons mediate the strong force. These three latest bosons (γ, W and Z) are the low-energy manifestation of the unified electroweak force developed in the next section. The Standard Model predicts an additional spin-0 boson, called the Higgs boson. This boson plays a key role in the electroweak symmetry breaking. The properties of the gauge bosons are summarized in table 1.2.

In particle physics, each force can be described by the Quantum Field Theory (QFT) which is renormalisable, unified and invariant under space-time (space, rotations and Lorentz boosts). In the case of the strong force and electromagnetism, the theory is respectively called Quantum Chromodynamic (QCD) and Quantum Electrodynamics (QED).

Gen.	Quark	Q/q_e	mass [Gev]	Lepton	Q/q_e	mass [Gev]
1	up (u)	$\frac{2}{3}$	$2.16^{+0.49}_{-0.26}$ x 10^{-3}	electron (e^-)	-1	0.511 x 10^{-3}
	down (d)	$\frac{-1}{3}$	$4.67^{+0.48}_{-0.17}$ x 10^{-3}	electron neutrino (ν_e)	0	$<$2 x 10^{-9}
2	charm (c)	$\frac{2}{3}$	$1.27^{+0.02}_{-0.02}$	muon (μ^-)	-1	0.106
	strange (s)	$\frac{-1}{3}$	$93.4^{+8.6}_{-3.4}$ x 10^{-3}	muon neutrino (ν_μ)	0	$<$0.19 x 10^{-3}
3	top (t)	$\frac{2}{3}$	$172.69^{+0.3}_{-0.3}$	tau (τ^-)	-1	1.777
	bottom (b)	$\frac{-1}{3}$	$4.18^{+0.03}_{-0.02}$	tau neutrino (ν_τ)	0	$<$18.2 x 10^{-3}

Table 1.1: Properties of quarks and leptons grouped into generations: the charge Q in electron unit q_e and the mass in GeV [3].

Boson	Q/q_e	mass [GeV]	spin	force
Photon (γ)	0	$<10^{-27}$	1	Electromagnetic
W boson (W)	$\pm$1	80.377$\pm$0.012	1	Weak
Z boson (Z)	0	91.1876$\pm$0.0021	1	Weak
Gluon (g)	0	$\leq 10^{-3}$	1	Strong

Table 1.2: Properties of the Gauge bosons in the Standard Model: the electric charge Q in electron charge unit q_e, the mass value or mass limit in GeV, the spin and the type of mediated force [3].

1.2 Symmetries in fundamental physics

The concept of symmetries in the description of the world of the infinitely small allows us to describe the interactions that exist between all particles. In the case of the Standard Model, the mathematical representation relies on the QFT and is given by:

$$SU(3)_C \times SU(2)_L \times U(1)_Y \tag{1.1}$$

The first term, $SU(3)_C$ non-abelian symmetry, characterises the quantum chromodynamics, i.e. the strong interaction with the coloured particles. This symmetry is made of eight generators corresponding to the eight 3×3 Gell-Mann matrices, that induce the presence of eight massless gluons colours. While the gluon has never been directly detected, the evidence of its existence has been probed by diverse experiments such as the observation of three jet events in e^+e^- annihilation [4, 5] in 1979.

The second term $SU(2)_L \times U(1)_Y$ refers to the electroweak interaction made of 4 generators $W^{\pm}$, Z, and γ bosons. $SU(2)_L$ and $U(1)_Y$ conserve respectively the handedness and the hypercharge defined as Y = 2(Q-I_3), where Q is the charge and I_3 the third component of the isospin.

The Lagrangian

The principle of least action considers that in each mechanical system, there is a certain integral called the action S, with an extremum value of the actual motion (δS =0). In fundamental physics as in classical mechanics, the Lagrangian $\mathcal{L}$ can be used to describe the action S, as the integral over the phase space of the Lagrangian density $\mathcal{L}$: $S = \int dtL = \int dx^4\mathcal{L}$. Starting from the Dirac Equation, the Lagrangian density can be derived :

$$\mathcal{L} = \bar{\psi}(i\not{\partial} - m)\psi = \bar{\psi}(i\gamma^\mu\delta_\mu - m)\psi$$

with m the mass of the system (particle), γ^μ is the Dirac matrices. ψ(x) is the Dirac spinor as the particle's wave function and its adjoint spinor $\bar{\psi} = \psi^\dagger\gamma^0$.
In case of a symmetric system, under arbitrary variation (infinitesimal) of the field, we assume that: $\mathcal{L}(\phi + \delta(\phi)) = \mathcal{L}(\phi)$. Because of the principle of least action, for an arbitrary variation of a field $\delta\psi$, we obtain the "Euler-Lagrange equation":

$$\delta_\mu\left(\frac{\delta\mathcal{L}}{\delta(\delta_\mu\psi)}\right) - \frac{\delta\mathcal{L}}{\delta\psi} = 0$$

The Lagrangian is a scalar under Lorentz transformation and parity transformations.

1.2.1 The electromagnetic interaction

As defined before, the electromagnetic interaction can be described by the quantum electrodynamics theory (QED). The Dirac Lagrangian is used to define mathematically a free fermion with a mass m, such as:

$$\mathcal{L} = \bar{\psi}(x)(i\gamma^\mu\delta_\mu - m)\psi(x)$$

Considering the Euler-Lagrange equation defined previously, we get:

$$(i\gamma^\mu\delta_\mu - m)\psi(x) = 0$$

As the Lagrangian is invariant under the local gauge transformation U(1) such as:

$$\psi(x) \rightarrow U(\alpha)\psi(x) = e^{i\alpha}\psi(x)$$

Then we introduce a covariant derivative to replace δ_μ such as $D_\mu = \delta_\mu + iqA_\mu$ with A_μ a vectorial field. Finally the full QED Lagrangian can be written as:

$$\mathcal{L}_{QED} = \bar{\psi}(x)(i\gamma^\mu\delta_\mu - m)\psi(x) - q\bar{\psi}(x)\gamma^\mu A_\mu\psi(x) - \frac{1}{4}F_{\mu\nu}(x)F^{\mu\nu}(x)$$

1.2.2 The strong interaction

The strong interaction can be described by quantum chromodynamics (QCD) and defined as the interaction between quarks and gluons. It follows the non-abelian symmetry $SU(3)_C$. A free quark with a mass m can be described by the following Dirac Lagrangian:

$$L = \sum_f \bar{q_f}(i\gamma^\mu\delta_\mu - m)q_f \qquad \text{with} \quad q_f = \begin{pmatrix} q_f^R \\ q_f^G \\ q_f^B \end{pmatrix}$$

This equation remains by definition invariant under the $SU(3)_C$ symmetry such as a unitary matrix U, which gives the linear combination of the eight Gell-Mann matrices.

$$q(x) \rightarrow Uq(x) = e^{i\frac{\lambda_a}{2}\theta_a}q(x)$$
$$\delta_\mu \rightarrow D\mu = \delta_\mu + ig_s\frac{\lambda_a}{2}G_\mu^a(x)$$

g_s is the coupling strength of the gluon field tensor $G_\mu^a(x)$. The final Lagrangian of the QCD can be written as:

$$L_{QCD} = \sum_f \bar{q_f}(i\gamma^\mu\delta_\mu - m)q_f - g_s\sum_f(\bar{q_f}\gamma^\mu\frac{\lambda_a}{2}q_f)G_\mu^a(x) - \frac{1}{4}G_{\mu\nu}^a(x)G_a^{\mu\nu}(x)$$

1.2.3 The Electroweak interaction

The electroweak interaction represents a unified definition of the electromagnetic interaction and the weak interaction. This interaction is described by the $SU(2)_L$ symmetry, where L represent the left-hand weak isospin. According to the chiral theory, meaning that nature treats left-handed and right-handed particles differently, we have for the left-handed leptons and quarks:

$$\psi_1(x) = \begin{pmatrix} \nu_e \\ e \end{pmatrix}_L, \begin{pmatrix} \nu_\mu \\ \mu \end{pmatrix}_L, \begin{pmatrix} \nu_\tau \\ \tau \end{pmatrix}_L \qquad \psi_1(x) = \begin{pmatrix} u \\ d \end{pmatrix}_L, \begin{pmatrix} c \\ s \end{pmatrix}_L, \begin{pmatrix} t \\ b \end{pmatrix}_L$$

and for the right-handed leptons and quarks:

$$\psi_2(x) = \nu_{eR}, \nu_{\mu R}, \nu_{\tau R} \qquad \psi_2(x) = u_R, c_R, t_R$$
$$\psi_3(x) = e_R, \mu_R, \tau_R \qquad \psi_3(x) = d_R, s_R, b_R$$

The Lagrangian for a free fermion can be written as:

$$L_{EW} = \sum_1^3 i\psi_j(x)\gamma^\mu \delta_\mu \psi_j(x)$$

This Lagrangian remains invariant under the symmetry $SU(2)_L \times U(1)_Y$. By consequence, the δ_μ can be replaced by the covariant derivative Dμ. $W^i_{\mu\nu}$ and $B_{\mu\nu}$ are introduced as the field tensors of the symmetries $SU(2)_L$ and $U(1)_Y$.

$$D_\mu \psi_1(x) = [\delta_\mu - igW_\mu(x) + ig' y_1 B_\mu(x)]\psi_1(x)$$

$$D_\mu \psi_{2,3}(x) = [\delta_\mu - +ig' y_{2,3} B_\mu(x)]\psi_{2,3}(x)$$

The g and g' are coupling strength factors for the respective field tensors
So the electroweak Lagrangian can be written as:

$$L_{EW} = \sum_1^3 i\psi_j(x)\gamma^\mu D_\mu \psi_j(x) - \frac{1}{4}B_{\mu\nu}B^{\mu\nu} - \frac{1}{4}W^i_{\mu\nu}W_i^{\mu\nu}$$

1.3 The Brout-Englert-Higgs mechanism

The electroweak theory unifies the long-range electromagnetic interaction and the short-range weak interaction. This unification implies a close relation between the massless photon and very massive W and Z bosons. Before the proposition of the Higgs mechanism, it was impossible to justify how a local symmetry could contain both massive and massless interaction carriers. In 1962, Goldstone's theorem demonstrated that spontaneous symmetry breaking can lead to a massless particle with a null spin. In 1964, R. Brout and F. Englert [6], P. W. Higgs [7], G. S. Guralnik, C. R. Hagen and T. W. B. Kibble [8] proposed independently a mechanism to resolve this incompatibility.

This mechanism introduces a scalar field as :

$$\Phi(x) = \begin{pmatrix} \phi^{(+)} \\ \\ \phi^0 \end{pmatrix} = \frac{1}{\sqrt{2}} \begin{pmatrix} \phi_3 + i\phi_4 \\ \\ \phi_1 + i\phi_2 \end{pmatrix}$$

This field can be mathematically described by the following Lagrangian:

$$L = (D_\mu \Phi)^\dagger D^\mu \Phi - V(\Phi) \tag{1.2}$$

where the first term corresponds to the kinetic energy and the second term corresponds to the potential of the Higgs field. The potential part can be defined as follows:

$$V(\Phi) = \mu^2 \Phi^\dagger \Phi + \lambda(\Phi^\dagger \Phi)^2$$

The parameters μ and λ are initially free parameters of the potential. Its shape is fully dependent on the value of parameter μ^2. If $\mu^2 \geq 0$, the potential reaches the minimum value at $\phi_1 = \phi_2 = 0$. If $\mu^2 < 0$, the ground state obtained in the spontaneous symmetry breaking is degenerated, meaning that it admits an infinite number of minimum energy states. Figure 1.2 shows the shape of this potential energy of the Higgs field, so-called the Mexican hat due to its form. The minimum in this case can be written as:

$$|\phi^0| = \sqrt{\frac{\phi_1^2 + \phi_2^2}{2}} = \sqrt{\frac{-\mu^2}{2\lambda}} = \frac{\nu}{\sqrt{2}}$$

with ν the vacuum expectation value (VEV). Thus, the energy in the centre is symmetric but remains in an unstable excited state. Due to its shape, the minimum so-called vacuum state is not symmetric but it is composed of an infinity of stable final states. This is the spontaneous symmetry breaking. The ground state must have a nonzero VEV and be electrically neutral, the scalar can be written as:

$$\Phi(x) = \frac{1}{\sqrt{2}} \begin{pmatrix} 0 \\ \\ \nu + h(x) \end{pmatrix}$$

with $h(x)$ the real field, it can be interpreted as a real particle, called the Higgs boson.
As a consequence, the Lagrangian can be written as:

$$L = \frac{1}{2}\delta_\mu H \delta^\mu H + (\nu + H)^2 (\frac{g^2}{4} W_\mu^\dagger + \frac{g^2}{8 cos^2 \theta_W} Z_\mu Z^\mu) - \lambda \nu^2 H^2 - \lambda \nu H^3 - \frac{\lambda}{4} H^4 \tag{1.3}$$

$$W_\mu = \frac{W_\mu^1 + i W_\mu^2}{\sqrt{2}} \qquad Z_\mu = \frac{g' W_\mu^3 + g B_\mu}{\sqrt{g^2 + g'^2}} \qquad cos\theta_W = \frac{g}{\sqrt{g^2 + g'^2}}$$

From this Lagrangian, the mass of the W and Z boson can be derived as well as the mass of the spin-0 scalar boson Higgs as:

$$m_w = \frac{g\nu}{2} \qquad m_Z = \frac{\nu}{2}\sqrt{g^2 + g'^2} = \frac{m_W}{cos\theta} \qquad m_H = \sqrt{-2\mu^2} = \nu\sqrt{2\lambda} \tag{1.4}$$

The value of the Higgs boson mass is not predicted by the standard model since λ and μ are free parameters. The λ leads to the trilinear and quartic self-coupling of the Higgs boson. This parameter has not been measured yet, but it remains one of the main interests of the physicists' community to characterize and understand the Higgs potential.

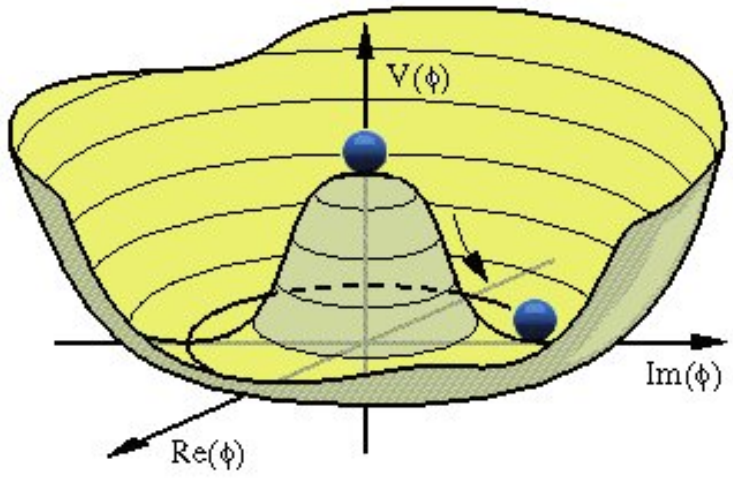

Figure 1.2: The potential energy of the Higgs field obtained with $\mu^2 < 0$[9]

1.3.1 The crucial position of the trilinear self-coupling of the Higgs boson

The Higgs potential for the Higgs field H can be written after the symmetry breaking as:

$$V(H) = \frac{1}{2}m_H^2 H^2 + \lambda_3 \nu H^3 + \frac{1}{4}\lambda_4 \nu H^4$$

where m_H is the Higgs mass, ν the VEV, λ_3 the trilinear Higgs self coupling and λ_4 quartic Higgs self coupling. The VEV is known from its relations to the Fermi constant as $\nu = (\sqrt{2}G_F)^{-1/2} = 246\,\text{GeV}$. The Higgs self-coupling is represented in figure 1.3:
Supposing a Higgs mass of 125 GeV, the λ_3 can be given according SM prediction by:

$$\lambda \pm \delta\lambda = \frac{m_H^2}{2\nu^2} + \frac{\delta m_H}{\nu^2} \sim 0.13 \pm 10^{-3}$$

Figure 1.4 shown the impact of the value of λ_3 over the Higgs potential shape.

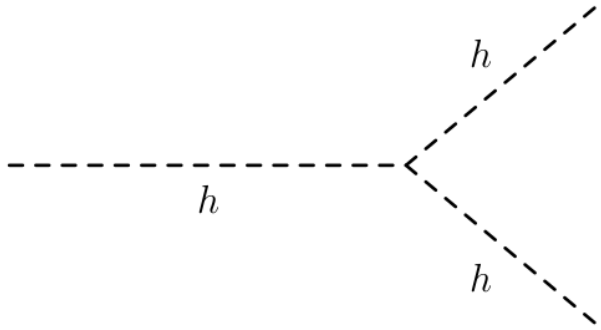

Figure 1.3: Higgs self-coupling representation

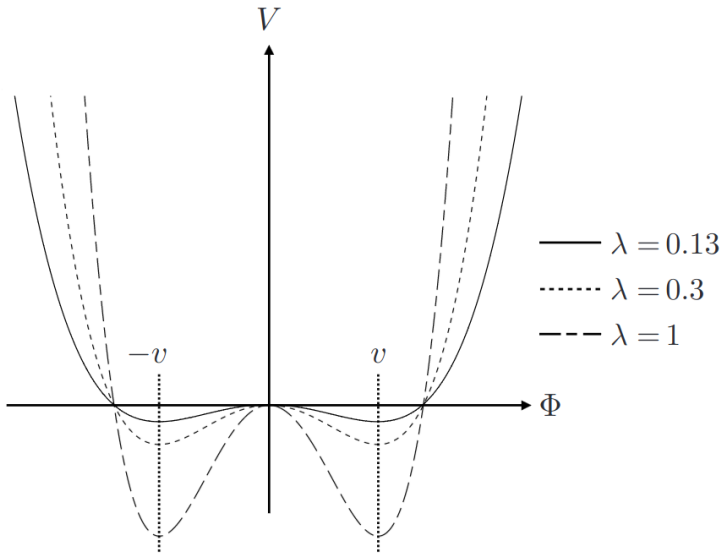

Figure 1.4: Higgs potential shape for different value of λ_3 [10]. For large value (dashed line) of λ_3 the minima are much more pronounced compared to minimal value of λ_3 (dotted line). The solid line represents the shape for the nominal value.

A precise measurement of the Higgs self-coupling is vital for the following reasons:

- Mass generation mechanism: As it has been shown, the Higgs self-coupling is intrinsically linked to the Higgs mechanism. It is through this self-interaction that the Higgs field imparts mass to itself and as a consequence to other particles. This self-coupling is a cornerstone of the Higgs mechanism.
- Standard Model Validation: As the standard model included a prediction of the Higgs self-coupling, a measurement of this coupling with a certain precision serves as a test of the SM prediction and will help to validate the overall framework of particle physics.

- New physics Searches: A deviation in the measurement of the Higgs self-coupling will imply the existence of new physics or additional interactions that modify the self-coupling value. For instance, considering beyond the Standard Model study as a strong first-order transition (SFOPT), it has been shown in [11] that a measurement of the HZZ coupling can rule out most of the value of the Higgs self-coupling. As a consequence, the value of λ_3 can validate or invalidate this model.
- Cosmic Implication: λ_3 coupling is essential for the understanding of the early Universe and its evolution. In fact, it plays a crucial role in the phase transition that occurred just after the Big Bang.

Experimental efforts to measure the Higgs self-coupling are ongoing, and the Large Hadron Collider (LHC) and future particle colliders play a vital role in this endeavour. The ability to precisely determine the self-coupling of the Higgs boson is not only a testament to the success of the Higgs mechanism but also a key step in unravelling the mysteries of mass, the fundamental forces, and the universe's early history.

1.4 The Higgs discovery at the Large Hadron Collider

Searches of the Higgs boson started in the mid-1970s [12], but its existence remained hypothetical up to 2012. The theoretical considerations determined the mass of the Higgs between 10 GeV and 1000 GeV. In 2000, the LEP was pushed to 206 GeV, its maximal center-of-mass energy and few Higgs-like events were observed with a 114.4 GeV lower mass limit at 95 % confidence level [13]. From 2010, the Large Hadron Collider (LHC) began operating at 7 TeV. This collider is the largest accelerator in the world, more details can be found in section 3.2. Preliminary results from ATLAS and CMS experiment, two multipurpose experiments of the LHC system, excluded at 95 % confidence level a standard Model Higgs boson in the range 155-190 GeV and 149-206 GeV [14, 15]. In 2012, the LHC reached a 8 TeV centre of mass-energy. The analysis of the two following decay modes of the Higgs H$\rightarrow ZZ \rightarrow 4\ell$ and H$\rightarrow \gamma\gamma$ in the data collected in 2011 and 2012, highlighted the presence of a particle compatible with the Higgs boson. In the H$\rightarrow \gamma\gamma$ channel as shown in figures 1.5a (ATLAS) and 1.5b (CMS), a bump can be identified in the distribution of the mass of the reconstructed photon pair. In parallel, this discovery has been observed in the channel H$\rightarrow ZZ \rightarrow 4\ell$ as shown in figures 1.5c (ATLAS) and 1.5d(CMS), which represent the distribution of the mass of the four reconstructed final leptons. On the 4th of July 2012, the announcement of the discovery was made, and remains currently one of the most important discovery in fundamental physics.
Since the discovery of the Higgs boson, its mass has been measured to be $124.94^{\pm 0.17\ (stat)}_{\pm 0.03(syst.)}$ GeV [18].

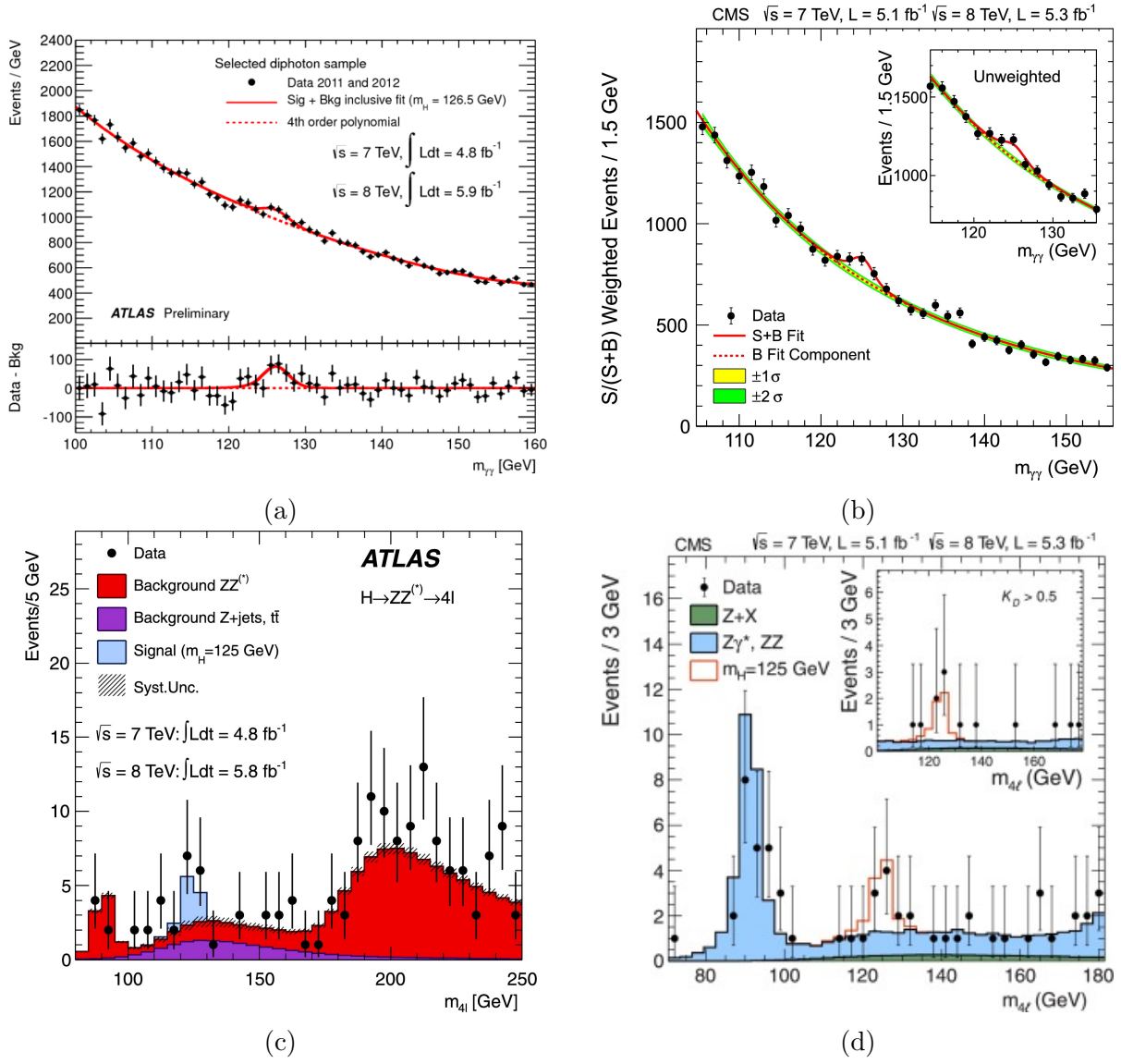

Figure 1.5: Higgs Boson discovery by the ATLAS experiment (on left)[16] and CMS experiment (on right)[17]. On top, the distribution of the invariant mass of the two photons in the channel H$\rightarrow \gamma\gamma$. On figures represent the distribution of the invariant mass of the four reconstructed leptons in the H$\rightarrow ZZ \rightarrow 4\ell$ channel.

What do we learn from this discovery?

Assuming the discovery of the particle with a mass at 125 GeV to be the Standard Model Higgs boson, the main parameters are known. It allows a fundamental constraint of the SM and consequently the evaluation of the validity of the model. The global fit of the electroweak

precision data of the SM with the measured Higgs mass demonstrated an agreement and the consistency of the SM as shown in figure 1.6. In addition, the knowledge of the Higgs mass improved the SM predictions of several key observable such as the uncertainties over the W mass and the top quark mass, which respectively decreased from 23 MeV to 15 MeV and from 1.6 GeV to 0.72 GeV

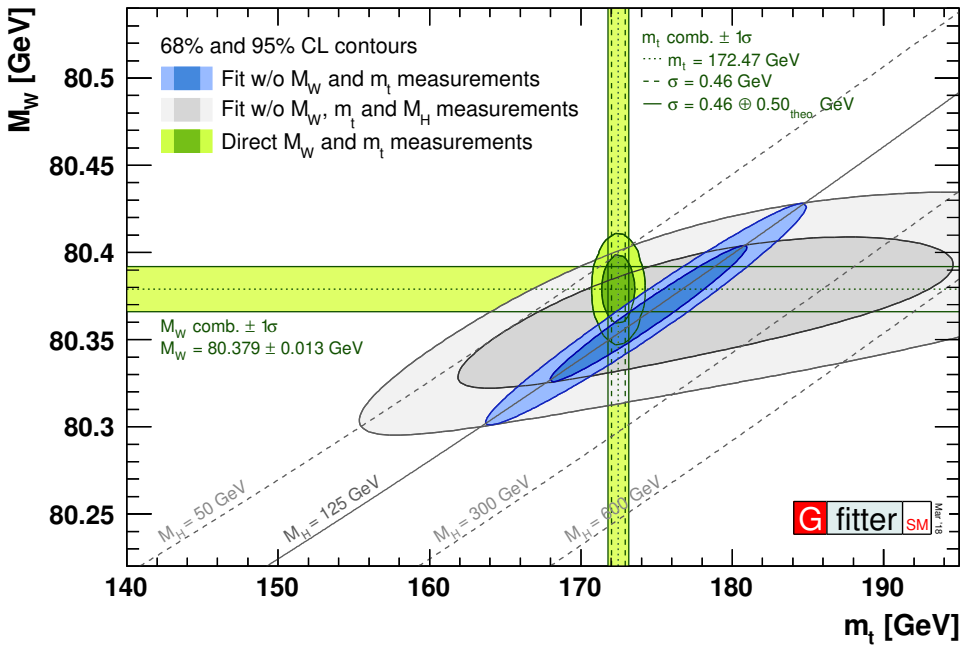

Figure 1.6: Scan of mass for W boson and top quark [19]. The blue area is the result of the fit including the mass of the Higgs measurement at 125 GeV. The green bands represents the 1σ region of the direct measurements.

Finally, the measurement of the Higgs mass provides important information on the Universe because a mass at 125 GeV places our universe in metastability. Since the SM is a renormalizable quantum field theory, the question of the scale of new physics fully relies on te renormalization evolution of some couplings constants, e.g. the Higgs boson self coupling λ. Fixing all parameters of the SM to their experimental values except the tp Yukawa coupling to the Higgs boson y_t, the renormalization group of the Higgs self coupling for various y_t values is shown in the figure 1.7. These various distribution present our universe as stable, metastable or instable state as a function of the y_t. As a consequence, the discovery of the Higgs boson is significant in the cosmology world too. It predicts the decay of the electroweak vacuum in the early Universe in a lower energy vacuum state.
The mass of the Higgs has been predicted in the minimal supersymmetric extension of the Standard Model and remains consistent with the measured Higgs mass considering the

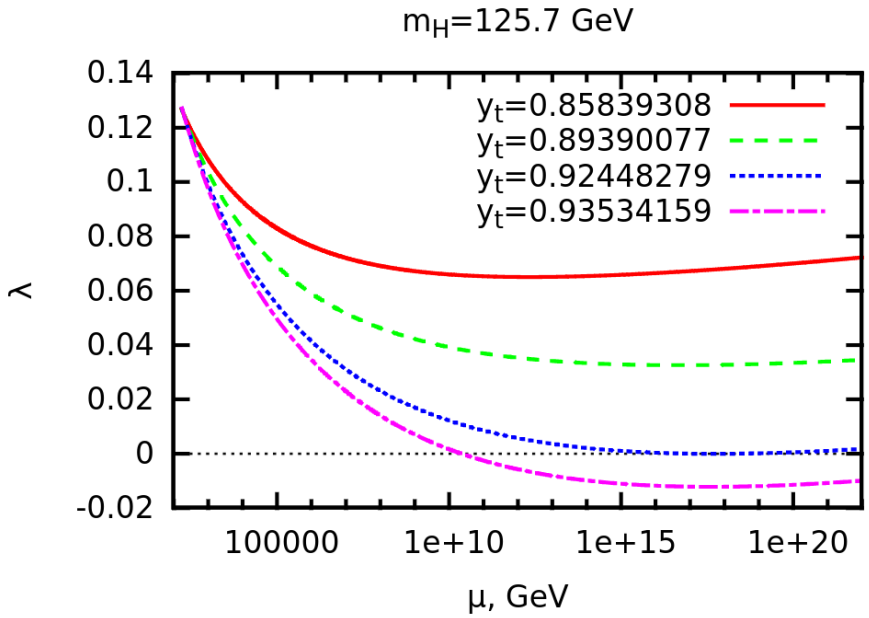

Figure 1.7: Renormalization group running of the Higgs coupling constant λ for the Higgs mass $M_H = 125.7\,\text{GeV}$ and several values of the top quark Yukawa y_t [20].

squarks are heavy.

1.4.1 Limitations of the Standard Model

The Standard Model of particle physics gives an explanation for many experimental results, yet there are several reasons to believe that a much more complex system is in place.

Gravity

Currently, the best description of gravity is given by the Theory of General Relativity. Although the theories of quantum gravity try to justify the existence of the graviton as mediation of the gravitational interaction, the current Standard Model remains incompatible with the Theory of General Relativity. The graviton (G) is predicted as a non-charged particle with a mass $<6 \times 10^{-41}\,\text{GeV}$ and a spin equals to 2.

Matter and anti-matter

In theory, the Big Bang should have generated an equal amount of matter and antimatter in the early Universe. But today, the presence of the antimatter in our universe is negligible. In the Standard Model of the matter, the only non-trivial difference between matter and

antimatter refers to the CP asymmetry, the CP-violating phase in the Cabibbo-Kobayashi-Maskawa (CKM) matrix. But this parameter remains too small to explain the asymmetry of the current Universe.

Neutrino mass

When the Standard Model was proposed, it was assumed that neutrinos were mass-less particles. The neutrino oscillation experiments suggest that muon neutrinos can transmute into an electron neutrino and vice-versa along their path [21]. Yet, this observation remains only possible for non-zero mass neutrinos.

Dark Matter and Dark Energy

The Standard Model only describes 5% of the Universe, but 95% of our Universe is made of Dark matter (23%) and Dark energy (73%). The existence of these latest has been proved for instance by the expansion of the Universe with an accelerated rate, by galaxy rotation curves and gravitational lensings.

1.4.2 The Higgs boson, a tool for future discovery

The Higgs is a portal towards a multitude of unsolved problems, and remain a key point to characterize and understand BSM physics. Figure 1.8 present the implication of the Higgs boson in various topics. Some topics are developed below:

- Origin of flavour: One of the open puzzles in particle physics is the origin of the flavour and more specifically the search for the lepton-flavour violation. The Higgs represents a portal to this exploration because it is suspected to interact with undiscovered physics particles such as dark matter particles. ATLAS and CMS collaborations try to probe for lepton-flavor violation in the Higgs boson decays. The phenomenon has been translated into constraints on the branching ratios for the process H$\rightarrow e\mu, \mu\tau, \tau e$. More details can be found in [22].

- Naturalness: The strategy of naturalness is the idea that a quantum field theory can describe nature with energy up to a certain scale. One of the most famous problems is why the weak force is 10^{24} times as strong as gravity. This problem relies on the Higgs boson mass and why this particle is lighter than the Planck mass.

- Stability of the Universe: The stability of the universe rests on two masses: the top quark mass and the Higgs boson mass. Yet, these two show that the universe is in a meta-stability state. It reveals whether our universe can persist in this state or not. Based on our knowledge, it could exist an additional lower energetic state of the SM vacuum.

- Hidden sector: The dark matter searches try to probe the existence of a mediator between dark particles and already known particles. The Higgs boson is a candidate for this task as a dark scalar (Dark Higgs). Physicists investigate exotic rare Higgs decays (such as H$\rightarrow ZZ_d \rightarrow 4\ell$) that could induce the production of dark particles or dark photons to probe this link to the Hidden sector.

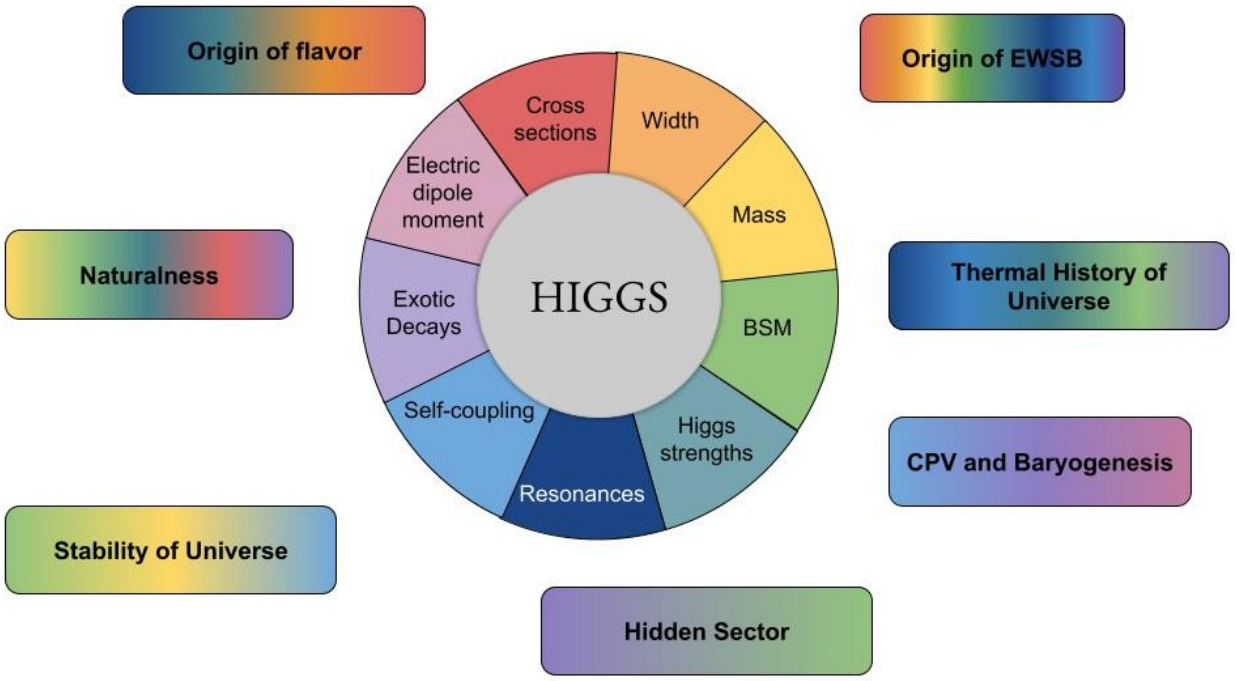

Figure 1.8: Implication of the Higgs searches in the unsolved current problem of fundamental physics.

Chapter 2

Phenomenology of proton-proton collision

This chapter presents the link between the Higgs self-coupling and the di-Higgs production at LHC in section 2.1. Section 2.2 introduces the decays channels while section 2.3 presents how the Monte Carlo simulations used in each analysis are produced.

2.1 Di-Higgs production at LHC

Assuming the electroweak symmetry breaking, the potential can be written as:

$$V(\psi) = -\lambda\nu^2 h^2 - \lambda\nu h^3 - \frac{1}{4}\lambda h^4 + const.$$

The first term of this potential corresponds to the Higgs mass m_H, this term was measured in 2012. The third term corresponds to the quartic Higgs self-coupling λ_4. This term cannot be measured at LHC due to a very small cross-section of the triple Higgs production. The second term of the potential corresponds to the Higgs self-coupling λ_3 that can be measured at LHC through the production of Higgs pairs.

$$m_H = \sqrt{2\lambda\nu^2} \qquad \lambda_3 = \frac{3m_H^2}{\nu} \qquad \lambda_4 = \frac{3m_H^2}{\nu^2}$$

with m_H the Higgs mass, measured at 125 GeV and ν the VEV expected at 246 GeV.
At LHC, di-Higgs can be produced through several production mechanisms. The observation of the Higgs-self coupling necessary includes the production of a single Higgs decaying into a Higgs pair. At $\sqrt{s}$ =13 TeV, Higgs are produced by gluon-gluon fusion (GGF), vector boson fusion (VBF), double Higgs bremsstrahlung from top quarks ($t\bar{t}$HH) and Higgs-strahlung (VH). The leading order Feynman diagrams of each production mode are shown in figure 2.1 and the respective cross-section are listed in table 2.1.

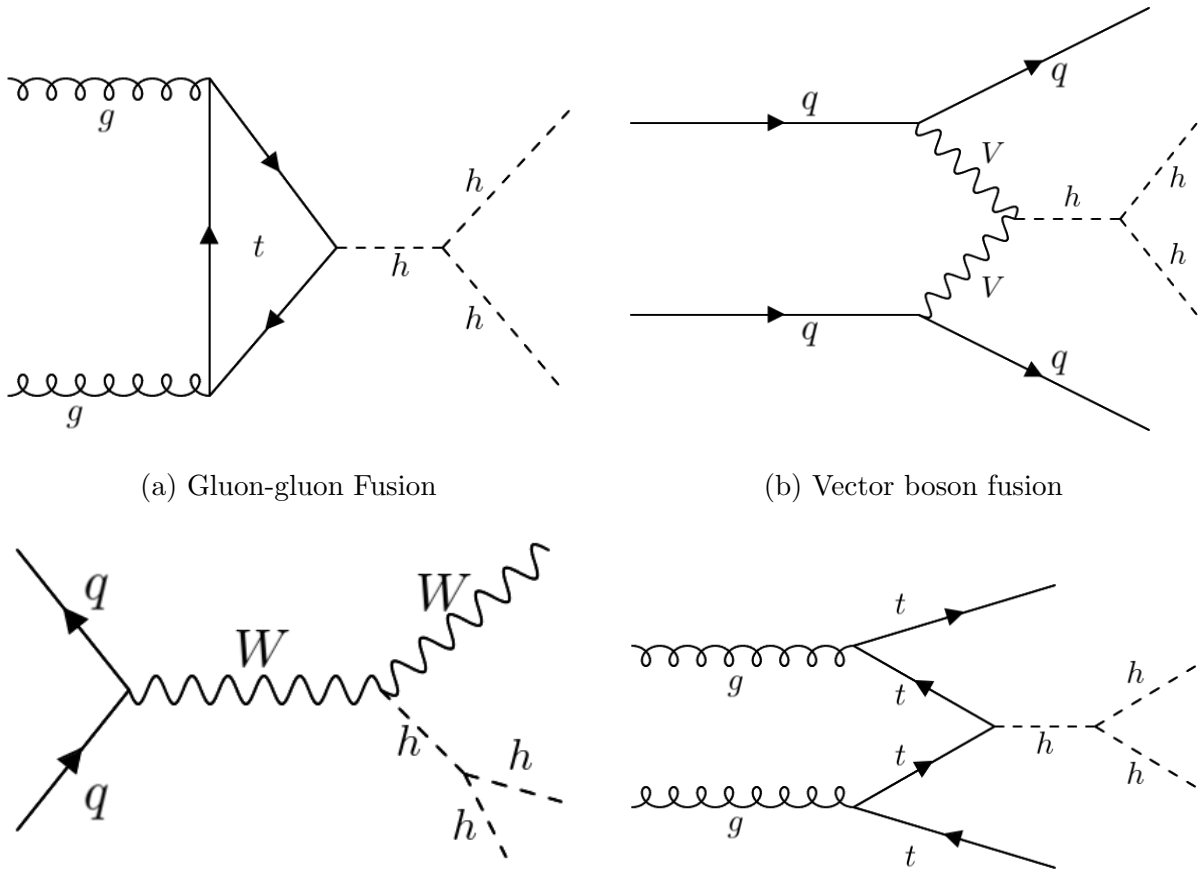

(a) Gluon-gluon Fusion

(b) Vector boson fusion

(c) Higgs-strahlung

(d) Top quark fusion

Figure 2.1: Dominant production modes of the Higgs pair at LHC for a 13 TeV centre of mass energy.

Figure 2.2 shows the evolution of the cross-section with respect to the centre of mass energy and the Higgs self-coupling [23]. In this thesis, only the two first production modes, i.e. GGF and VBF, are considered with a cross-section of 31.05 fb and 1.73 fb respectively.

X	$gg \to$ HH	$q\bar{q} \to HHq\bar{q}$	t$\bar{t}$HH	ZHH	W$^+$HH	W$^-$HH	tjHH
σ(pp$\to$ X) [fb]	31.05	1.73	0.775	0.363	0.329	0.173	0.0289

Table 2.1: Cross section for each production mode of the di-Higgs at $\sqrt{s}$=13 TeV [24].

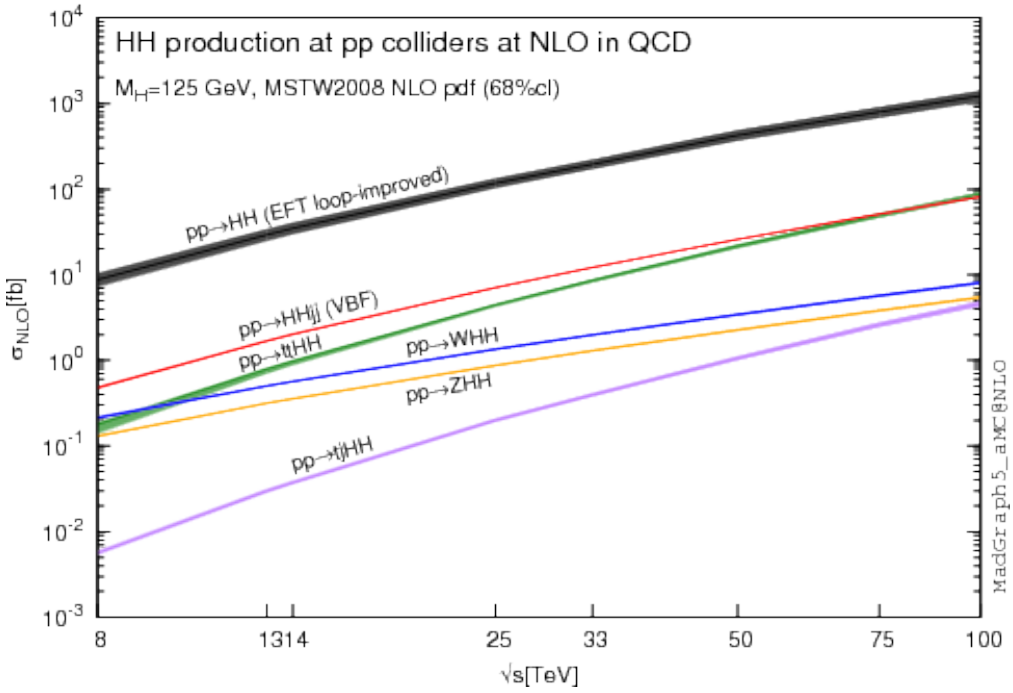

Figure 2.2: Evolution of the cross-section for the HH production mode at pp collider at NLO with respect to the centre of mass energy

2.2 Higgs pair decays

The Higgs boson decays in many possible final states as shown in the table 2.2.

Decay channel	Branching ratio [%]
$H \to b\bar{b}$	(53 ± 8)
$H \to W^+W^-$	(25.7 ± 2.5)
$H \to gg$	8.187
$H \to \tau\bar{\tau}$	(6.0 ± 0.8)
$H \to c\bar{c}$	(± 0.30)
$H \to Z^+Z^-$	(2.80 ± 0.30)
$H \to \gamma\gamma$	(0.25 ± 0.020)
others	$< 0.2\%$

Table 2.2: Branching ratio of the Higgs boson for each decay channel [3].

The ATLAS collaboration exploits different final states in the measurement of the Higgs self-coupling. The analysis developed in the chapter 7 of this thesis concerns multi-lepton final states.

Assuming that $\lambda_3 = \lambda_3^{SM}$, the Higgs self-coupling is not expected to be measured until the High-luminosity phase of the LHC, it is possible to constrain BSM theories. The objective is to measure a limit over the λ_3 value. The relation between the cross-section of the di-Higgs production and the Higgs self-coupling, expressed as $\kappa_{\lambda_3} = \frac{\lambda_3}{\lambda_3^{SM}}$ is shown in figure 2.3.

Figure 2.4 shows two $gg \to HH$ processes, one via the Higgs self-coupling and one via a top quark square loop. The first diagram is dependent on the λ_3 and the top quark Yukawa coupling y_t while the second is only dependent on y_t^2. These two diagrams will interfere and it causes the shape of the cross-section/κ_{λ_3} function seen in figure 2.3. The rest of the production has, as ggF HH, a destructive interference diagram.

	$b\bar{b}$	W^+W^-	gg	$\tau\bar{\tau}$	$c\bar{c}$
$b\bar{b}$	33.9				
W^+W^-	24.9	4.6			
gg	9.5	3.5	0.7		
$\tau\bar{\tau}$	7.3	2.7	1.0	0.4	
$c\bar{c}$	3.4	1.2	0.5	0.4	
Z^+Z^-	3.1	1.1	0.4	0.3	0.2
$\gamma\gamma$	0.3	0.1			

Table 2.3: Branching ratio of the decay of a Higgs pair according to the final state in %.

2.3 Monte Carlo Simulation Chain

In High Energy Physics, the Monte Carlo (MC) event generators are widely used in experimentalists' analysis but also by theorists. These generators are extremely important for developing predictions for collider experiments, developing techniques and verifying theoretical models. This section aims to explain the physics and the methodology behind the production of MC samples. There are several MC event generators, specialized in LHC physics and ATLAS detectors. Even if the structure of each generator is similar to the others, each generator uses different parameters and models. As a consequence, the choice of the generator needs to be considered and will be added as a systematic uncertainty in the analysis. These simulations are done following different consecutive steps, the event generator, the detector simulation and the digitization, as shown in figure 2.5. The simulations are then reconstructed and derived to be used by analysers.

2.3.1 Hard scattering

Event simulation in Monte Carlo event generators starts with the computation of the hard scattering cross section by considering all Feynman diagrams up to a given order in perturbation theory. In a proton-proton collision, the total cross-section for the flux of the incoming

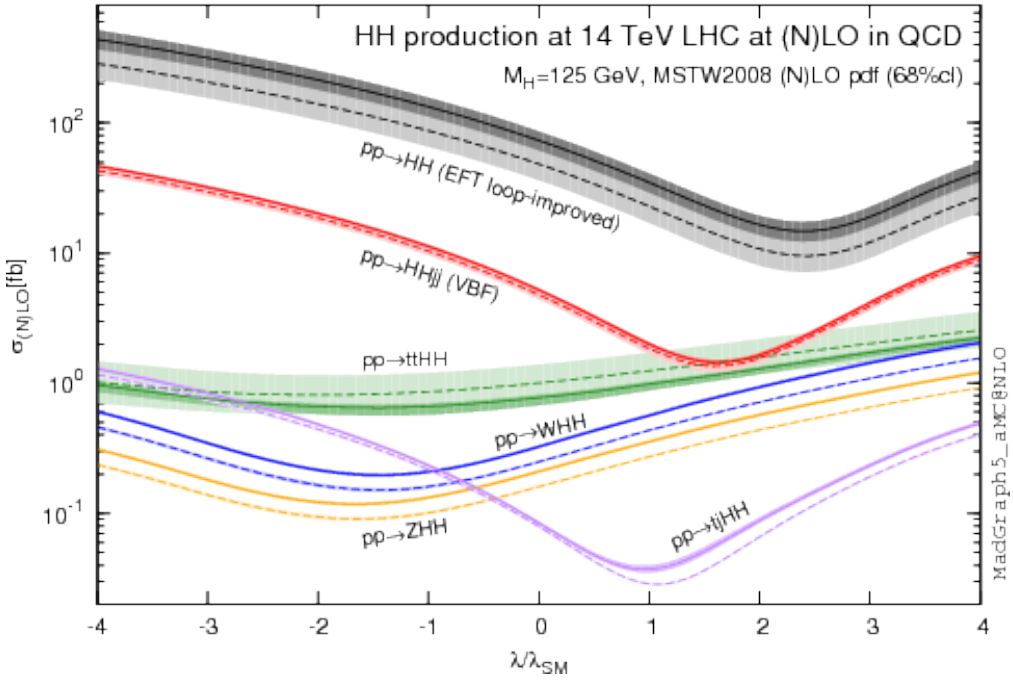

Figure 2.3: Evolution of cross-section of each production mode of the Higgs pair as a function of the $\kappa_{\lambda_3} = \frac{\lambda_3}{\lambda_3^{SM}}$

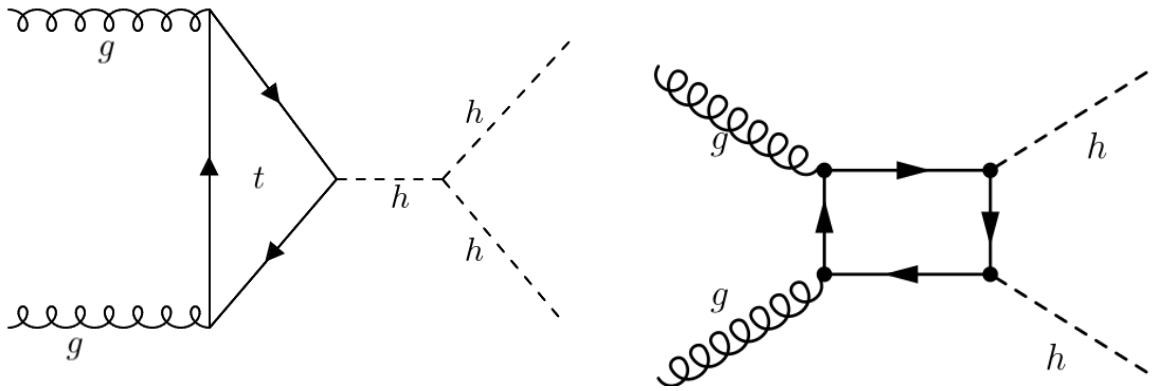

(a) Via Higgs self-coupling

(b) Via top loop box

Figure 2.4: Gluon gluon fusion involving a Higgs self coupling for figure 2.4a or involving a top quark square loop for figure 2.4b

partons i and j in the two incoming hadrons A and B can be written as :

$$\sigma = \sum_{i,j} \int\int\int dx_1 dx_2 dt f_i^{(A)}(x_1, Q^2) f_j^{(B)}(x_2, Q^2) \frac{d\sigma_{i,j}}{dt}$$

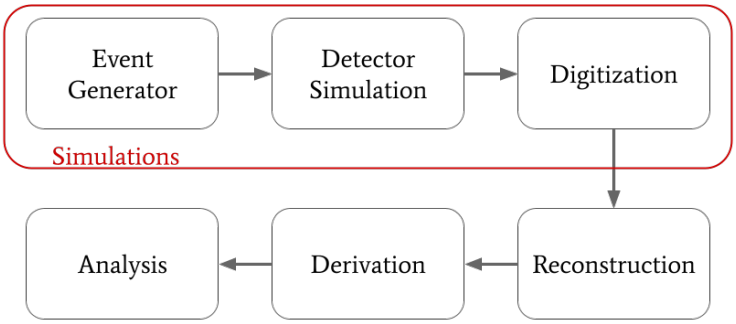

Figure 2.5: The ATLAS MC simulation flow. The grey boxes represent the different algorithms. The simulation includes three algorithms: the generation of the primary particles from LHC collisions, the simulation of the detector's response and the digitization of the data. The reconstruction transforms the output of the digitization into physics objects. The derivation is like applying a filter of the physics objects to produce usable data for analysis.

where x is the momentum fraction of partons and f, corresponds to the parton density function. Usually these calculations are done at next-to-leading-order (NLO) precision but complex processes or rare processes can be computed respectively at leading-order (LO) and next-next-to-leading-order (NNLO).

2.3.2 Parton Shower

The parton shower refers to the cascade of partons induced by the accelerated coloured partons that emit gluons. These colour charge carriers can therefore emit further radiations, leading to the cascade. This principle is a higher-order correction of the previous hard process, but due to the difficulty in calculating the higher-order correction, an approximation is used. The collinear parton splitting and the soft gluon emission create the initial (Final) state radiations.

2.3.3 Hadronization

The previous process is based on perturbative QCD but the parton is not the final state particle that comes out of the collision and that is detected. Hadronization is a nonperturbative process to describe the transition from partons to hadrons. Two hadronization models are mostly used in the ATLAS MC simulation: the Lund String model [25] in Pythia and the cluster model [26] in Herwig.

2.3.4 Underlying events

The underlying event is an important element of the hadronic environment. It describes all additional activity in a hadronic collision on top of the hard process. These events are generally a source of additional soft and semi-hard jets.

2.3.5 Monte Carlo generators used in the analysis

In the CERN collaboration, there are various Monte Carlo simulation generators. Each model is based on various assumptions, parameter values can differ as well as the implementation. It implies that the simulation needs to be evaluated and compared with other generators. The analysis presented in chapter 7 has been done using the three following generators:

- Pythia: This generator contains a multitude of theories and models for different aspects. It is possible to simulate hard and soft interaction, parton distribution, IFS parton showers or multiparton interactions. For the hadronization, Pythia uses the string fragmentation model instead of the cluster model as Herwig and Sherpa. In general, Pythia is combined with Matrix element generator.

- Herwig: This generator is a multipurpose generator but it is particularly efficient on the QCD calculations. It used an angular-ordered parton shower.

- Sherpa for Simulation of High-Energy Reactions of PArticles: This generator can provide simulation in LO and NLO accuracy.

- MadGraph_aMC@NLO : This generator is a matrix element MC generator, which computes hard process calculations at NLO or LO accuracy. It is combined with Pythia for the parton showering.

Chapter 3

Large Hadron Collider and ATLAS Experiment

This chapter presents an overview of the experimental context of this thesis. An overview of the CERN and the Large Hadron Collider is given in sections 3.1 and 3.2. Then section 3.3 presents the ATLAS detector, which is the subject of this thesis.

3.1 The CERN

The European Organisation for Nuclear Research, known as CERN for 'Conseil Européen pour la Recherche Nucléaire', is an international organisation dedicated to the research in particle Physics. It was initially founded after the Second World War, by 12 European countries, as a way to stop the European brain drain and to gather European countries together. In 1954, the construction of the CERN began at the Franco-Swiss border (next to Geneva). Now, CERN is a symbol of an international collaboration, where physicists can deal with nuclear physics in-depth, without a link to military requirements, and all results of its theoretical or experimental work are made public, see figure 3.1.
The accelerator complex is composed of 11 accelerators shown in figure 3.2. This accelerator complex is a succession of machines that accelerate the particle beam to higher energy before injecting it into the next machine. The Large Hadron Collider (LHC) is the last accelerator or the chain, it remains the most powerful and the largest particle accelerator in the world.

3.2 Large hadron collider - LHC

The Large Hadron Collider (LHC) is placed in an underground tunnel with a 26.7 km ring of superconducting magnets with accelerating components along the path to raise or maintain particles' energy. The LHC is specialised in the collision of hadrons, using mainly protons

Article II

Purposes

1. The Organization shall provide for collaboration among European States in nuclear research of a pure scientific and fundamental character, and in research essentially related thereto. The Organization shall have no concern with work for military requirements and the results of its experimental and theoretical work shall be published or otherwise made generally available.

Figure 3.1: Extract of the original CERN convention, second article [27]

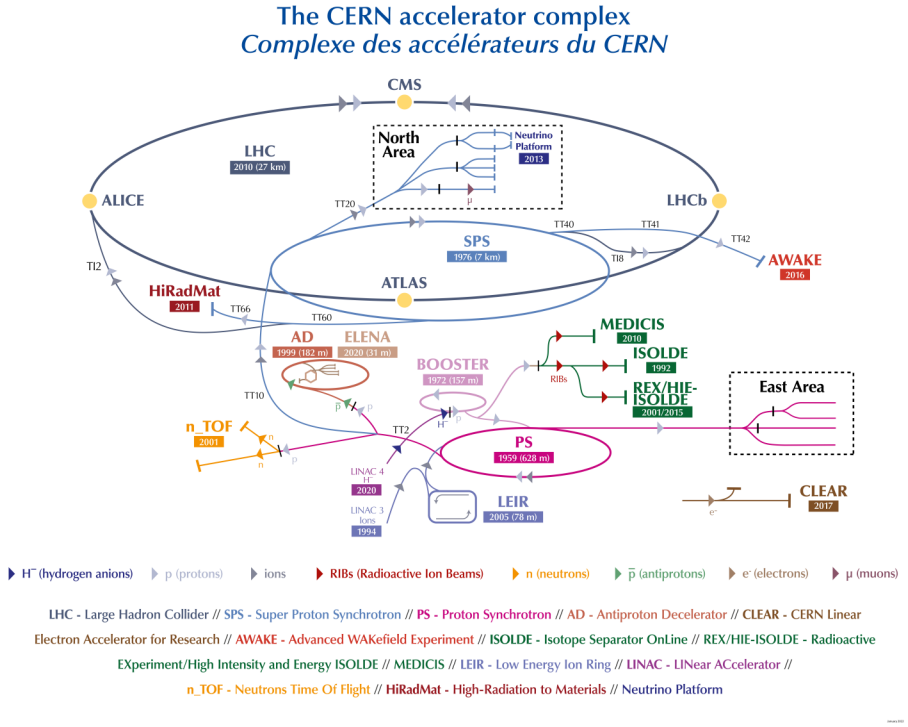

Figure 3.2: CERN accelerator complex [28]

and punctually lead ions to study the particles. Protons are accelerated up to 99.9999991% speed of light in opposite directions and collide at four different points corresponding to the 4 major experiments of LHC.

- **A Large Ion Collider Experiment (ALICE)** is a detector dedicated to heavy-ion physics and especially to the exploration of the quark-gluon plasma and understanding quark deconfinement. This detector has been optimized to study heavy ion (Pb-Pb

nuclei) collisions at a centre of mass energy of up to 5.02 TeV per nucleon pair, creating states of matter similar to those formed just after the Big Bang.

- **A Toroidal LHC ApparatuS (ATLAS)** is a general experiment investigating a large range of physics, including the characterisation of the Higgs boson and the dark matter. As this detector is the main purpose of my work, the ATLAS detector is described in section 3.3.
- The **Compact Muon Solenoid (CMS)** is the second general purpose detector. Its physics program and scientific goals are similar to ATLAS, but technologies and design differ. The design of the CMS includes a huge solenoid magnet formed by a cylindrical coil of superconducting fibres in the centre of the detector and concentric layers of components (tracker, calorimeters and muons chambers) [29].
- **Large Hadron Collider beauty (LHCb)** is specialised in the investigation of rare decays of B hadrons and precise measurements of CP violation. These investigations will pave the way to the understanding of the matter/anti-matter differences through beauty quark searches. This detector is built of a series of subsystems designed to detect forward particles.

In addition, the LHC serves for five smaller experiments as TOTEM and LHCf, respectively placed on the forward region of CMS and ATLAS experiments, far from the interaction point to focus on the forward particles. MoEDAL-MAPP is situated close to the LHCb interaction point and is involved in the search for magnetic monopoles. FASER and SND@LHC are placed close to the ATLAS experiment and are focused on new light particles and neutrino searches.

3.3 ATLAS Detector

ATLAS (A Toroidal LHC ApparatuS) is one of the 2 general-purpose detectors at the LHC. It has been designed in order to investigate a wide range of Physics, from the search of particles included in the Standard Model, such as the Higgs boson, to the Beyond Standard Model searches, including extra dimensions studies. This detector is located at the point P1 interaction site, in a cavern 100 m underground.
The ATLAS detector is composed of a multitude of layers, measuring 46 m long, 25 m high and 25 m wide. This 7000-tonne detector is the largest particle detector ever constructed. This detector has to detect the track of millions of particles with a 10 µm spatial resolution in a $23 \times 10^3\,\mathrm{m}^3$ volume.

3.3.1 Coordinate system in ATLAS

ATLAS uses a right-handed coordinate system, as shown in figure 3.3, with a centre set at the interaction point. The x-axis points radially toward the interaction point, the z-axis points in the axis of the beamline and the y-axis is defined upward to the x-z surface.

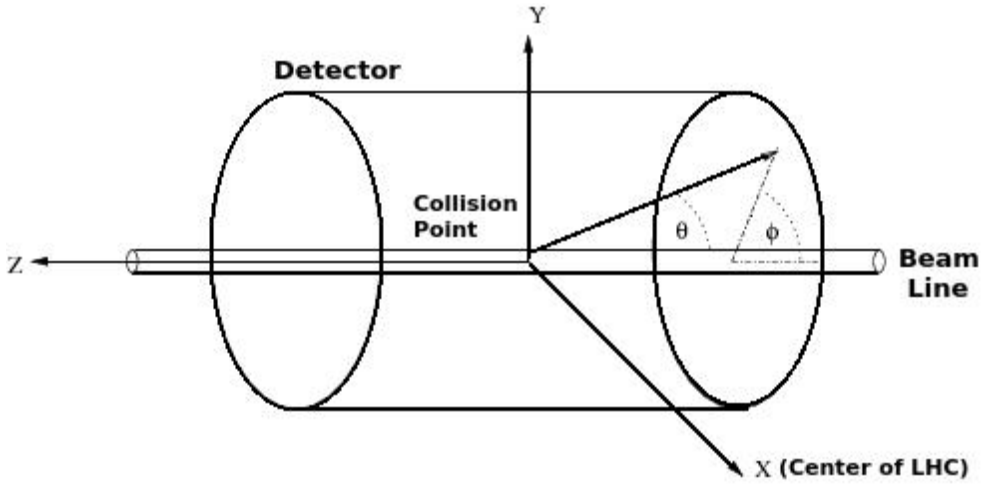

Figure 3.3: Coordinate system in the ATLAS detector [30]

In this coordinate system, the polar angle (θ) and the azimuthal angle (ϕ) are defined as the angle from the beam axis and the angle measured around the beam in the x-y plane, respectively. Using these coordinates various particle characteristics can be measured.

- The momentum vector of each particle can be written as $p = (p_T cos(\phi), p_T sin(\phi), pz)$ with p_T the transverse momentum defined as $p_T = |p| sin(\theta)$
- The polar angle is meanly used through the pseudo-rapidity parameter defined as: $\eta = -ln(tan(\frac{\theta}{2}))$.
- The angular distance in the $\phi - \eta$ plane between two particles can be defined as: $\Delta R = \sqrt{\Delta\phi^2 + \Delta\eta^2}$

3.3.2 The magnet system

The measurement of momentum and charge for charged particles is allowed by the bending of trajectories. The ATLAS detector is equipped with a magnet system based on 2 superconducting magnet systems: solenoid and toroidal magnets. The magnet structure is shown in figure 3.4.
The central solenoid magnet surrounds the inner detector close to the interaction point. This powerful magnet provides a 2 T magnetic field in 4.5 cm thickness. This thickness has been

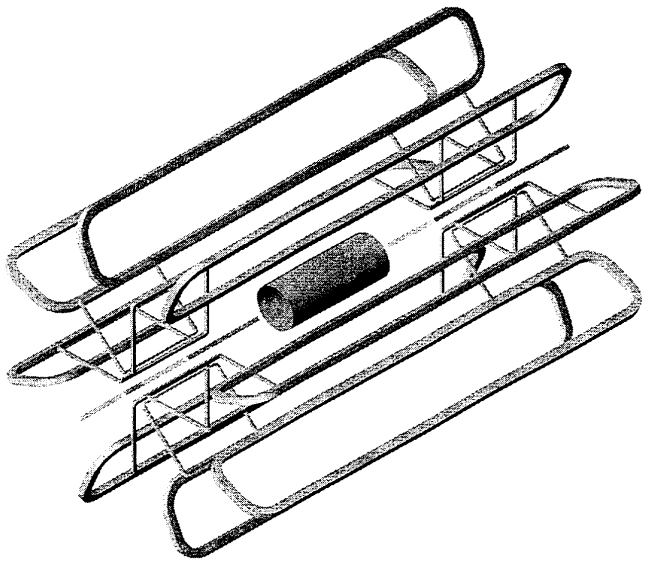

Figure 3.4: Magnet structure of ATLAS detector [31].

optimized in order to minimize the impact of the layout on the calorimeter performances. It results in a contribution of the solenoid assembly at ∼0.66 radiation lengths at normal incidence. ATLAS uses 3 toroid magnets: 2 placed at the end of the detector and another surrounding the centre of the experiment. The latest, called air-core barrel toroid (BT), measures 25.3 m in length, and remains the largest toroidal magnet ever constructed. The 2 air-cored End-Cap Toroids (ECT) are aimed to extend the magnetic field to particles leaving the detector at a small angle with respect to the beamline. Each toroid magnet provides a 3.5 T magnetic field.

3.3.3 The Inner Detector

The Inner Detector (ID) [32] is the closest to the interaction point and measures the direction, the momentum and the charge of charged particles produced during collisions. This detector is made of 3 main components developed below and shown in figure 3.5.

- The Pixel Detector: This detector is the first point of detection (at 3.3 cm from the interaction point). It is made of 92 million silicon pixels divided into four layers. The size of a pixel varies from 50 µm×250 µm for the internal layer and 50 µm×400 µm for the external layer. The deposited energy left when a particle crosses the detector is recorded. Then the signal is measured with a precision of 10 µm to determine the origin and the momentum of the particle. These silicon sensors provide at least three measurements per track. The innermost layer is essential for the identification of jets from

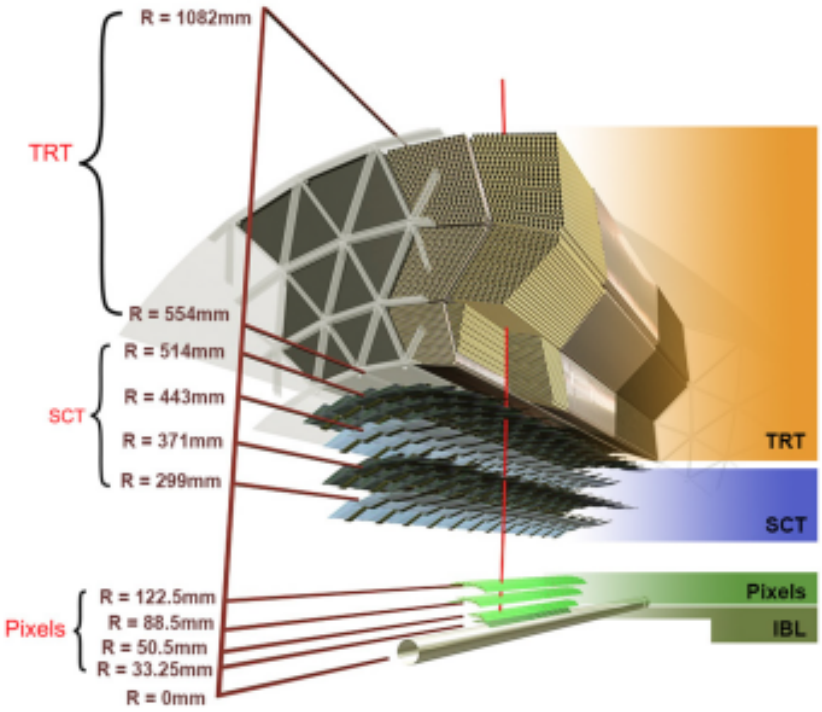

Figure 3.5: Structure of the ATLAS Inner Tracking detector [33]

a b quark decays (b-tagging) because it determines the impact parameter resolution.

- The SCT: This detector surrounds the previous detector. It is made of 6 million 'micro-strips' silicon detectors divided into two double layers of silicon. The SCT provides between four and nine measurements per particle with a precision of up to 25 µm.

- The Transition Radiation Tracker: This detector is the latest layer of the inner detector and is composed of 300000 thin-walled drift tubes. It identifies the particle through the detection of the transition radiation. When the particle crosses the detector, it will ionise the gas mixture inside and create a detectable signal that, for a given momentum, will differ from a photon, an electron or charged hadrons.

3.3.4 The Calorimeter System

The calorimeter is dedicated to the identification and characterization of hadrons, electrons and photons. The composition of these sub-detectors forces them to leave their energy and as a consequence they are stopped in the detector. Two kinds of calorimeters are mounted

in the ATLAS cavern: the electromagnetic calorimeter and the hadronic calorimeter. Figure 3.6 shows the structure of the calorimeter system.

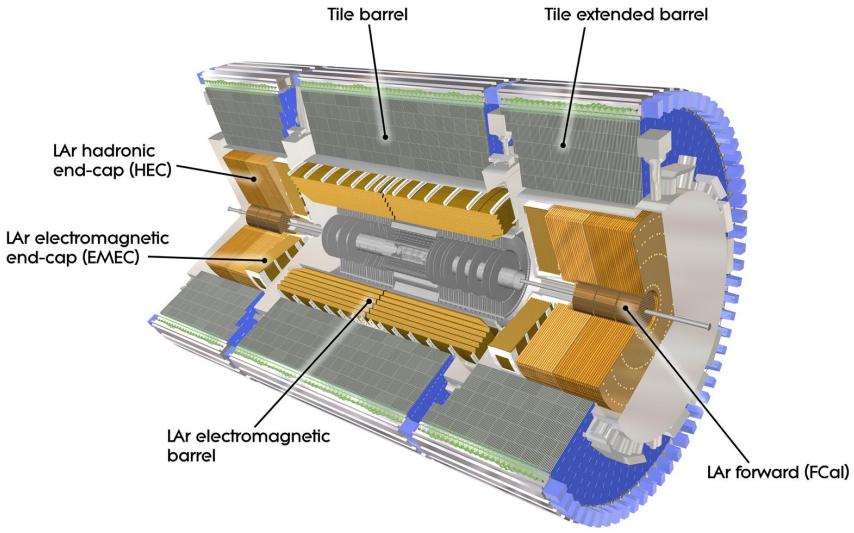

Figure 3.6: Composition of the hadronic and electromagnetic calorimeters in the ATLAS experiment [34].

- The Liquid Argon Calorimeter [35]: The structure of this detector is made of layers of metal (lead), dedicated to the conversion of the incoming particle into a shower of lower energy particles. Between each layer, liquid argon is present to be ionised by particles, creating an electric current. The argon is kept to its liquid form thanks to a charged very low working temperature, at $-184\,°\mathrm{C}$. The 'accordion-shape' provides full coverage in ϕ and a fast extraction of the signal. The combination of all currents can be assimilated with the energy of the initial particle. This detector is made of a barrel covering the regions up to $|\eta| < 2.5$, two detectors covering a larger range of pseudo-rapidity (up to $|\eta| < 3.2$) and the forward calorimeter for particles with a pseudo rapidity between 3.2 and 4.9. Mainly designed for the characterization of electrons and photons, a part of the LAr calorimeter is dedicated to the detection of hadrons. The forward detector has been designed differently and is made of a Tungsten slug structure filled with electrode tubes. The LAr calorimeter covers a large dynamic range (from 10 MeV to few TeV).The energy resolution is conventionally depending of the particle energy such as:

$$\frac{\sigma_E}{E} = \frac{a}{E} \otimes \frac{b}{\sqrt{E}} \otimes c$$

with a the noise term, b is the sampling term and c the constant term (imperfections in the detector system). A brief summary of the resolution and coverage of each calorimeter is provided in table 3.1.

- The Tile Hadronic Calorimeter [36]: The Tile surrounds the different parts of the LAr calorimeter and is dedicated to the measurement of hadronic particle energy which did not depose all their energy in the LAr Calorimeter. It is composed of 420000 plastic scintillator tiles, layers of steel and 9500 photo-multiplier tubes. When a particle crosses this detector, the interaction with the steel generates a shower. Light generated in the scintillating tiles is collected on two sides of the tile and transmitted via fibres to photomultiplier tubes (PMTs). The intensity of the resulting current depends on the original particle's energy.

Detector	Design resolution	Coverage
Electromagnetic Calorimeter	$\frac{10\%}{\sqrt{E(GeV)}} \otimes 0.7\%$	$\|\eta\| < 3.2$
Hadronic End-cap Calorimeter	$\frac{50\%}{\sqrt{E(GeV)}} \otimes 3\%$	$1.5 < \|\eta\| < 3.2$
Forward Calorimeter	$\frac{100\%}{\sqrt{E(GeV)}} \otimes 10\%$	$3.1 < \|\eta\| < 4.9$
Tile Hadronic Calorimeter	$\frac{50\%}{\sqrt{E(GeV)}} \otimes 3\%$	$0.8 < \|\eta\| < 1.7$

Table 3.1: Design energy resolution and coverage for each subdetector of both calorimeters.

3.3.5 The Muon Spectrometer

The outer layer of the ATLAS detector is the muon spectrometer [37]. As a heavy charged particle which does not interact strongly, the muons are not stopped by the layers of calorimeters. Their momentum is measured from the magnetic deflection of tracks induced by toroidal magnets. Depending on the incidence of the muons, various technologies will be used to measure the position of muons with an accuracy of less than 0.1 mm. The structure of the spectrometer is shown in figure 3.7.
The Monitored Drift Tubes (MDT) and the Cathode strip chambers (CSC) provide accurate measurement of the track coordinates. The MDT covers almost all η-ranges while CSC covers a range $2 < |\eta| < 2.7$. In the barrel and end-cap regions, Resistive Plate Chambers and Thin Gap Chambers are respectively used. These latest chambers are used in the trigger system, providing precise timing measurements (between 1 ns to 3 ns), a well-defined transverse impulsion and coordinates.

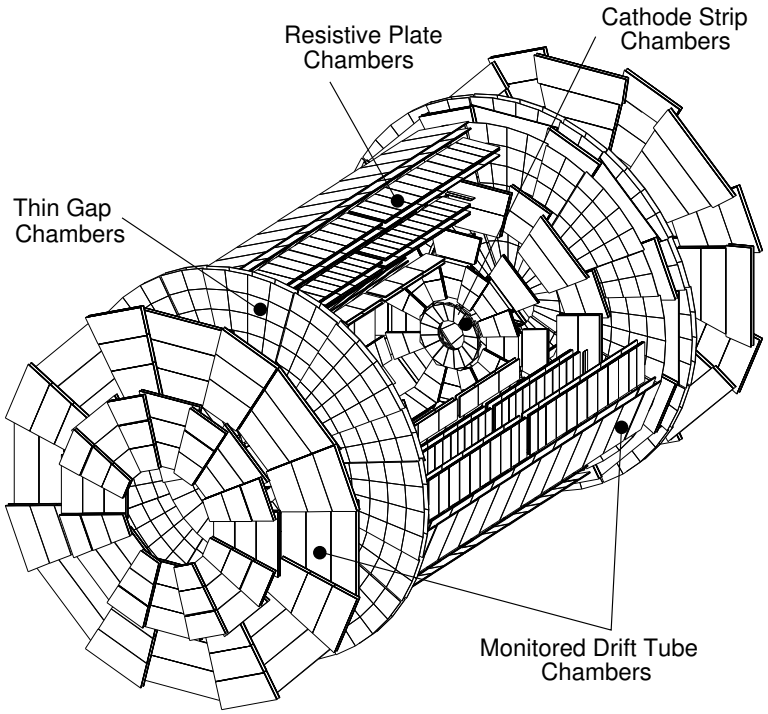

Figure 3.7: Muons spectrometer structure of the ATLAS experiment [37].

3.4 Trigger and Data Acquisition Systems

The LHC was initially designed for an instantaneous luminosity of $10^{34}\,\mathrm{cm\,s^{-1}}$ with a bunch-crossing rate of 25 ns (40 MHz). Each bunch-crossing will generate an average of 20 interactions, leading to an incoming data flow volume higher than 60 million megabytes per second. Only a part of these events will contain interesting characteristics for discoveries. To reduce this flow of data, ATLAS uses a trigger and data acquisition system (TDAQ) [38], designed to pick the physics of interest with high efficiency and an event rate of 200 Hz (300 MB/s). The ATLAS trigger system is performed in two stages to reduce the bandwidth.

Hardware-based Level 1 trigger (L1) is the first step of the system, it works on a set of information from calorimeters and muon spectrometers. It extracts events with high transverse momentum objects and defines a region of interest (ROI) in less than 2.5 µs. For events passing the selection, they pass on to the second trigger level.

High-Level Trigger (HLT or L2) is the software-based trigger, composed of fast and complex algorithms that conduct in 200 µs very detailed analyses on the reconstruction and identification of particles. The second trigger level will select an average of 1000 events per second and passes them to the data acquisition system for offline analysis.
The Data Acquisition system (DAQ) monitors the data storage and is in charge of the collection of the detector data (Read-out detectors - RODs), the digital conversion and the transfer to the permanent storage of CERN. The working principle of the DAQ and its exchanges with the trigger system is shown in figure 3.8.

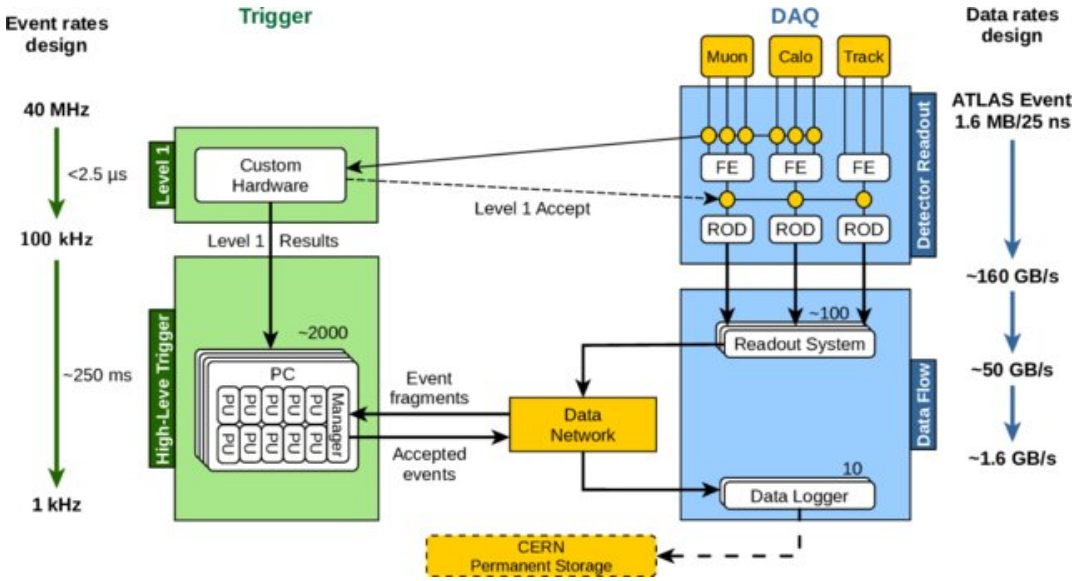

Figure 3.8: Schematic representation of the TDAQ system [39].

3.5 Luminosity measurement

The luminosity in pp collisions can be calculated as:

$$L = \frac{R_{inel}}{\sigma_{inel}} = \frac{\mu n_b f_r}{\sigma_{inel}} \tag{3.1}$$

where σ_{inel} is the cross-section of inelastic collision, R_{inel} is the rate which depends on the revolution frequency (f_r), the number of bunch pairs per revolution (n_b) and the average number of inelastic interactions per bunch-crossing (μ).

ATLAS uses two dedicated detectors to monitor with precision the luminosity, with different performances, acceptance and efficiency:

- The Beam Condition Monitor (BCM) is based on radiation hard pCVD diamond sensors mounted around the beam pipe, in the Pixel detector ($|\eta| \sim 4$). This detector uses fast and radiation-tolerant electronics to measure the difference in time of flight between the forward and backward stations.

- The LUminosity measurement using Cherenkov Integrating Detector (LUCID) is placed at $\sim$17 m from the interaction point. This detector is focused on pp inelastic scattering in the η-range $5.6 < |\eta| \sim 4$. This system is a Cherenkov detector.

More details on the luminosity measurement can be found in [40].

The integrated luminosity is defined as the time integration of the instantaneous luminosity and expressed in inverse femtobarns fb^{-1}. This measure is used to quantify the amount of data delivered by the LHC or recorded by the ATLAS detector. During the second run of the LHC, from 2015 to 2018, the ATLAS detector recorded 147 fb^{-1} at 13 TeV centre-of-mass energy, either 94 % of the LHC delivered luminosity. Then the recorded data are reconstructed and data affected by data quality problems are excluded. The resulting good-for-physics proton-proton collision dataset amounted 139 fb^{-1}, either 88 % of the LHC delivered luminosity: 36 fb^{-1} in 2015-2016, 43 fb^{-1} in 2017 and 60 fb^{-1} in 2018. Figure 3.9 shows the cumulative luminosity for the Run II with ATLAS experiment.

Due to the high instantaneous luminosity delivered by bunch crossing, and the high frequency of the bunch crossing, multiple particles are produced from secondary interactions or collisions occurring between two bunches or proton cross. This effect is known as pileup and pollutes the final state of the interesting collision. Pileup is measured by the mean number of interactions per bunch crossing μ, its distribution is shown in figure 3.10 for the Run II. This source of background needs to be considered for physics analysis.

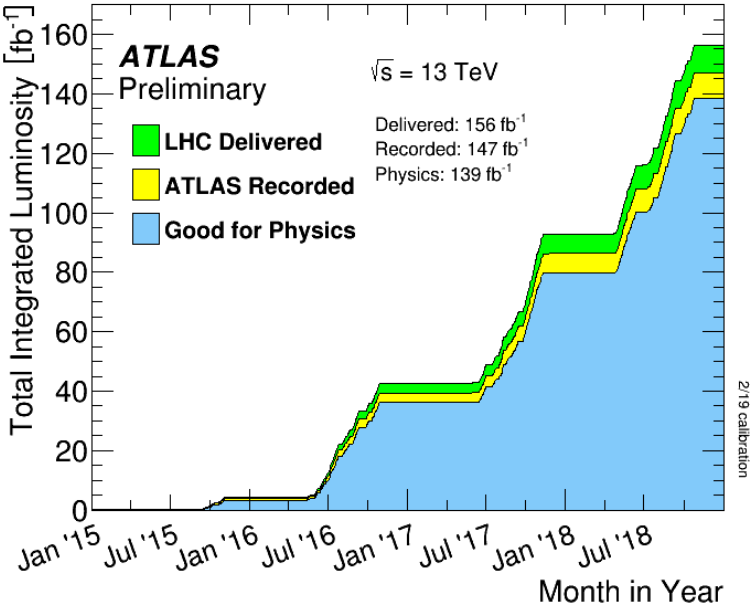

Figure 3.9: Cumulative luminosity for Run II versus the time, delivered by the LHC (in green) and recorded by the ATLAS detector (in yellow). The luminosity in blue represents the amount of data qualified as 'good for physics' [41].

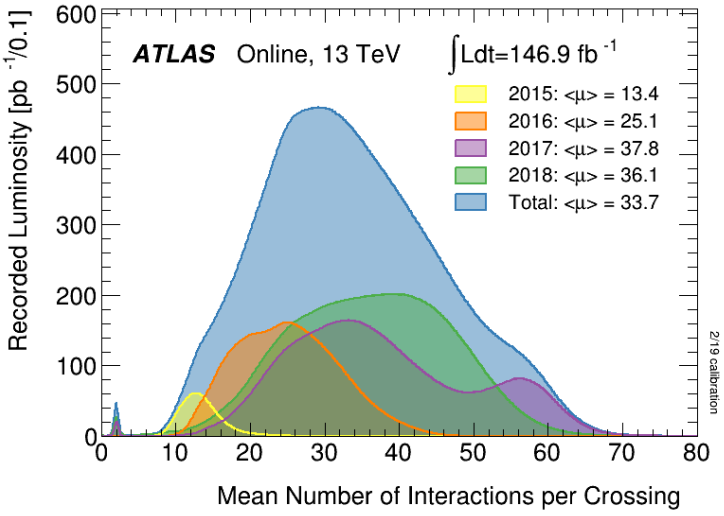

Figure 3.10: Luminosity-weighted distribution of the mean number of interactions per bunch crossing from 2015 to 2018 in the ATLAS detector [41].

Chapter 4

High luminosity upgrades and HGTD

Run 3 started in July 2022 and should end in 2024. Then the LHC will enter in its last upgrade, the high luminosity phase. Setup in 2010 by the CERN Director for Accelerators and Technology, Dr. Steve Myers, the High Luminosity LHC (HL-LHC) has been thought in order to change the strategy and merge upgrades Phase I and Phase II in one unique project. The project was financially approved in 2011, becoming the first priority of the two following decades. This project includes various upgrades and changes in each experiment and injection process to counterbalance the increase of the pileup. In the case of the ATLAS experiment, the upgrade includes the design of a High Granularity Timing Detector (HGTD) in the forward region. This chapter aims at presenting the ATLAS HGTD upgrades in the context of HL-LHC and provides several notions and keys used to describe my contribution in chapter 5.

4.1 High luminosity Large Hadron Collider

4.1.1 The project overview

After Run 3, the statistical gain in operating LHC without a significant increase of the luminosity beyond its nominal capacity will become minor. With the same characteristics, approximately ten years should be needed to halve the statistical error. As a consequence, and to respect the objective to exploit the physics potential of the LHC, the high luminosity phase of the LHC became one of the main priorities in the development of high-energy physics. To boost the potential for discoveries, the integrated luminosity will increase by a factor of 10 beyond the LHC's original design (Run 2) after 2029. The increase leads to a multiplication of the number of collisions per bunch crossing by a factor of 5 (from $\langle\mu\rangle$=30 to $\langle\mu\rangle = 200$), paving the way for the observation of rare processes.

The ambitious project is to reach the integrated luminosity up to $4000\,\mathrm{fb}^{-1}$ in 10 years of operation. Considering a 25 ns bunch gap, the instantaneous luminosity should equal $5 \times 10^{34}\,\mathrm{cm}^{-2}\,\mathrm{s}^{-1}$. This results from a complete optimisation of each luminosity-dependant parameter [42]:

- Maximization of the number of particles per bunch crossing
- Maximization of the number of bunches
- Minimization of the beam size

To maximize the productive time of the LHC, all upgrades will be installed in parallel during the long shutdown 3 (LS3) from 2025 to 2028. The general schedule of the LHC is shown in figure 4.1. These upgrades include the replacement of the inner triplet magnets and all hardware changes essential to guarantee the expected luminosity. Below, a description of the main upgrades is given for the two general experiments of the LHC: CMS and ATLAS.

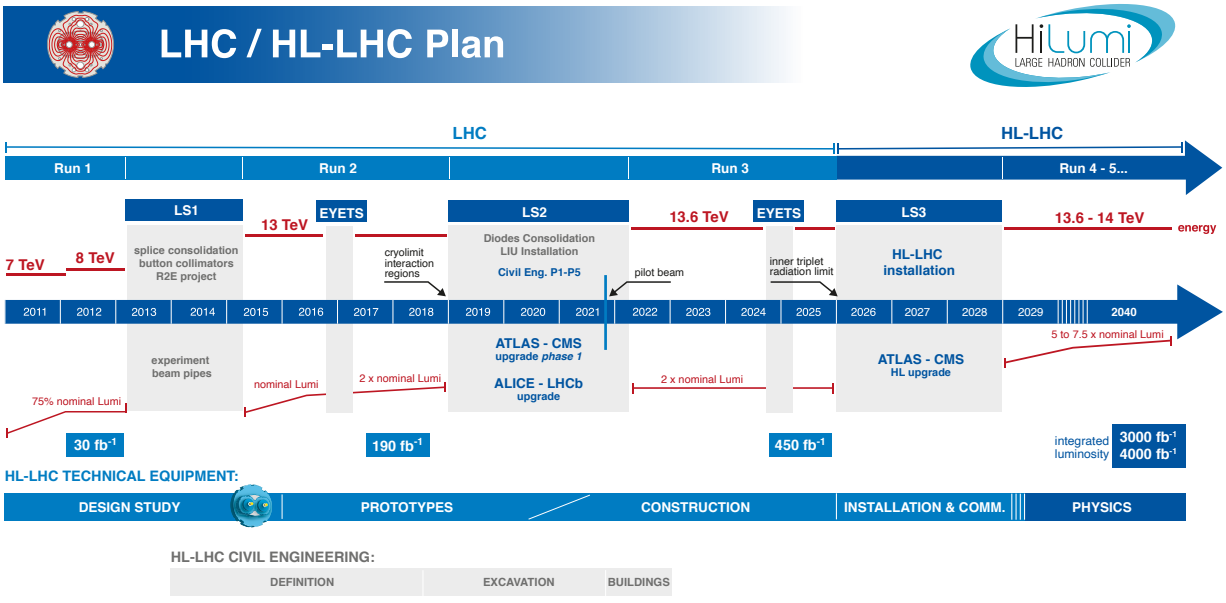

Figure 4.1: Long-term LHC planning with a projection of performances[43].

CMS

By the end of the Run III, **the tracker** and **the Calorimeter endcap** will need to be completely replaced due to significant radiation damage. The new tracker will be designed with an increase of the granularity by a factor 4 of the outer tracker and the pixel system in order to ensure an adequate track reconstruction performance. Various improvements on the outer tracker will lead to a general improvement of the p_T resolution and a lower rate of γ-conversions. The pixel system is also designed thinner and smaller to improve resolution and two-track separation.
The High Granularity Calorimeter (HGCAL) will replace the calorimeter endcaps [44] and will be composed of two sections, electromagnetic and hadronic, providing 3D shower imaging for pattern recognition. HGCAL will include around 27000 modules based on silicon sensors.

The CMS muon system will be upgraded only in terms of electronics. In fact, the detector longevity of the CMS muons system highlights that each layer will support the 10 years of HL-LHC, and keep a good muon reconstruction efficiency. The main limitation will be the radiation hardness of the electronics. The solution was to use faster communication electronics (bandwidth, optical links and to increase data transmission speed) to prevent any irradiation corruption [45].

The latency of the L1-trigger will be improved from 3.4 µs to 12.5 µs providing an adequate time for the hardware track reconstruction and the matching of the track to muons and calorimeter information. As a consequence, the L1 trigger rate will increase from 500 kHz to 750 kHz requiring an increase in the bandwidth. To follow these upgrades, the data acquisition will be upgraded to deal with a larger event size, a higher L1-trigger rate and the greater complexity of the reconstruction in a high pileup environment.

ATLAS

With an average of 200 collisions per bunch crossing, the ATLAS detector must be upgraded to correspond to the radiation environment. The radiation hardness is set to a fluence of around $1 \times 10^{16}\,\mathrm{n_{eq}/cm^2}$ and an irradiation dose up to 10 MGy. The major upgrades target the Inner Detector with the installation of a new tracker called ITk, a new timing detector called HGTD, the Liquid Argon (LAr) Calorimeter, the Tile calorimeters, the muon spectrometer and the trigger and data acquisition (TDAQ) system. Figure 4.2 represents the ATLAS detector with the key upgrades.

The Inner Tracker (ITk)[46, 47] is an all-silicon detector designed with technologies providing higher granularity and readout speed. It is made of pixels for the five first layers and made of strips for the external layers. The detector modules are mounted to form a system of cylindrical layers in the central region of the detector, called barrel layers, and a system of

rings at the two sides, called end-cap rings. The pixel and strip system is made of five barrel layers and end caps ring, and four barrel layers and six end-cap rings, respectively. The ITk detector provides highly granular coverage up to $|\eta| = 4$ with at least 9 points per track in the barrel region and 13 in the end-caps regions to improve pattern recognition. The detector will cover an area close to $180\,\mathrm{m}^2$ with more than 5 billion channels.

The new High granularity Timing Detector (HGTD)[48] is a sub-detector built to exploit the time spread of the interactions to distinguish collisions too close in space but well separated in time. This detector will be installed in a specific region with a pseudorapidity between 2.4 and 4.0, between the future ITk detector and the end-cap calorimeter. My work on the HL-LHC upgrades is about this sub-detector, so more details can be found in section 4.2.

The Liquid Argon Calorimeter is upgraded to meet the new trigger and data acquisition requirements and to resist the high expected radiation environment. The upgrades affect particularly the readout electronics of the LAr: amplifiers and shapers are changed for low-power versions [49]. Then, to be compatible with the trigger rate, the clock frequency of the digitalization of the data has been increased up to 40 MHz.

The Hadronic Tile Calorimeter (TileCal) will have its on and off detector electronics replaced during the shutdown of 2026-2028 [50]. All TileCal cells and the readout electronics are designed to work at 40 MHz, including the digitization, the signal reconstruction and the storage. This improved readout architecture allows more complex trigger algorithms that need to be developed.

The muon spectrometer upgrades consist of the installation of new detectors aiming to replace the trigger and the readout electronics in order to maintain the current MS performances and keep a low trigger threshold [51]. The small wheels are completely replaced by the new small wheels, providing the muon Level-1 trigger and maintain a good tracking at End-Cap. Then, new Monitored Drift Tubes and Resistive Plate Chambers will be installed with smaller thicknesses and higher coverage. Then as the two previous detectors, the trigger and the readout electronics have been redesigned to work at a rate of 1 MHz, using new electronics (FPGAs) allowing more complex and flexible algorithms.

The ATLAS TDAQ are improved, as for the CMS detector, to correspond to higher readout rates. These upgrades comprise a hardware-based low latency real-time trigger operating at 40 MHz, a data acquisition readout dealing with 5.2 TB/s input and an event filter running at 1 MHz, combining offline-like algorithms and hardware tracking [38]. The event filter, which consists of a CPU-based processing farm and a Hardware Track Trigger co-processor, will play a major role in the reduction of the pileup effects and will limit the final output rate to a proper disk storage value.

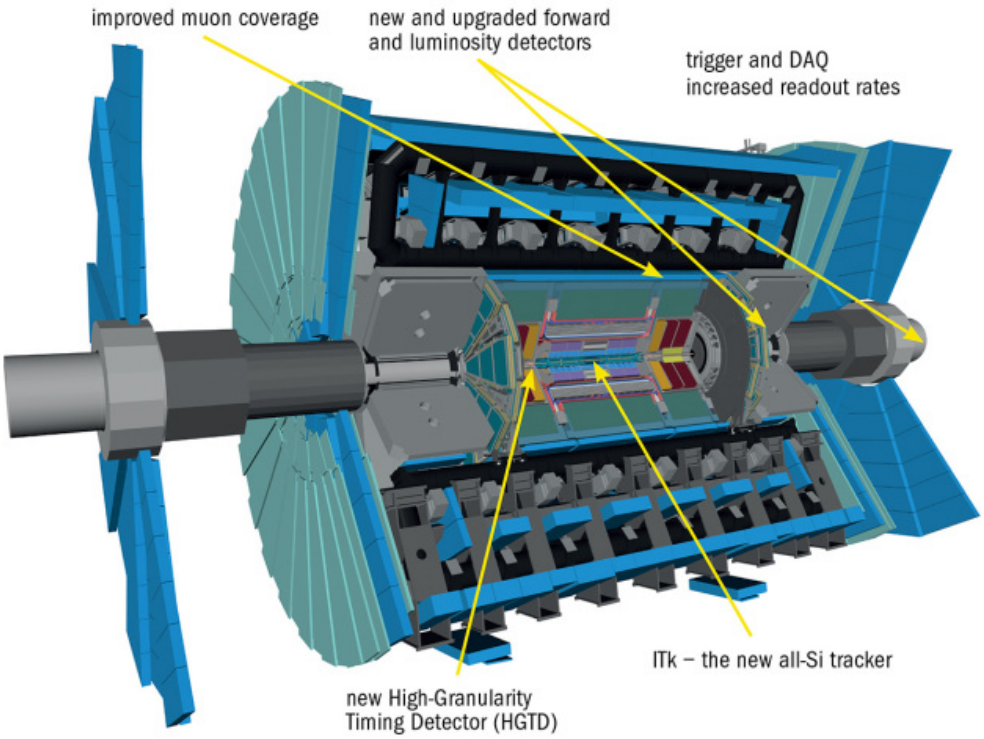

Figure 4.2: ATLAS detector with the main key upgrades [52]

4.1.2 Physics potential of HL-LHC

The HL-LHC era represents an immense physics potential to push the reach of precise and sensitive measurements well beyond what was originally assumed possible. This idea to collect data with a large integrated luminosity emerged from different exchanges on future activities during workshops. Despite the highly challenging experimental physics due to the multiplication of the number of collisions per bunch crossing, the condition will pave the way to a multitude of new or more precise measurements. With a ten-fold larger data amount than LHC, the HL-LHC era is expected to improve in particular the electroweak exploration, strong interaction field or top quark physics.

Electroweak exploration and Higgs field

The primary target of the HL-LHC era is the determination of the Higgs properties and their connection to the electroweak symmetry breaking. Since its observation in 2012, the Higgs

boson has rapidly become one of the major programs to investigate in depth as developed in chapter 2.

Strong interaction field

With the increase of the integrated luminosity, an increase in the light and heavy flavour jet production is expected as well as the photon production. This improvement will affect in addition the experimental systematic uncertainty on the jet calibration as well as the understanding of the parton density functions.

Top quark physics exploration

The HL-LHC phase will have an impact on specific processes such as 4 top quarks production. This rare process has a large sensitivity to a variety of new physics effects, from the effective field theory to anomalous top-Higgs couplings or complex QCD processes. The HL-LHC will offer the possibility to reach a top production with high rapidity, which could provide a link between top measurements performed in ATLAS or CMS experiments and LHCb. HL-LHC should be affected by the increase in the number of collisions and the diminution of the systematics in the following non-exhaustive measurement: top quark cross section, mass top quark and top quarks coupling.

A precise measurement of the luminosity

At LHC, the measurement of the production cross-section is limited by the uncertainty of the integrated luminosity. This uncertainty is currently about 2 %. The design of the upgrades has been done in order to reach an uncertainty about 1 %.

4.2 High Granularity Timing Detector - HGTD

As mentioned in the previous section, the High Granularity Timing Detector (HGTD) will be placed between the future ITk and the end-cap calorimeter, in a forward region of the current ATLAS detector covering $2.4 < |\eta| < 4.0$. The objective of this detector is to improve the reconstruction of the ATLAS detector thanks to a precise time measurement of the track. This section aims to describe the key design point of HGTD and especially introduce the Front-end electronics and the Low Gain Avalanche Detector (LGAD) technology.

4.2.1 Motivations

As developed in the chapter 2, the assignment of tracks to a primary vertex is essential in the physics analyses, especially in the b-tagging and the lepton isolation [53]. The association of

the tracks to primary vertices will become more challenging with the high pileup environment. With a maximum average of 200 simultaneous proton-proton interactions, the expected pileup density is 1.8 vertices/mm as shown in figure 4.3a. Tracks and vertices are associated if they are geometrically compatible in the longitudinal axis z. The separation of the vertices is ensured if the following equation is satisfied:

$$\frac{|z_0 - z_{vertex}|}{\sigma_{z_0}} < s_z \tag{4.1}$$

with s_Z a significance cut that equals typically 2.5 or 3, σ_{Z_0} is the per track resolution of the longitudinal impact parameter Z_0. The spatial resolution of the current ATLAS detector satisfies the previous equation 4.1 for a luminosity of $160\,\mathrm{fb}^{-1}$, corresponding to the LHC luminosity. To deal with this increase, upgrades include a replacement of the ATLAS Inner Tracker detector (ITk) and a change of trigger and data-acquisition systems. ITK has been designed to provide, at HL-LHC, similar performances than Run II LHC for a region with a pseudo-rapidity up to 2.4 as shown in figure 4.3b.

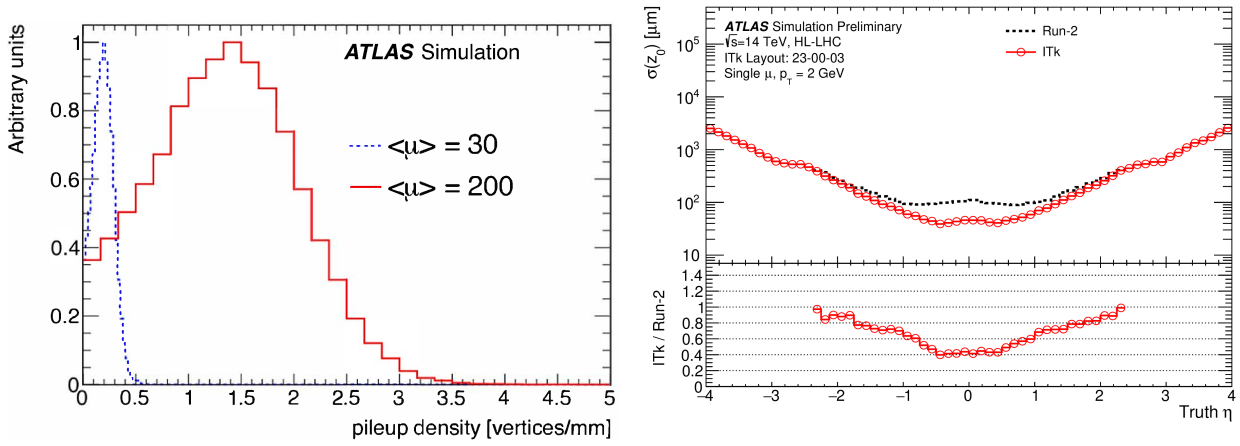

(a) (b)

Figure 4.3: (a): Pileup densities comparison for Run II and HL-LHC phase: $< \mu >= 30$ and $< \mu >= 200$. (b): Evolution of the longitudinal resolution of tracking as a function of pseudo-rapidity range $|\eta|$. [48]

In the forward region defined with an absolute pseudo-rapidity $|\eta|$ from 2.4 to 4.0, the resulting spatial resolution will decrease significantly. This latest region is called the forward region. The solution results in the combination of the longitudinal impact parameter of a track (measured by ITK) with a high-precision time measurement of all tracks associated with the primary vertex, since the two parameters are orthogonal to each other. As a consequence, an additional detector will be installed in the forward region, satisfying the following equation:

$$\frac{t_{track} - t}{\sigma_t} < s \tag{4.2}$$

with s a significance cut (set at 2 or 3), σ_t is the sum in quadrature of the vertex t and the track-time t_{track}.
The development of a timing detector as HGTD, providing the charge track-time information with a resolution of 50 ps per track, enhances the identification of the particles' tracks. HGTD will have a direct impact on ATLAS performances including the tracking of the particles.

4.2.2 From times to tracks

The association of the HGTD timing measurement to the tracks is based on a progressive extrapolation of the tracks reconstructed in the ITK, using the last measurement of the track in the inner tracker as input. The extrapolation in the HGTD surfaces is done by a progressive Kalman filter, producing clusters around the extrapolated hit for each track. The association of hits in the first active layer and the extrapolated position is performed by a Chi-squared test, satisfying at least $\chi^2/n.d.f = 5.0$. The steps are repeated for the next layers.
Each hit in the HGTD is corrected by a TOF correction in order to match the reconstructed track times and the truth track time. Simulation shows that this correction does not exceed 1 ps. This term is measured assuming the particle track between its origin and the hit as a straight line. The path divided by the speed of light and subtracted by the hit time gives the Time Of Flight (TOF) correction. The extrapolation resolution is shown in figure 4.4a. This resolution does not exceed for the majority of the track the pad size of an HGTD sensor (1.3 mm×1.3 mm). This resolution is dependent on materials used in ITk or between ITk and HGTD.

4.3 Global architecture of the High Granularity Timing Detector

The HGTD will be installed in a gap between the ITK detector and the end-cap calorimeter, in a very tiny space of 12.5 cm in z-axis, at approximately ±3.5 m from the interaction point, as shown in figure 4.5. During the Run-II, this place is occupied by the Minimum-Bias Trigger Scintillator (MBTS) which will be removed during the long shutdown LS3. The detector will cover a radius from 110 mm to 1000 mm with an active area from 120 mm to 640 mm. This active area corresponds to an absolute pseudorapidity $|\eta|$ between 2.4 and 4.0.

This detector is designed in multiple layers as shown in figure 4.6. Each HGTD end-cap is made of two instrumented double-side layers, two moderators placed on both sides of a

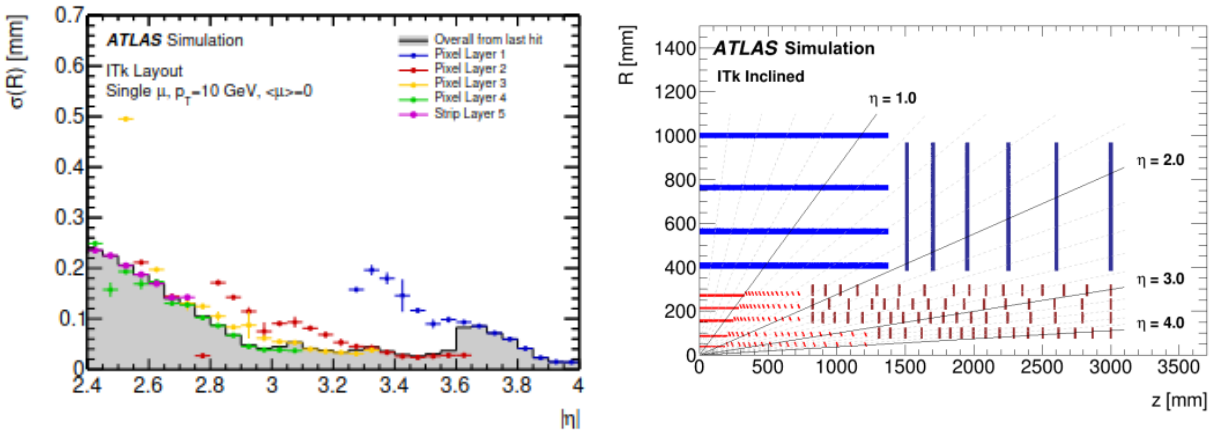

(a) (b)

Figure 4.4: Figure (a): The resolution of the extrapolation in radius to HGTD surface for tracks with a transverse impulsion $p_T = 10\,\text{GeV}$ [48]. The different colors rely from the actual layer in the ITk where the last hits are located. The structure of ITk is shown in figure 4.4b. Figure (b): Schematic layout of one quadrant of ITk. The pxel detectors are represented in red (barrel layers in light red and the end-cap ring in dark red) [54]. The active layers of the barrel and the end-cap Strip Detector are shown in blue.

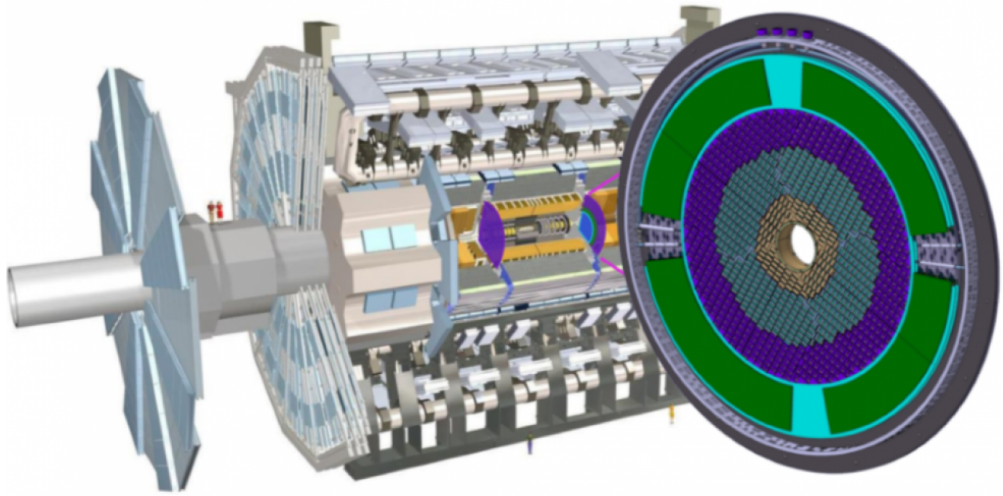

Figure 4.5: ATLAS detector with the HGTD module, installed at 3.5 from the interaction point, on both sides.[48]

hermetic vessel and support disks.

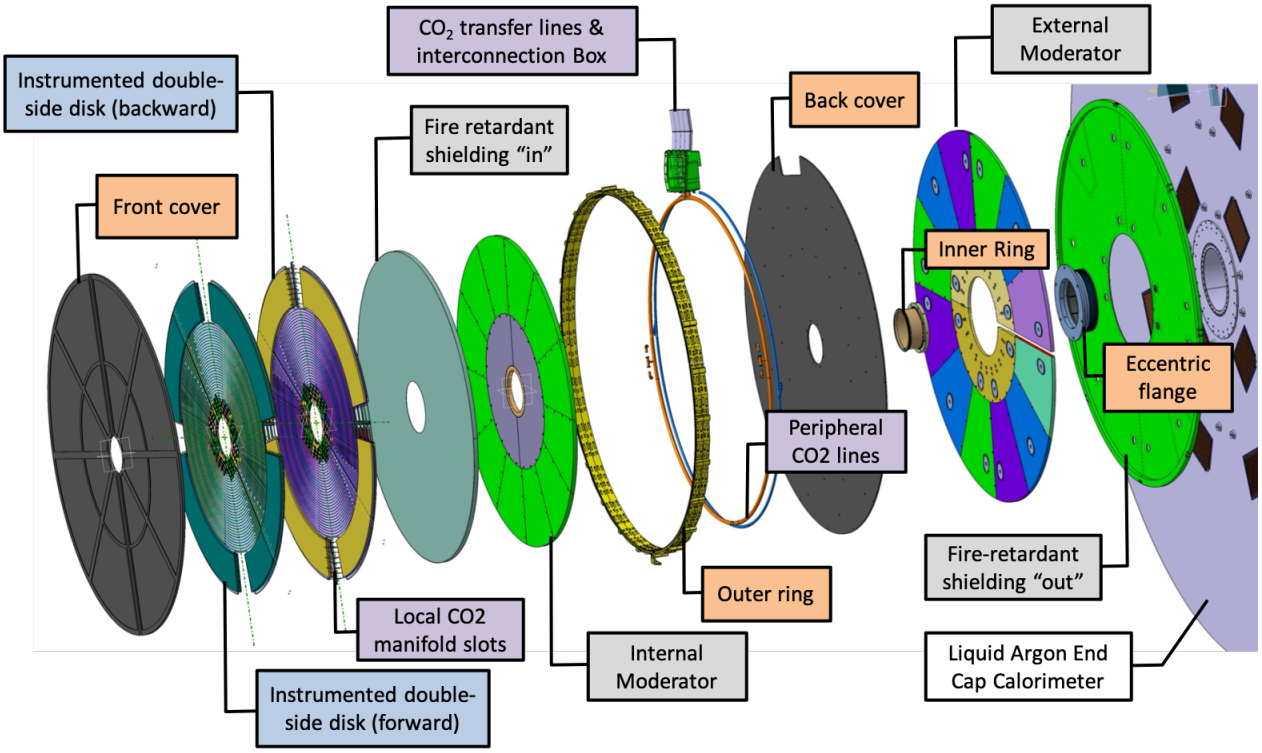

Figure 4.6: Detailed view of the different layer of the HGTD.

4.3.1 The hermetic vessel

The hermetic vessel is made of four main components, which provide a support for instrumental double-side disk, and ensure a cold and dry working environment. It includes two covers at the front and the back. Each of them is made by a sandwich structure made of two Carbon Fibre Reinforced Plastics (CRFP) separated by a Nomex honeycomb core.

4.3.2 The CO_2 cooling system

As discussed in the section 4.4, the temperature inside the vessel has to be maintained at $-35\,°C$ to prevent the increase of the LGAD leakage current. To ensure this temperature, a cooling system made of two separated half circles is designed. It will be directly integrated into the ITk system [54]. As various systems in ATLAS detectors, the cooling system is based on the 2-Phase Accumulator Controlled Loop (2PACL) developed initially for the AMS-Tracker and the LHCb-VELO CO_2 cooling systems. This system is based on the change in

phase of the CO_2 [55]. The CO_2 is one the best cooling liquids because of its high-pressure evaporation conditions, its low viscosity and high latent heat. Due to these properties, the CO_2 vapour stayed compressed in small diameter tubes and less flow is needed in the pipes to regulate temperature. The principle of the 2PACL system is shown in figure 4.7.

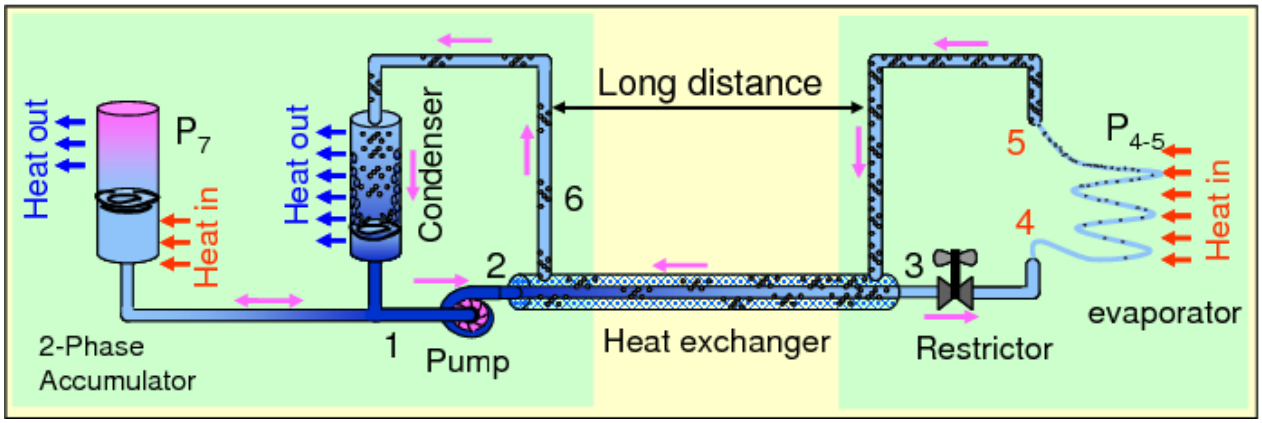

Figure 4.7: Representation of the CO_2 cooling system in the ATLAS detector [55].

In addition, considering the radiation environment of the HL-LHC phase, radiation hardness and the low activation properties of the CO_2, make it the ideal candidate.
The moderators placed in the back of the active area, with a thickness of 50 mm, are used to protect the HGTD and ITK detector from the back-scattered neutrons produced in the calorimeters.

4.3.3 The instrumented double-side layers

The instrumented area is composed of two layers of modules mounted on each side of a cooling plate. A module is composed of a Low Gain Avalanche Diode sensor bump bonded on an electronic Front-End Application-Specific Circuit (ASIC). More description on sensors and ASIC is given in the sections 4.4 and 4.5. The second instrumented layer is rotated with respect to the first layer by 20 °C to ensure optimal hit efficiency. This rotation facilitates the entrance of the cooling pipes inside the cooling disk while minimising the regions with zero hits (called dead zones) between the readout and the inner radius. The active area is divided into three areas as shown in figure 4.8:

- The inner ring: It covers a pseudorapidity from 3.5 to 4.0. In a given row, the gap between two modules equals 25.5 mm that leads to a 70% overlap of all modules and ensures an average of 2.7 hits per track in the ring.
- The middle ring: It covers the region corresponding to a pseudorapidity from 2.7 to 3.5. The modules have a step of 28.4 mm, so the overlap of 54% ensures an average of

2.5 hits per track in the ring.

- The outer ring: A pseudorapidity from to 2.7 is covered by the outer ring, made with a 20% overlap (34.5 mm step) ensures an average of 2.1 hits per track in the ring.

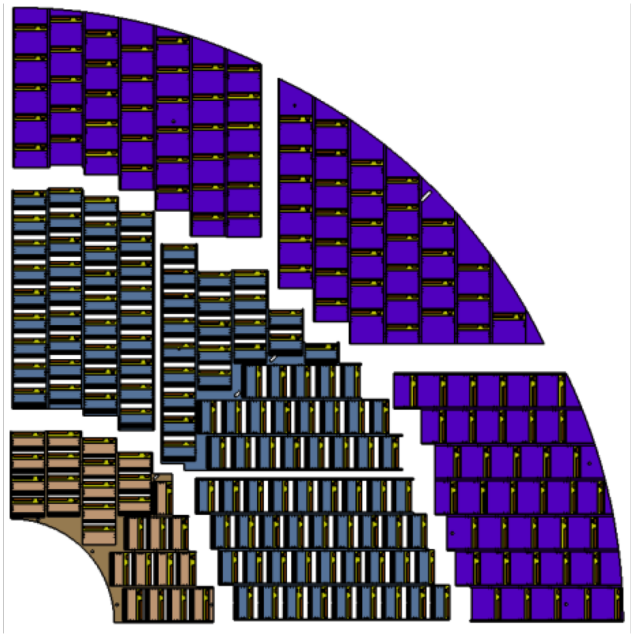

Figure 4.8: Representation of the three instrumented rings. The inner ring is represented in brown, the middle ring is in blue and the outer ring is in purple.

The choice of these three rings is motivated by the fact that the fluence and the irradiation dose received by the modules are depending on the radius, as shown in figure 4.9. As a consequence, the inner ring will be replaced every $1000\,\mathrm{fb}^{-1}$, and the middle ring will be replaced at $2000\,\mathrm{fb}^{-1}$. In addition, the rotation of the layers optimizes the overlap of the module and takes into account the space needed for the peripheral electronics and connectors. The evolution of the overlap is shown in the figure 4.10. The overlap between modules is optimized to give a uniform performance as a function of the radius.

4.3.4 Modules

The active layers of the HGTD detector will be made of 8032 modules. These fundamental units of the HGTD detector are an assembly of two parts: two Low Gain Avalanche Diode sensors bump-bonded to two ASICs and a flexible printed circuit board, see figure 4.11. The flex cable ensures the communication, the power distribution and the data transfer. The modules will be installed and glued on a support unit as shown in figure 4.8. The

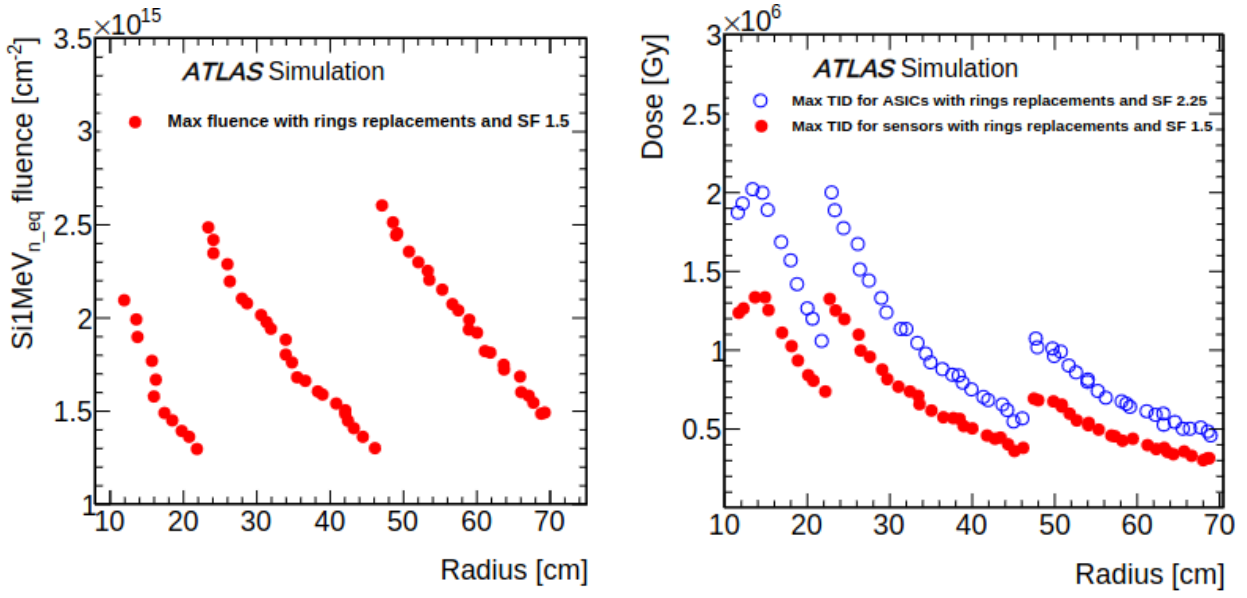

(a) (b)

Figure 4.9: Simulation of the evolution of the expected SiMeV$_{n_{eq}}$ fluence (a) and the irradiation dose (b) as a function of the radius R [48].

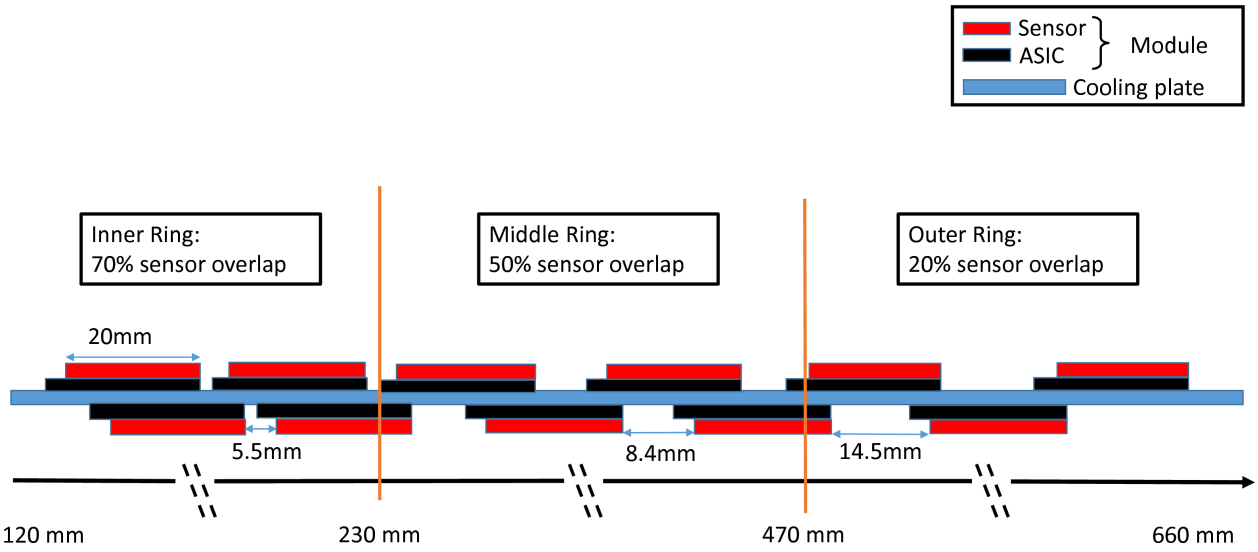

Figure 4.10: Evolution of the overlap along the instrumental area of HGTD. The overlap of the inner, middle and outer ring equal to 25.5 mm, 28.4 mm and 34.5 mm, respectively [48].

main constraints of the mechanical design arise from the very strict thickness constraints (7.5 cm) and the optimized geometry in order to get at least two hits per track. Finally, each

module will be connected to the Peripheral Electronics Boards (PEB) through a flex cable (represented in green in figure 4.5). These electronics provide the power and the clock and ensures the data transfer. One PEB receives the data of up to 55 modules, aggregates and transmits them via optical fibers at 10.24 Gbit/s to the off detector electronics. At the time of writing the thesis, the module tests and the development of the DAQ are ongoing.

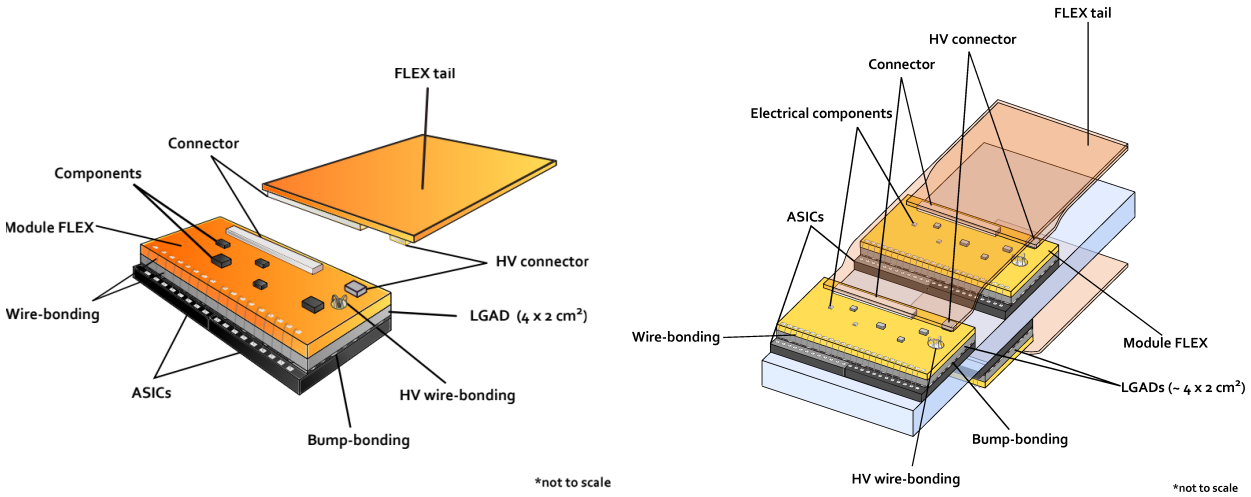

(a) (b)

Figure 4.11: Representation of an HGTD hybrid module (on left) made of a flex tail, a module flex and one LGAD bum-bonded on two ASICs. Representation of three HGTD hybrid modules (on right) mounted on the cooling plate (in blue) [48].

4.3.5 Time Resolution

As mentioned before, the main challenge in the design of the HGTD is to provide good time resolution. This time resolution can be expressed as:

$$\sigma^2_{total} = \sigma^2_{landau} + \sigma^2_{clock} + \sigma^2_{electronics}$$

with σ_{landau} is the Landau fluctuation the deposited charge in the silicon sensor, σ_{clock} is the non-deterministic and irreducible contribution of the clock and $\sigma_{electronics}$ the contribution of the electronics readout. This latest is expected to be the dominant contribution approaching the 30 ps. The landau contribution is fully dependent on the thickness of the sensor (thinner is better). With a 50 µm thick LGAD sensor, the landau contribution approaches 25 ps. The clock contribution is expected to be around 15 ps and is mainly from the low-power Gigabit Transceivers (lpGBT) and the flex cable. This lpGBT is responsible for the fast command transfer between the TDAQ and the ASIC.

The contribution of the sensor and the electronics are detailed in sections 4.4.3 and 4.5.1, respectively.

4.4 The Silicon Low Gain Avalanche Gain Diode sensors

The sensors of the future HGTD are based on doped silicon detector technology, they are called Low Gain Avalanche Detectors (LGAD). This sensor type has been specifically designed for the HGTD detector. This section describes the design and the main requirements of the LGADs.

4.4.1 Silicon detectors in High energy physics

Since the 1980s, semiconductor silicon-based detectors have been used in the detection of particles in calorimeters or as detectors. Its success is due to its abundance, the existence in nature of a silicon oxide and its possibility to create various gap properties by the injection of impurity atoms, called doping.
In a semiconductor, the concentration of holes p and of electrons n in the valence band are equal to the intrinsic concentration as $n_i = n = p = 1.45 \times 10^{10}\,cm^{-3}$ at 27 °C. The insertion of an additional state in the forbidden region increases the probability of a particle to excite electrons or holes. This process is called "doping". Depending on the type of injected impurities, the material is qualified as a n-type material or a p-type. In the first case, the alteration is done by adding an element from group V in the periodic table (with five valence electrons) as phosphorous or arsenic. It leads to an excess of electrons in the conduction band and is called donor (n>>p), as shown in figure 4.12. In the p-type case, the alteration comes from the injection of a type-III element, with three valence electrons such as boron, aluminium or gallium. This process increases the number of holes in the material and is called acceptor (p>>n), see figure 4.12.

4.4.2 Low Gain Avalanche Gain structure

The sensors designed in HGTD are based on Low Gain Avalanche Diodes (LGAD) technology. Initially designed by the Centro National de Microelectronica Barcelona in 2014 [56], LGAD technology has been developed during the last 7 years by the CERN community in order to make it a perfect candidate for the detection of the minimum ionizing particles. The idea to have an LGAD for the high luminosity phase of the LHC is built on the signal degradation induced by radiation damage that can be counterbalanced by the charge multiplication already present in unirradiated devices.

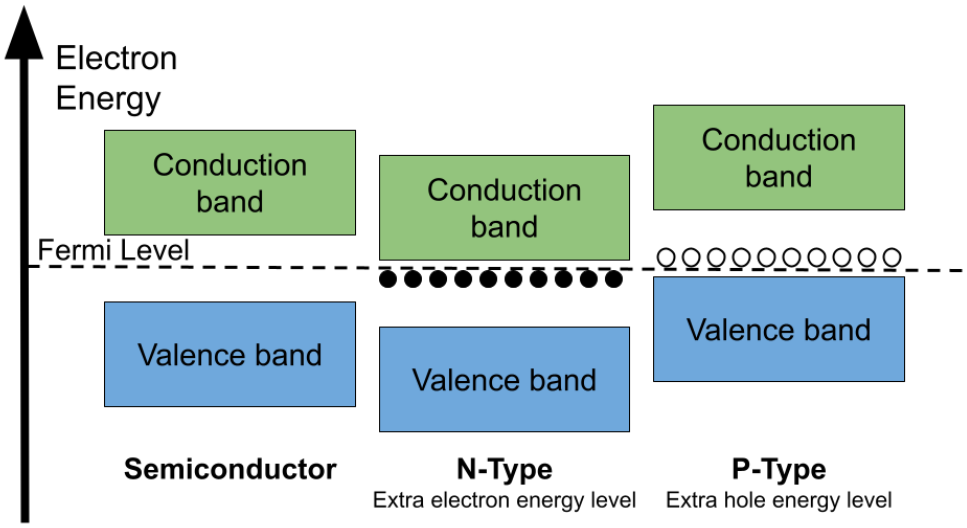

Figure 4.12: A diagram showing the valence and conduction bands of semiconductors, N-types and P-types semiconductors. The Fermi level is the name given to the highest occupied electron orbital at absolute zero temperature.

Low Gain Avalanche Diode is a recent class of silicon sensors that attracts the attention of physicists in high-energy physics due to their excellent time resolution and radiation hardness. This detector is made by a highly-doped p-layer below an n-p junction: a large and shallow n+ covering a deep p+ gain layer.

When a charged particle arrives in the detector, the drift of the charge carrier in the silicon produces a current. For electrons reaching the gain layer, the high electric field will cause an avalanche, a multiple new electrons/hole pairs are created. Gained h holes drift to the p+ region while the gained electron will be kept by the cathode. The charge amplification is referred to as the gain of the LGAD, much higher than the standard sensors, providing an excellent time resolution lower than 30 ps at the start of the HL-LHC and 70 ps at the end of the lifetime. In order to ensure a gain of 20, the active thickness (p-layer in figure 4.13) is set at 50 μm while the total thickness is set at 250 μm.

The HGTD sensors are designed and produced by various laboratories and vendors including the Centro National de Microelectronica (CNM - in Spain), Hamamatsu Photonics (HPK - in Japan), Fondazione Bruno Kessler (FBK - in Italy), Micron (in the UK), Brookhaven National Laboratory (BNL - in the USA), Institute of High energy physics for the design (IHEP - in China) and the Institute of Microelectronics of the Chinese Academy of Science for the fabrication (IME - in China), Institute of Microelectronics of the Chinese Academy of Science (China), University of Science and Technology of China (USTC - in China) and

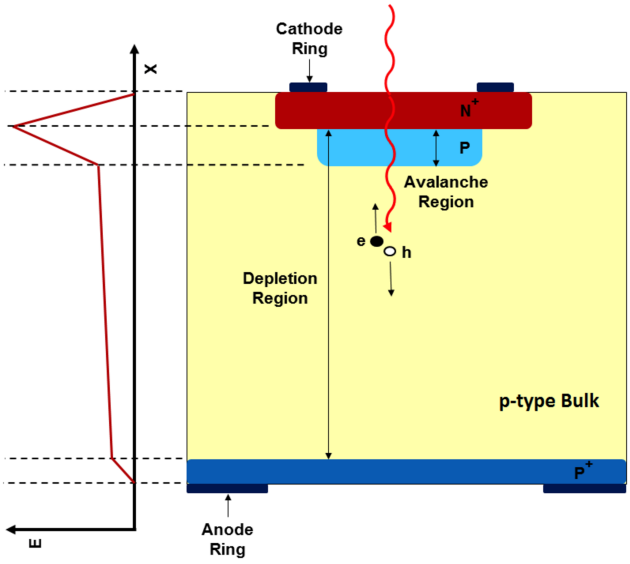

Figure 4.13: Cross section plan of a Low Gain Avalanche Diode [48]. The active area of the sensor corresponds to the p-layer region.

more recently National Nano Device Laboratory (in China). The production of the sensors is mainly done with boron as a dopant for the p-type multiplication layer. To improve the radiation hardness of the sensors, a carbon implantation has been studied, these sensors are called carbon-enriched sensors.

4.4.3 Sensors requirements for HGTD project

The design of the sensor is based on an optimal time resolution. The following table 4.1, lists the different parameters and requirements for the design of the LGAD sensor.
The sensitive point of this design will be based on the optimal time resolution objective. As the main contribution of the sensor to this time resolution is based on the landau distribution, the active thickness is settled at 50 µm. The landau fluctuation corresponds to the non-uniform deposit charge along the particle path in the sensor. Considering an active thickness of 50 µm, the expected landau contribution is 25 ps.

4.5 Front-end ASIC

The LGAD sensor will be bump-bonded to the Application-Specific Integrated Circuit (ASIC) chip. This Front-End (FE) electronics chip is called ALTIROC for ATLAS LGAD Time Read Out Chip. The global architecture of the ASIC is presented in figure 4.14 and is made of a matrix of 225 channels organiwed along columns for the read-out and with common digital

Technology	Silicon Low Gain Avalanche Detector (LGAD)
Time resolution	35 ps (start); 70 ps (end of lifetime)
Time resolution uniformity	No requirement
Min. gain	20 (start); 8 (end of lifetime)
Min. charge	4 fC
Min. hit efficiency	95%
Granularity	1.3 mm × 1.3 mm
Max. inter-pad gap	100 µm
Max. physical thickness	300 µm
Active thickness	50 µm
Active size	39 mm × 19.5 mm (30 × 15 pads)
Max. inactive edge	500 µm
Radiation tolerance	$2.5 \times 10^{15}\,\mathrm{n_{eq}/cm^2}$, 1.5 MGy
Max. operation temperature on-sensor	−30 °C
Max. leakage current per pad	5 µA
Max. bias voltage	800 V
Max. power density	100 mW/cm2

Table 4.1: Sensor parameters and requirements

electronics at the bottom.

The main challenge in the design of the ASIC remains to have a small contribution to the time

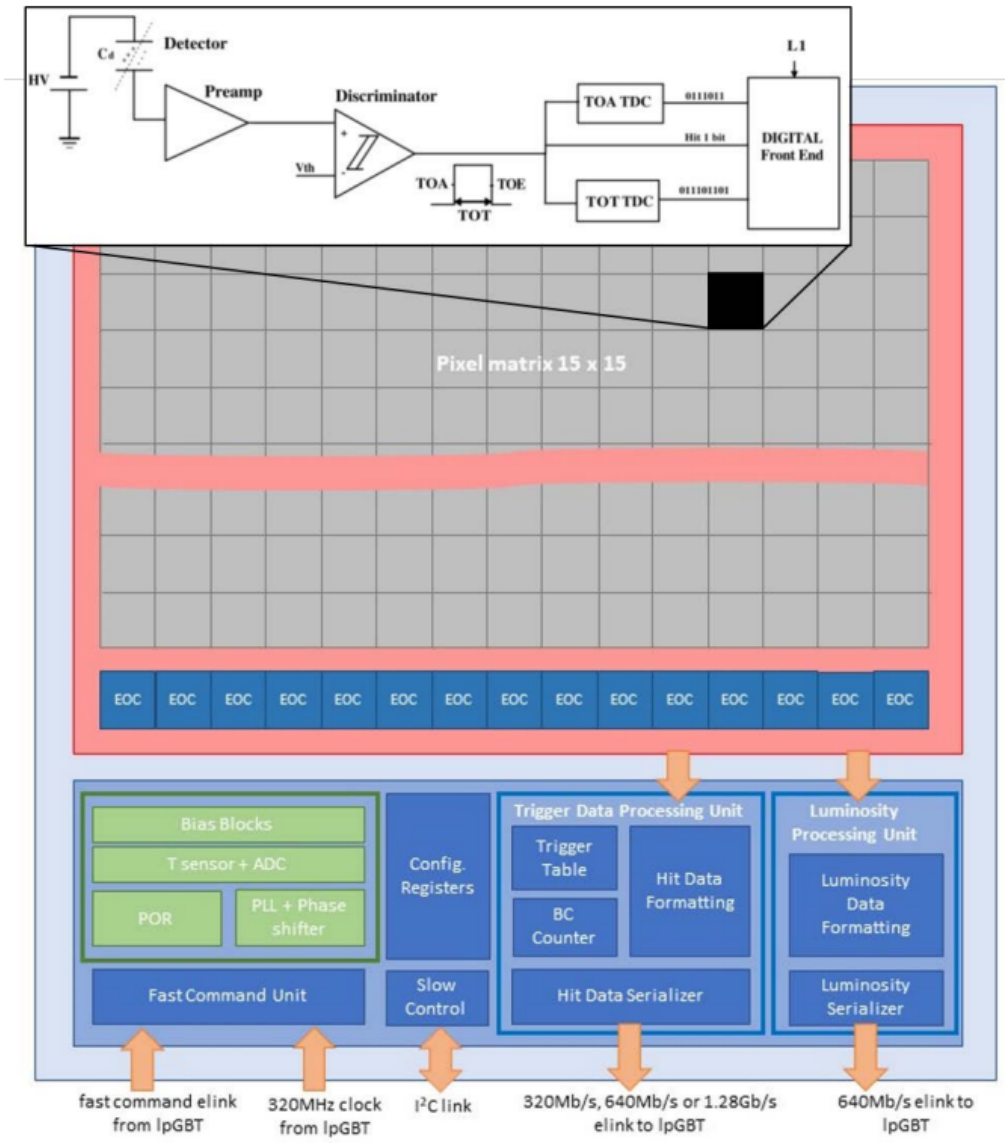

Figure 4.14: Global architecture of ALTIROC [48].

resolution in order to match the LGAD performance. The ASIC aims to extract the time-of-arrival (TOA) and the time-over-threshold (TOT) from the LGAD signal. A representation of the pulse including the TOA and the TOT is shown in figure 4.15.
The TOA and the TOT information are transferred to the data acquisition system when the trigger L0/L1 is received with a latency up to 35 µs.

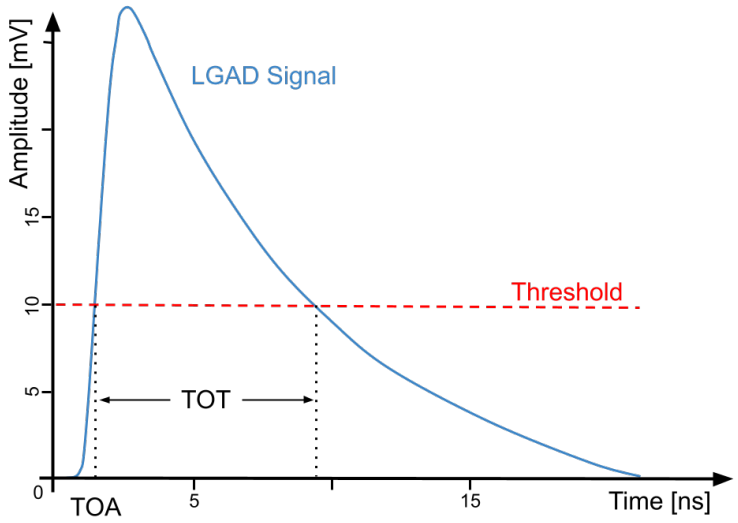

Figure 4.15: Representation of the LGAD signal. The Time Of Arrival (TOA) and the Time Over Threshold (TOT) are defined with respect to the threshold. For figure, the threshold has been set randomly at 10 mV.

4.5.1 General requirements

The ASIC requirements can be divided into two categories: the operational environmental and the performance requirements. These requirements are quoted in the two following tables 4.2 and 4.3.

Pad size	$1.3\,\text{mm} \times 1.3\,\text{mm}$
Voltage	$1.2\,\text{V}$
Power dissipation per ASIC	$300\,\text{mW}\,\text{cm}^{-2}$
Temperature range	$-40\,^{\circ}\text{C}$ to $40\,^{\circ}\text{C}$
Ionization hardness	$2.0\,\text{MGy}$ and $2.5\,\text{n}_{\text{eq}}\text{cm}^{-2}$
Full Chip SEU probability	$<5\,\%\,\text{h}^{-1}$

Table 4.2: Geometrical and operational environment requirements for the HGTD ASIC

The power dissipation of the ASIC will have a severe impact on the global temperature of

the HGTD system. For a power dissipation of the ASIC of 1 W, the temperature increases by 4.6 °C. The power dissipation per ASIC is settled at 300 $\mathrm{mWcm^{-2}}$ in order to preserve the global thermal resistance and a maximal temperature difference of 7.6 °C around the nominal value −35 °C.

Maximum leakage current	5 µA
Single-pad noise	0.5 fC
Cross-talk	<5 %
Threshold dispersion after tuning	<10 %
Maximum jitter	25 ps at 10 fC
	70 ps at 4 fC
TDC contribution	<10 ps
Time Walk contribution	<10 ps
Minimum threshold	2 fC
Dynamic range	4 fC to 50 fC
TDC conversion time	<25 ns
Trigger rate	1 MHz L0 or 0.8 MHz L1
Trigger latency	10 µs L0 or 35 µs L1
Clock phase adjustment	100 ps
TID tolerance	2.0 MGy
Neutron fluence	$2.5 \times 10^{15}\ \mathrm{n_{eq}cm^{-2}}$

Table 4.3: Performance requirement of the ASIC

Contributions to the time resolution

The electronic contribution $\sigma_{electronics}$ can be written as follow:

$$\sigma^2_{electronics} = \sigma^2_{jitter} + \sigma^2_{timeWalk} + \sigma^2_{TDC}$$

with each term expressed as:

$$\sigma_{jitter} = \frac{N}{dV/dt} \sim \frac{t_{rise}}{S/N} \qquad \sigma_{timeWalk} = [\frac{t_{rise}V_{th}}{S}]_{RMS}$$

The jitter represents the uncertainty of the time measurement due to the presence of electronic noise in the circuit. This latest affects the signal and as a consequence the precision of the time measurement. This term is equal to the noise N divided by the slope of the signal $\frac{dV}{dt}$. Assuming a constant slope, the jitter can be modelled by the ratio of the rise time to the signal-over-noise ratio. The rise time t_{rise} corresponds to the time needed for the rising edge of a signal. As a consequence, to minimise the jitter, the fastest preamplifier is needed. The jitter contribution should be smaller than 25 ps.

The second term corresponds to the time walk contribution. The time walk is an effect in the time measurement of the pulse for a given threshold due to the fact that a large signal reaches the threshold faster than a smaller signal. This term is proportional to the rise time t_{rise}, the given threshold V_{th} and the signal S. This contribution can be corrected with an additional correction term fully proportional to the signal amplitude. The time walk can be usually corrected using a Constant Fraction Discriminator (CFD), the amplitude of the signals or by TOT corrections. In the case of HGTD, the time-walk correction is performed with the Constant Threshold Discriminator method, using the TOT measurement (correlated with the pulse amplitude) computed from the discriminator and from the Time to Digital Converter (TDC). This correction method leads to a residual error $\sigma_{timeWalk}$ less than 10 ps. This contribution can be considered as negligible.

The last term corresponds to the contribution of the TDC, induced by the digitization of the time data. It corresponds to an error induced by the binning of the TDC circuit. In the case of a perfect TDC, the contribution of the TDC equals the maximum quantization error of the least significant bit (LSB/$\sqrt{12}$).

4.6 The front-end electronics design

The ASIC chip is composed of a matrix of 15x15 channels, each channel has an area of 1.3 mm×1.3 mm. Among various versions of the ASIC that have been designed, this section will present the ALTIROC2 version. Each single channel is composed of an analog chain

followed by a digital chain. The first part contains a preamplifier, a discriminator and a Time-to-digital converter. The second integrates the local storage of the data, the configuration of the chip and the luminosity measurement. The readout electronics chain is shown in figure 4.16.

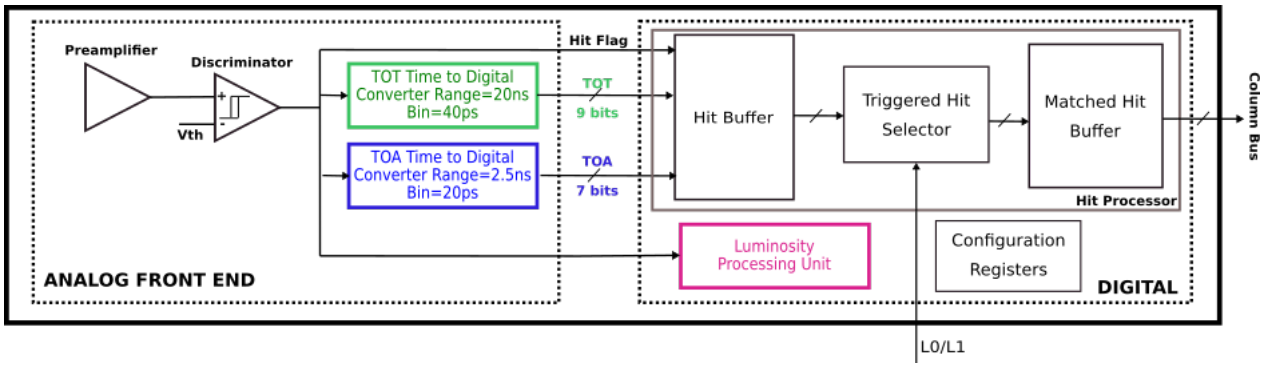

Figure 4.16: Schematics of the full readout electronics chain of a single-channel [48].

4.6.1 The preamplifier

The preamplifier receives a signal from the LGAD sensor or from the internal pulser. According to the version of the ASIC, different types of preamplifiers have been designed. Two categories can be considered for the ASIC: the voltage preamplifier (named VPA) and the trans-impedance amplifier (named TZ). A schematic of each amplifier is given in figures 4.17 and 4.18.

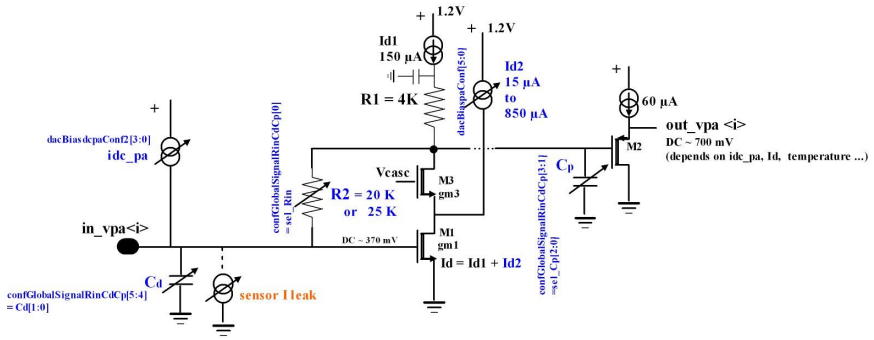

Figure 4.17: Schematics of the voltage preamplifiers [48].

Both preamplifiers are built from a common source configuration. The gain of the preamplifier depends on the input transistor transconductance ("gm1" in figures 4.17 and 4.18) and the drain current (Id=Id1+Id2). The drain current is made by the sum of a fixed current and

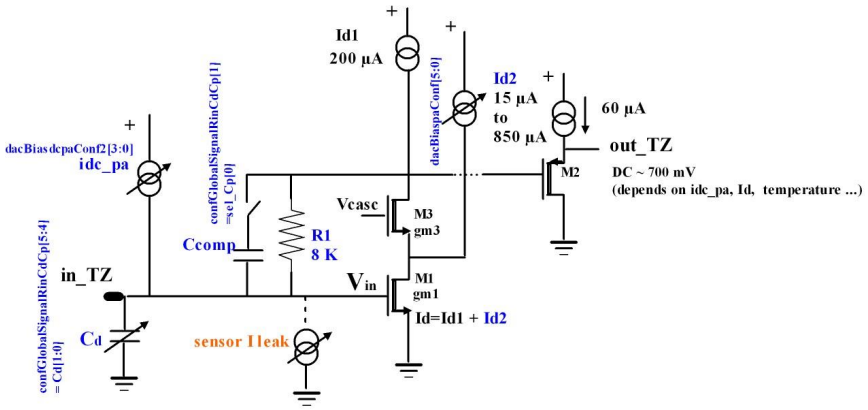

Figure 4.18: Schematics of the trans-impedance amplifier [48].

a variable current, adjustable by a slow control. The architecture and the gain of both preamplifiers are very similar, yet the shape of the output signal differs. The main difference comes from the input impedance (1 kΩ for VPA and 300 Ω for TZ) that affects particularly the TOT range as shown in figure 4.19.

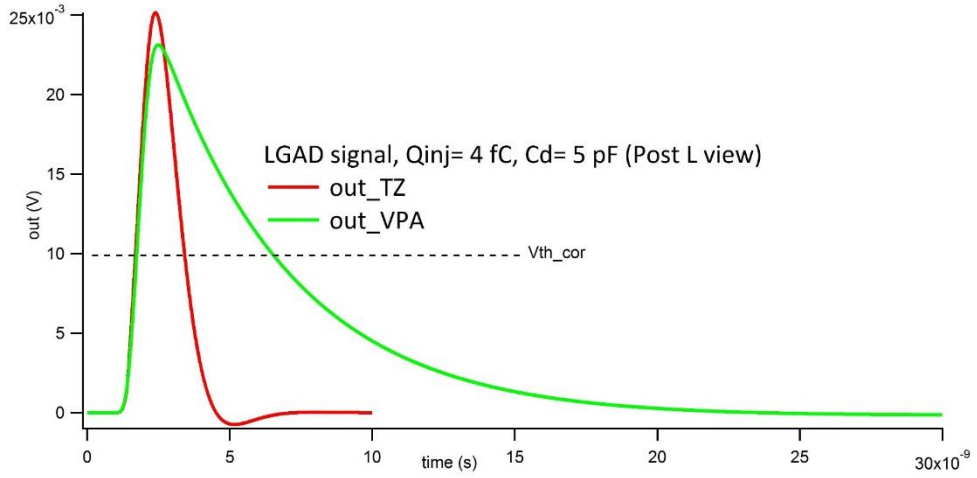

Figure 4.19: Representation of the output amplitude of the preamplifier for a given LGAD signal as a function of time. The green output corresponds to voltage preamplifiers and the red output to the trans-impedance amplifier.

Since the production of the ALTIROC2 version, only trans-impedance amplifiers are used for ALTIROC3 (and futur versions).

4.6.2 The discriminator

The TOA and the TOT are defined with respect to a threshold, so the extraction of these times is done by the discriminator. The principle of the discriminator is basic, the input voltage is compared to a reference voltage. While the input amplitude is higher than the threshold, the output is set to 1, else the output is ground. The output signal is consequently square.
To ensure a very precise measurement and a very small jitter on the TOA, the discriminator is designed with a high-speed leading edge, including a hysteresis to avoid re-triggering effects. In the ASIC, there is a common threshold defined by a 10-bit DAC (V_{th}). Each preamplifier will provide a different offset so in order to harmonize the response of the matrix for a given charge, an additional individual threshold, called V_{thc}, can be used to compensate for differences between channels. This V_{thc} is set by a 7-bit DAC.

4.6.3 The Time to Digital Converter - TDC

The Time to Digital Converter (TDC) is a device used to provide a digital representation of the TOA and TOT of each signal. Because the target quantization step of the TDC for the TOA is below the gate-propagation of the 130 nm technology, a Vernier delay line configuration is used. This configuration corresponds to a succession of delay line cells, with a voltage signal used to adjust the delay. A graphical representation of the TDC's working principle is shown in figure 4.20. The start pulse is received and is propagated to the discriminator. In the case of the TOA, the rising edge of the discriminator signal will initialize the TOA TDC and the signal will be propagated to the slow delay line, composed of 140 ps delay cells. The Stop signal corresponds to the rising edge of the 40 MHz clock following the start signal and will be propagated to the Fast Delay line, composed of 120 ps delay cells. The delay between the two signals corresponds to the digitization time, so the TDC bin. The number of cells necessary for the stop signal to surpass the start signal represents the TDC conversion of the expected time. The TOA will be measured with a 2.5 ns window using a 7-bit register, so 128 delay cells will compose the TDC. In the case of the TOT TDC, the start and stop signals correspond to the rising and falling edge of the discriminator. The working process remains the same as for the TOA, with respectively 120 ps and 160 ps for the slow and fast delay line. The TOT TDC provides a 9-bit digitization bin, to extend the TOT dynamic range up to 20 ns, with a delay step of 40 ps. As mentioned before the voltage can adjust the delay of each delay line. Three control voltages are necessary to the TDC: V_{ctrl_120},V_{ctrl_140} and V_{ctrl_160}.

4.6.4 The internal pulser

In order to test independently the digital chain and the full chain with various configurations and parameters, an internal pulser is integrated. The pulse injected in the analogue part of

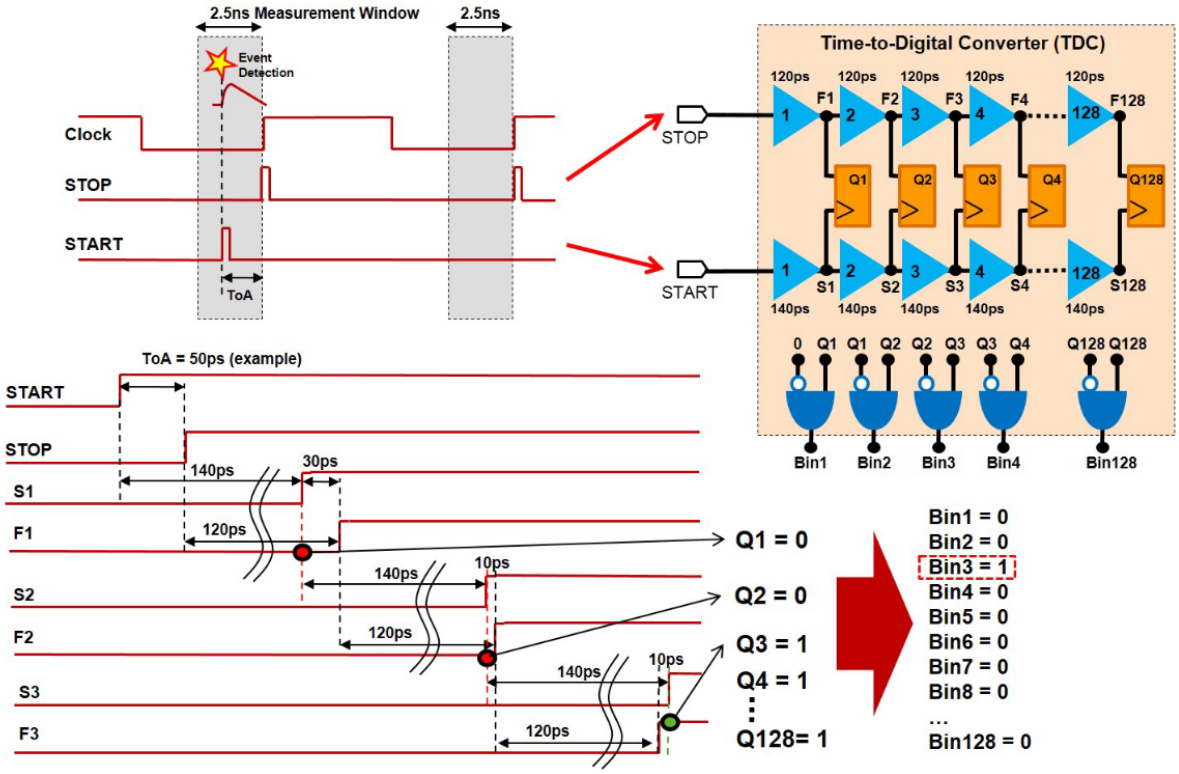

Figure 4.20: Representation of the working principle of the Time to Digital Converters [48].

each channel mimics various input charges up to 50 fC and can be delayed with respect to the clock. This pulser is used to calibrate the matrix of 225 channels and to measure the performance of the ASIC.

The internal pulser principle is shown in the figure 4.21. A 6-bit DAC adapts a DC current from 0 to 7.3 µA. This current flows continuously through 50 kΩ resistor (R) providing a voltage up to 250 mV to a 200 fF capacitor (Ctest). Some switches are added in order to short the resistor to the ground through a command, producing the pulse. The injected voltage (Vstep) can be monitored by a PAD that, in the final version of the ASIC, will serve to perform calibrations by using an external pulse generator.

4.6.5 The digital part

The output of the Analog part is completed with the digital stage that provides two different types of data: the luminosity measurement and the time measurement.

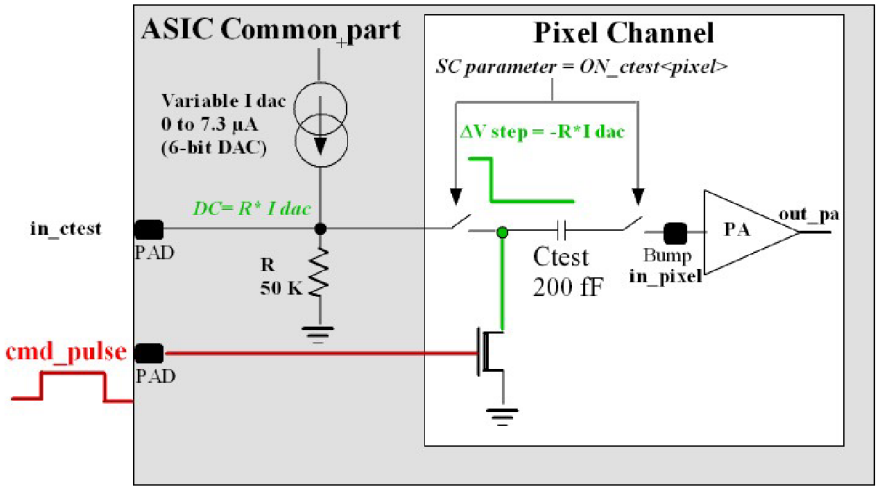

Figure 4.21: Circuit plan of the internal pulser: The variable DC current configurable by a 6-bit DAC providing a voltage Vstep as input to the capacitor Ctest [48].

Local memory unit

The local memory is composed of three main blocks: The hit buffer, the triggered hit selector and the matched hit buffer. The first one will receive from the TDC 16-bit data corresponding to the time measurement and a bit for the hit flag, which indicates if a hit has been detected in the bunch crossing. The hit buffer will store them up to the arrival of an L0/L1 trigger signal (every 35 µs). When the trigger signal is received by the Triggered hit selector, the data is transferred to the second buffer called the matched hit buffer. This buffer will store the information until the full transmission request through the column bus.

Luminosity Processing Unit

The instantaneous luminosity corresponds to the number of detected hits in the pixel matrix per bunch crossing (every 25 ns). Because of the large area of the chip, the measurement of the luminosity is performed on each channel. The luminosity block receives a signal from the discriminator and is deported to the peripheral electronics because of the large area of the chip. This deportation uses a metal line of several millimetres, that will generate a delay in the transmission. In addition, the length of this delay depends on the position of the channels on the surface, so the delay will be proper for each channel. One solution to compensate for this effect is the use of windows instead of the discriminator signal. The windows are distributed to all channels by metal lines as a clock tree. If the hit is received during the window signal, a signal is transmitted to the end-of-column (EOC). The EOC sums the luminosity measurements of the whole column per bunch crossing and then sums the luminosity measurements of columns.

4.6.6 Radiation hardening

At the end of the HL-LHC phase, with an integrated luminosity around 4000 fb^{-1}, the neutron-equivalent fluence of the HGTD should reach a maximum of $4.9 \times 10^{15}\,\mathrm{n_{eq}/cm^2}$ with a 1.5 safety factor ($5.6 \times 10^{15}\,\mathrm{n_{eq}/cm^2}$), while the total ionizing dose should reach 2.2 MGy with a safety factor of 1.5 (3.3 MGy), as shown in figure 4.22. As the electronics is more sensitive to the TID, the sensors are required to sustain a neutron-equivalent fluence of maximally $2.5 \times 10^{15}\,\mathrm{n_{eq}/cm^2}$ and a TID of 1.5 MGy, including a 1.5 safety factor. The level of radiation considered for HGTD can cause a multitude of effects on the electronics, going from a corruption of the data to a complete destruction of electronic components.

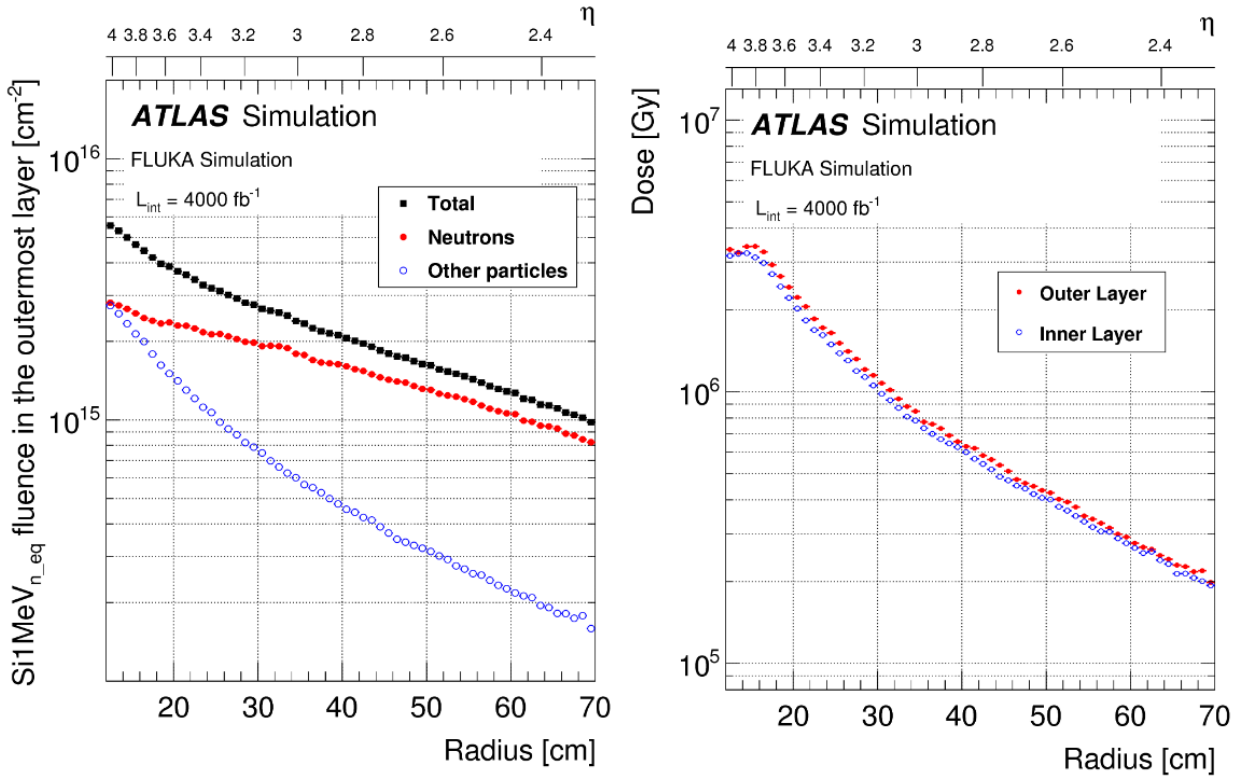

(a) (b)

Figure 4.22: Simulations of the Total ionizing dose (4.22b) and the maximum neutron-equivalent fluence (4.22a) as function of the radius R, in the first (blue) and last layer (red) of HGTD for an integrated luminosity of 4000 fb^{-1} [48].

As shown in figure 4.23, the effects of radiation can be divided into multiples categories as a function of the origin and the induced damages. In HGTD, the radiation effects are studied in particular on sensors and on ASICs.

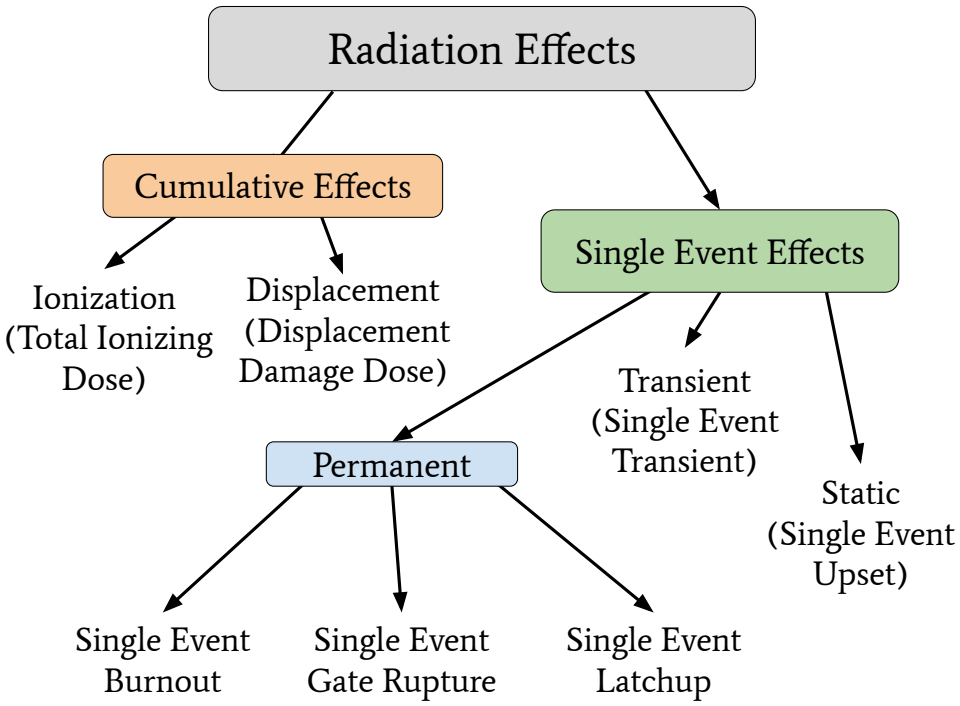

Figure 4.23: Classification of the radiation effects as function of their origin and the damages.

Cumulative effects

Cumulative effects take place through continuous radiation exposure during the lifetime of the electronics. The more the electronic is exposed to radiation, the more the damages are important, leading to making them out of specifications. The effects are permanent and a power cycle can not solve the problem. The cumulative effects can be sub-categorized into Total Ionizing Dose (TID) and Displacement Damage Dose (DDD).
In microelectronics, the ionizing dose effects predominate and are the consequence of an accumulation of trapped charges in the field oxides of the electronic circuit. The displacement damages are the result of nuclear interactions, typically scattering, which cause atomic displacement by collision between an incoming particle (from the beam) and a lattice atom.

4.6.7 Single Event Effects

Single-event effects are triggered by a charged particle passing the electronic device. The incoming particle ionizes the matter and creates hole-electron pairs over its path. The excess of charge depends on the nature of the particle and the material. The charge is collected in the drain/source diffusion, modifying potentially the voltage. This change in voltage can

induce a multitude of effects on the electronics as follows:

- **Single Event Upset (SEU)** is a change of state in a micro-electronics device, such as SRAM. The change of state results from the change of voltage close or in an important node of a logic element, such as a flip flop or a latch. In ALTIROC prototypes, two kinds of data can be affected by SEU: The bits from the configuration and bits of data. An SEU in one of the configuration registers can affect the total configuration of the ASIC or can be solved with a complete reboot of the ASIC. The second category will corrupt the data.
- **Single event latch-up (SEL)** is a short circuit or a low impedance path between the power and ground that can occur in the integrated circuit. This event is caused by the passage of a single particle, inducing a parasitic interference in the junction (npnp structure) in CMOS technologies. In many cases, a simple reboot of the integrated circuit allows to solve the problem but latchups can cause permanent and destructive effects on devices.
- **Single Event Gate Rupture (SEGR)** is a permanent destruction of the ability of the gate to regulate current flow from the source to the drain.
- **Single Event Burnout (SEB)** is a localized high-current state in a device or an electronic component, resulting in an irreversible failure.

Triple modular redundancy method

In order to prevent the effects of the SEE and more specifically the effect of the SEU, a triple modular redundancy (TMR) method is used. This method triplicates each bit of an important register and uses a majority voting system to produce a single output. If any one of these triplicated bits fails, the other two bits can correct and mask the fault. A representation of the system is shown in figure 4.24.
In the SEU study, the situation represented in figures 4.24b and 4.24c are called single error and double error, respectively. In other words, the study aims to estimate the number of single and double errors. These errors can occur in a 25 ps time interval due to the actualisation cycle. The probability of observing three errors on the same triplicated bit system is supposed to be negligible.

4.7 The ASIC board versions

Since the start of the HGTD project in 2016, various prototypes of the front-end electronics have been designed. In this section, the details of each version of the front-end electronics and the most important changes are described. During these 3 years, I had the chance to work

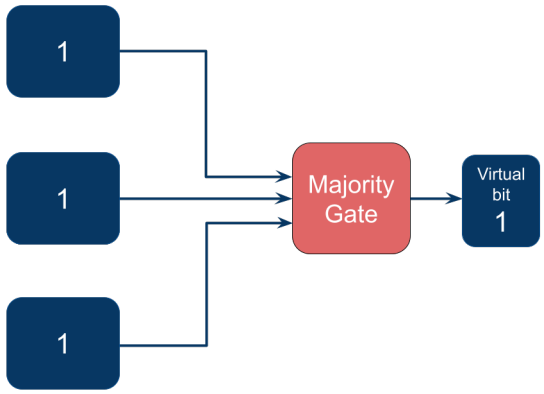

(a) No SEU observed

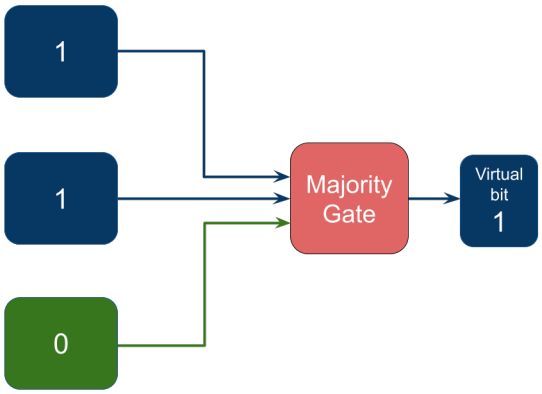

(b) Autocorrection or single error

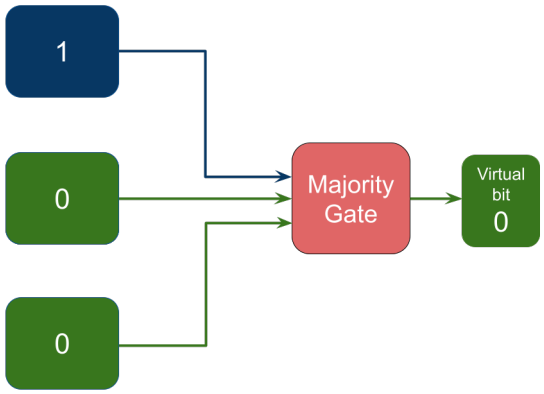

(c) Autocorrection failure or double error

Figure 4.24: Representation of the Triple Modular Redundancy method. Figure (a) represents the case where any error is observed. Figure (b) represents the case where a bit-flip is observed in one of the three triplicated bits. The structure of the TMR corrects automatically this error. Figure (c) represents the case where two bit-flips are observed on two bits of a triplicated bit system, as a consequence, the autocorrection fails.

with three versions of the ASIC: ALTIROC1, ALTIPIX, and ALTIROC2. The previous description of the ASIC was based on the ALTIROC2 structure and requirements, but in total five versions of the ASIC have been designed. At the time of the thesis writing, the pre-production version called ALTIROCA is under design.

ALTIROC0

ALTIROC0 is the first prototype of the HGTD project, designed in CMOS 130 nm by OMEGA microelectronics centre. This version integrates 8 channels made of preamplifiers (4 TZ and 4 VPA), followed by discriminators. It was designed in order to prove the feasibility of reaching the timing requirement of the HGTD [57]. The result of the test bench measurements of ALTIROC0 shows a jitter at 27 ps for an injected charge at 10 fC that corresponds to 1 MIP.

ALTIROC1

ALTIROC1 integrates 25 complete front-end channels, it contains the full analog chain (preamplifiers, discriminators and TDCs) and a digital chain composed of a local memory. This version integrated 25 channels, a matrix of 5x5 sensor cells, with a phase shifter. Various iteration of this version were designed, integrating minor changes such as the nature of the preamplifier (a mix of VPA and TZ or all VPA). This version was also bump-bonded with LGADs in order to be tested in a test beam campaign as described in chapter 5.

ALTIPIX

The **ALTIPIX** board is a one-pixel prototype of the ALTIROC2 chip. It includes a complete pixel with the analogue and the digital electronics. It includes an I2C module, that gives access to the control registers of the chip, it configures the one-pixel electronics and the bias block at the periphery. This last block generates all the bias voltages and currents of the analogue cell. The pixel includes an analogue and a digital part. The first part includes a voltage preamplifier(**PA**) connected to a discriminator and finally to two Time-to-Digital-Converters (**TDC**) in order to measure the Time-Over-Amplitude(**TOA**) and a Time-Over-Threshold (**TOT**). Then, the digital part is composed of the hit processor (**SRAM**) that stores the TDCs samples, a Trigger hit selector and the matched hit buffer.

ALTIROC3

This latest version does not differ highly from the ALTIROC2 version. One of the most important corrections includes the complete and optimal triplication to protect data from irradiation corruption. In addition, the preamplifier is only a trans-impedance amplifier type for all columns. The TOT TDC is using a 9-bit DAC with a 40 ps bin instead of an 8-bit DAC with a 120 ps bin for previous versions. The clock management has been also changed from a source clock at 40 MHz to 320 MHz for the peripheral electronics.

Chapter 5

The performance tests of the front-end prototypes ASIC for HGTD

In this chapter, my work on the characterization of the front-end prototype ASIC for HGTD are presented. In section 5.1 results obtained in laboratory and SEE test results are presented. My contribution on ALTIPIX characterization allowed me to be qualified as ATLAS author. A second section 5.2 presents the performances tests done on ALTIROC2 including test bench results, irradiation test and cooling test. Finally, section 5.3 is on the test performed on ASIC and LGADs with beam of particles, I participated to these test beam as a shifter. A general description of each prototype has been already given in the previous chapter, section 4.7.

5.1 Characterization of ALTIPIX

As mentioned in the previous chapter, ALTIPIX is an ALTIROC prototype with only one channel. This version is composed of a complete electronics chain. The characterization of this prototype can be divided into two parts: the configuration of the ASIC and the measure of its performances.
The configuration includes the validation of the multiples bias voltages and references currents. These voltages and currents provide good information about the state of the board and each major component. As mentioned in section 4.5, the ASIC chain integrates a Time-to-digital converter. This latest digitises the TOA and the TOT, and its Least Significant Bit (LSB) needs to be adjusted. As a reminder, the LSB is the rightmost bit in a binary number and corresponds to the minimal digitized variation of time in a TDC. Finally, the threshold tuning is essential to the configuration of the ASIC. This threshold aims to reject the noise, and the measure of the TOT and the TOA is fully dependent on this threshold.

The LSB and the threshold are adjusted thanks to various control registers in the internal I2C. The tests of performances of the ALTIPIX board aims to measure the jitter, i.e. the noise of the TOA signal, and to determine its evolution with respect to the injected charge.

The test bench

Whatever tests are done on ALTIPIX, the test bench remains the same and is shown in figure 5.1. ALTIPIX is integrated on a Printed Circuit board (PCB), called for the rest of the thesis the ALTIPIX PCB, in red square in figure 5.1a. ALTIPIX, in light blue in figure 5.1a is protected by a black resin to protect the wire bonding. The ALTIPIX PCB is connected to a Field-Programmable Gate Array (FPGA) through a flex cable in order to receive the command of the test, the 40 MHz clock, the power supply and transfer the data. This FPGA is connected by an Ethernet cable to a computer to run the Python codes. ALTIPIX PCB is also connected to an external I2C and a Raspberry Pi (yellow in figure 5.1a). The external I2C is used to communicate with the internal I2C of ALTIPIX because the control registers cannot be configured with the FPGA. Finally, the ALTIPIX PCB is connected to a small PCB to control the power supply of ALTIPIX. This small PCB contains three potentiometers to adjust the LSB of the TDCs.

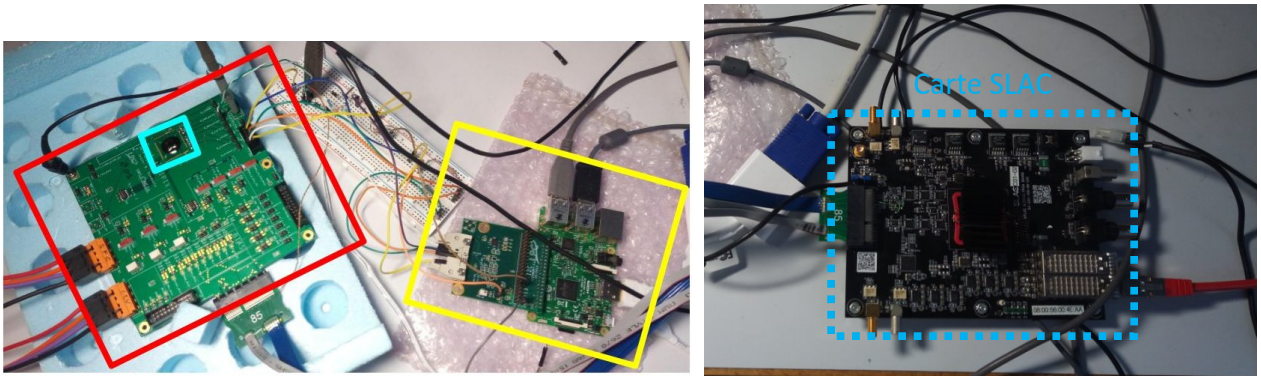

(a) (b)

Figure 5.1: Setup of the test bench. ALTIPIX is in the centre of the light blue square in 5.1a, the ALTIPIX PCB is in the red square, the external I2C monitored by the Raspberry is in the yellow square and the FPGA board in figure 5.1b.

5.1.1 Configuration of ALTIPIX

To have a monitoring of the ALTIPIX state during the test, the design of the ALTIPIX PCB includes pins to extract bias voltages and reference currents. All bias voltages have been checked and compared to their theoretical value, see table 5.1. It can be noticed an overall

good agreement between the theoretical values of the voltages (predicted in simulations) and the measured values. The difference does not overpass the 5 % of disagreement except for the bandgap reference voltage and the cascode voltage of the preamplifier and discriminator (staying below 13 % of disagreement). In addition, the effect of these small voltage drops does not seem to affect the output voltage of the preamplifier and the discriminator.

Bias or ref. voltages	**Theoretical values [mV]**	**Measured values [mV]**
Threshold voltage V_{th}	868	868
Bandgap reference voltage $V_{bg_{1V}}$	1001	884
Bias of the input of the preamp. V_{bi_pa}	507	535
Bias of the cascode preamp. V_{casc_pa}	703	618
Bias of the output of the preamp. V_{bo_pa}	509	522
Bias of the input of the discri. V_{bi_disc}	354	360
Bias of the discri. (input transistor) V_{bm1_disc}	854	838
Bias of the cascode discri. $V_{b\_casc\_disc}$	1000	878
Bias of the output of the discri. V_{bo_disc}	648	578
Bias of the temperature V_{b_rf}	804	782
Bias of the follower V_{b_fol}	322	322
Bias of the DAC $V_{b\_dac\_cor}$	287	302

Table 5.1: Bias voltages and reference voltages

TDC adjustment

In ALTIPIX, there are two TDCs, one for the TOA digitization and one for the TOT, called TDC_{TOA} and TDC_{TOT}. The structure of the TDC provides three different potentiometers to adjust the digitisation step, known also as the Least Significant Bit (LSB). Each potentiometer is a three-terminal resistor with a rotating contact to adjust the voltage signal (V_{ctrl}). The adjustment of the TDC_{TOA} is performed with the V_{ctrl_S} and V_{ctrl_F}, while the adjustment of the TDC_{TOT} is performed with the V_{ctrl_S} and V_{ctrl_C}.
In ALTIPIX, the LSB of the TDC responsible for the digitization of the TOA (TOT) is expected to be 20 ps (160 ps). These conversion values can be measured with the evolution of the TOA and TOT with respect to the injected signal. The principle of these tests is to iteratively check the linearity of the time (TOT or TOA) with respect to the pulse, and adjust the three voltages while the LSBs do not correspond to the expected values. The adjustment leads to the values given in the table 5.2.

Potentiometers	Voltages
V_{ctrl_F}	790 mV
V_{ctrl_C}	810 mV
V_{ctrl_S}	854 mV

Table 5.2: Values of the three V_{ctrl} potentiometers for the expected value 20 ps for the LSB of the TDC_{TOA} and 160 ps for the LSB of TDC_{TOT}.

As defined in the section 4.5, an external trigger was designed to mimic the discriminator output in the ASIC. The main advantage of this external trigger remains that the signal can be tuned, independently of the discriminator using two control registers: `pulseSet` and `pulseReset`, defined as follows:

- `pulseSet`: time corresponding to the rising edge of the square injected signal
- `pulseReset`: time corresponding to the falling edge of the square injected signal

In the case of the adjustment of the TDC_{TOA} can be performed by varying with `pulseSet` parameter with a `pulseReset` set to its maximal value. In other words, each injection is delayed with respect to the previous one, in order to scan the full dynamic range of the TOA. Figure 5.2a represents the evolution of the TOA with respect to the `pulseSet`. Then the LSB is extracted by a linear fit of the curve on its dynamic range (2.5 ns). In figure 5.2a,

the conversion factor corresponds to the expected 20 ns.

In the case of the adjustment of the TDC_{TOT}, the value of the `pulseSet` is set to its minimal value and the `pulseReset` is scanned from 3 ps to 40 ps with 10 ps steps to scan the full dynamic range of the TOT. In other words, each injection is performed with an increasing charge. Figure 5.2b represents the evolution of the TOT with respect to the `pulseReset`. As before, the LSB is extracted by a linear fit and the potentiometers are adjusted if the resulting bin differs from 160 ps. In figure 5.2b, the TOT is reset when its maximal value (127 in decimal) is reached, increasing the overflow by one.

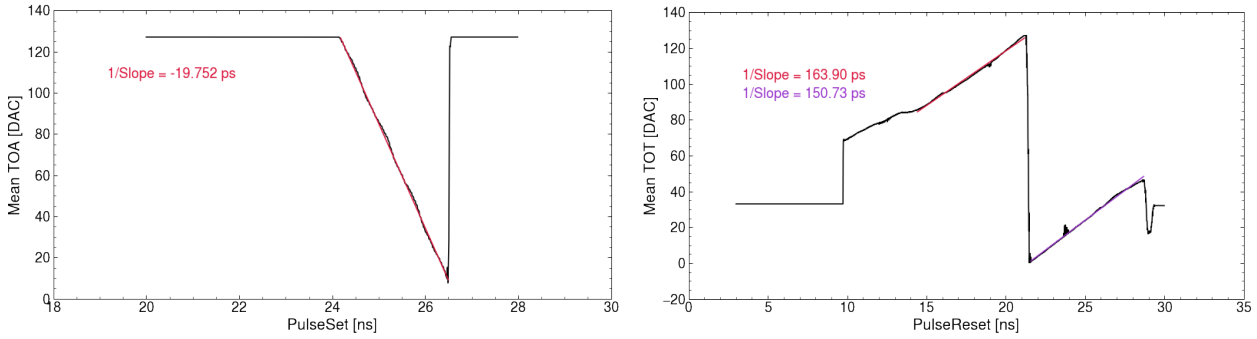

(a) TOA linearity

(b) TOT linearity

Figure 5.2: Linearities of the Time Over Threshold and the Time of Arrival, respectively by scanning of pulseReset and pulseSet parameters. The inverse of the fitted slope (in red or purple) gives the value of the LSB. Each point on the curve corresponds to a mean of fifty identical pulses.

Measurement of the analog noise

In order to check the proper operation of the chip, various signals or voltages can be checked with the oscilloscope using the pins. In ALTIPIX an unexpected noise has been observed at the preamplifier's output. This noise, shown in figure 5.3, has an amplitude of ±100 mV and an 80 MHz frequency. Its origin has been investigated to ensure that it will not be observed in the future ALTIROC2 prototype. Using an external clock, the following observation has been done:

- The frequency of the noise is correlated to the frequency of the 40 MHz clock
- The amplitude of the noise is not correlated to the amplitude of the 40 MHz clock
- The amplitude of the noise is correlated to the supply voltage

Figure 5.3: Output of the preamplifier seen at the oscilloscope, with the observed 80 MHZ noise.

This noise appears as a coupling between a signal before the amplifier and the clock. Its origins remain not perfectly known due to the difficulty of accessing the upstream preamplifier signal. Finally, this coupling is not observed in the simulations and is not expected in ALTIROC2 because the analog part has been designed differently.

Threshold measurement

The ALTIPIX prototype is made of a complete analog and digital chain as shown in section 4.5. In order to reject the noise and to select a minimal charge for the particle detection, a threshold is determined in the discriminator. The threshold measurement is performed with the internal pulser. The pulse, chosen with the maximal amplitude is injected for various thresholds V_{th} going from 855 mV to 890 mV. The jitter, i.e. the noise over the TOA, is extracted and shown as a function of the threshold in figure 5.4. The noise is considered rejected when the value of the jitter is stable, providing the minimal value for the threshold, set at 868 mV.
In the previous version, ALTIROC1, this value was set to 800 mV. This increase in the minimum threshold can come from the coupling between the clock and the input of the

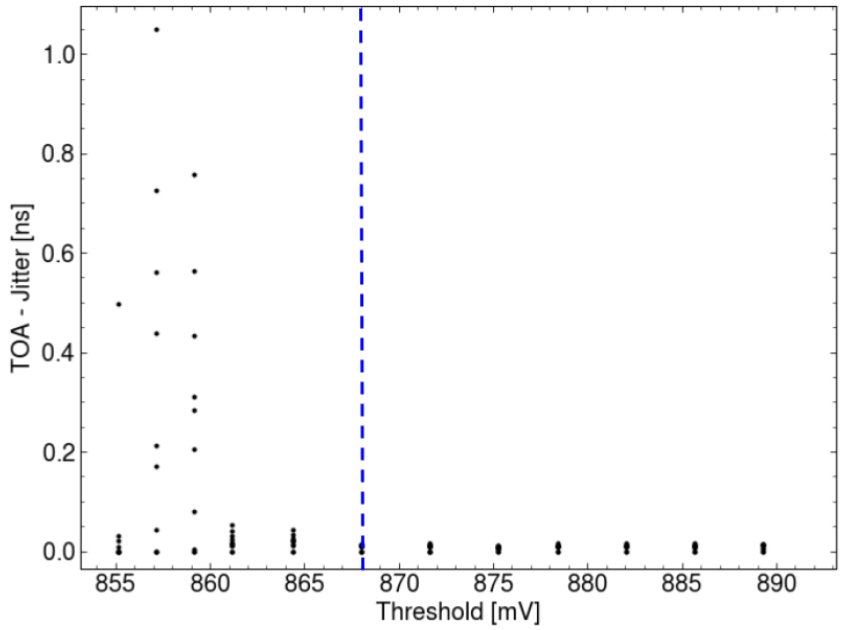

Figure 5.4: TOA Jitter as a function of Threshold, with the injected charge settled at 10 fC, for various pulseSets (from 19 ns to 23 ns, with 0.5 ns step). The dashed blue line corresponds to the chosen threshold, 868 mV.

preamplifier, leading to an increase in the noise.

Jitter measurements

As mentioned in the section 4.5.1, the jitter is one of the key measurements of the performance. This jitter is associated with the noise over TOA measurement. As a consequence, for a given threshold (settled at 868 mV) and a given charge, N pulses have been injected using the internal pulser. Figure 5.5 represents the distribution of the N pulses for a charge settled at 10 fC. Then the jitter is extracted as the standard deviation of these N TOA measurements, this latest equals 16.9 ps in figure 5.5. A scan of the injected charge is performed in order to observe the evolution of the jitter with respect to the charge, shown in figure 5.6. The test has been done from 4.92 fC to 10 fC. The requirement for HGTD is a jitter below than 25 ps for an injected charge higher than 10 fC, this requirement seems satisfied. The test could not be performed for an injected charge below 4.92 fC due to the observed noise introduced in the section 5.1.1.

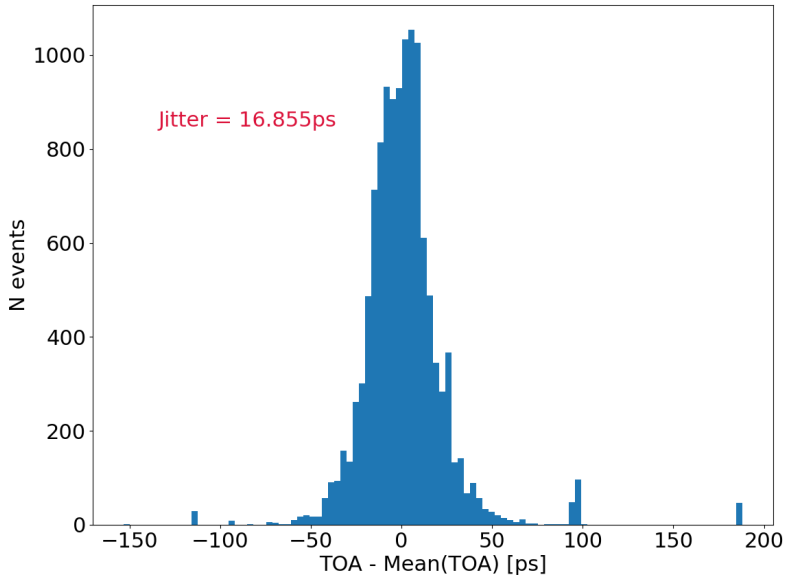

Figure 5.5: TOA distribution for an injected charge at 10 fC. The jitter is measured as the standard deviation of the TOA distribution and equals 16.9 ps.

5.1.2 Single Event Errors tests

ALTIPIX has been used to test the Single Event Upset (SEU) hardness of the FE-electronics. The irradiation effects are listed in section 4.6.6. My work on the SEE tests using ALTIPIX leaded to the publication of the following article [58].

The SEU test has been organised at the Centre Antoine Lacassagne in June 2021, using the MEDICYC cyclotron [59]. This cyclotron provides a proton beam with an energy up to 65 MeV, dedicated to the treatment of ocular tumours. In the context of the SEU test, the measurement was performed on the low-energy treatment line with an energy of 62 MeV and an intensity up to 300 nA. At this intensity, two hours of irradiation corresponds to ten years of HL-LHC.

The design of ALTIPIX integrates sixty-four-8-bit registers dedicated to SEU counting, their value has no impact on the chip. Each bit of these registers is triplicated using the TMR method described in section 4.6.7. In case of a bit flip, the voter will automatically correct the value of the faulty flip-flops and raise an error flag. This last one increments four new 8-bit registers, dedicated to count the number of bits flipped in the sixty-four registers grouped into four groups of sixteen registers, and the sum of these four counters is saved into another 8-bit

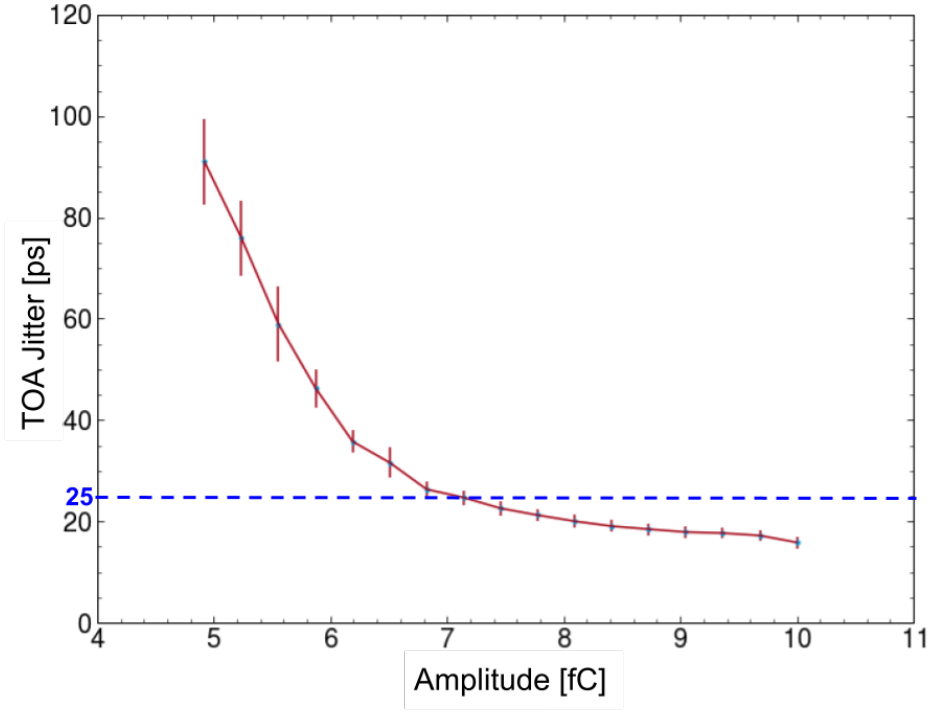

Figure 5.6: Evolution of the jitter in ps with respect to the injected charge. The scan is performed for a charge going from 4.9 fC to 10 fC. The dashed blue line represents the limit of the 25 ps.

register. Each register is accessible by the I2C port. Each triplicated flip-flop is spaced by at least 15 µm in the layout. The position of all the registers in the ASIC is shown in figure 5.7.

The implementation of the TMR in ALTIPIX is done using a 2008 version of the CERN TMRG tool [60]. This tool automatizes the process of triplication and optimizes automatically the position of the flip-flops in the layout. In this prototype, a few elements remain nonetheless not triplicated, including the 40 MHz clock, the reset of the counter and control signals.
The setup of these tests has been organized as follows and remains very close to the usual test bench. The ALTIPIX PCB is placed on the beamline, aligned with a laser in such a way that the ALTIPIX matrix is covered by the beam. The FPGA, the external I2C, the Raspberry Pi and all other electronic devices are placed below the beamline, under a lead shelter, to protect them from radiation. The irradiation time was organized with two beam intensities, four periods at high intensity (299.9 nA cm^{-2}) and one period at low intensity (3.1 nA cm^{-2}).

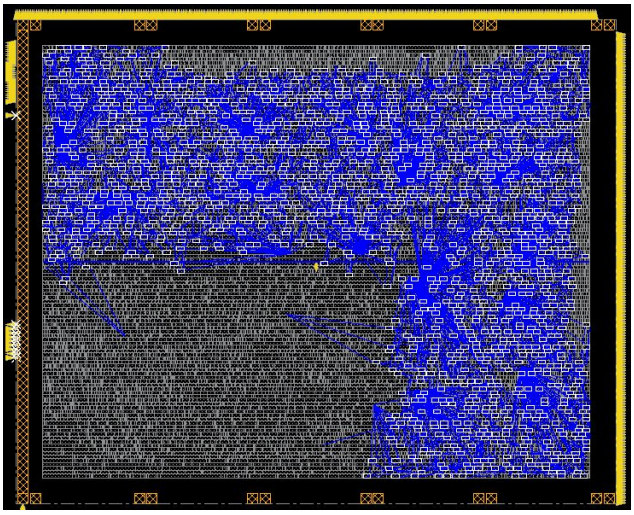

Figure 5.7: Position of the flip-flops in the ASIC represented by the white square. The blue lines link the 3 triplicated bits

The measurement of the SEU is done in two different ways developed below: the direct observation of the auto-correction failure, and, the extrapolation of the auto-correction failure from the single error rate.

The direct observation of the auto-correction failures

The direct measurement is performed through the sixty-four 8-bit registers, filling them with three default values in decimal (in binary) system : 0 (`00000000`), 254 (`11111110`) and 255 (`11111111`). The 0 and 255 values have been chosen in order to test the impact of the SEU in registers filled only with `0`, or `1` bit because the SEU effect is expected to be asymmetric [61, 62]. Then the 254 intermediate case, aims to fill all bits with a `1` without saturating the value of the register. All the register values are regularly stored in an output file to monitor the possible double errors.

This monitoring has been performed at high intensity because the double errors are expected to be a rare phenomenon. Alternatively, all the registers will be configured with the frame `11111111`, `11111110` and `00000000` for a 10 minutes duration each. In the two first periods, no double errors were observed, while in the latest period, nine errors were observed. The table 5.3 summarizes the information extracted from these three periods.
When no errors are observed, an upper limit at 95% confidence level can be calculated. With a Poisson distribution, a maximum of three errors is compatible with the observed zero error. Then, the maximal number of events per triplicated bit for one day at the HL-LHC N^{bit}_{HL-LHC}

Frame	Duration [s]	Errors	N^{bit}_{HL-LHC}	N^{ASIC}_{HL-LHC}
00000000	530	9	$3.9\ 10^{-7}$	$2.9\ 10^{-3}$
11111110	740	0	$< 0.9\ 10^{-7}$	$< 0.7\ 10^{-3}$
11111111	610	0	$< 1.1\ 10^{-7}$	$< 0.8\ 10^{-3}$

Table 5.3: Table summarizing the information extracted from the number of double errors observed in the high-intensity periods. The N^{bit}_{HL-LHC} and N^{ASIC}_{HL-LHC} corresponds to the number of double errors observed in one day of HL-LHC per bit or ASIC respectively.

can be extrapolated assuming a quadratic dependence to the fluence. Finally considering the 7200 triplicated bits per ASIC, the upper limit of the number of events per ASIC for one day at the HL-LHC N^{ASIC}_{HL-LHC} is deduced. Finally, the nine errors were observed with the sixty-four registers filled with the `00000000` frame correspond to one single-bit flip in the frame. Figure 5.8 represents the position of the nine registers affected by a double error. It can be noticed that no correlation exists between the auto-correction failure and the position of the triplicated bit in the ASIC.

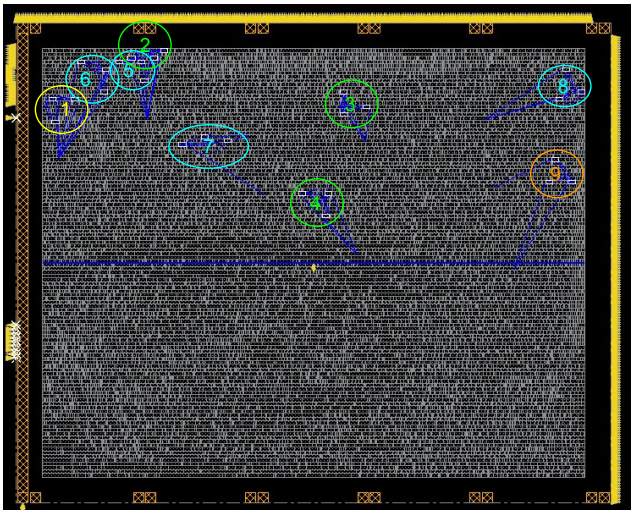

Figure 5.8: Position of the flip-flops in the ASIC represented by the white square. The blue lines link the 3 triplicated bits. Colourful circles show the position of the 9 errors in the ASIC.

From the direct observation of the auto-correction failures, the following cross-sections can

be extracted:

$$\sigma_{\mathrm{SEU}^{1\to0}} < 1 \times 10^{1}\,\mathrm{cm}^2$$
$$\sigma_{\mathrm{SEU}^{0\to1}} = 1 \times 10^{1}\,\mathrm{cm}^2$$

It has been noticed that the nine errors happened just before the failure of the Raspberry Pi which is essential in the configuration of ASIC and more specifically the configuration of the registers. As a consequence, these nine errors may be produced by another phenomenon than SEU effects.

Extraction of the double error rate from the single error rate

It can be considered that the auto-correction failure corresponds to the probability of two bit-flips on two triplicated flip-flops in the range of 25 ns. In this context, the SEU measurement exploits the single-bit flip rate to extrapolate the probability of getting auto-correction failure according to the following expression:

$$P = C_3^2(\int_0^{T_c} \sigma_{SEU} f dt)^2 = 3\sigma_{SEU}^2 f^2 T_c^2$$

with T_c equals to 25 ns, f the instantaneous fluence assumed to be equal to 10^8 $\mathrm{n}_{eq}^{1\ MeV} s^{-1}$ at high intensity and σ_{SEU} the single bit flip rate.
The single bit rate is measured by the evolution of the counter with respect to time as shown in figure 5.9a. A treatment of the data is applied in order to compensate for the bit flip that could affect the counter, the reset signal or to compensate for the reset when the counter reaches its maximal value of 255 in decimal. The resulting plot is shown in figure 5.9b. This work is repeated for the three register frame values 0, 254, 255.
Finally, the slope is extracted by a linear fit and normalized by the triplicated bit number and the intensity to get the cross-section summarized in the table 5.4. Assuming a Poisson distribution for the occurrence of SEE errors, the following cross-section can be estimated:

$$\sigma_{\mathrm{SEU}^{1\to0}} = (7.90 \pm 0.13)\ 10^{-14}\ cm^2$$
$$\sigma_{\mathrm{SEU}^{0\to1}} = (6.77 \pm 0.41)\ 10^{-14}\ cm^2$$

The asymmetry observed in the two cross-sections is not perfectly known but has already been observed in the SEU results, eg. in ref [61]. This phenomenon is assumed to originate from the nature of the latch and the nature of the used substrate.

The auto-correction failure number for th HL-LHC phase is then estimated assuming an instantaneous fluence of $10^8\,\mathrm{n}_{\mathrm{eq}}^{1MeV}\mathrm{s}^{-1}$. The table 5.5 presents the number of auto-correction failure per triplicated bit or per ASIC for one day at HL-LHC.
The SEE tests performed with ALTIPIX provide a first measurement of the SEU cross-section. The test has been limited by the exposition of the raspberry to the radiation. After one hour, the Raspberry failed and the radiation intensity made impossible the reboot of the setup.

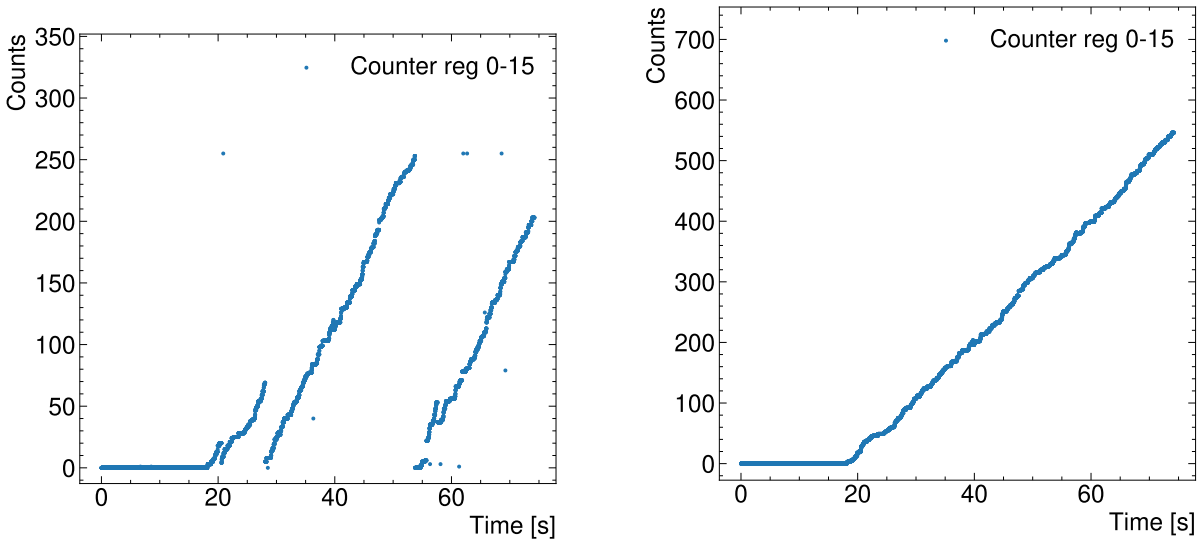

(a) (b)

Figure 5.9: Evolution of one counter, counting the single error in the first sixteen dedicated registers. The plot on the left shows the evolution of the counter before the correction. The plot on the right represents the evolution of the counter after correction.

5.2 Characterization of ALTIROC2

ALTIROC2 is the first prototype of the ASIC with a matrix of 15x15 pixels fully instrumented. As for the ALTIPIX version, the characterization can be divided into two parts: the configuration of the ASIC and the measure of its performance.

5.2.1 The test bench

ALTIROC2 is integrated on a PCB, called for the rest of the thesis the ALTIROC2 PCB, shown in figure 5.10a. In this figure, the ALTIROC2 is protected by a 3D-printed black shelter. As for the ALTIPIX PCB, the ALTIROC PCB integrates various pins to extract the bias voltages and reference currents. To ensure the exchange between the user and the ALTIROC2 PCB, the PCB is connected by a flex cable (ASP flex) to a mezzanine board. This custom interface board contains various regulators or programmable delays and ensures the translation between the FPGA and the ASIC. It also provides power supplies and clock managers or is also used to extract various voltages and signals. The mezzanine is plugged on a commercial FPGA ZC706 board, shown in figure 5.10b. A computer is used to send commands to the ASIC by the FPGA using an ethernet cable. On the contrary of the

ALTIPIX board, internal I2C communicates directly with the FPGA.

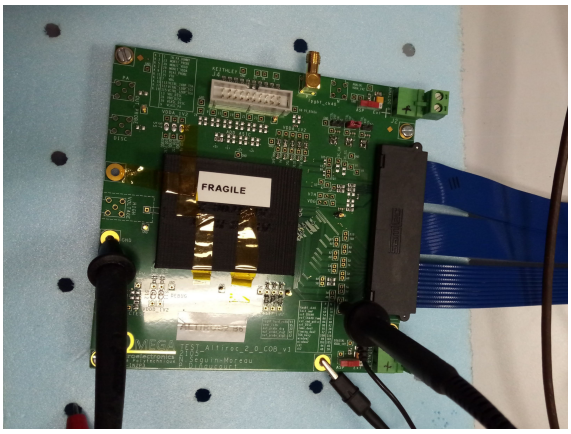

(a)

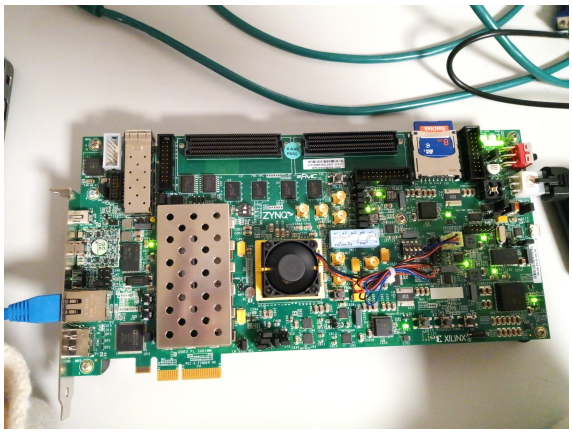

(b)

Figure 5.10: Test bench setup including ALTIROC2 PCB in figure 5.10a and the FPGA board in figure 5.10b. The communication between them is insured by a flex cable.

The power supply can be provided in two different ways: externally or internally. The external power supply is provided directly on the ALTIROC2 PCB using the external power supply system, delivering 1.2 V to 1.4 V depending on the board. This option has been planned to decouple the analogue and the digital parts of the electronic chain and has the advantage of compensating for the voltage drop in the flex cable. The internal power supply is provided through the flex cable, providing the 3.5 V to power the mezzanine and the ASIC.

The TDC LSB verification

In the ALTIROC2 version the matrix is composed of 225 independent chains, and as a consequence contains 225 pairs of Time to Digital Converters (TDC). In this version, the TDCs are supposed to be correctly adjusted by various resistors, but these resistors remain accessible to be changed in case of failure. For ALTIROC2, the TDC LSB's expected values are respectively 20 ps and 120 ps for TOA and TOT.
The LSB of the TDC_{TOA} and TDC_{TOT} are measured with the the external pulser. This pulse is customizable by two registers: the `pulseWidth` and `PSdelay`. The first one tunes the width of the external pulser, in other words the amplitude of the charge while the second parameter tunes the delay between the injection of the pulse with respect to the 40 MHz TDC clock. The pulse length can be changed from 781.25 ps to 25 ns.

The TOA TDC bin is extracted for each channel by the linear fit of the resulting plot, obtained by the scan of the `PSdelay` as shown in figure 5.11a. Respectively the TOT TDC bin is extracted by the linear fit of the `pulseWidth` scan as shown in figure 5.11b. The

measurement is repeated for the 225 pixels. The resulting LSB matrices are shown in figures 5.11c and 5.11d.

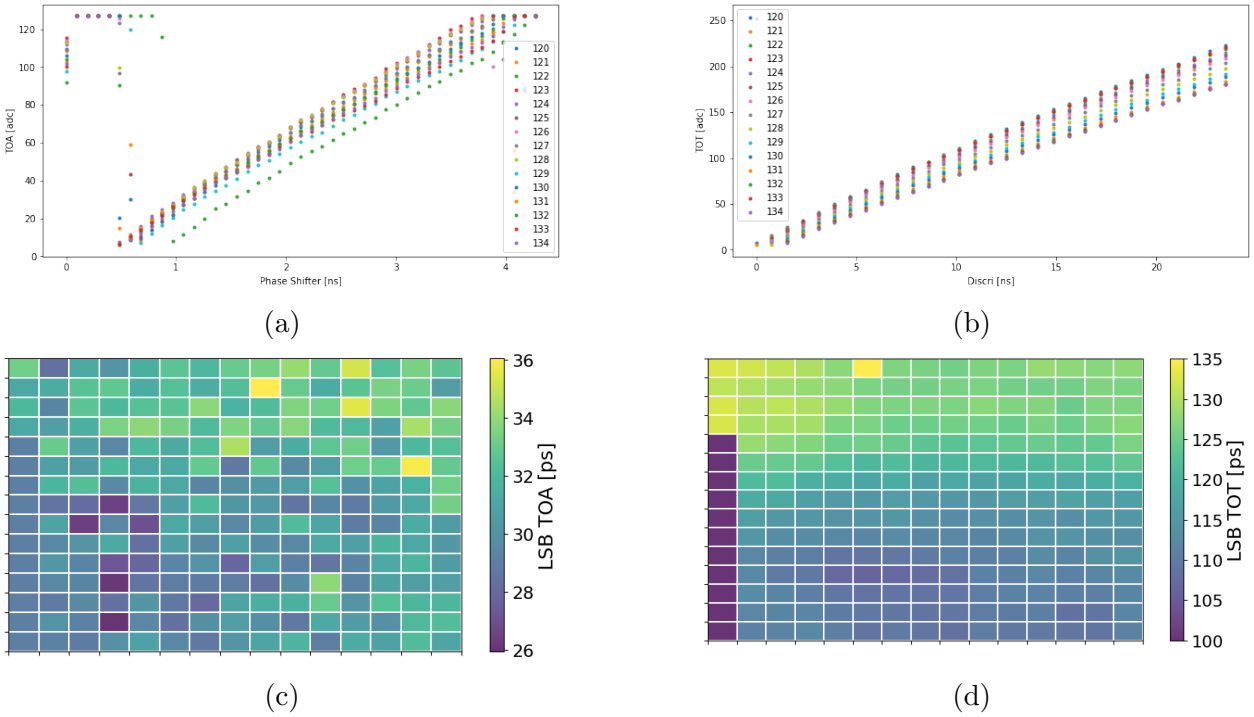

Figure 5.11: TDC bins measurement for TOA (left) and TOT (right). The top figures show the linearity of each channel over a column. The bottom figures show the TDC bin values on the full matrix.

The results shown in this section have been obtained with the ASIC alone, with the board 6. The resulting conversion value of the TOA is between 26 ps and 36 ps, and between 106 ps and 135 ps for the TOT. These values correspond to the expected values.

The alignment of pedestals

The ASIC needs to be configured for the detection of particles with a certain charge. As a consequence, the threshold of each discriminator needs to be adapted to the charge. The following measurement shows how the pedestals are tuned to various given charges.

Each channel has a different offset in the input signal of the discriminator. To adjust the threshold with respect to the input offset, the tuning is done in two steps: The first step is to determine the global threshold value: The same threshold over all the matrix. This threshold will be linked to the chosen injected charge. The second step is to calibrate the V_{thc} of each pixel with respect to the global V_{th}. This is a corrective threshold, to compensate for the

offset of each preamplifier.

The measurement is performed as follows:

- N pulses are sent with the same given charge Q.
- The efficiency is calculated as the ratio between the number of detected pulses and the total number of pulses N.
- The measurement is repeated for each channel.
- The V_{th} is set in order to get a 50% occupancy over the matrix for the given charge Q.
- The V_{thc} is set in order to get 50% efficiency on each channel over the matrix for the given charge Q.

When V_{th} and V_{thc} are extracted, their value is saved in the configuration of the ASIC. The result of this tuning is shown in figure 5.12.
This tuning is done with various charges and on various boards. For some boards, the tuning has been done for a minimal charge equal to 3 fC. For a complete module board, the minimal charge was set to 4.5 fC. Instead of considering the total matrix, the tuning can be done on a unique column. The rest of the matrix can be deactivated and the tuning is refined. In this condition, the minimal usable charge is respectively 1.5 fC and 3 fC for the ASIC alone and the module.

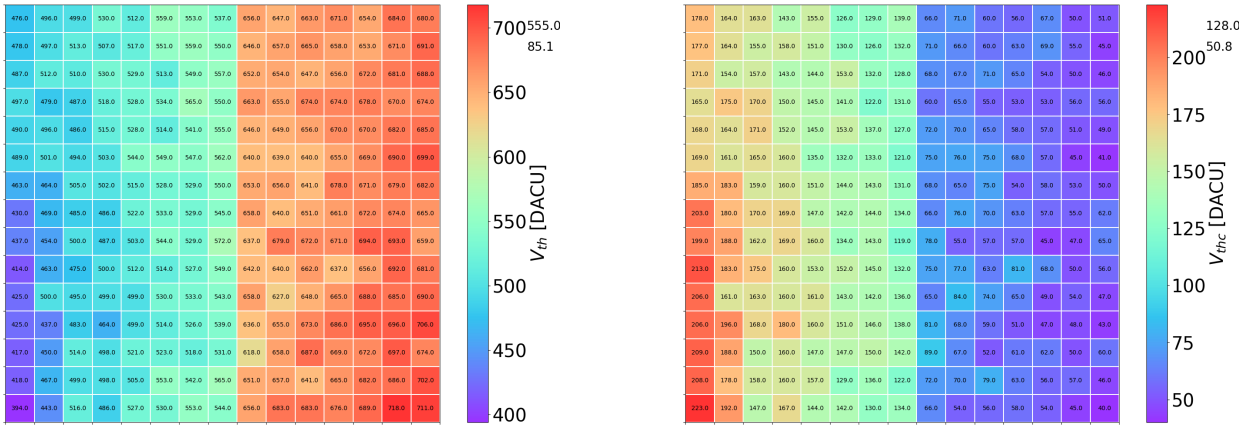

(a) Vth scan values

(b) Vthc scan values

Figure 5.12: Map obtained during the scan of the global threshold (on left) and of the corrective threshold considering a global threshold at 586 DACU (on right).

Measurement of the Jitter

For a given charge and a given threshold, the jitter can be measured by the injection of N pulses with the same characteristics (amplitude and delay). The noise of the TOA is then extracted from the standard deviation of the TOA measurement over the N pulses. Figure 5.13 represents the jitter for each pixel measured for an injected charge settled at 12 fC. The jitter is measured between 5.8 ps and 44 ps over the matrix, this value corresponds to the requirements. It can be noticed in figure 5.13 that five pixels in the matrix have a jitter higher than the required 25 ps.

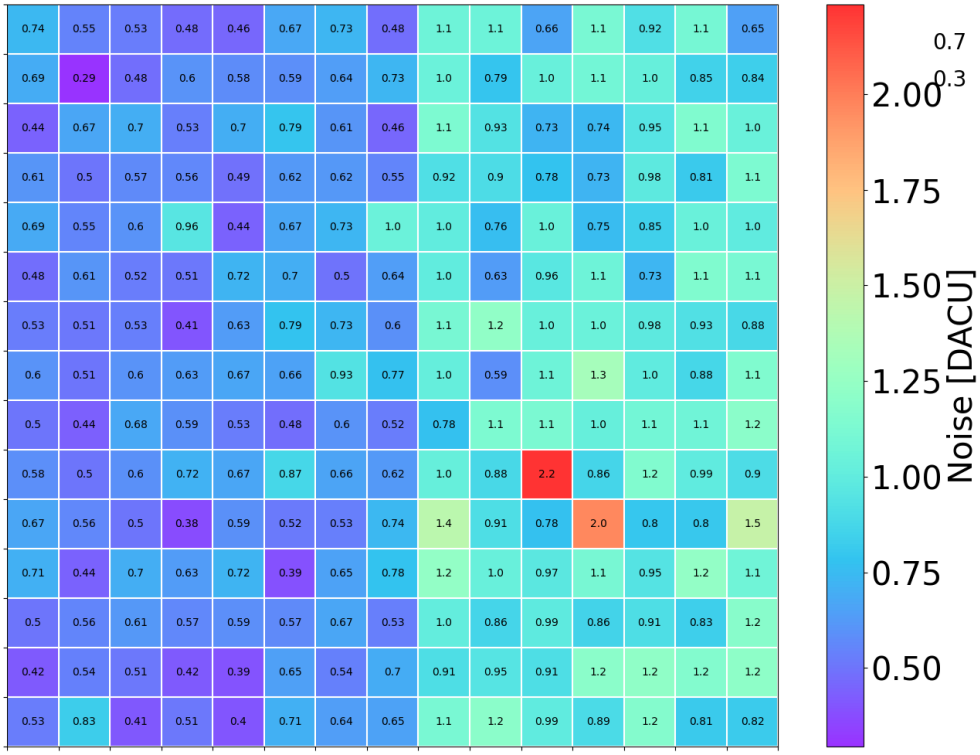

Figure 5.13: Jitter map for a 12 fC injected charge. The jitter is between 5.8 ps and 44 ps. The conversion factor in 20 ps/DACU.

5.2.2 Tests at low temperature

The performance tests of the front-end electronics include a test at low temperature. These tests are performed using a Votsch VT 4002 EMC climate chamber. This box can control the temperatures from −30 °C to 100 °C.

In the case of ALTIROC2, the temperature has been limited to the following values: −30 °C, −20 °C, −10 °C and 20 °C. An Arduino card connected to a sensor is used to monitor the humidity and the temperature inside the box. The test includes a routine including a TDC LSB monitoring (for TOA and TOT), a V_{th} threshold tuning for a charge at 12 fC, a V_{thc} tuning and the monitoring of the usual bias voltages. Each test is performed on all pixels in the matrix but the following plot are shown for columns 7 and 8.

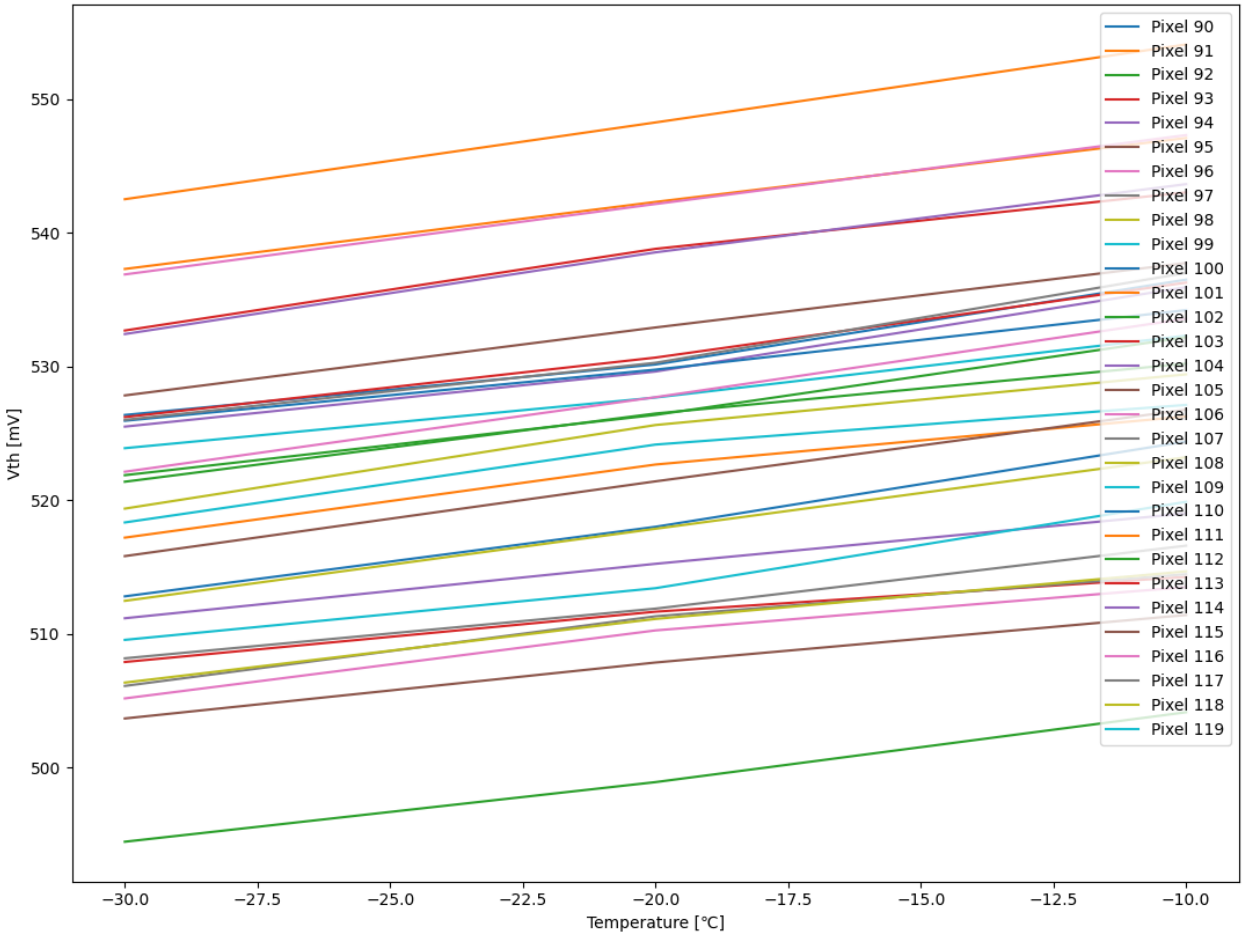

Figure 5.14: Evolution of the V_{th} threshold for a 12 fC injected charge as a function of the temperature for columns 7 and 8.

Figures 5.14 and 5.15 show the evolution of the TDC_{TOT} LSB and V_{th} with respect to the temperature. A drift is observed in both plots, lower than 3% while the TOA TDC bin remains constant. For bias voltages and reference currents, the same observation can be done, a 3% drift appears between 20 °C and −30 °C.

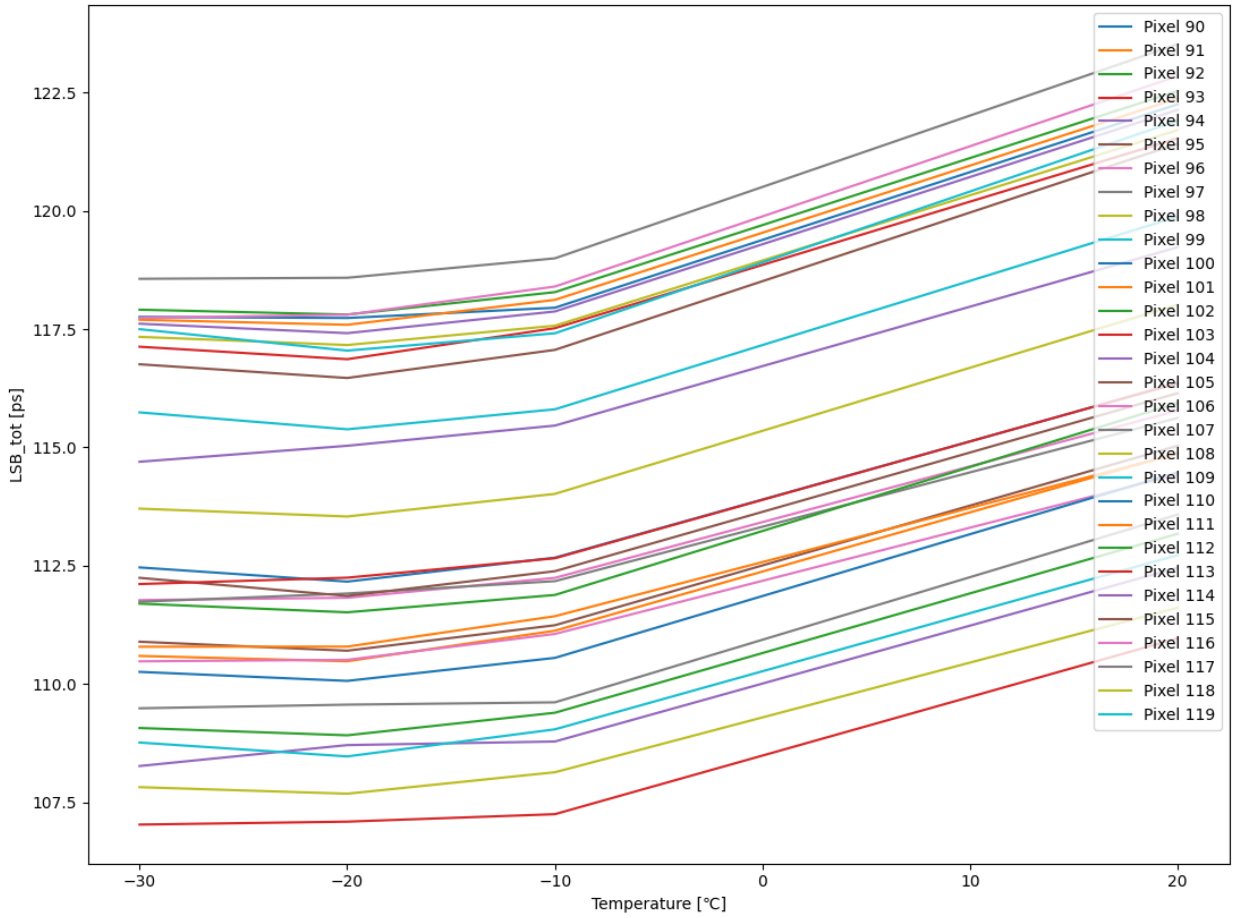

Figure 5.15: Evolution of the TOT TDC LSB as a function of the temperature for the columns 7 and 8

5.2.3 Irradiation tests

As described in section 4.6.6, the irradiation effects can be separated into two groups: the cumulative effects and the single effects. Respectively, they include the total ionizing dose and the single event upset tests. ALTIROC2 has been tested for each effect.

Total Ionizing Dose tests

Total Ionizing Dose test has been performed at CERN with a X-Ray X-RAD iR160 irradiator [63]. Initially developed as a biological irradiator, it is now used to study the impact of irradiation on electronics and sensors. This machine is composed of an irradiation chamber, a control panel, a HV system and a cooling box.

The experimental setup is similar to the test bench setup, including the ALTIROC PCB, the FPGA and the mezzanine. A multimeter is connected to monitor various bias voltages and reference currents during the test. The test has been performed on the column 7 and 8 of the ASIC, including respectively a VPA and TZ preamplifier.
The test loop includes a TDC LSB check for TOA and TOT, a threshold scan and finally an injected charge scan. The performance of the board did not appear to be impacted by the radiations up to 200 Mrad. Yet, few drifts have been noticed in some bias voltage lower that, see figures 5.16, 5.17.

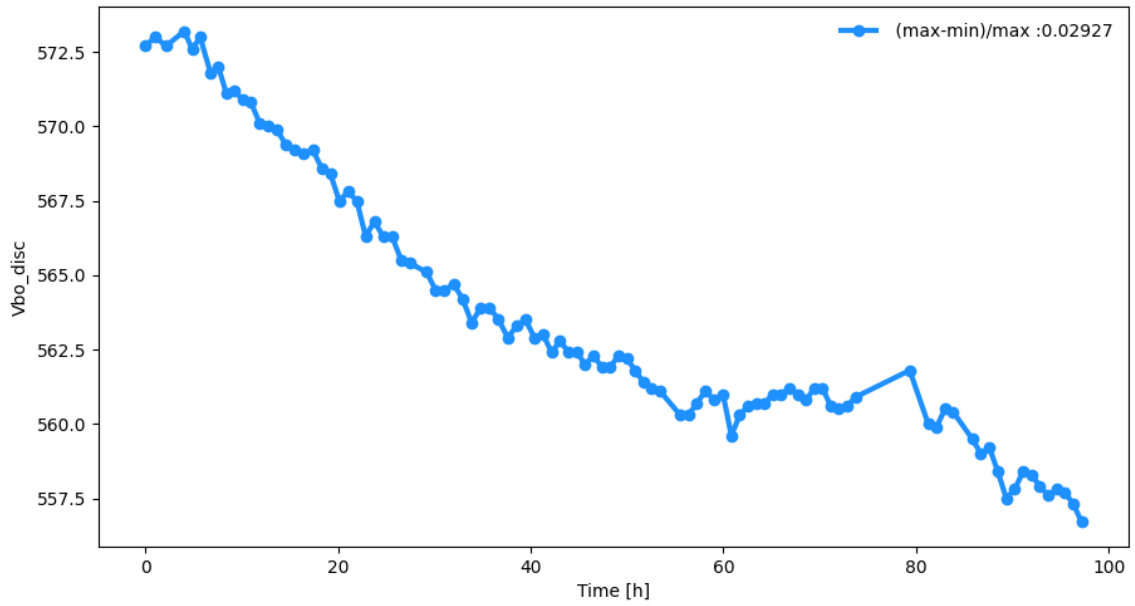

Figure 5.16: Evolution of the output voltage of the discriminator as a function of the irradiation time.

This test shows that the ASIC was low impacted by the total ionizing dose, except for a few channels, the jitter remains constant with the irradiation dose. The ASIC can work under irradiation until 200 Mrad, agreeing with the requirement.

Single Event Upset

As it has been done for ALTIPIX, SEU tests were organized for ALTIROC2 in June 2022, using the board 6 at le centre Antoine-Lacassagne. This time, the sensitive component of the setup has been protected by polymer blocks to prevent the FPGA from any unwanted irradiation. The irradiation time was organized as follows:

- 2 hours at low intensity (I = 2.70 10^9 p.cm^{-2}.s^{-1})

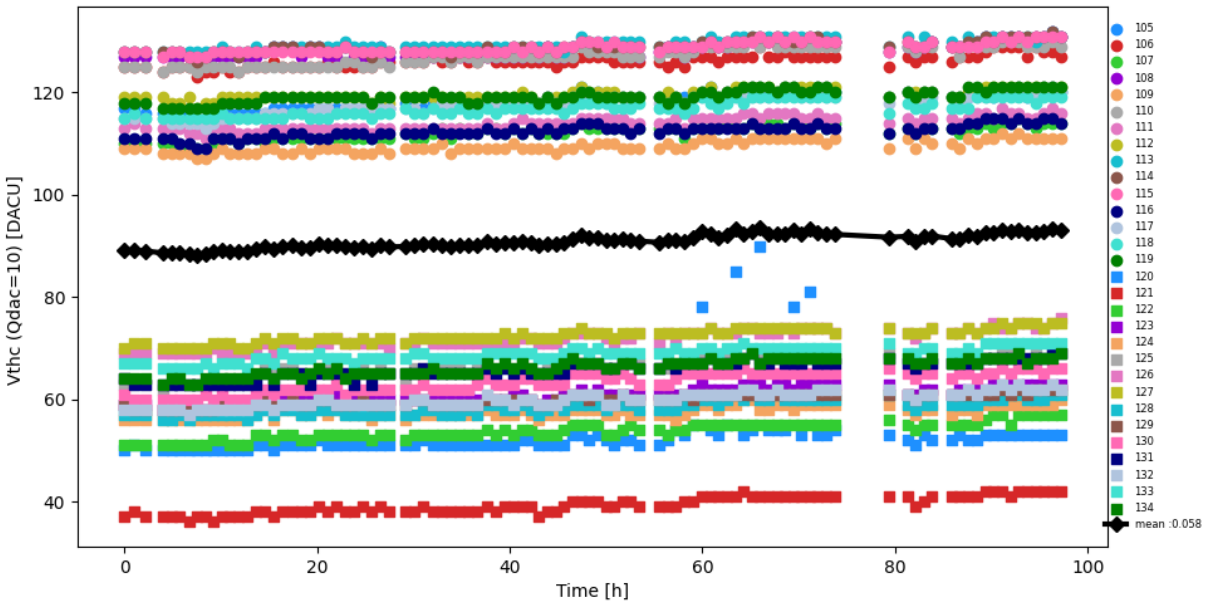

(a)

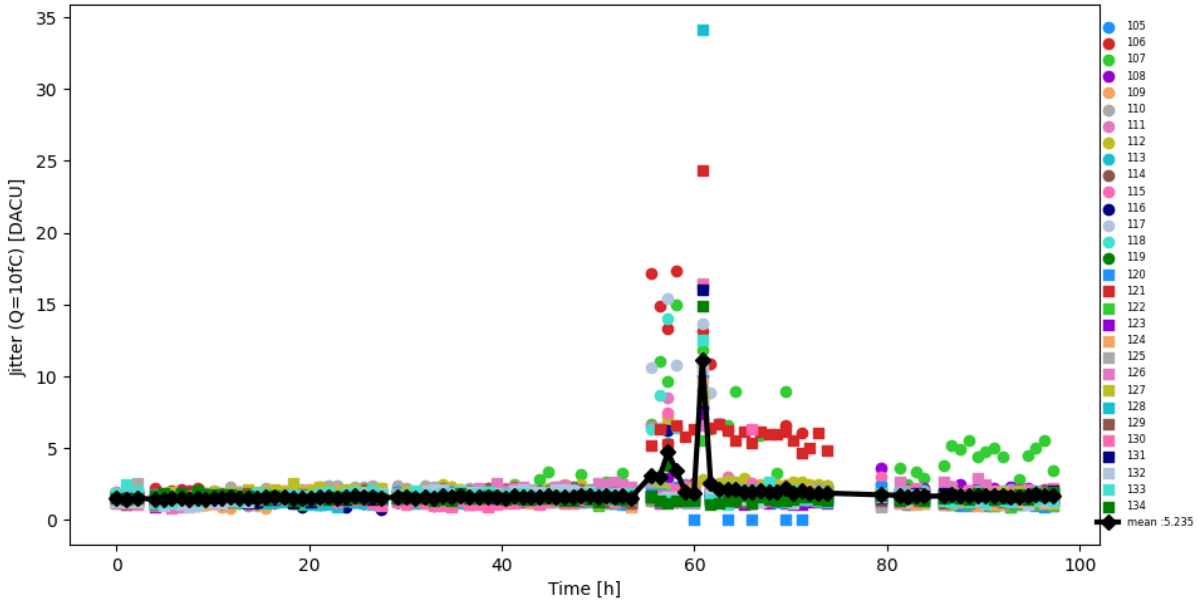

(b)

Figure 5.17: Evolution of the corrective threshold (on top) and the jitter (on bottom) with respect to the irradiation time.

- 1 hour at high intensity (I = 9.00 10^{10} p.cm^{-2}.s^{-1})

The distribution of the beam is shown in figure 5.18.

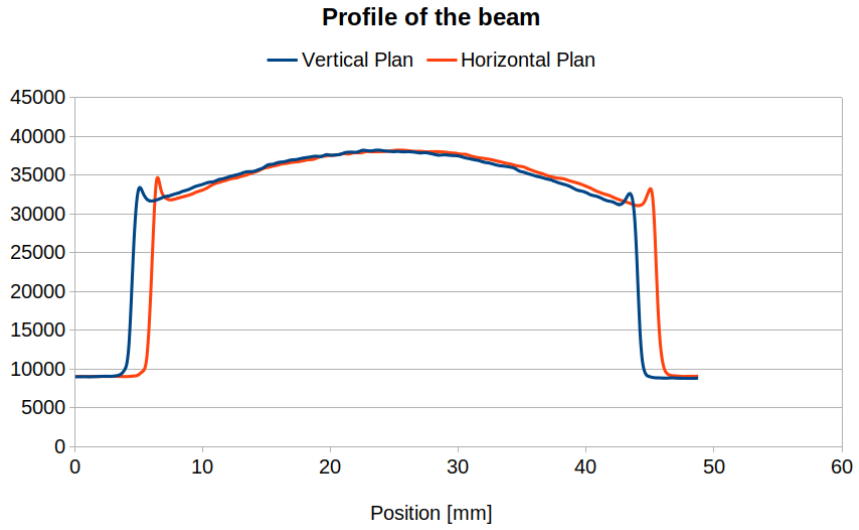

Figure 5.18: Beam profile for SEU tests on ALTIROC2.

ALTIROC2 do not integrate dedicated registers or counters as ALTIPIX but the methodology was similar: write a given value on each register and check regularly the value. An additional test has been performed in order to check the impact of the SEU on the SRAM. The objective is to inject a well-known TOA and TOT, and check the value in the SRAM considering different latencies. A monitoring of common bias voltages and reference currents has been done in parallel.
In ALTIROC2, the optimization of the TMR is automatized and the data is expected to be more protected than for ALTIPIX due to the structure of the triplication. But few elements remain not triplicated, including the PLL the SRAM and some outlying registers.

The direct measurement of the auto-correction failure is performed through the nine hundred 8-bit registers dedicated to pixels. Registers were divided into 3 groups and filled with three values: 0, 127, 255.
For the low-intensity phase, no errors have been observed for each frame. As it has been done for ALTIPIX, the number of errors per ASIC for one day of HL-LHC can be extrapolated by considering a Poisson distribution and an upper limit of 3. The result is presented in the table 5.7.
For the high-intensity phase, the measurement of the auto-correction failure was limited by the PLL. Since the PLL was not triplicated, the clock has been affected by the irradiation.

The consequence of this effect has been the loss of the synchronisation of the ASIC, by consequence the FPGA is not able to communicate with the ASIC and the board had to be rebooted. The data obtained during high intensity are not exploitable.

5.2.4 Tests performed with a hybrid using a strontium source

The performance of the associated LGAD bump-bonded over an ALTIROC, called hybrid, has been tested with a strontium source Sr^{90}. This source undergoes β^- decays (74 MBeq) and is placed on top of the LGAD matrix, as shown in figure 5.19. The rest of the setup remains the same as the test bench.

Figure 5.19: Strontium Sr^{90} placed on top of the LGAD bump-bonded on ALTIROC2.

The source has been used to verify the bonding and the pixel responses. Figure 5.20 represents the pixel responses of the matrix. The colour of this figure illustrates the number of hits on the signal registered by the ASIC. It can be noticed that some pixels do not register any hits, they are considered as dead pixels. This failure can come from a failure in the bump-bonding, in the sensor or from the ASIC. In the case of figure 5.20, the failure came from the bump-bonding or the sensor because the test of the ASIC through the injected charge does not reveal any failure in the ASIC.
The tests of performance already introduced with the ASIC alone can be performed on a hybrid ASIC. The tests performed on various hybrid board demonstrates that the signal is noisier than with the ASIC alone board. This leads to an increase in the minimal detected

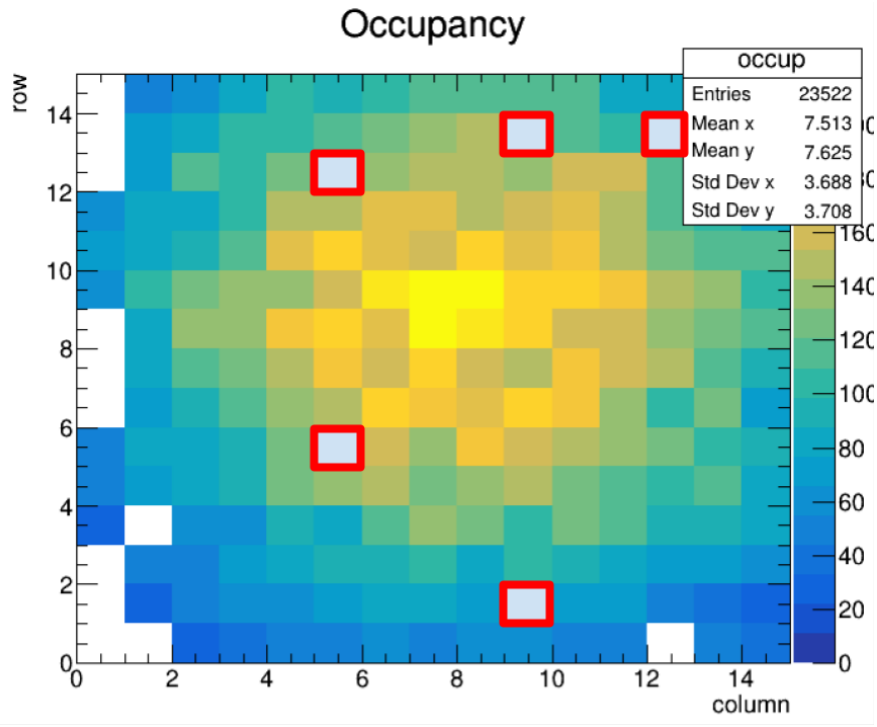

Figure 5.20: Occupancy map of an hybrid ALTIROC2 (ASIC+LGAD bump-bonded). The red squares represent the position of the dead pixels in the matrix.

charge: 4 fC for the full matrix on instead of 3 fC for the ASIC alone, the full matrix on. A solution has been found to remove the high-voltage capacitors for the sensor, to lower this limit.

5.3 Performances during test beam

5.3.1 Performance test with an hybrid ALTIROC

The hybrid version of ALTIROC has been tested during a test beam campaign in order to determine the performances in a high irradiation environment. At the time of writing this thesis, two versions of the ASIC have been tested during my thesis: ALTIROC1 and ALTIROC2. As the difference in the setup between ALTIROC1 and ALTIROC2 remains negligible, the setup is described for a given ALTIROC hybrid version. I participated in these test beams as a shifter and expert in the ASIC.
The ALTIROC hybrid board has been exposed up to 120 GeV pions at CERN-SPS. The setup is composed of a EUDET telescope made of six MIMOSA pixel planes (three planes of each side of the DUT) to perform the tracking of particles. In front of the upstream MIMOSA

planes, two scintillators are placed perpendicularly to each other for the trigger. At the downstream, a Silicon PhotoMultiplier combined with a quartz bar is placed, it provides a time reference used in the data acquisition (DAQ). Finally, a special FE-I4 plane is placed close to the DUT (ALTIROC hydrid). This device is a pixel detector with a pixel size of 50 µm×250 µm and has been designed initially for the ATLAS IBL detector. It is used to define a region of interest in order to accept only the tracks seen by the ALTIROC matrix. As on the test bench, the ALTIROC PCB is connected with the FPGA connected to a computer to run the code. Depending on the test beam campaign, the ALTIROC2 hybrid has been sometimes integrated into a climate chamber to keep the temperature at −30 °C. Figure 5.21a shows the setup previously described.

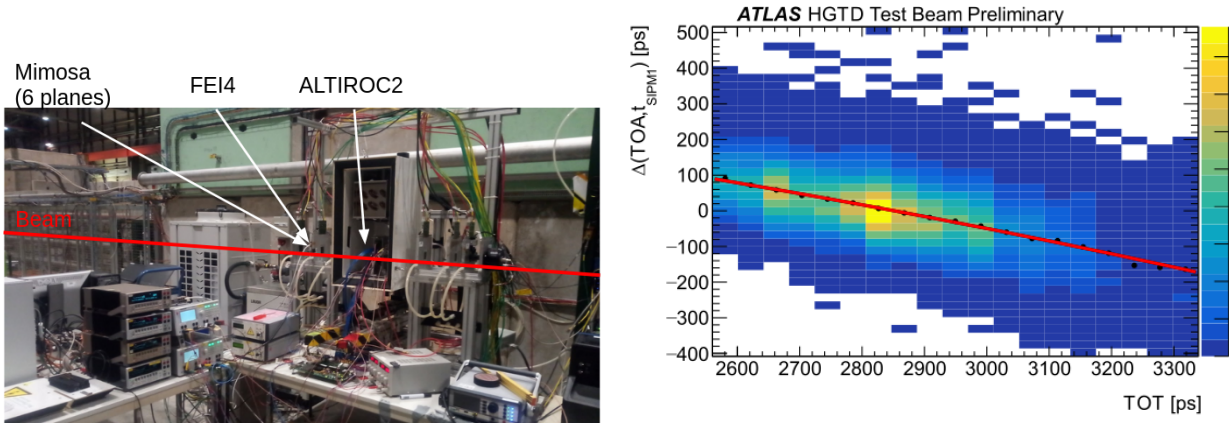

(a) (b)

Figure 5.21: (a):Photo of the setup used at CERN-SPS, with 120 GeV pions beam. (b): A fit of the TOA with respect to the TOT. This method is used to determine the time-walk correction [64].

Due to the dependency of the TOA with respect to the amplitude of the injected signal, a time walk correction based on a fit of the TOA with respect to the TOT measurement is used, as shown in figure 5.21b. After this time-walk correction, the resolution of the combination ALTIROC+LGAD can be estimated, reaching approximately 45 ps with a jitter contribution estimated at 40 ps. The efficiency is defined as the ratio of the reconstructed tracks associated with a signal above the threshold (set at 4.8 fC) to all reconstructed tracks that traverse the active area. The efficiency map, shown in figure 5.22a has been obtained with the ALTIROC2 hybrid version with 75 GeV charged pions in Autumn 2022. An efficiency about 100 % was achieved for each pixel in the non-inter-pad region. This interpad region is defined as the region between two pixels where the efficiency is lower than 50 %, as shown in figure 5.22b.

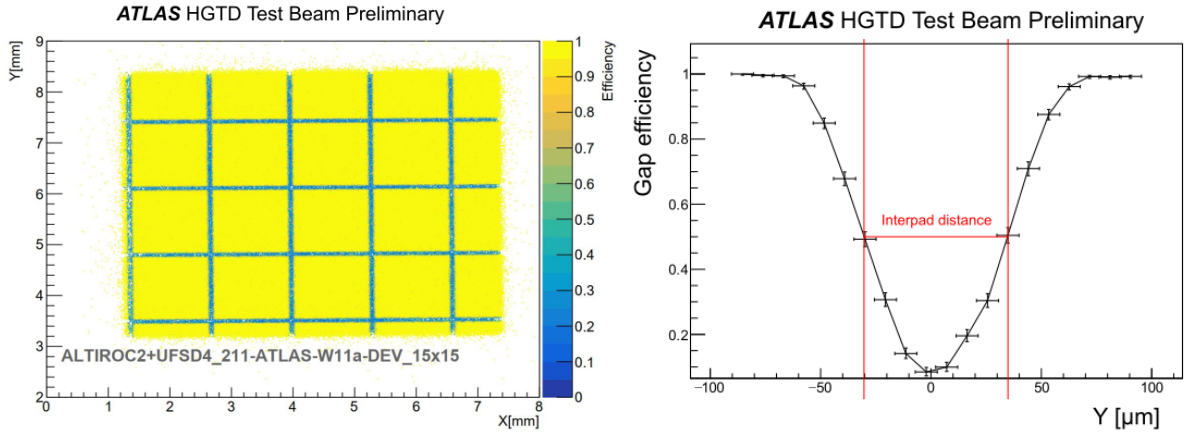

(a) (b)

Figure 5.22: (a): Efficiency map ALTIROC2+UFS LGAD measured as the ratio of the reconstructed tracks associated with a signal above the 4.8 fC threshold to all reconstructed tracks that traverse the active area [64]. (b):Efficiency of ALTIROC2+UFS LGAD measured in the interpad region [64].

Single Event Burnout on LGADs

At the end of the HGTD lifetime, the LGADs are expected to resist a fluence of $2.5 \times 10^{15}\,n_{eq}cm^{-2}$. In September 2020, during a test beam campaign to test the performances of the LGADs, some permanent burnouts were observed on irradiated LGADs. This phenomenon results from an instantaneous alteration in the devise response after high-energy particle interactions, leading to a permanent failure. Figure 5.23 shows the impact of that failure on an LGAD sensor. This phenomenon was not observed at laboratories using a strontium source because the range of energy is lower than during the test beam, with at maximum 2.3 MeV in the active zone of the LGAD.
To understand this phenomenon various test beam campaigns have been organized to test 64 sensors with different characteristics (thickness and HV range) at DESY using 3 GeV electron beam or at CERN using 120 GeV pions beam. These tests have been organized in order to identify the robust technologies. I participated in these test beams as a shifter.
Whatever if the test has been done at DESY or at CERN, the setup remained the same: a train of 16 sensors shared by pairs on 8 PCBs are aligned using a mechanical rail in the beam line, as shown in figure 5.24. Each PCB board has been designed in order to extract a current defined as the voltage drop on the bias resistor. Two scintillators are placed in front and at the end of the train of PCBs to align the train with respect to the beam line. Then each sensor is supplied in high voltage using a CAEN N472 HV power supply, remotely monitored from the control room. The train of PCBs is placed into a climate chamber (at CERN) or an isolated box cooled down by dry ice (at DESY) in order to maintain a temperature between

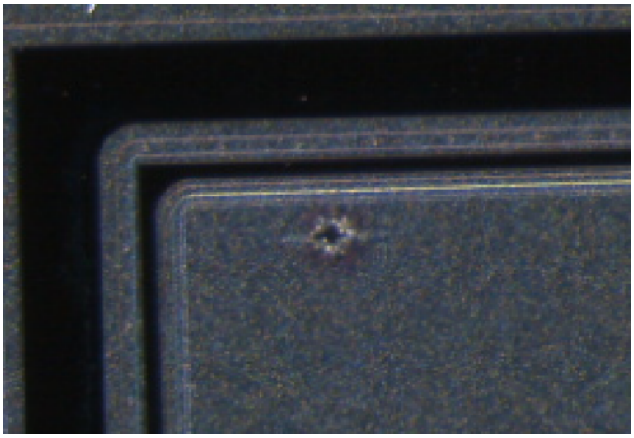

Figure 5.23: Microscopic picture of a Single Event Burnout observed on an HPK wafer irradiated to $2.5 \times 10^{15}\,\mathrm{n_{eq}cm^{-2}}$.

$-40\,^{\circ}\mathrm{C}$ and $-25\,^{\circ}\mathrm{C}$ along the test. A humidity and temperature sensor is installed close to the train of PCBs for monitoring.

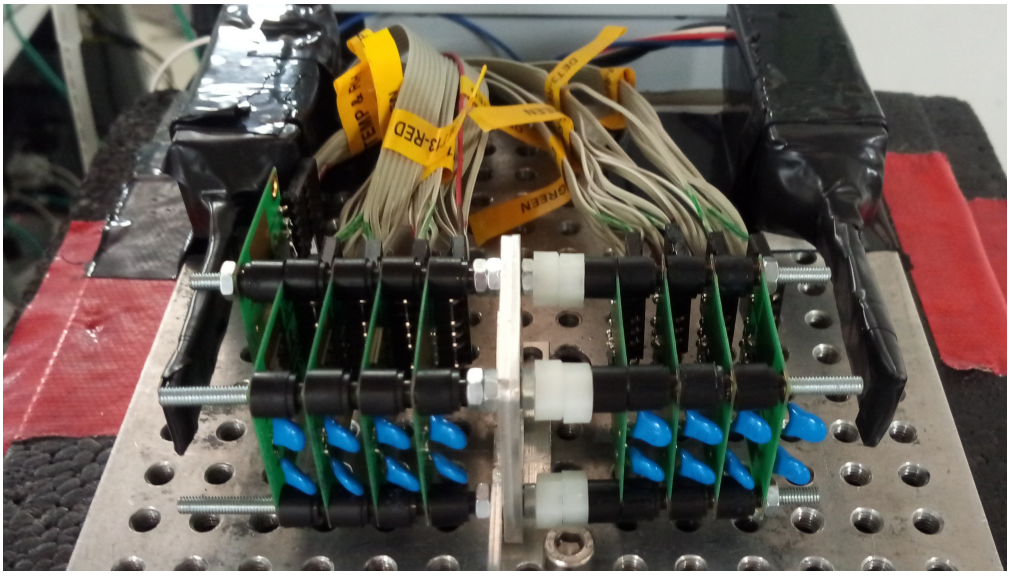

Figure 5.24: Train of PCBs placed in a cold box in the beam, each PCB contains two LGAD sensors. Two scintillators are placed on both sides of the train for alignment with the beam line.

It has been shown that the risk of observing burnout is governed by the electric field, whatever the design of the LGAD is. A critical upper limit of $11\,\mathrm{V/\mu m}$ has been determined as a safe limit, as shown in figure 5.25. In addition, the use of carbon-enriched sensors is preferred

because they can operate with a low electric field, which solves burnout risk.

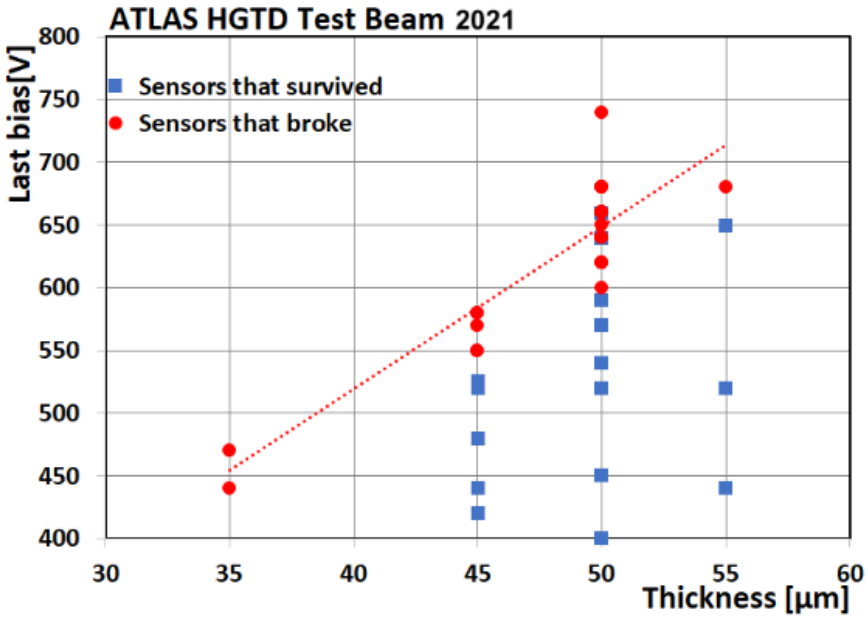

Figure 5.25: Comparison of the last tested bias voltage with respect to the thickness of the LGAD sensor, for sensors that survived (in blue) and sensors that broke (in red), [65].

Intensity $[nA.cm^{-2}]$	Frame	Registers	σ_{SEU} $[10^{-14}\ cm^2]$
3.1 ± 0.1	0000000	1	7.97 ± 1.13
		2	6.37 ± 1.01
		3	5.74 ± 0.96
		4	7.01 ± 1.06
	Average		6.77 ± 0.41
299.9 ± 1.3	11111111	1	6.88 ± 0.25
		2	7.50 ± 0.25
		3	7.30 ± 0.25
		4	7.11 ± 0.25
	11111111	1	8.52 ± 0.36
		2	7.74 ± 0.34
		3	8.64 ± 0.36
		4	8.61 ± 0.36
	11111111	1	7.60 ± 0.12
		2	7.75 ± 0.12
		3	7.82 ± 0.12
		4	7.89 ± 0.12
	11111111	1	8.21 ± 0.30
		2	8.48 ± 0.31
		3	8.13 ± 0.30
		4	8.20 ± 0.30
	Average		7.90 ± 0.13

Table 5.4: SEE cross-sections per bit for the 64 dedicated registers according to the intensity and the frame. The uncertainty on the average is computed using the spread of the individual measurements.

	N^{bit}_{HL-LHC}	N^{ASIC}_{HL-LHC}
$1 \rightarrow 0$	$(4.0\pm0.1)\ 10^{-13}$	$(2.9\pm0.1)\ 10^{-9}$
$0 \rightarrow 1$	$(3.0\pm0.4)\ 10^{-13}$	$(2.1\pm0.3)\ 10^{-9}$

Table 5.5: Predicted number of auto-correction failures due to SEUs, per triplicated bits and per ASIC.

Distance from the X-rays source	10.1 cm
Dose frequency	2.99 Mrad.h^{-1}
Beam diameter	5.1 cm
Beam area	19.9 cm^2
Beam current	18 mA
Temperature	20 °C
Time to target to reach 200 Mrad	44.9 hours

Table 5.6: X-Ray machine configuration for the TID test done at CERN

Frame	Errors	N^{bit}_{HL-LHC}	N^{ASIC}_{HL-LHC}
00000000	0	$< 8.5\ 10^{-5}$	< 0.61
10101010	0	$< 7.4\ 10^{-5}$	< 0.52
11111111	0	$< 6.1\ 10^{-5}$	< 0.43

Table 5.7: SEU results obtained with ALTIROC2 version during low intensity rate

Chapter 6

Objects reconstruction in ATLAS experiment

The particles from the proton-proton collisions in the ATLAS detector are spread in all directions until they reach a layer of a sub-detector described in chapter 3. Each particle leads to an ensemble of electric signals along its path. These responses are then interpreted as the presence of a certain type of particle. This process is called the reconstruction. It is followed in general by the identification algorithm. This chapter concerns the algorithms applied to the information collected from all sub-detectors in order to reconstruct the final objects used in physics analyses. Only objects used in the analysis (chapter 7) are described: the leptons in section (6.1, jets in section 6.2, as well as the missing transverse energy (MET) in section 6.3.

6.1 Leptons

As described in the chapter 1 leptons include two classes of particles: the charged leptons (electron, muons and tau) and the neutral leptons (neutrinos). In this section, only charged lepton reconstruction is broached. As a neutral particle, neutrinos cannot interact with sub-detectors of the ATLAS experiment but enter into the account of the MET as described in section 6.3.

6.1.1 Electrons

Electrons are reconstructed using the energy deposits measured in the electromagnetic calorimeter and their matched tracks in the inner detector. In this section, the reconstruction, the identification and the isolation of electrons procedure are explained.

Reconstruction

An electron can lose an important amount of its energy through a Bremsstrahlung when it interacts with matter along its paths. The induced photon can decay into an electron-positron pair. This interaction takes place in the ID detector or in the beam pipe which generates multiple tracks in the ID. The reconstruction of the electron is based on a three-step process:

- EM Cluster reconstruction: The electromagnetic calorimeter is divided into towers of $\Delta\eta\times\Delta\phi$=0.025×0.025, using all layers. A sliding-window algorithm scans over the cells to search the localised energy deposit. The cluster corresponds to an energy deposit with a transverse energy above 2.5 GeV. If two seed cluster candidates are found in close proximity, only the higher transverse energy is kept.

- Track reconstruction: This algorithm uses the information collected by the ID, composed of the pixel, SCT and the TRT subdetectors: track seeds are formed from a set of three space points. The reconstruction starts in three steps: pattern recognition, ambiguity resolution and the TRT extension. Track candidates are then fitted in a global ATLAS χ^2 fitter. considering additional potential energy losses. Then, a Gaussian-sum Filter (GSF) [66] is applied to the cluster measurements to match tracks with silicon hits to EM clusters. This algorithm has been designed to take into account the non-linear effect related to bremsstrahlung. Finally, the TRT tracks (reconstructed only in TRT) are associated with tracks with silicon hits.

- Track association with the cluster: track with momentum higher than 0.5 GeV are extrapolated from their last point in the middle layer of the EM calorimeter. The extrapolated coordinates in the (η, ϕ) space are compared with the corresponding cluster position. An electron is considered reconstructed if at least one track is matched with a cluster. In the case of multiple matches, the smallest distance $\Delta R = \sqrt{(\Delta\eta)^2 + (\Delta\phi)^2}$ is chosen.

Identification

The identification of prompt electrons is performed with a likelihood-based (LH) method defined as:

$$L_{S(B)}(x) = \prod_{i=1}^{n} P_{S(B),i}(x_i)$$

with x the vector that contains multiple discriminating variables. $P_{S,i}(x_i)$ is the PDFs for the variable i at the value x_i for the signal S. This algorithm extract information from cluster-to-track information, and calorimeter showers. This method aims to improve the recognition between a prompt electron, e.g. an electron originates from the primary vertex, and a non-prompt electron. These latest are produced from photon conversion, misidentified jets, and

semi-leptonic decay of heavy and light flavour hadrons. Then for each electron candidate, a discriminant d_L is calculated:

$$d_L = \frac{L_S}{L_S + L_B}$$

The distribution of this variable remains limited between zero and one and has two peaks, at unity(zero) for signal (background). This distribution is not in favour of the definition of various working points (WPs). As a consequence, an inverse sigmoid function is used to transform this distribution of d_L, leading to a distribution shown in figure 6.1.

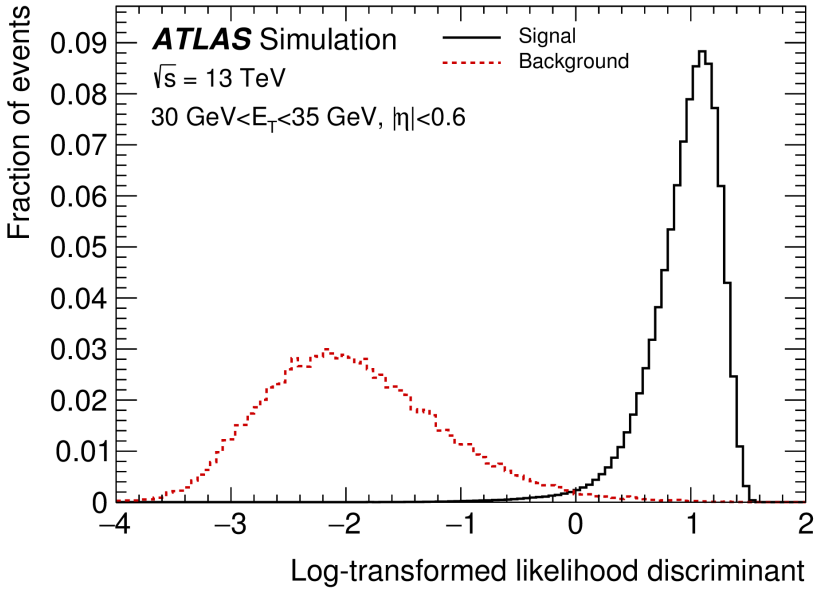

Figure 6.1: The transformed LH-based discriminant d'_L for reconstructed electron candidates with 30 GeV$< E_T <$30 GeV and $|\eta| <$0.6. The signal in black corresponds to $Z \to ee$ simulation sample, while the background is in red[67].

Isolation

Another criterion remains important for the physics analysis, especially in terms of non-prompt background estimate: the isolation of the electrons. A characteristic signature of these events is represented as an unexpected activity in the area surrounding the reconstructed electron. In physics analysis, two variables are built for this purpose:

- The calorimetric isolation energy $E_T^{cone\Delta R}$, defined as the sum of the transverse energies of topological clusters whose barycentres fall within a cone of radius $\Delta R = 0.2$.

- The track isolation variable $p_T^{varcone\Delta R}$, defined as the sum of transverse momenta of all tracks satisfying the quality requirement, in the cone radius $\Delta R = \max(10\,\text{GeV}/p_T,$ 0.2-0.4).

The implementation of the isolation criteria remains specific to each physics analysis needs. Yet, several isolation operating points are estimated using one of the previously defined isolation variables or both simultaneously. The requirements for the three operating points are defined in E_T and η bin-ranges:

- Loose isolation: Targets a fixed value of the isolation efficiency, uniform in η and E_T.
- Gradient isolation: Targets a fixed value of the isolation efficiency, uniform in η and E_T dependant.
- Fixed isolation: Imposes fixed requirements on the value of the isolation variables.

Electron-charge identification

The charge of the electron is identified by the curvature of the associated track in the ID. A misidentification of the charge (QmisID) will have a severe impact on the analysis presented in chapter 7. The misidentification of the charge of an electron can result from the matching of an incorrect track to the electron candidate or from the failed measurement of the curvature. The probability of bremsstrahlung emission of a photon, decaying into an electron-positron pair is fully dependent on the amount of matter traversed by the initial particle as shown in figure 6.2. With a probability ϵ for an electron to be reconstructed with a wrong charge (η, E_T) binning, the total number of the event for a pair of electron signature to be same-charged (SC) can be expressed as follow:

$$N_{ij}^{SC} = N_{ij}^{OS+SC}[(1-\epsilon_i)\epsilon_j + (1-\epsilon_j)\epsilon_i]$$

with N_{ij}^{OS+SC} the total number of events, the sum of opposite charge event (OC) and same charge events, for two electrons i,j.
The QmisID rate for the reconstructed electron candidate is reduced using a discriminant Boosted Decision Tree output. The training of this variable is performed on simulated single-electron samples using 8 variables distribution related to the quality of the tracking.

Photon VS Electrons

The interaction produced by a photon and an electron in the electromagnetic calorimeter generates similar showers, and photons do not interact in the ID. As a consequence, their reconstruction is performed in parallel in the EM calorimeter, with a distinction over the nature of the particle on the existing (electron) or absence (photon) of tracks in the ID. The identification of photon candidates in the ATLAS detector relies on selection over different

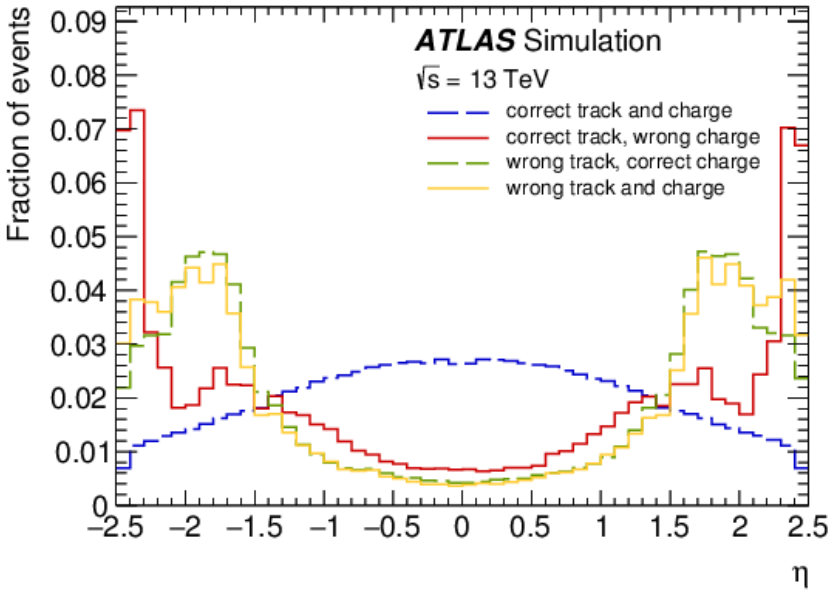

Figure 6.2: Psuedorapidity for electrons in $Z \to ee$ samples in case of electrons with correct or wrong track and charge [67].

calorimetric variables, which provide a good distinction between prompt and non-prompt photons. Usually, the expected energy deposit of prompt photons in the EM calorimeter is narrower compared to non-prompt photons.

6.1.2 Muons

Reconstruction

The reconstruction of the muons is based on the track receipted by the ID and the MS independently. In the ID, the muon is reconstructed as another charged particle, as described for the electron in section 6.1.1. This section is focused on the description of the muon reconstruction in the MS. The information from individual sub-detectors is combined to form the muon tracks used in various physics analyses.
The MS reconstruction starts with a hit pattern in each muon chamber to form track segments. Then hits associated with each track are fitted with a χ^2 fit. The track candidate is accepted if the result of the global χ^2 fit fits the selection criteria. Finally, the final track candidate is determined by the combination of tracks from the ID, using the following algorithms:

- Combined (CB) muons: This algorithm combines the tracks from MS and ID in a global refit. In this procedure, the hits from MS can be added to or removed from

the track to improve the fit quality. In general, the reconstruction of muons is done with an outside approach, meaning that muons are firstly reconstructed in the MS and then extrapolated inward and matched to an ID track. But this algorithm is completed with an additional inside-out combined approach, in which the ID track is extrapolated outward and matched to MS tracks. This kind of muons is the most used in physics analyses.

- Segment-tagged (ST) muons: A track in the ID is identified as a muon if once extrapolated to the MS, the CSC or MDT chambers contain at least one track segment. This algorithm is used when muon hits only one layer of MS chambers, due to the low p_T or when it falls in not instrumented regions of the MS.

- Calorimeter-tagged (CT) muons: A track in the ID is identified as a muon if the track corresponds to a MIP-compatible energy deposit in the calorimeter. This algorithm performs the lowest purity of all muon particles as it does not use data from MS. But it recovers a region where the ATLAS muon spectrometer is partially instrumented, for the region $|\eta| < 0.1$ and a momentum range of $15\,\text{GeV} < p_T < 100\,\text{GeV}$.

- Extrapolated (ME) Muons: The reconstruction of the trajectories is MS-based only with loose requirements on compatibility with primary vertex origin. The muon is required to hit at least two layers. This algorithm extends the acceptance for muon reconstruction in the region not covered by the ID ($2.5 < |\eta| < 2.7$).

Identification

After reconstruction, muon candidates used for physics analysis are selected by a set of requirements referred to as working point (WP). Analysis needs different requirements in terms of efficiency of prompt-muon identification, resolution of the momentum measurement and rejection of the non-prompt muons.

- Medium selection WP is the standard criteria for muons in the ATLAS analyses because it provides efficiency and purity that suits a wide range of analyses, and keeps the systematics uncertainties in the prompt-muon efficiency and background small.

- Loose selection WP has been optimized initially for the Higgs boson decays in the four-muon final state. Due to the high multiplicity of the muon in this channel and the large signal-to-background ratio, the WP provides a higher efficiency but a lower purity and larger systematic uncertainties.

- Tight selection WP provides the highest purity and is in favour of physics analysis with a high non-prompt muon background.

Isolation WP	Discriminating variables	Definition
LooseTrackOnly	$p_T^{varcone30}/p_T^{\mu}$	99% efficiency, constant in η and p_T
Loose	$p_T^{varcone30}/p_T^{\mu}$, E_T^{cone20}/p_T^{μ}	99% efficiency, constant in η and p_T
Tight	$p_T^{varcone30}/p_T^{\mu}$, E_T^{cone20}/p_T^{μ}	96% efficiency, constant in η and p_T
Gradient	$p_T^{varcone30}/p_T^{\mu}$, E_T^{cone20}/p_T^{μ}	99% efficiency at 60 GeV
GradientLoose	$p_T^{varcone30}/p_T^{\mu}$, E_T^{cone20}/p_T^{μ}	99% efficiency at 60 GeV
FixedCutTightTrackOnly	$p_T^{varcone30}/p_T^{\mu}$	$p_T^{varcone30}/p_T^{\mu}$¡0.06
FixedCutLoose	$p_T^{varcone30}/p_T^{\mu}$, E_T^{cone20}/p_T^{μ}	$p_T^{varcone30}/p_T^{\mu} < 0.15, E_T^{cone20}/p_T^{\mu} < 0.30$

Table 6.1: Definition of the seven working points for the isolation of muons.

Two additional working points are designed for specific analysis: High-p_T and Low-p_T. The High-p_T WP has been designed to ensure an optimal momentum resolution for muons candidates with momentum higher than 100 GeV. This WP is usually used in W and Z searches. Ton the contrary, the Low-p_T WP targets muons with low momentum, exploiting a large set of variables to provide a good separation between prompt muons and from light-hadron decays muons. This WP is used in the quark-mixing sector and searches of super-symmetry.

Isolation

As for electrons, the isolation for reconstructed electrons uses the track-based and calorimeter-based isolation variables. A list of a selection of seven working points is measured in data and simulation in $Z \to \mu\mu$ decays: LooseTrackOnly, Loose, Tight, GradientLoose, FixedCutTightTrackOnly and FixedCutLoose. Each WP are defined with different criteria and discriminating variable as shown in table 6.1. This isolation helps in the discrimination of muons from the heavy flavour decays (expected to be more isolated) than muons from semileptonic decays. Figure 6.3 shows the

6.1.3 Taus

The τ-lepton is extremely massive compared to the two other leptons (1.777 GeV) and has a very short lifetime (2.9×10^{-13} s, $c\tau = 87\,\mu$m). As a consequence, it decays in the beam pipe, even before reaching the detector, but can be observed through its decay products. The τ is the only lepton which decays into both leptons (35%) and hadrons (65 %). In the ATLAS detector, only the hadronic decays are considered in the reconstruction due to the challenge

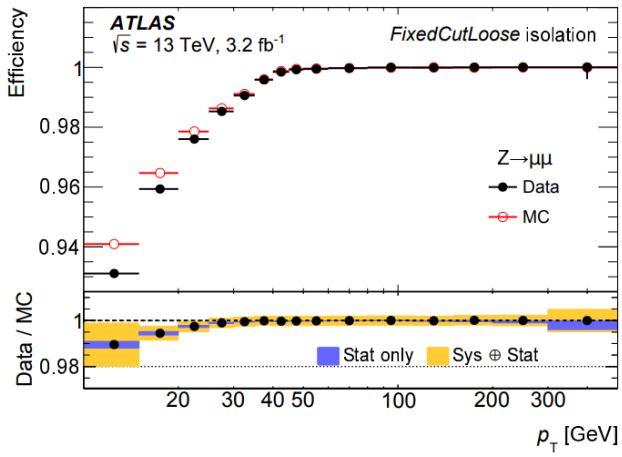

Figure 6.3: Distribution in p_T of the efficiency for the FixedCutLoose working point, in $Z \to \mu\mu$ decays[**Aad˙2016**]

in the distinction of the leptonic decay product with the real prompt leptons.
The hadronic decay is usually characterized by the production of one or three charged pions in 72% and 22% of all cases respectively, with a ν_τ. In 68% of all hadronic decays, an additional neutral pion is produced [24]. Charged and neutral hadrons are called hadronic taus τ_{had} and are associated with a shower in calorimeters with a track in the ID of the ATLAS detector. The reconstruction of the τ is based on the method used for the jets as developed in section 6.2, formed from a topo-cluster passing into the anti-k_t algorithm. The tau identification algorithm uses a Boosted Decision Tree [68] or a neural network (NN) [69, 70] trained with simulated $Z/\gamma* \to \tau\tau$ for signal and di-jets events for background. Figure 6.4 shows the evolution of the rejection of fake hadronic tau with respect to the true hadronic tau identification efficiency.

6.2 Jets

A jet usually results from the hadronization of the quarks and gluons present in profusion in pp collisions at the LHC and it is constructed as a collimated spray of hadrons. These jets tend to be highly collimated and require a small angle for their reconstruction (radius parameter R=0.4). Occasionally, jets are produced from the hadronic decay of massive particles (H, Z/W, t, ...). These jets have a larger angular separation so need to be reconstructed with a large radius parameter (R=1). The signature of jets in the ATLAS detector is a cluster of energy deposits in the calorimeter associated with charged particle tracks in the ID. In this thesis, the jet multiplicity is used to define the signal region and control regions.

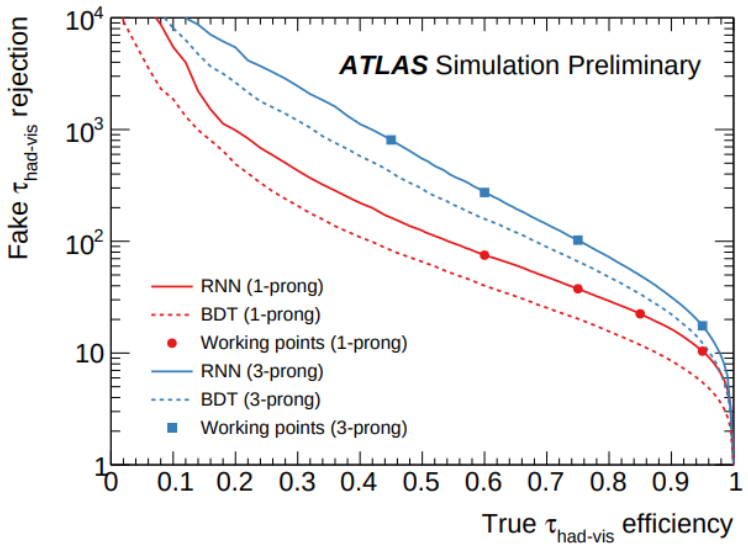

Figure 6.4: Evolution of the rejection of fake hadronic tau with respect to the true hadronic tau identification efficiency [69]

6.2.1 Reconstruction

Jets are reconstructed based on their energy deposit in the electromagnetic and the hadronic calorimeters. The reconstruction of the jets starts with the topo-clustering algorithm, designed to build 3D clusters with the response of the calorimeter cells. This algorithm localizes the seed cell which contains a significance, e.g. signal VS noise ratio, above 4σ. The noise is defined as a quadratic sum of electronic signal RMS and pileup contribution noise. Then neighbouring cells with a significance higher than 2σ in the 3D space are added iteratively to construct the cluster.
The Anti-k_T Jet clustering algorithm performs the identification of jets. This method consists of the identification of the smallest distance between 2 particles d_{ij} and between the entity i and the beam d_{iB} defined as:

$$d_{ij} = min(k_{ti}^{-2}, k_{tj}^{-2})\frac{\Delta_{ij}^2}{R^2} \qquad d_{iB} = k_{ti}^{-2}$$

where $\Delta_{ij}^2 = (y_i - y_j)^2 + (\phi_i - \phi_j)^2$ and k_{ti}, y_i and ϕ_i are the transverse momentum, the rapidity and the azimuth of the particle i. If d_{iB} is the smallest, the entity i is called a jet and removed from the list of events. The algorithm iterates until the end of the list. Four levels for jets are defined, with increasing levels of fake jet rejections: Looser, Loose, Medium, and Tight. The Looser selection corresponds to the highest jet efficiency with the lowest background rejection. The tight selection corresponds to the lowest efficiency but the highest background rejection. The definition of selection depends on the number

of reconstructed tracks matching the jets and the jet energy deposited distribution in the direction of the shower.

6.2.2 Calibration

After the reconstruction of jets, they need to be calibrated to prevent various effects. The total procedure is shown in figure 6.5

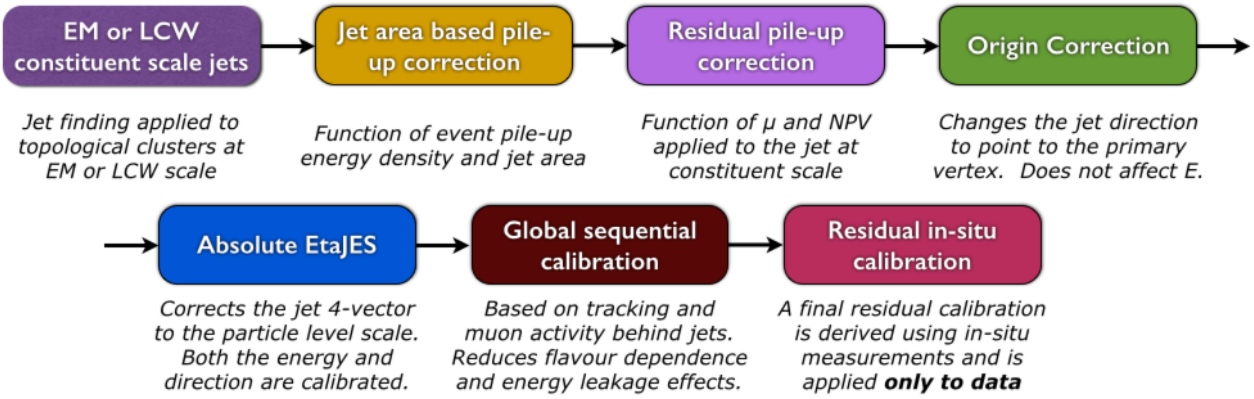

Figure 6.5: Jet calibration procedure illustration [71]

Three main steps can be described: the pileup contribution, the calibration to the Monte-Carlo truth scale and finally the in-situ calibration.

Pileup contribution

The pileup removal of the jet energy is performed by an event-by-event subtraction method. This technique called the active jet areas technique defines a median p_T density in the $\eta \times \phi$ space for each event, providing the global pile-up energy in the region $|\eta| < 2.0$. Applied to the jet are A^{jet}, the resulting final correction is defined as:

$$p_T^{corr} = p_T^{jet} - \rho A^{jet} - \alpha(N_{PV} - 1)\beta\mu$$

with α and β are the correction factors and N_{PV} the number of reconstructed primary vertices.

MC calibration

After the pileup contribution removal, the calibration of the jet consists of using the MC truth information. This aims to correct the fraction of the energy that remains invisible for subdetectors, such as strong for interactions. This calibration uses MC simulation by comparing the reconstructed jets to truth jets. The ratio of these two terms leads to the correction

term of the Jet Energy Scale (JES), dependent of the binning in η and E_T. Finally, the value is refine by the application of the Global Sequential Calibration (GSC), using additional jet response, a punch-though (jets not completely contained in calorimeters) correction and jet flavours. This refinement aims to decrease the Jet Energy Resolution (JER).

In situ calibration

After the two previous calibrations, which are purely data-derived, it is necessary to consider the impact of data bias on the jet energy and jet mass. As a consequence, the in situ correction corrects the data VS MC simulation differences in two steps. The first correction, called the η-calibration, corrects the forward jet response with respect to the well-understood central jet response. The second correction uses a well-known object to calibrate the central jet region ($|\eta| < 0.8$). This in situ correction technique provides very precise results (JES uncertainties below 1%).

6.2.3 B-jets tagging

The identification of the jets from the b quarks is an essential tool in physics analysis that includes high-p_T b-jets in the final state but also the identification of backgrounds. In this thesis, the multiplicity of the b-jets is used in the definition of the signal region with a B-Veto, and the definition of the control region is used to estimate fake backgrounds by some data-driven methods.
Compared to lighter hadrons, the b-hadron has a longer lifetime before its decay into the ID. This difference leads to a displacement of the secondary vertex, helping in the identification of the b jets as the large mass and the large impact parameter (d0) as shown in figure 6.6.
Three algorithms are employed by the ATLAS experiment: the Impact Parameter (IP2D or IP3D [73]) based, the secondary vertex (SV [74]) based and the decay chain reconstruction algorithm (JetFitter [75]). Each algorithm provides a set of complementary information which are combined into a multivariate MV2 and DL1, using a Boosted Decision Tree (BDT) and a Deep Neural Network (DNN) respectively. These classifiers are trained with a combination of charm and light jet background to improve charm rejection. Four working points (WPs) are finally refined in order to provide 60%, 70%, 77% and 85% b-jet tagging efficiencies for b-jets in simulated $t\bar{t}$ samples. Figures 6.7 show the b-jet tagging efficiency and the c-jets rejection as a function of the transverse momentum of the jet for different algorithms.

6.3 Missing transverse energy

The missing transverse energy (E_T^{miss} or MET) is one of the essential parts of the reconstruction because this energy relies on the existence of "non-interacting" particles, e.g. neutrinos

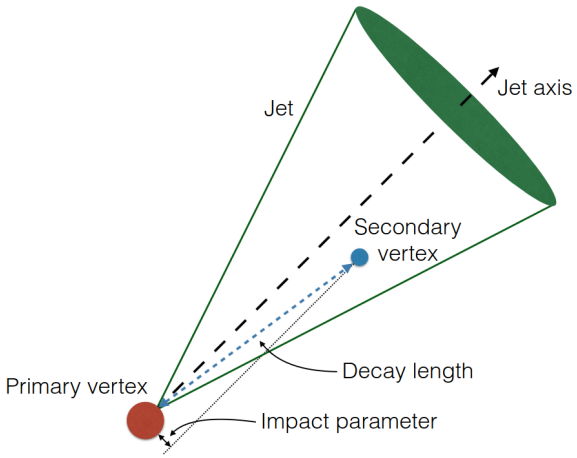

Figure 6.6: Illustration of the production of a b-jet and representation of key parameters for b-tagging [72]

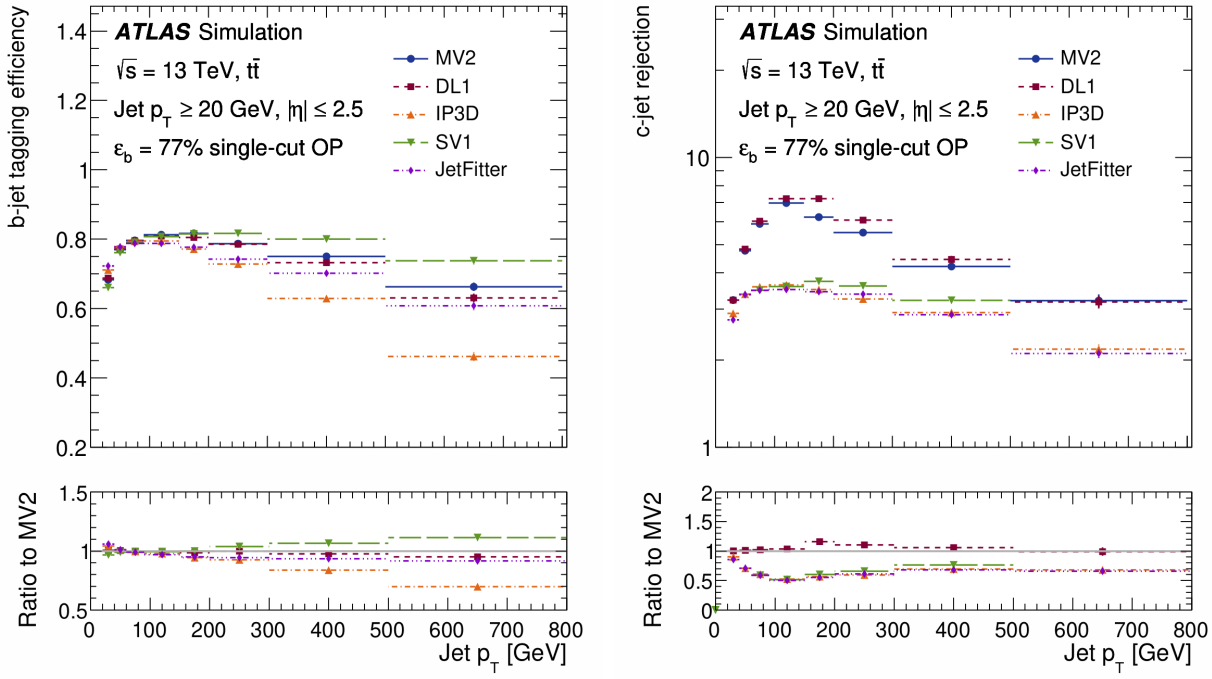

Figure 6.7: The b-jet tagging efficiency (on left) and the c-jet rejection (on right) as a function of the transverse momentum p_T for several b-tagger algorithms [76].

or dark matter particles. The momentum conservation states that the amount of momentum remains constant. As a consequence, the total momenta of particles before the collision equals the total momenta of particles after the collision. At LHC, the collision is supposed to be head-to-head along the beam axis, meaning that the sum of the transverse momentum of particles must be null.
In the ATLAS detector, the E_T^{miss} is calculated as the negative vector-sum of the transverse moment of all reconstructed physics objects (electron, photon, muons, ...) and the unclustered energy known as soft tracks. The latest includes tracks with low p_T associated with the primary vertex and not assigned to hard objects.

$$E_T^{miss} = -\sum_{electrons.} p_T^e - \sum_{muons} p_T^\mu - \sum_{\tau-leptons} p_T^\tau - \sum_{photon} p_T^\gamma - \sum_{jets} p_T^{jets} - \sum_{soft\ tracks} p_T^{soft}$$

The main algorithm for the reconstruction of the soft term in the ATLAS experiment during Run II is called the Track Soft Term (TST). This algorithm is robust to pile-up conditions but does not consider the contribution of the neutral particles.

Chapter 7

Search for di-Higgs production in 2ℓSS channel

The search for the di-Higgs pair production decaying into two light leptons with the same charge (SS) at a 13 TeV centre of mass energy during the Run2 is presented in this chapter. The dataset corresponds to a 139 fb^{-1} integrated luminosity registered between 2015 and 2018 using the ATLAS detector. In this channel, so-called 2ℓSS in this section, the term "lepton" refers to light leptons only (e and μ). Three dominant backgrounds need to be considered, knowing the di-boson (VV) production, a boson (V+jets) production and $t\bar{t}$. As the two latest, are qualified as non-prompt backgrounds because their contribution in 2ℓSS channel comes from heavy-flavour hadron decays and photon conversions.
This chapter describes the dataset and the MC simulation samples used in this analysis in section 7.2. It is followed by the definition of the pre-selections and selections, essential to extract the signature from the dataset and to guarantee the orthogonality with other channels in section 7.3. Then, the background estimate is presented in section 7.5, which includes in particular the description of the method used in non-prompt background estimate. The strategy elaborated intending to build a final discriminant variable, optimized in the distinction of the signal and the background concerned in section 7.4. The section 7.6 is about the systematic uncertainties relevant to the analysis. Finally, this chapter ends with the combination of the 2ℓSS channel with the other di-Higgs to multilepton channels in section 7.8.
My contribution in the 2ℓSS analysis was to elaborate the strategy to build the final discriminant variable and its optimization, using various hyper-parameters for the fit or finding the optimal input variables. I also contributed to the non-prompt background estimates (QmisID and non-prompt lepton backgrounds), with their validation region. In particular, this contribution brought me to be the HDBS isolation and fake forum contact, a role I played for a year mandate. Finally, I contributed to the generation of the dataset MC samples.

7.1 Introduction to multilepton channels

The search of the Higgs pair decaying into multileptons channels. This analysis combines nine channels together, shown in the figure 7.1. Three channels includes only light leptons (ℓ = *e or* μ): 2ℓSS, 3ℓ and $b\bar{b}4\ell$; and three others with at least one hadronic tau τ_{had}: 2ℓSS $+1\tau_{had}$, $2\ell + 2\tau_{had}$ and $1\ell + 2\tau_{had}$. Then three signatures with di-photon production are included: $\gamma\gamma + 1\ell 0\tau_{had}$, $\gamma\gamma + 0\ell 1\tau_{had}$ and $\gamma\gamma + 2L$ (with L= ℓ *or* τ_{had}). In the rest of the thesis, these three channels will be referred to as $\gamma\gamma + ML$. These several final states target the following HH decay modes: 4W, WW$\tau\tau$, WWZZ, 4Z, ZZ$\tau\tau$, 4τ, $\gamma\gamma + WW$, $\gamma\gamma + ZZ$ and $\gamma\gamma + \tau\tau$.

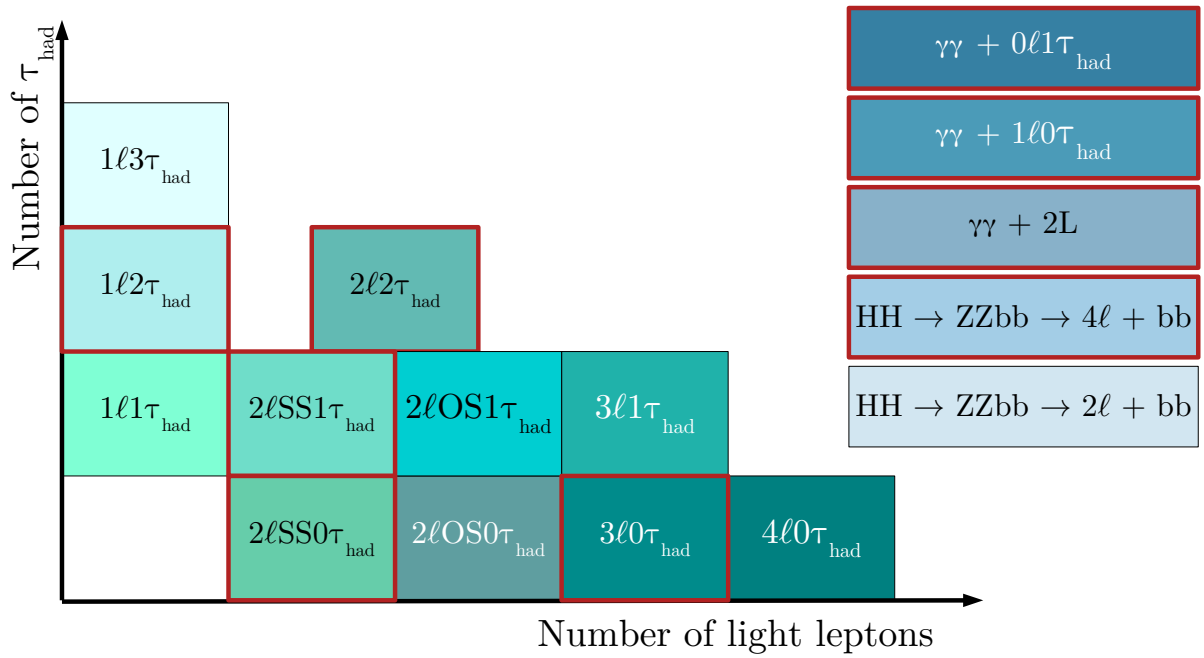

Figure 7.1: Possible leptonic decay of the Higgs pair map. The red boxes indicate the signature used in the multilepton analysis.

In the nine channels analysis which compose the multilepton analysis, the selections are optimized as a function of the given signature and its backgrounds, respecting the orthogonality between each channel. Table 7.1 lists the dominant background as a function of the channel. The baseline for an electron is a Loose isolation criteria, with an $|\eta| < 1.37$ or $1.52 < |\eta| < 2.5$ to reject the crack region of the ATLAS detector, a transverse momentum higher than 9 GeV and a $d_0(z_0)$ cut at 5(0.5 mm). An additional tight WP is used for the isolation/identification criteria in the case of 2ℓSS and 2ℓSS $+1\tau_{had}$. The baseline criteria for

a muon is loose isolation and identification, with an $|\eta| < 2.5$ and a $p_T > 9\,\text{GeV}$. Then for jets, photons and hadronic taus, the p_T is required to be higher than 20 GeV, a $|\eta|$ below 2.5 with a veto on the crack region. The tight (medium) isolation WP is required for photons and jets (taus). In order to ensure the orthogonality with other di-Higgs analyses, the b-tagging is required to be estimated with a 77 % efficiency.

Signature:	Dominant backgrounds
2ℓSS	VV, V+jets, $t\bar{t}$, Vγ
$2\ell 1\tau$	VV
3ℓ	VV, Vγ, Z+jets, VH
4ℓ + 2b	$t\bar{t}$, VV, Z+jets, Single H
$2\ell + 2\tau$	VV, V+jets, $t\bar{t}$/Stop
$\gamma\gamma + ML$	H, $V\gamma\gamma$, $\gamma\gamma$+jets

Table 7.1: Dominant background processes for each channel in ML analysis.

7.2 Data and Monte Carlo simulation samples

The dataset used in this analysis has been prepared with xAOD format and further produced to a more specialized format derived xAOD (DxAOD), using the HIGG8D1 derivation framework. The xAOD to DxAOD framework called the GN1 framework, is derived from the ttH multilepton analysis, which allows us to focus on leptonic final state events. This restriction results from the application of smart slimming which removes the unnecessary variables, followed by thinning (removing the unnecessary objects), augmenting (adding specific variables) and additional skimming on MC and data samples. The GN1 framework is then followed by the GN2 framework used for generating the samples, used in the analysis. While the GN1 framework ran collectively for the entire multilepton channel, the GN2 framework ran independently for each channel up to the latest version.

7.2.1 The data

The dataset used in this analysis was recorded by the ATLAS detector during proton-proton collision at LHC from 2015 to 2018, which represents an integrated luminosity of $140\,\text{fb}^{-1}$. The dataset is divided into four periods because while the centre-of-mass-energy

($\sqrt{s}$ =13 TeV) and the bunch spacing (25 ns) remain the same during the Run2, the pileup increased from $< \mu >$ = 13.4 (in 2015) to $< \mu >$=36.1 (in 2018). The used dataset verifies the data quality cuts and is in the recommended Good Run List [77]:

Year	Integrated luminosity	$< \mu >$	IBL
2015	$3.22\,\text{fb}^{-1}$	13.4	on
2016	$32.988\,\text{fb}^{-1}$	25.1	partially operational
2017	$44.307\,\text{fb}^{-1}$	37.8	on
2018	$58.450\,\text{fb}^{-1}$	36.1	on

Table 7.2: Characteristics of the data registered by the ATLAS detector per year: the integrated luminosity, the mean number of interactions per crossing $< \mu >$ and the Insertable B-layer status.

7.2.2 Monte Carlo samples

Three Monte Carlo campaigns are used to simulate processes, MC16a, MC16d and MC16e. Each campaign corresponds to a set of different assumptions for the distribution of the number of interactions per bunch crossing, respectively for the 2015 to 2016, 2017 and 2018 periods. Each campaign is produced with specific statistical EVGEN events and the same EVGEN configuration, so they can be combined for Run 2 analyses. As the pileup is a phenomenon hardly predicted with precision and is supposed uncorrelated, the matching of the number of interactions in data and in MC is ensured by a reweighting [78]. Then each sample is normalized with its respective cross-section. In the multilepton analysis, the dataset has been divided in two, for the photon-free channels and channels with photons. The MC simulations are produced independently for signal or background processes using various configurations/generators. The full detailed list of the production MC samples is provided in appendix .3.

Gluon-Gluon Fusion signal samples

The nominal ggF signal samples are produced at the next-to-leading order (NLO) accuracy with `Powheg-Box-V2` for matrix element calculation, interfaced with `Pythia8` generator with A14 tune [79] and the `NNPDF 2.3 LO PDF` set [80] for the parton showering and the hadronization of particles. The b and c hadrons are modelled using EvtGen [81]. The detector's influence is simulated using `AltfastII` (AF2) [82], which considers a fast simulation of the calorimeter ATLAS sub-detector. For the photon-free channels, the Higgs are forced to

decay into WW, ZZ or $\tau^+\tau^-$ decay modes only, with a branching ratio set at 0.706, 0.087 and 0.207 for the $H \to W^+W^-$, $H \to ZZ$ and $H \to \tau^+\tau^-$ decays modes respectively. In the case of the channels with photons, one of the Higgs is forced to decay into a photon pair, while the other is forced to decay into WW, ZZ or $\tau^+\tau^-$. Finally, a lepton filter is applied to constrain the kinematics properties of the light leptons, such as a p_T >7 GeV and $|\eta| < 3$. Alternative ggF signal samples are produced with `Powheg-Box-V2` interfaced with `Herwig7`, using a `PDF4LHC15 PDF` set. This set is used in the determination of the parton shower uncertainties.

Vector boson fusion signal samples

The nominal VBF signal samples are simulated at leading-order (LO) accuracy using `adGraph5_aMC@NLO 2.2.X or 2.3.X` for matrix element calculation, interfaced with `Pythia8` generator with A14 tune [79] and the `NNPDF 2.3 LO PDF` set [80] for the parton showering and the hadronization of particles. The detector's influence is simulated using `AltfastII` (AF2) [82], for a fast simulation of the calorimeter ATLAS sub-detector. In the photon-free channels (except for $bb4\ell$), the branching ratio of the intermediate particle is set at 0.706, 0.087 and 0.207 for the $H \to W^+W^-$, $H \to ZZ$ and $H \to \tau^+\tau^-$ decays modes respectively, considering only multileptons decays. Then a lepton filter (`ElecMuTauThreeFilter`) is applied to constrain the lepton (tau) kinematic properties at p_T >7 GeV (13 GeV) and $|\eta| < 2.8$. For $bb4\ell$ signature, the $H \to$ZZ branching ratio is set at 0.5 and no filter is applied. In the case of channels with photons, the branching ratio is set at 0.353, 0.043, 0.104 and 0.5 for $H \to W^+W^-$, $H \to ZZ$, $H \to \tau^+\tau^-$ and $H \to \gamma\gamma$ decay modes respectively, knowing that one Higgs decays to a photon pair.
Alternative samples are simulated by `MadGraph5_aMC@NLO 2.2.X or 2.3.X` [83] interfaced with `Herwig7`, using a `PDF4LHC15 PDF` set for the study of the parton shower uncertainties.

Backgrounds samples

This sub-section will list all the backgrounds considered in this analysis and their simulation processes (in order of importance in 2ℓSS analysis).

- **VV**: normalised using the cross sections computed by `Sherpa` [84], assigned with a 10% normalization uncertainty.
- **V+jets**: simulated with Sherpa 2.2.1 [84] using the `NNPDF 3.0 NNLO PDF` [80]set and showered by the `Sherpa` built-in implementation which has matrix elements for up to 2 additional jets at NLO and up to 4 additional jets at LO. The cross-section to normalize the simulations is calculated at NNLO accuracy in QCD and includes EW corrections at NLO accuracy.

- **V+γ:** generated at LO using `Sherpa` with up to two additional partons in the matrix element and are merged with the `Sherpa` parton shower (`MEPSatLO`). Photons from the matrix elements are required to be isolated (d_0=0.1) with a p_T >17 GeV and have an invariant mass larger than 80 GeV. Additionally, a separation between the photons and the leptons of $\Delta R = 3$ is imposed.

- **$t\bar{t}$:** generated with `Powheg-Box` v2.0 [85] and interfaced with `Pythia8` [86] for the parton showering and fragmentation with A14 tune for showering. The single top events are simulated with `Powheg-Box` and interfaced with `Pythia8`, where the interference between Wt and $t\bar{t}$ production is handled with the DeltaR overlap removal procedure [87].

- **$t\bar{t}W$:** generated using SHERPA-2.2 with a multi-leg configuration with `0,1j@NLO+2j@LO`. Both the factorization and renormalization scales are set to $H_T/2$, where the quantity H_T is defined as:
$$H_T = \Sigma_i m_T, i = \Sigma_i \sqrt{m_i^2 + p_T^2}, i,$$
which is a sum over all outgoing partons in the matrix element calculation. The sample is generated using NLO accuracy for matrix elements for up to one additional jet and LO accuracy for up to two additional jets. The additional partons are matched and merged with the `Sherpa` parton shower based on Catani-Seymour dipole factorization using the `MEPS@NLO` [88, 89] prescription with CKKW merging scale of 30 GeV. The virtual QCD correction for matrix elements at NLO accuracy is provided by the `OpenLoops2` [90] library. Samples are generated using the `NNPDF3.0NNLO PDF` set [80]. The LO electroweak contributions are obtained from a dedicated sample simulated with `Sherpa-2.2.10` [84] and stitched together with the NLO QCD sample described above.

- **VH:** simulated using `Powheg-Box` v2 with the `NNPDF3.0 NLO` [80] parton distribution function and interfaced with `Pythia` 8.230 [86] for parton shower and non-perturbative effects. Separate W^+H, W^-H, $qq \to ZH$ and $gg \to ZH$ samples are produced. The cross-section is normalized at NNLO in QCD with NLO electroweak corrections for $q\bar{q} \to VH$ and at NLO and next-to-leading logarithm accuracy in QCD.

- **$t\bar{t}H$**: obtained from a generator setup of `Powheg-Box` [85] generator at NLO. This sample uses `NNPDF3.0nlo PDF` [80] set. The h_{damp} parameter [1] is set to $3/4 \times (m_t + m_{\bar{t}} + m_H) = 325$ GeV.

- **$t\bar{t}t\bar{t}$:** modelled using the `Madgraph5_aMC@NLO` v2.6.2 [83] generator which provides matrix elements at NLO in the strong coupling constant α_S with the NNPDF3.1 NLO

[1] The h_{damp} parameter controls the transverse momentum (p_T) of the first additional emission beyond the leading-order Feynman diagram in the PS and therefore regulates the high-p_T emission against which the $t\bar{t}$ system recoils

[80] parton distribution function. The functional form of the renormalization and factorization scales are set to $\mu_r = \mu_f = m_T/4$ where m_T is defined as the scalar sum of the transverse masses $\sqrt{m^2 + p_T^2}$ of the particles generated from the matrix element calculation. Top quarks are decayed at LO using `MadSpin` to preserve all spin correlations. The events are interfaced with `Pythia` 8.230 [86] for the parton shower and hadronization, using the A14 set of tuned parameters and the NNPDF2.3 LO PDF set.

- **other rare contributions (tZ, ttWW, ttWH, WtZ and VVV):** normalized using their NLO theoretical cross sections, then assigned with a 50% normalization uncertainty, except for tZ which is assigned to a 5% normalization uncertainty.

7.3 Preselection and signal region

The reconstruction and the identification of each object in the ATLAS collaboration are developed in chapter 6. This section concerns the baseline criteria used in 2ℓSS analysis.

- The primary vertex is chosen as the vertex with the highest quadratic sum $\sum p_T^2$ of all associated tracks, and all events with a significant noise in the calorimeter or corrupted data are removed.

- The Single-lepton or di-lepton Trigger (SLTorDLT) is used. A scale factor (SF) associated with the trigger is calculated for each event.

- The trigger matching corresponds to the matching between the reconstruction of leptons with the triggered objects from the trigger chain.

- Electrons are chosen with a p_T >4.5 GeV and $|\eta| < 2.5$. All electrons from the crack region (the transition region between the barrel and endcap calorimeter) are vetoed. To reject some non-prompt events, a selection is applied on the longitudinal impact parameter, z_0, and transverse impact parameter significance, d_0. Then a loose ID and loose isolation WP are required as a baseline, with an ambiguity bit selection. To reject some QmisID events, the electron candidate needs to pass a medium misidentification BDT working point [91].

- The muon candidate are selected with a p_T >3 GeV and $|\eta| < 2.5$. They are required to pass at least the loose identification and the loose isolation WP. As for the electron, a cut is applied on the d_0 and z_0 impact parameters.

- The τ_{had} candidate is required to verify a p_T >20 GeV and a $|\eta| < 2.5$ excluding the crack region. The candidate has to pass the medium tau ID working point, reconstructed with either one or three associated tracks and a total charge of ± 1.

- Jets: reconstructed with a radius parameter R=0.4, the jet candidates have to pass the jet cleaning algorithm (Loose) and a Tight JVT cut. Then only jets with a p_T >25 GeV and $|\eta| < 2.5$ are considered.
- Flavour-tagged jets are chosen with a 77 % efficiency in order to keep the orthogonality with other di-Higgs analyses.

7.3.1 Event Selections

In the 2ℓSS channel, events passing the following selections are required:

- **Trigger Selection**:
  - Global Trigger Decision.
  - Trigger matching with Tight electrons or muons for a single Lepton trigger or Dilepton trigger.
- **Leptons definition**:
  - Exactly Two leptons at preselection level with the same electric charge.
  - The transverse momentum of each lepton has to be larger than 20 GeV.
  - Tight and Medium ID respectively for electrons and muons
  - Both leptons must satisfy tight prompt lepton veto isolation working point.
  - The invariant mass of the two leptons has to be larger than 12 GeV. The cut is to prevent low mass resonance background from entering the signal region.
- **Hadronic tau veto**: All events with at least one hadronic tau are vetoed
- **Jet multiplicity**
  - A b-jet veto is required: events with b-jets are discarded.
  - At least 2 jets are required.

7.4 Background discriminating strategy

The separation of the background and the signal is performed thanks to a selection applied to the discriminant variable. This one can be constructed using multivariate analysis (MVA), for the classification of the $HH \rightarrow$ Multileptons. In the case of the 2ℓSS signature, a boosted decision tree is used to build this multivariate.

The strategy

In the 2ℓSS signature, the final discriminant has to be optimized to face the three main backgrounds presented in section 7.2.2. Considering the diversified kinetic characteristics of each source of background, three specific BDTs have been trained to target the three dominant background processes: VV, V+jets and $t\bar{t}$. Each specific Boosted BDT (GradientBoost) is trained, with one of the dominant backgrounds VS 2ℓSS signal, using a list of variables optimized for the given background. Then, the three specific outputs are combined into a final discriminant variable. The combination is performed through the training of a BDT (GradientBoost), using the three specific BDTs as inputs and all backgrounds (not only the three dominants) VS signal.

7.4.1 Background specific training

- $M_{\ell\ell}$: The invariant mass of the two leptons. This variable is used to identify Z+jets background (Z peak region), especially events for which a charge has been not been identified correctly.
- M_{all}: The invariant mass of all objects (jets + leptons). Including the mass of the jets, this variable is particularly useful for the identification of the VV (VV+jets + WZ) background.
- $M_{\ell_0 j}$: The invariant mass of the leading lepton and its closest jet.
- $M_{\ell_1 j}$: The invariant mass of the subleading lepton and its closest jet.
- $M_T^{W_0}$: The transverse mass of the leptonically decay W boson (reconstructed by the MET with leading lepton).
- $M_T^{W_1}$: The transverse mass of the leptonically decay W boson (reconstructed by the MET with subleading lepton).
- E_T^{miss}: transverse missing energy. As the reflect of the production of neutrinos, this variable is efficient for the Z+jets background, non-prompt leptons and QmisID events.
- H_T: scalar sum of the transverse momentum.
- $H_T(lep)$: scalar sum of transverse momentum of the leptons.
- Dilep_type: The flavour of the two leptons, equals 1 if $\mu\mu$, 2 if μe and 3 if ee.
- Total charge: Sum of the charge of the leading (ℓ_0) and subleading lepton (ℓ_1). This variable has been used in the training of the VV specific BDT, as VV is mainly due to WZ, a charge asymetry is expected on the contrary of HH events.

- N_{jets}: The number of jets. The signal 2ℓSS can be produced with an expected high multiplicity of jets. On the contrary, background as $t\bar{t}$, is expected to be produced with a low multiplicity of jets.
- $|\eta_0|$ and $|\eta_1|$: The absolute value of the pseudorapidity of the leading and the subleading leptons. These variable reflect the angular distribution of the leptons, particularly usefull when the particle are emitted back-to-back, as the Zjets.
- $\Delta\eta$: The absolute value of the η_0-η_1. Same justification of the previous variables.
- $\Delta R_{\ell\ell}$: Distance between the leading and the subleading lepton. As in the case of $|\eta|$ variables, the distance between lepton provides spatial information over the leptons (or jets). These variables are the most important discriminating power for all background specific BDTs.
- $\Delta R_{min\ell 0jets}$: The minimum distance between the leading lepton and its closest jet. Used as $\Delta R_{\ell\ell}$ variable.
- $\Delta R_{min\ell 1jets}$: The minimum distance between the subleading lepton and its closest jet. Used as $\Delta R_{\ell\ell}$ variable.

During the training phase, the BDT determines the optimal selection for each variable and as a consequence, it measures their corresponding separation power. Among the variables listed above, the most powerful are the distance between two leptons or between a lepton and a jet, and the pseudorapidity of each lepton. The table 7.3 presents the five most powerful variables in the training of each specific BDT. The separation power and the ranking of all BDTs inputs are shown in Appendix .1.

Rank	V+jets VS HH	$t\bar{t}$ VS HH	VV VS HH
1	$\Delta R_{\ell\ell}$	$\Delta R_{min}(\ell, jets)$	$\Delta R_{min}(\ell, jets)$
2	$\Delta R_{min}(\ell, jets)$	$\|\eta_0\|$	$\Delta R_{\ell\ell}$
3	$\|\eta_0\|$	$\Delta R_{\ell\ell}$	$\|\eta_0\|$
4	$\|\eta_1\|$	$M_{l_1 j}$	$\|\eta_1\|$
5	HT	$\|\eta_1\|$	$M_{l_0 j}$

Table 7.3: The five most important variables in the training or the three specific BDTs

The separation power of each variable depends on its correlations with the rest of the variables. The correlation matrices are shown in figure 7.2a and 7.2b for the VV-specific BDT,

with the signal and the background sample respectively. The other correlation matrices obtained for the other specific BDTs are shown in the appendix .2.

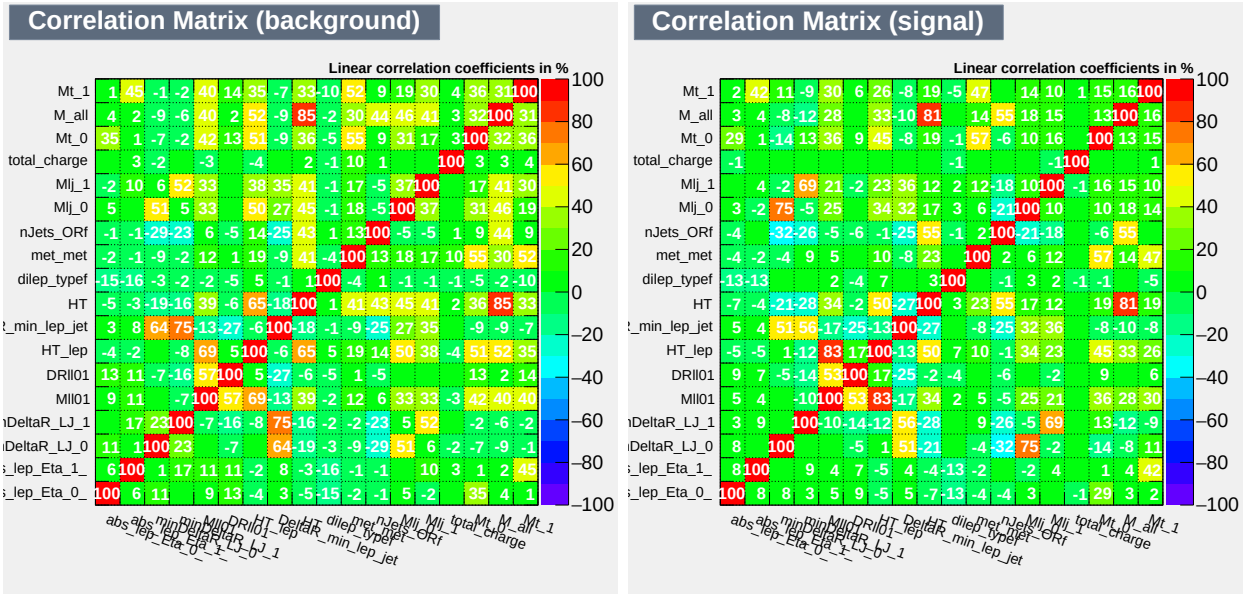

(a) (b)

Figure 7.2: Correlation matrices obtained for the training of the VV-specific BDT for the background (left) and signal (right). The colour corresponds to the correlation percentage.

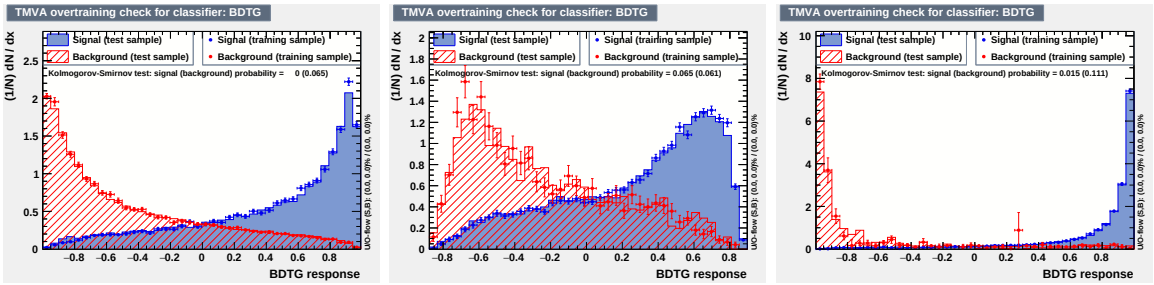

Figure 7.3: Specific BDT distributions. From left to right are the BDT specific to di-boson, $t\bar{t}$ and V+jets backgrounds.

7.4.2 Combined BDT training

The three outputs of the specific training are combined into a final discriminant variable. The distribution of the three inputs is shown in figures 7.3. The separation power of each specific

BDT and the correlation is shown in table 7.4 and figures 7.4, respectively. In this training, all MC-backgrounds have been included, and the hyperparameters have been optimized in order to maximise the area under the ROC curve.

Rank	Variable	Separation
1	BDT_tt	4.623e-01
2	BDT_VV	4.028e-01
3	BDT_Vjets	1.350e-01

Table 7.4: Separation power for each specific BDT in the training of the combined BDT.

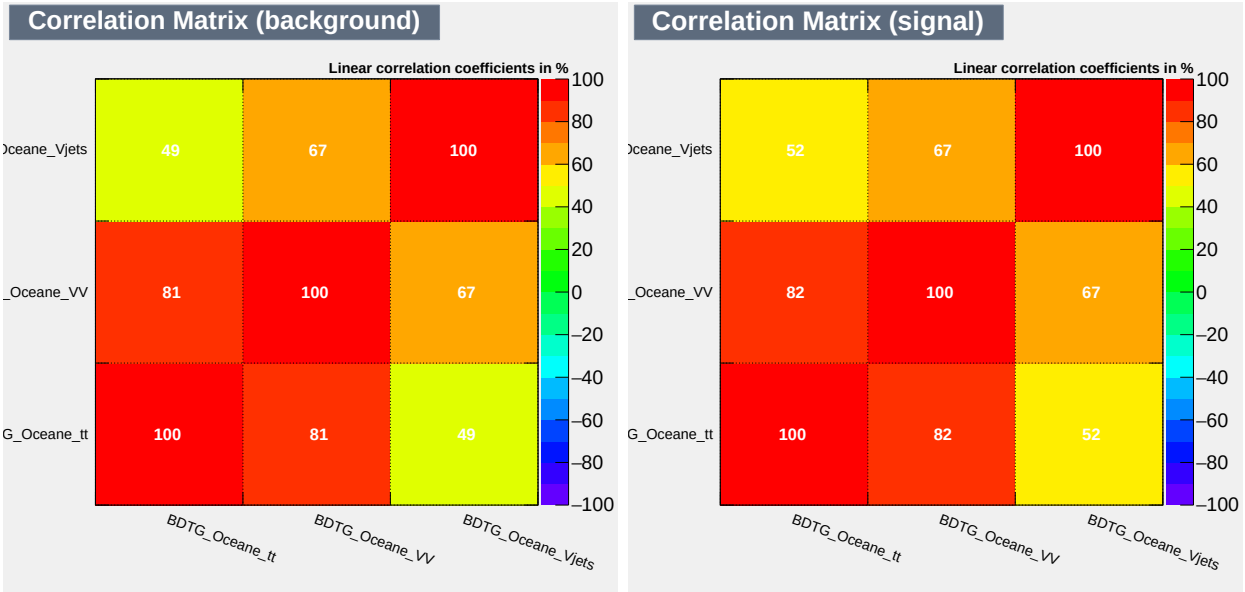

(a) (b)

Figure 7.4: Correlation matrices obtained for the training of the combined BDT for the background (left) and signal (right). The colour corresponds to the correlation percentage.

The distribution of the resulting BDT is shown in figure 7.5, for the signal and the different backgrounds.

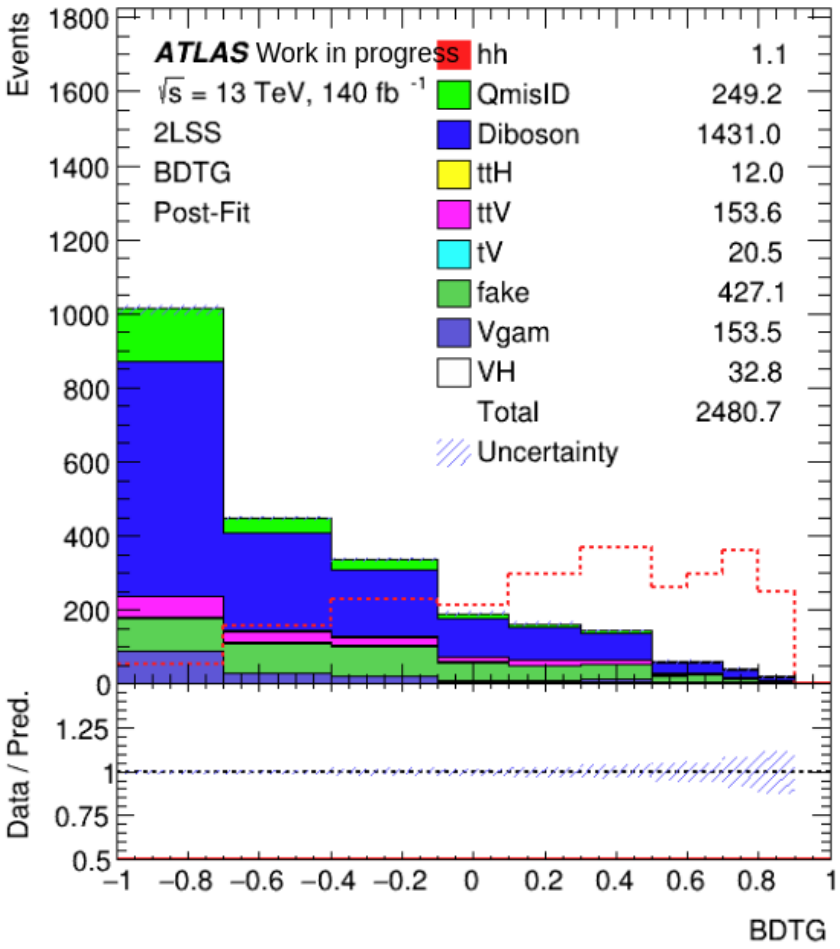

Figure 7.5: Combined BDT output, rescaled for the signal HH.

7.5 Background estimate

For each analysis, two kinds of backgrounds can be identified. The *irreducible* background leads to the production of the same signature, these backgrounds are also called prompt backgrounds. The *reducible* background includes all processes faking the targeted signature, they originate from various non-prompt processes and depend on the detector and identification algorithm performances.

7.5.1 Irreducible backgrounds

The origin of the irreducible background is mainly the di-boson processes VV, with V standing for W or Z boson. These backgrounds are also called instrumental backgrounds because they

originate from electronic noise, miscalibration, dead material, bremsstrahlung or additional proton-proton collision (pileup). To put it differently, an ideal detector would not have this background.

Di-boson production

The di-boson production combines all processes with two vector bosons through a Z boson or a W boson production. This production leads to leptonic or hadronic decays with a final state composed of up to four light leptons, with neutrinos production. The contribution of the VV background in the 2ℓSS channel is mainly due to prompt backgrounds but may contribute (below 5% in the signal region) as fake leptons (neglected in this analysis) and/or QmisID events. The largest origin of this background is WZ→ $\ell\nu\ell\ell$, covering 37% of the signal region background contribution. It is followed by the VV+jj processes (WZ+jj or WW+jj) which contribute to 13.6% in the signal region. A study on VBS processes shows that the MC simulation underestimates the cross-section of these processes in data. In order to counterbalance this lack, two normalization factors are derived, one for the correction of WZ constraint in a trilepton channel CR and one for the VV+jj events constraint in a 2ℓSS VV control region.

Other

Minor other SM processes contribute to the 2ℓSS signal region, such as VVV, VH, $t\bar{t}t\bar{t}$, $t\bar{t}H$. These processes have a very small contribution in the signal region and are modelled by the MC simulation.

Backgrounds	N_{event}	Contamination [%]
VV	1114.5	50%
ttV	77.36	3.5%
Other	117.4	5.2%

Table 7.5: Contamination of each prompt-backgrounds in the signal region defined as $BDT_{combined}$ higher than -0.4.

7.5.2 Reducible backgrounds

In the 2ℓSS channel, the non-prompt leptons, meaning all backgrounds not produced at tree level, represent an important source of background. In the 2ℓSS channel, various categories of non-prompt backgrounds are considered.

- Charge misidentification (QmisID): it corresponds to a process called trident $e^{\pm} \rightarrow \gamma^* e^{\pm} \rightarrow e^+ e^- e^{\pm}$, as shown in figure 7.6a. An electron (positron) will create per Bremsstralhung a photon which decays into an electron-positron pair, where the positron (electron) is reconstructed with a high p_T.
- Photon conversion: it corresponds to the process $\gamma^* \rightarrow \ell\ell$, a radiated photon decays in an electron-positron pair with one electron reconstructed as prompt, as shown in figure 7.6c. The photon conversions category includes material conversions and QED conversions. The difference remains in the position of the conversion before the detector (QED) or in the detector (material).
- Semi-leptonic decay of heavy flavour (HF) and light flavour(LF) hadrons: It corresponds to one or more lepton candidates originating from the b-hadron or c-hadron decays. So-called semileptonic decay or fakes, a representation of this process is given in figure 7.6b.

Table 7.6 summaries the number of event N_{event} and the contamination in % in the signal region. The main contamination in the signal region comes from the QmisID and the muons from HF decay.

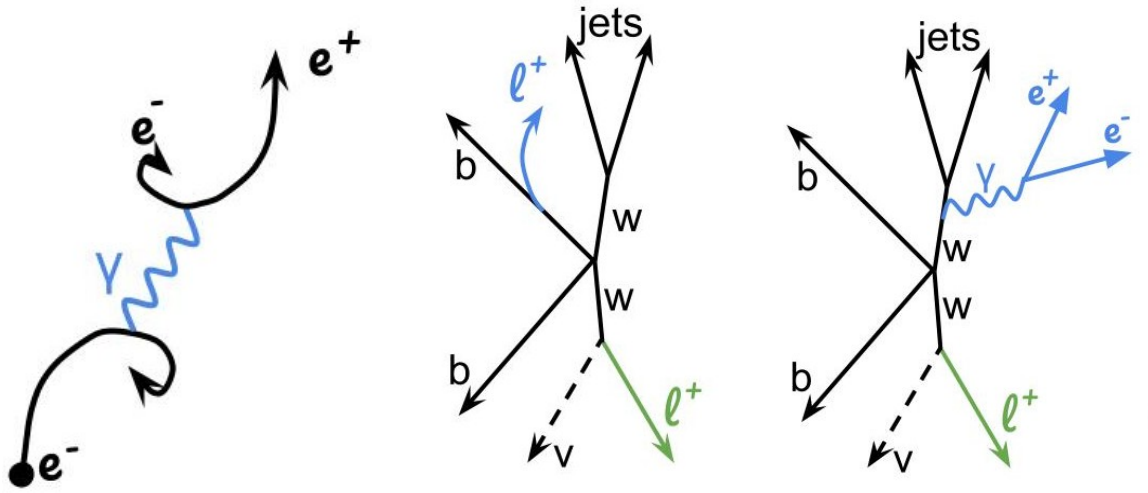

(a) Trident (b) Semi-leptonic decay (c) Photon conversion

Figure 7.6: Representation of some non-prompts processes leading to 2ℓSS signature.

Charge misassignment background

As introduced in section 6.1.1, the misassignment of the charge is a significant background in the 2ℓSS channel. The charge-flip events originate mainly from Z+jets, $t\bar{t}$ and di-boson

Backgrounds	N_{event}	Contamination [%]
QmisID	246.4	11%
Material conversion	104.8	4.7 %
QED	32.3	1.4%
Fakes muons	352	15.8%
Fakes electrons	117.5	5.3%

Table 7.6: Contamination of each non-prompt background in the signal region defined as $BDT_{combined}$ higher than -0.4.

processes. This process is expected to affect only electrons (so ee and $e\mu$ di-lepton types), the muon charge flip is negligible in this p_T range scale.
Considering an event of two electrons with an opposite charge (e^+e^-) and a probability ϵ_i (ϵ_j) to misidentify the charge of the electron(positron) i(j), the event can be reconstructed as follow:

- e^+e^-: The two leptons are correctly reconstructed with a probability of $(1-\epsilon_i)(1-\epsilon_j)$
- $e^\pm e^\pm$ One lepton is correctly reconstructed while the other is reconstructed with a wrong charge, with a probability of $\epsilon_i + \epsilon_j - 2\epsilon_i\epsilon_j$
- e^-e^+: The two leptons are reconstructed with a wrong charge, with a probability of $\epsilon_i\epsilon_j$

With N the real number of opposite sign events, the number of reconstructed same (opposite) sign events N^{SS} (N^{OS}) can be written as:

$$N^{SS} = (\epsilon_i + \epsilon_j - 2\epsilon_i\epsilon_j)N$$
$$N^{OS} = (1 - \epsilon_i - \epsilon_j + 2\epsilon_i\epsilon_j)N$$

leading to:

$$N^{SS}_{ee} = \frac{(\epsilon_i + \epsilon_j - 2\epsilon_i\epsilon_j)}{(1 - \epsilon_i - \epsilon_j + 2\epsilon_i\epsilon_j)} N^{OS}_{ee} \quad \text{for } ee \text{ channel}$$
$$N^{SS}_{e\mu} = \frac{\epsilon_i}{(1-\epsilon_i)} N^{OS}_{e\mu} \quad \text{for } e\mu \text{ channel}$$

The probability ϵ, called QmisID rate is derived from the data using $Z \to ee$ decays in a very characteristic region of the invariant mass of the two electrons, m_{ee}, called the Z-boson peak.

As the charge flip process depends on the path of the particle and its kinematic, the rates are measured in function of four parameters:

- η: The amount of matter on the path has a direct impact on the probability of having a charge flip.
- p_T: The QmisID rates are expected to be larger in the high p_T range where the curvature is smaller.
- Electron selection: fully relies on the identification and isolation criterion of the electron. To enrich the signal and control regions in QmisID events, tight events are combined with anti-tight events.
- Mass of the vertex: this variable is used to identify electrons likely arising from conversions.

The Z peak is obtained by a signal + background fit. A side-band method is used to subtract the background and consequently extract the number of events coming from the charge misidentification. The anti-tight events are combined with tight events to enrich statistically the region. The side-band regions are defined by a $\pm 4\sigma$ width for each side of the Z peak region, as listed in table 7.7. As shown in figure 7.7, the mass of the two electrons in 2ℓSS signature is shifted compared to the opposite sign signature due to the loss of momentum in the trident.

Signature	low side-band [GeV]	Z mass peak region [GeV]	high side-band [GeV]
$\ell^{\pm}\ell^{\pm}$	[51.7,76.5]	[76.5,101.3]	[101.3,126.0]
$\ell^{\pm}\ell^{\mp}$	[54.7,78.5]	[78.5,102.3]	[102.3,126.0]

Table 7.7: Definition of the side-bands and the Z mass peak region.

Then, assuming that all observed same-sign events in the Z peak window, once the background subtraction is done, come from charge misidentification, they follow a Poisson distribution around the expected value:

$$f(k,\lambda) = \frac{\lambda^k e^{-\lambda}}{k!} \qquad \Rightarrow \qquad f(N_{ij}^{SS}|N^{SS}(\epsilon_i,\epsilon_j)) = \frac{((\epsilon_i+\epsilon_j-2\epsilon_i\epsilon_j)N^{ij})^{N_{ij}^{SS}} e^{-(\epsilon_i+\epsilon_j-2\epsilon_i\epsilon_j)N^{ij}}}{N_{ij}^{SS}!}$$

where k is the number of observed events ($k = N_{ij}^{SS}$) in the bin (i,j) and λ is the excepted numbers ($\lambda = (\epsilon_i + \epsilon_j - 2\epsilon_i\epsilon_j)N^{ij}$). The likelihood function L obtained by the combination of all possible configurations of the electron pair gives:

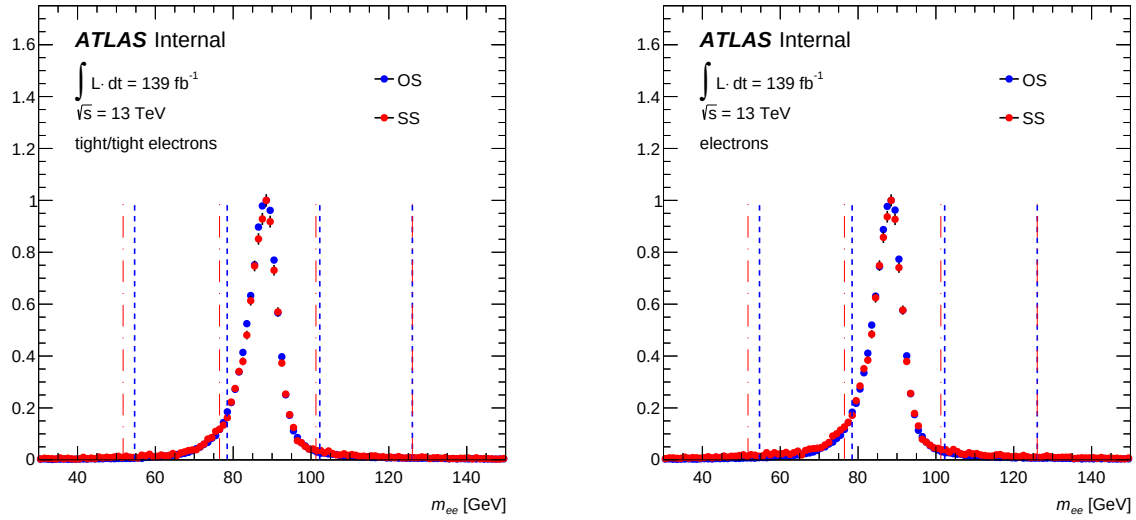

(a) (b)

Figure 7.7: Distribution of the invariant mass of the two electrons in opposite charge (OS) and same charge (SS). Figure (a) includes only leptons passing the tight selection, while figure (b) includes all electrons (tight and anti-tight).

$$L(\vec{\epsilon}|N^{SS}) = \prod_{i,j} f(N_{ij}^{SS}|N^{SS}(\epsilon_i, \epsilon_j))$$

The rates are then measured by the maximisation of the likelihood, i.e. the minimization of the $-2ln(L)$ function, performed by MIGRAD. Figures 7.8 show the QmisID rates as a function of the electron η and p_T.
A validation region for the QmisID estimate, defined as $\text{BDT}_{combined} < -0.4$ has been shown in figure 7.9. The comparison of the data and the MC predictions shows a overall good agreement within 5 %.
Rates estimated with $\mathbf{p_T}$ continuous range: As mentioned before, the rates are dependent on the binning in $|\eta|$ and p_T. To mitigate the statistical uncertainties caused by the size of the dataset, some p_T bins are merged (same rate) in the case of the conversion CR. Figure 7.10a represents the distribution of p_T for the expected and observed same sign signature in data. The discrepancy observed of 200 % in the 60-80 GeV range and higher in the 150-200 GeV are due to the merging of rate in p_T bins.
In order to counterbalance this effect, a p_T modelling of the rates is used. For a given p_T, the rate is estimated by the weighted sum of the rates adjacent p_T bins. As shown in figure 7.10b, this modelling reproduces the p_T dependency distribution.

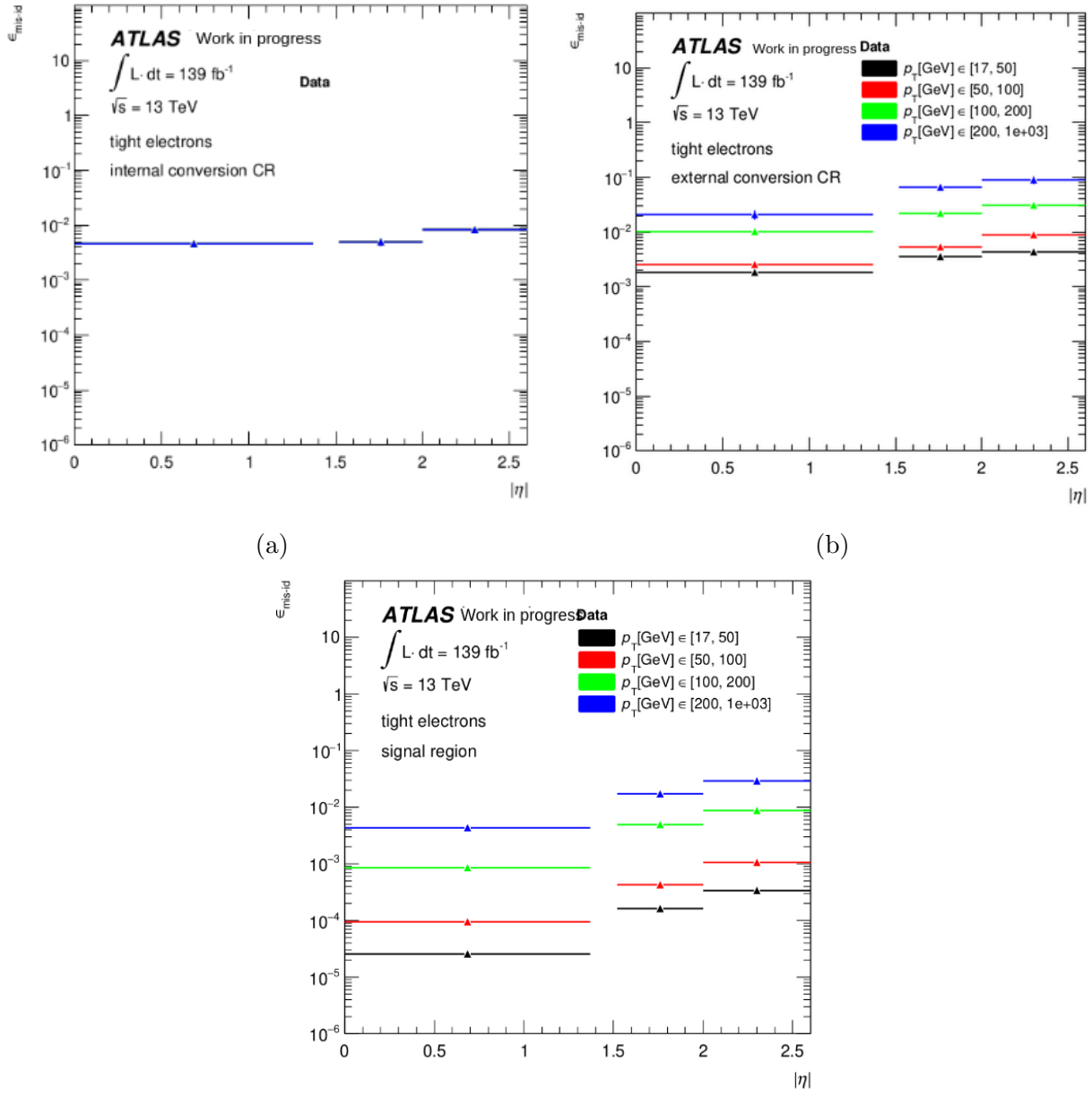

(a) (b)

(c)

Figure 7.8: Electron QmisID rates derived from the data, as a function of η and p_T, for QED conversions 7.8a CR, external conversion 7.8b CR and signal region 7.8c.

Validation with a truth closure test: In order to validate this likelihood method, the rates are compared with rates based on MC truth information. The comparison is shown in

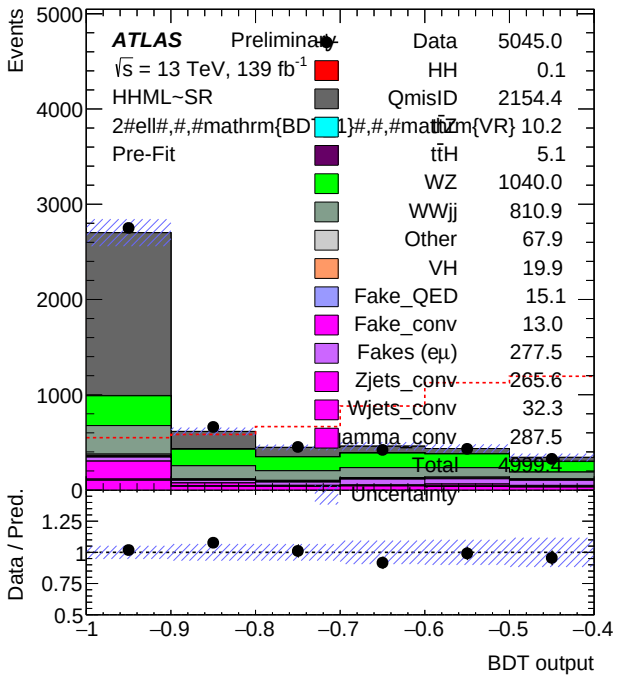

Figure 7.9: Validation region of the QmisID.

figure 7.11 as a function of $|\eta|$ and p_T. No important disagreement is observed in material conversion CR and the signal region. A disagreement of ∼50 % is observed in the QED conversion CR. The discrepancy between the rates extracted from the simulated Z+jets events and the truth information is used as systematic uncertainty as developed in section 7.6.2.

Non-prompt lepton backgrounds

In spite of the tight selection introduced in the 7.3, non-prompt backgrounds and fakes represent an important background in the 2ℓSS channel. These events are an ensemble of lepton from the semi-leptonic decays of a heavy flavour (HF) or a light flavour hadron (LF) or from a photon conversion. Apart from the QmisID estimated in the previous section, two processes involve photon conversion: material conversion and QED conversion. The MC simulation of these events is particularly complex and remains partially unreliable. A Template Fit (TF) method is used to estimate these non-prompt lepton backgrounds. This semi-data-driven method consists of a simultaneous fit of various Control Regions (CR) enriched in each non-prompt background to evaluate their contribution. The classification of events is based on the truth information as follows:

- QmisID events: the truth information directly identifies the QmisID event in MC sim-

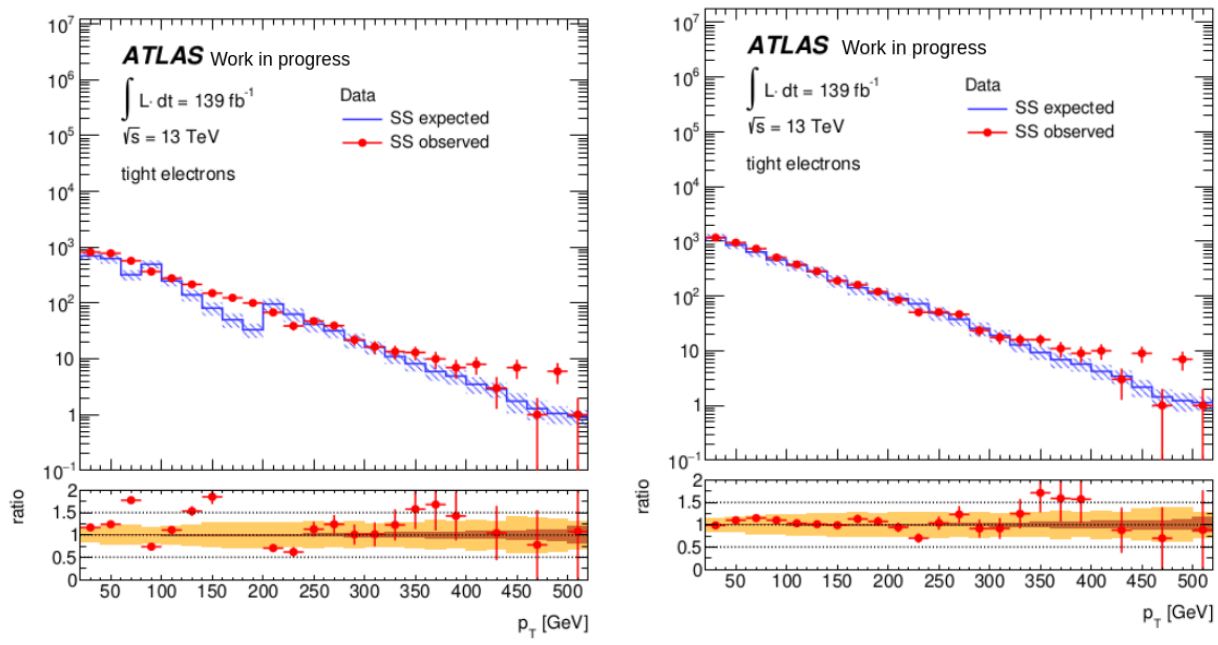

(a) (b)

Figure 7.10: p_T distribution for expected (blue) and observed (red) same sign events in data. The prediction of the rates are performed with continuous p_T distribution in figure (b) and binned in p_T in figure (a). The dashed bands represent the uncertainty over the estimation (statistical +systematics).

ulation. As the QmisID events are identified, all QmisID events are vetoed in MC simulation. QmisID is estimated independently by the data-driven method.

- Photon conversion: Electrons from a photon conversion, excluding Bremsstrahlung radiations.
  - Material conversion: Decay radius R higher than 20 mm and invariant mass of the track associated with the electron and its closest track (from conversion) measured at the conversion vertex ($m^{atCV}_{track-track}$) between 0 and 100 MeV.
  - QED conversions: Excludes all material conversion and an invariant mass of the track associated with the electron and its closest track (from conversion) measured at the primary vertex ($m^{atPV}_{track-track}$) between 0 and 100 MeV.
- HF decays: selection of the leptons from b decay or c decay, using the truth origin selection.

The main contribution to the non-prompt lepton background comes from $t\bar{t}$ and V+jets processes. When the classification of the event is done, four free-floating Normalization Factors

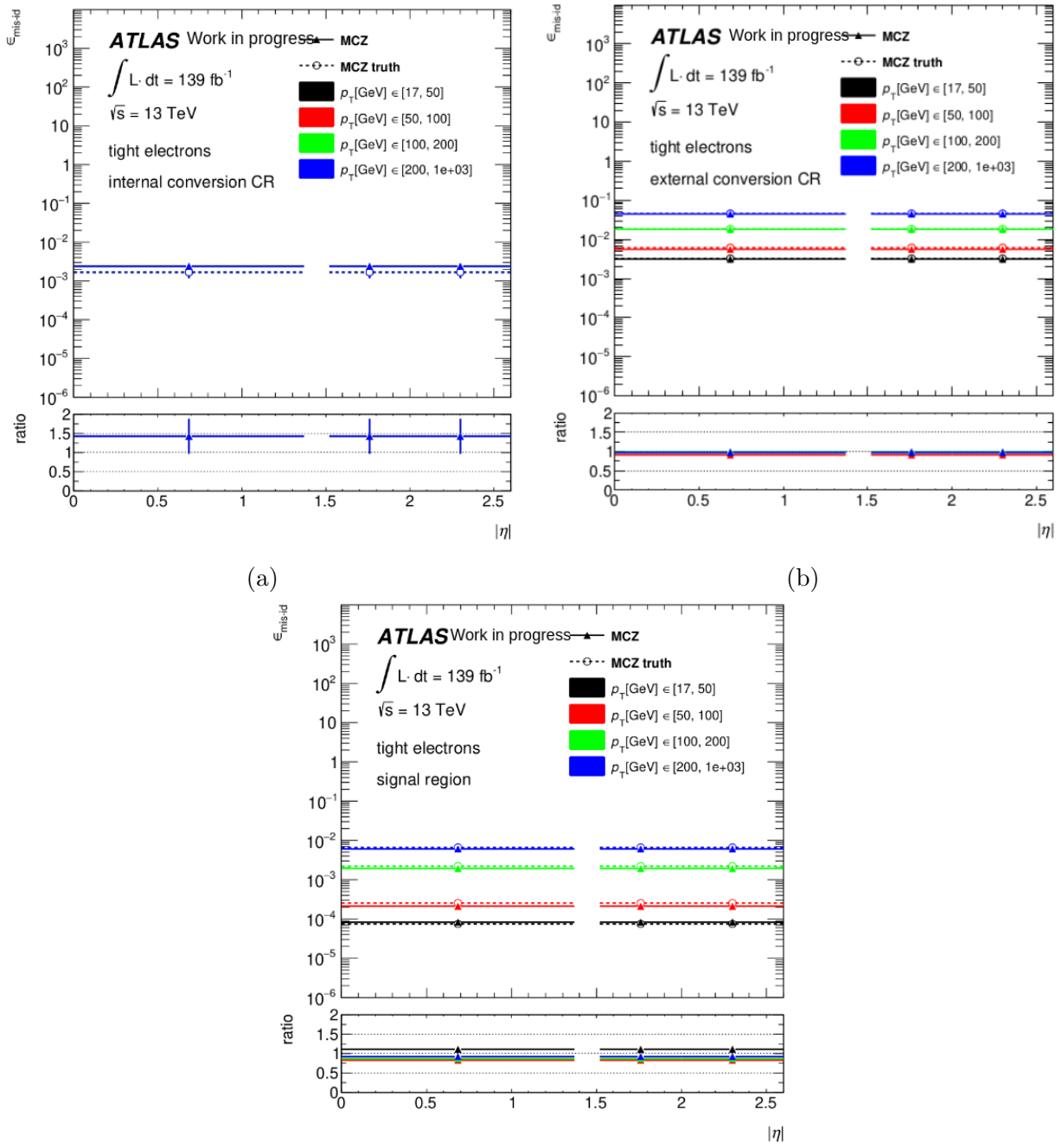

Figure 7.11: Electron QmisID rates derived from the data, as a function of η and p_T, for QED conversions 7.11a CR, external conversion 7.11b CR and signal region 7.11c.

(NF) are then extracted from the data using some dedicated control regions. Then each NF is assigned to the corresponding background to scale the amplitude of the Monte-Carlo (MC) sample while keeping the predicted kinematics properties of the events unchanged. The four NFs are defined as follows:

- $\mathrm{NF}^{MatConv}$: The NF applied to electrons originating from the photon material conversion.
- NF^{QED}: The NF applied to electrons originating from the photon QED processes.
- NF_{e}^{HF+LF}: The NF applied to electrons originating from heavy-flavour hadron and light-flavour hadron decays.
- NF_{μ}^{HF}: The NF applied to muons originating from heavy-flavour hadron and light-flavour hadron decays.

Due to the choice of the data sample, the light flavour electron and the heavy flavour electrons are assigned to one NF. The NFs are constrained by some control regions enriched in top quarks, a source of multiple non-prompt lepton backgrounds. In addition, the MC mismodelling of the photon conversion (QED and material) and their high correlation imposes to define low N_{jets} CR (N_{jets} <3). In addition, the orthogonality with the SR is ensured by requiring at least a b-tagged jet. The following variable distributions are used to derive the NF:

- N_{events} in $ee + e\mu + \mu e$ channel, with a R<20 mm and 0<$\mathrm{m}_{track-track}^{atPV}$ <100 MeV to estimate NF^{QED}.
- N_{events} in $ee + e\mu + \mu e$ channel, with a R>20 mm and 0<$\mathrm{m}_{track-track}^{atCV}$ <100 MeV to estimate $\mathrm{NF}^{MatConv}$.
- $\Delta R_{\ell\ell}$ in $ee + e\mu$ channel, with exactly one b-jet to estimate NF_{e}^{HF+LF}
- HT_{lep} in $ee + e\mu$ channel, with at least two b-jet to estimate NF_{e}^{HF+LF}
- HT_{lep} in $\mu\mu + \mu e$ channel, with at least one b-jet to estimate NF_{μ}^{HF}

It can be noticed that one norm factor is defined for HF and LF hadron decay. This is due to the choice of the region, enriched in top quark, which by definition contains few LF events. As the analysis is still blinded, the template is fitted to the data using CR only. The result presented in this thesis corresponds to a blinded full fit in order to get the expected sensitivity from an Asimovfit. When the unblinding is accepted, the simultaneous fit is performed using control and signal regions, in order to obtain the observed sensitivity (results not presented in this thesis). The CR regions of the unblinded full fit are shown in figures 7.12,7.13,7.14,7.15, (pre-fit and post-fit), and the resulting normalization factors in figure 7.16.

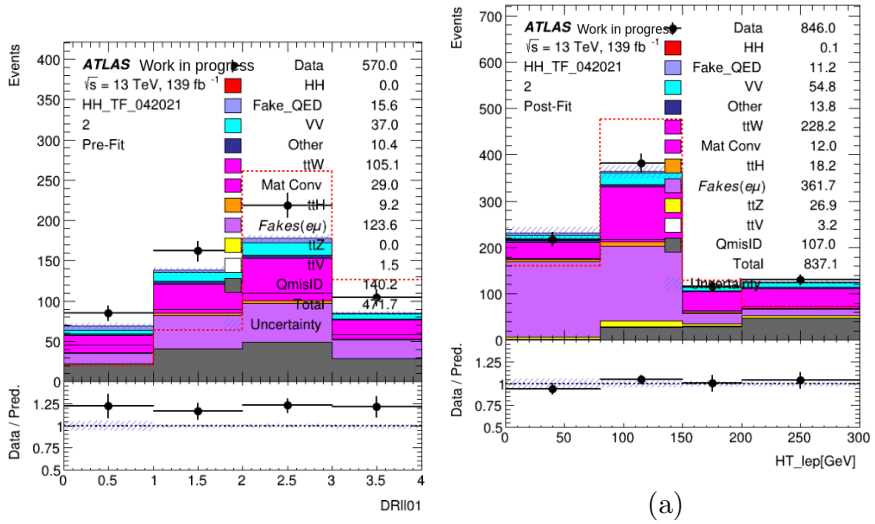

(a)

Figure 7.12: Low N_{jets} CR enriched dedicated for the constrain of the heavy flavour hadron decay in ee+eμ channel. The figure on the left shows the pre-fit distribution and the right figure shows the post-fit distribution.

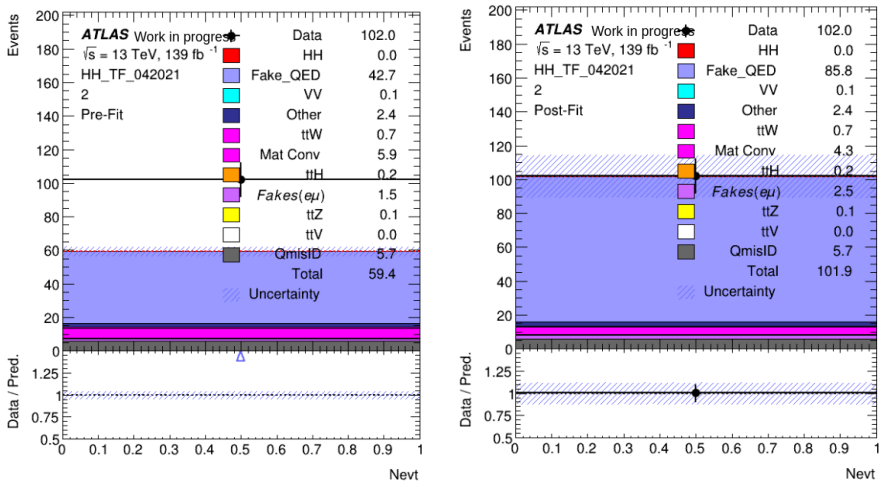

(a) (b)

Figure 7.13: Distribution of the control region dedicated to the constrain of the QED conversions. The figure on the left shows the pre-fit distribution and the right figure shows the post-fit distribution.

An overall good agreement is observed in the post-fit distribution, shown in figure 7.12a, lower than 5 % of discrepancy. Then, the norm factors are between 0.88 and 1.99.
The agreement between data and background estimate is validated in a validation region

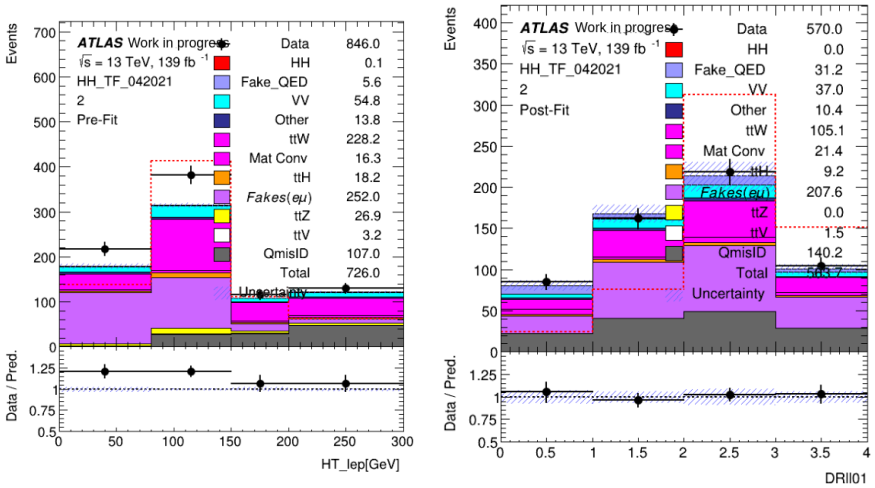

(a) (b)

Figure 7.14: Low N_{jets} CR enriched dedicated for the constrain of the heavy flavour hadron decay in $e\mu + \mu\mu$ channel. The figure on the left shows the pre-fit distribution and the right figure shows the post-fit distribution.

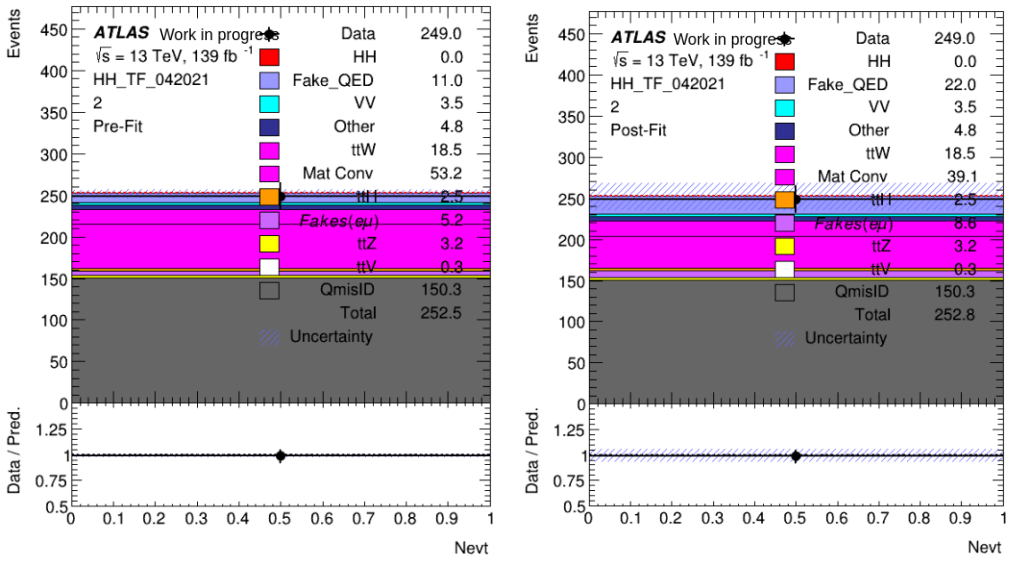

(a) (b)

Figure 7.15: Low N_{jets} CR enriched dedicated for the constrain of the material conversion. The figure on the left shows the pre-fit distribution and the right figure shows the post-fit distribution.

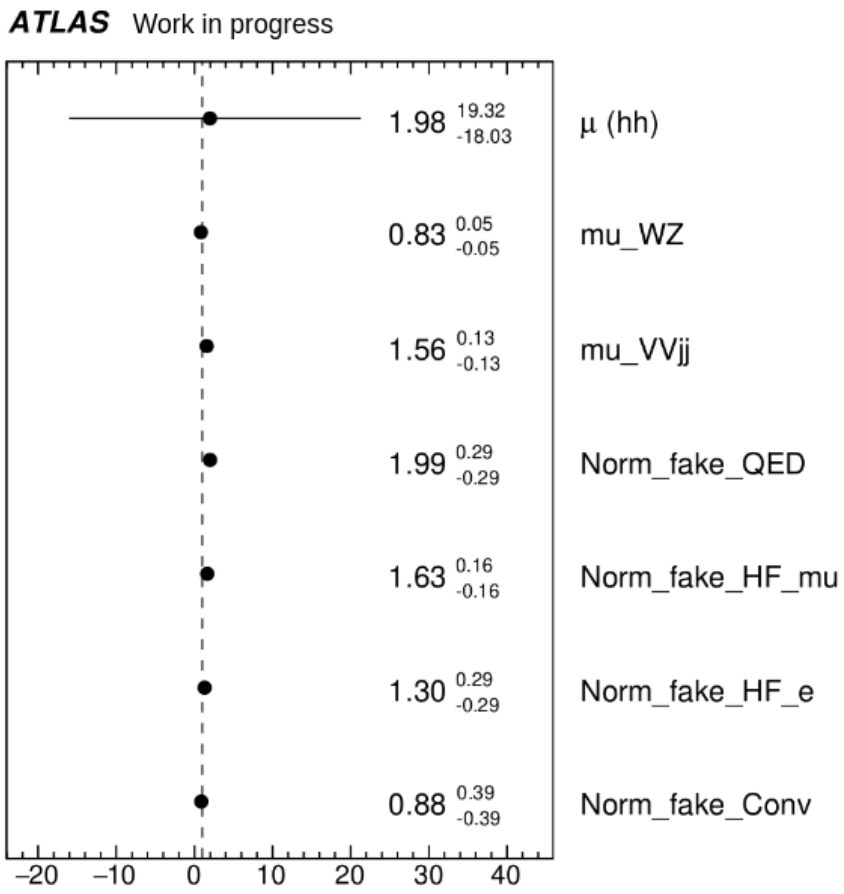

Figure 7.16: Norm factors extracted from the simultaneous fit of the five control regions.

(VR) defined as a low combined BDT region such as $BDT_{combined} < -0.4$. This selection aims to be orthogonal to the signal region. The validation region is shown in figure 7.17.

7.6 Systematic uncertainties

In this section, various sources of systematic uncertainties are introduced. These uncertainties have an impact on the final result and affect particularly the shape and/or the normalization of each distribution. The systematic uncertainties are implemented in the fit as a normalization factor or as a shape variation. Two categories can be considered: the experimental uncertainties and the signal and background theoretical modelling uncertainties.

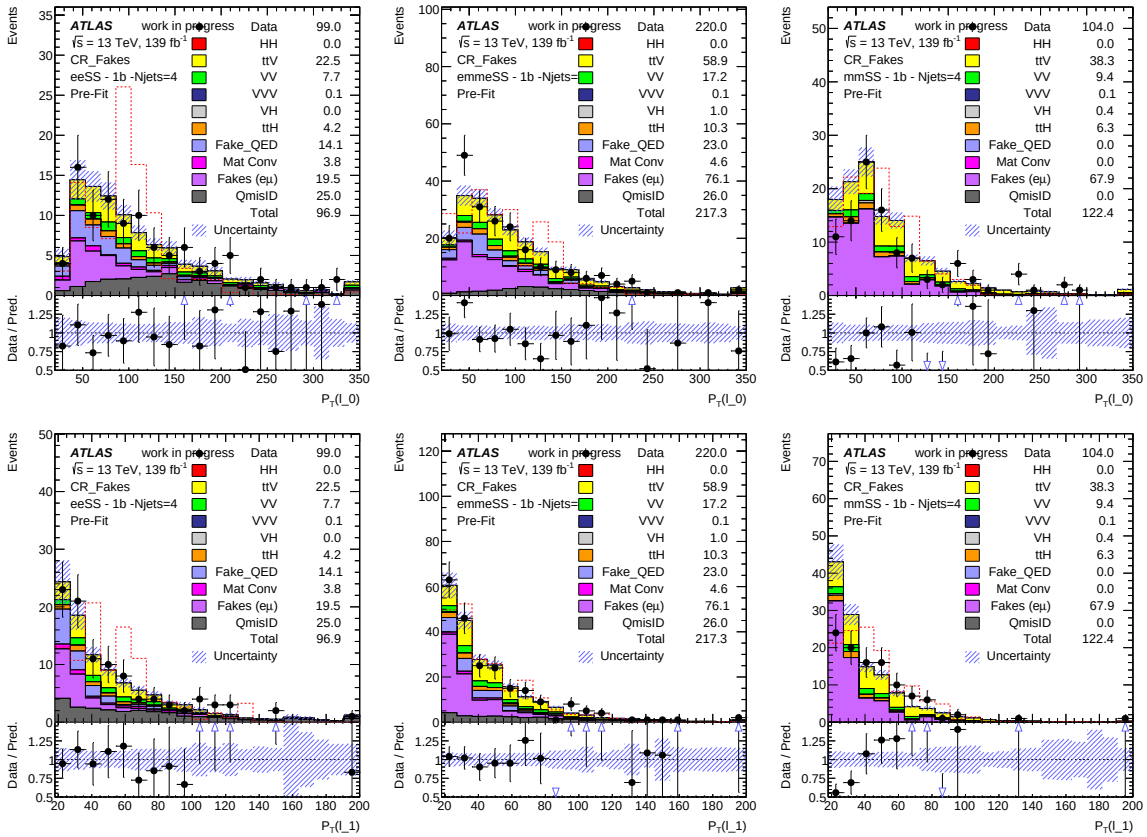

Figure 7.17: Validation regions dedicated to the non-prompt background estimate, using the p_T distribution of the leading lepton (top) and sub-leading lepton (bottom), for ee (on left), eμ (middle) and $\mu\mu$ (right) channel.

7.6.1 Experimental uncertainties

The experimental uncertainties fully rely on the reconstruction and the identification of objects in the ATLAS detector, composed of light leptons, taus, jets, MET and the integrated luminosity of the dataset. The ATLAS SUSY group [92] provides the experimental uncertainties for each object:

- Photons: The uncertainties are provided in two categories [93]: the calibration and the efficiency. The uncertainties linked to the calibration, which affect the photon kinematics properties, cover the resolution, the scale and the ATLFAST2 scale. The uncertainties linked to the efficiency, affecting the normalization, cover the ID efficiency, the isolation and the trigger. Each of them corresponds to one nuisance parameter.

- Pileup: The pileup uncertainty is a scaling factor (one nuisance parameter) applied to

the data, measured as the variation of the average number of interactions per collision $< \mu >$ in data with respect to simulated samples.

- Jets: The systematic uncertainties of jets [94] are associated with the jet energy scale (JES) calibration, the jet energy resolution (JER) and the jet vertex tagger (JVT) efficiency. The two first have an impact on the jet kinematic properties while the third affects the normalization.

- Flavour Tagging: The uncertainties of the flavour tagging rely on the efficiency of identifying jets with b-hadrons, c-hadrons or light hadrons (3 NPs). Then two other nuisance parameters come from the extrapolation of the b-tagging weight to the high p_T regimes. All uncertainties affect the normalization.

- MET: The missing transverse energy uncertainties are modelled by three nuisance parameters: one for the track soft term scale and two for the track soft term resolution. These variations are estimated by comparing events without E_T^{miss}. The resulting difference becomes the uncertainty [95].

- Electrons: As for the photon, the uncertainties over the electron can be divided into two categories [93]: calibration and efficiency. The calibration uncertainties affect the shape of the electron kinematic properties while the efficiency uncertainties affect the normalization. In addition to those already quoted for the photon, the charge-related uncertainties and the trigger efficiencies need to be considered. In total, eleven nuisance parameters are associated with the electron.

- Muons: Five Nuisance Parameters (NPs) are identified, modifying the kinematic properties of the muon, such as the smearing of the muon in the ID or the MS track and the variation in the scale and resolution of the momentum of the muon. Ten other NPs affect only the normalization of the distributions, they cover the reconstruction, the isolation, the trigger and the track-to-vertex association efficiency.

- Taus: The uncertainties relying on the hadronic taus [96], include the reconstruction, identification or trigger efficiency for NPs associated with the normalization, and the energy scale for the shape uncertainties.

The luminosity uncertainty of the full Run2 dataset is evaluated to be 1.7 %. This measurement is derived from the calibration of the luminosity scale, performed each year using the x-y beam-separation scans. More detail can be found in [97].
The trigger uncertainty defined for light leptons (e and μ) are measured as a scale factor following the recommendation [98]. The full list of the nuisance parameters is given in appendix .4.

7.6.2 Theoretical modelling uncertainties

The modelling of the signal and the background brings various sources of systematic uncertainties. One of the main sources is on the production cross-section. Then each generator assumes the value of theoretical and phenomenological parameters in the modelling. The associated systematic uncertainties are then extracted by comparing the nominal MC samples with their parameter-varied versions. Then, in the case of the data-driven background introduced in section 7.5, the uncertainties are derived from a data-MC comparison in the dedicated control regions.

Signal

ggF HH: The QCD scale uncertainty is obtained by varying the renormalization and the factorization, independently and simultaneously by a factor two around the central scale $\mu_0 = m_{HH}/2$, where m_{HH} is the invariant mass of the Higgs pair (with $m_H = 125\,\text{GeV}$ and $m_t = 175.2\,\text{GeV}$. It results an uncertainty of $^{+2.1}_{-4.9}$. Then, the PDF (combined with the α_S strong coupling uncertainties) and the m_t dependence are estimated following the LHC-HH group recommendations [99]. It leads to the PDF uncertainty of $^{+3}_{-3}$ and a m_t uncertainty of $^{+4}_{-18}$.

VBF HH: The value of the cross-section uncertainty follows the working group recommendations.

QmisID estimate

Four sources of uncertainties can be considered in the measurement of the QmisID rates, combined in a quadratic sum:

- The systematic uncertainty linked to the variation with the Z-boson mass window m_Z
- The systematic uncertainty from the likelihood maximisation, statistically dependent on the chosen CR
- The systematic uncertainty on the likelihood method, extracted from the comparison with the truth-matching on simulated $Z \to ee$ events
- The systematic uncertainty of the low mis-modelling of the invariant mass m_{ee}.

Template Fit uncertainties

Since the template fit method is a semi-data-driven method and relies on the MC samples, the modelling of the non-prompt (NP) leptons in MC simulations has to be included. The

associated uncertainties are estimated by comparing the NP leptons in data with the MC-identified fakes. To further enrich each region in photon conversion or heavy flavour decays, the isolation criteria are relaxed for the subleading lepton, while other lepton selections remain the same.

Heavy flavour systematic uncertainties: The heavy flavour systematic uncertainty is estimated by relaxing the isolation criteria of the sub-leading leptons. The uncertainty is extracted from the distribution of the combined BDT using the ratio: $\Delta NF = \frac{Data - Prompt}{Fakes_{HF}^{MC}} - NF$, with Data and Prompt the number of data events and prompt events. The resulting discrepancy between data and MC simulations is extracted bin per bin and implemented in a branch for the final fit. The QmisID is estimated through a data-driven method, introduced in section 7.5.2. The low N_{jets} CR with relaxed isolation criteria is shown in figure 7.18, for relaxed electrons and muons, while the final discriminant variable is shown in figure 7.19. The resulting uncertainty range is 1 to 6 % for the electrons and 3 to 9 % for muons.

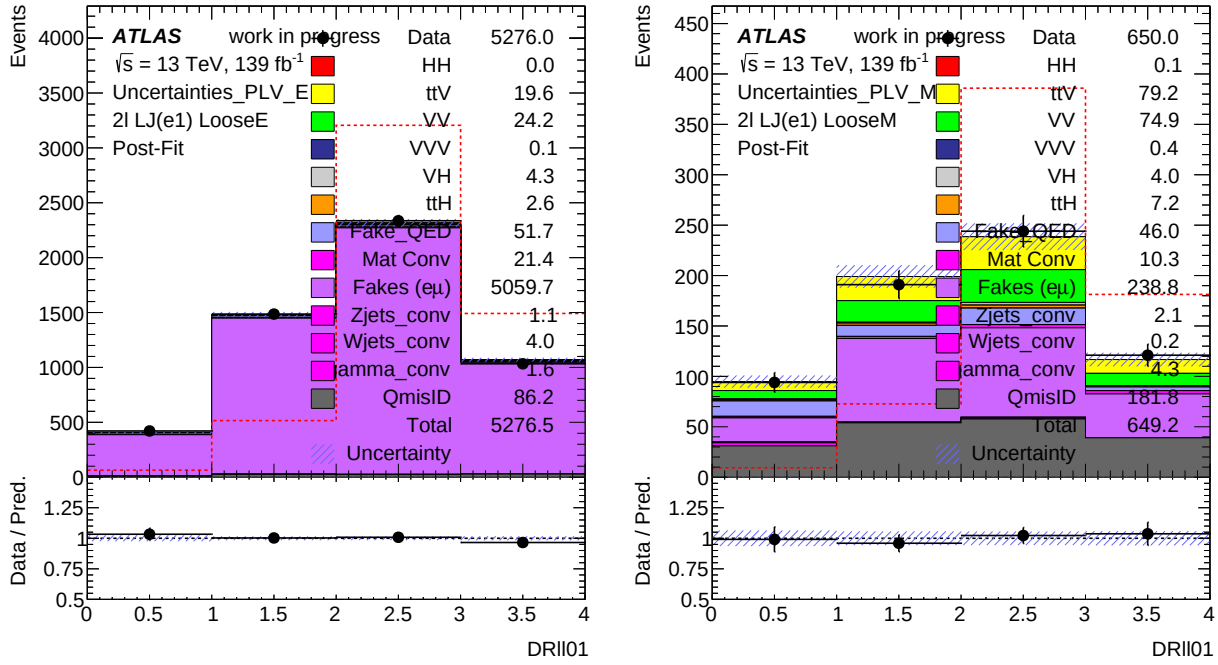

Figure 7.18: Low N_{jets} CR with relaxed isolation WP for the electron (on left) and muons (on right).

Photon conversion systematic uncertainties: The photon conversion systematic uncertainties estimate is performed for the heavy flavour systematic uncertainties. In order to enrich the low N_{jets} CR with photon conversion, the isolation criterion is relaxed and the ambiguity criteria are inverted (> 0 for electron passing the selection). The resulting low

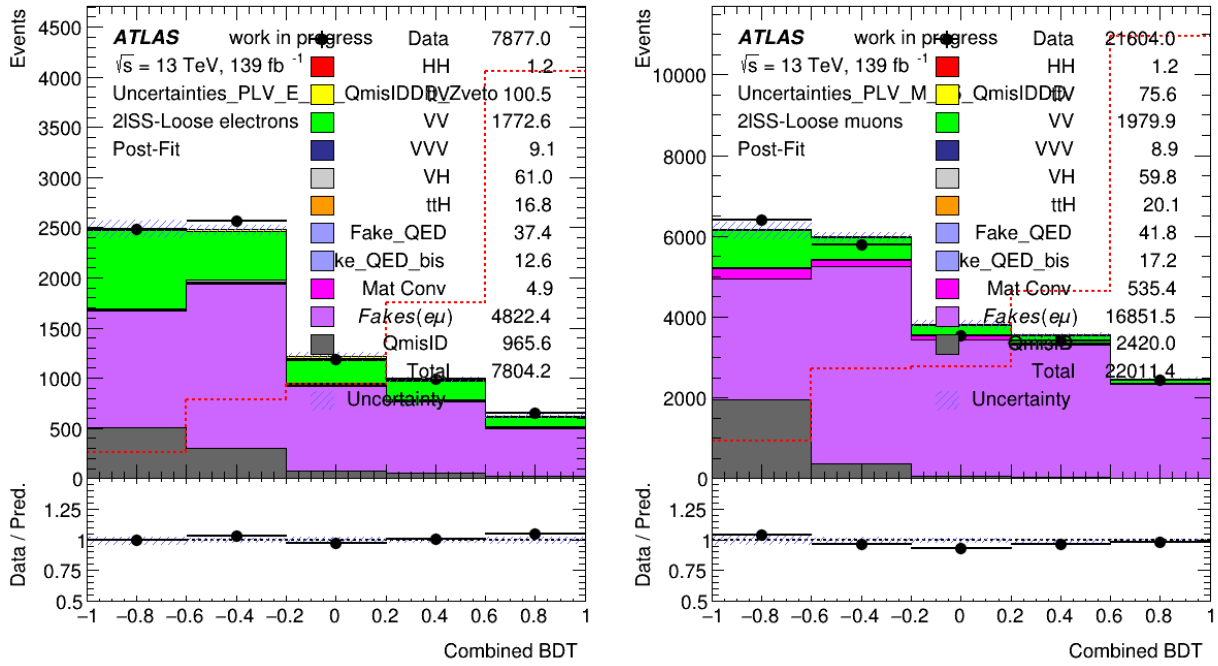

Figure 7.19: Combined BDT with relaxed isolation WP for the electron (on left) and muons (on right).

N_{jets} CR are shown in figure 7.20. Then the uncertainty is measured using the final discriminant variable distribution, defined as the following ratio $\Delta NF = \frac{Data - Prompt}{Fakes^{MC}_{Conv}} - NF$. The discrepancy between Data and MC simulation in the BDT distribution, shown in figure 7.21, is dependent of the BDT bin value. The QmisID is estimated through a data-driven method, introduced in section 7.5.2.

$t\bar{t}$ modelling uncertainties The $t\bar{t}$ represents a source of fakes in the 2ℓSS signature, by photon conversion or heavy flavour decays. Therefore the template fit method depends on MC non-prompt modelling. The uncertainties on $t\bar{t}$ modelling are extracted using alternative samples, i.e. parameter-varied samples. Three sets of alternative samples are alternatively used in this analysis, with a different choice of Parton Shower (PS) modelling, a different Matrix Element (ME) generator, and a different hdamp parameter value (IFS/FSR). The uncertainty estimates take into account the shape of the distribution only, all distributions are normalized.

- Initial-State and Final-State radiation uncertainty: This uncertainty in the modelling of the Initial-State radiation is estimated using Powheg+Pythia8 samples, comparing nominal non-all hadronic sample having hdamp = $1.5\,m_t$ with alternative samples having hdamp = $3.0\,m_t$ and the varying the showering.

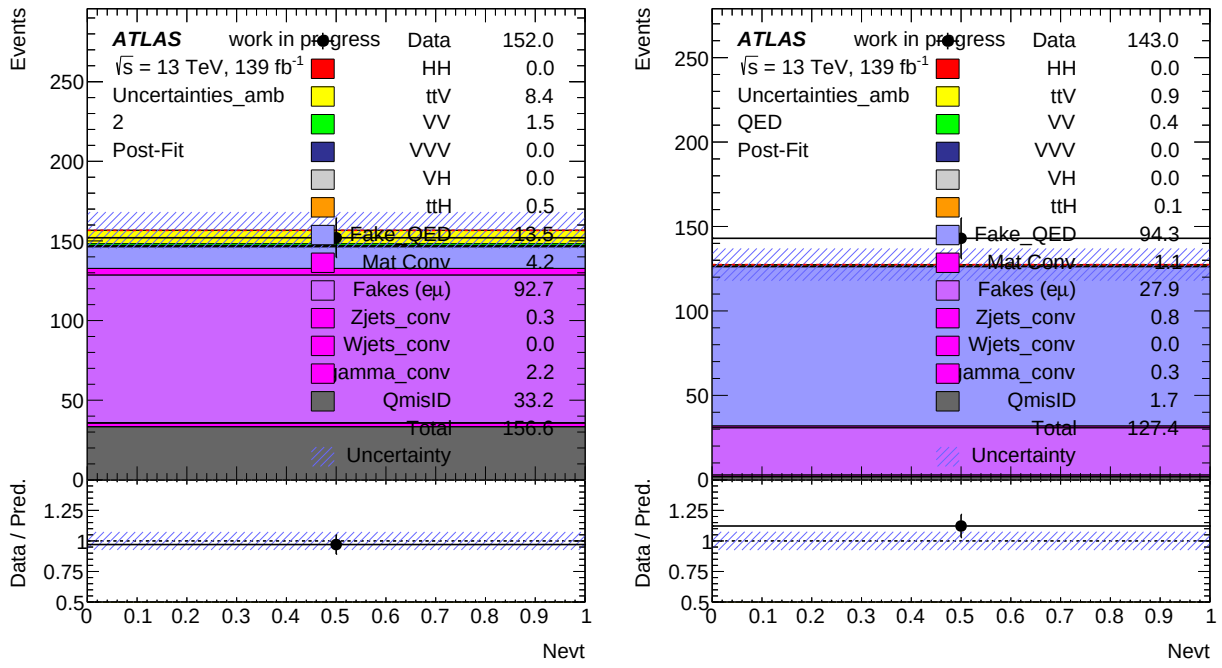

Figure 7.20: Low N_{jets} CR with relaxed isolation WP and inverted ambiguity criteria for the region enriched in material conversion(on left) and in QED conversion (on right).

- The fragmentation and hadronization modelling uncertainty: Alternative samples produced with the same Powheg parameters as the nominal $t\bar{t}$ sample in terms of PDF choice, renormalisation and factorisation scales or hdamps parameters. These samples are interfaced by the Herwig7 alternative generator instead of Pythia8. These uncertainties affect the distribution normalization, but only effects on the distribution shape are considered. The latter, however, are small and are pruned in the fit in almost all cases.

- NLO matching uncertainty: This uncertainty can be estimated by comparing the Powheg generator nominal sample with alternative generator aMcAtNlo samples. These samples compare NLO matching and Matrix Element Correction (MEC) at the same time.

The estimated TF uncertainties are presented in the table 7.8, as a function of the BDT bin.

7.7 Possible improvements

This section presents various possible improvements to the analysis performed in this thesis.

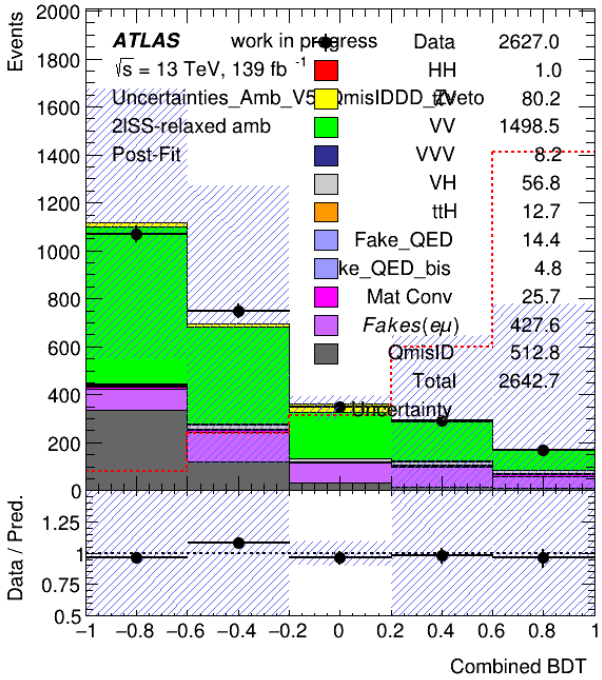

Figure 7.21: Combined BDT distribution with relaxed isolation WP and inverted ambiguity criteria.

	Combined BDT score range				
Uncertainties	[-1,-0.6]	[-0.6, -0.2]	[-0.2, 0.2]	[0.2, 0.6]	[0.6, 1]
HF + LF electrons	1%	4%	2%	1%	6%
HF muons	9%	5%	4%	6%	3%
Material conversions	10%	12%	30%	4%	3%
$t\bar{t}$ modelling	$< 1\%$				

Table 7.8: Template fit uncertainties as a function of the BDT bin and the origin of the fakes

Alternative MVA method

As discussed in the section 7.4, the final discriminant variable is estimated using a Boosted Decision Tree (BDT) method. Yet, other machine learning can be considered. In the case of the 2ℓSS signature, one method can appear: the multi-class NN algorithm. This latest differs from the usual classification (as performed with the BDT) because instead of defining two

output categories (background VS signal), the multi-class NN algorithm defines N output layers (N-1 degrees of freedom) as shown in figure 7.22.

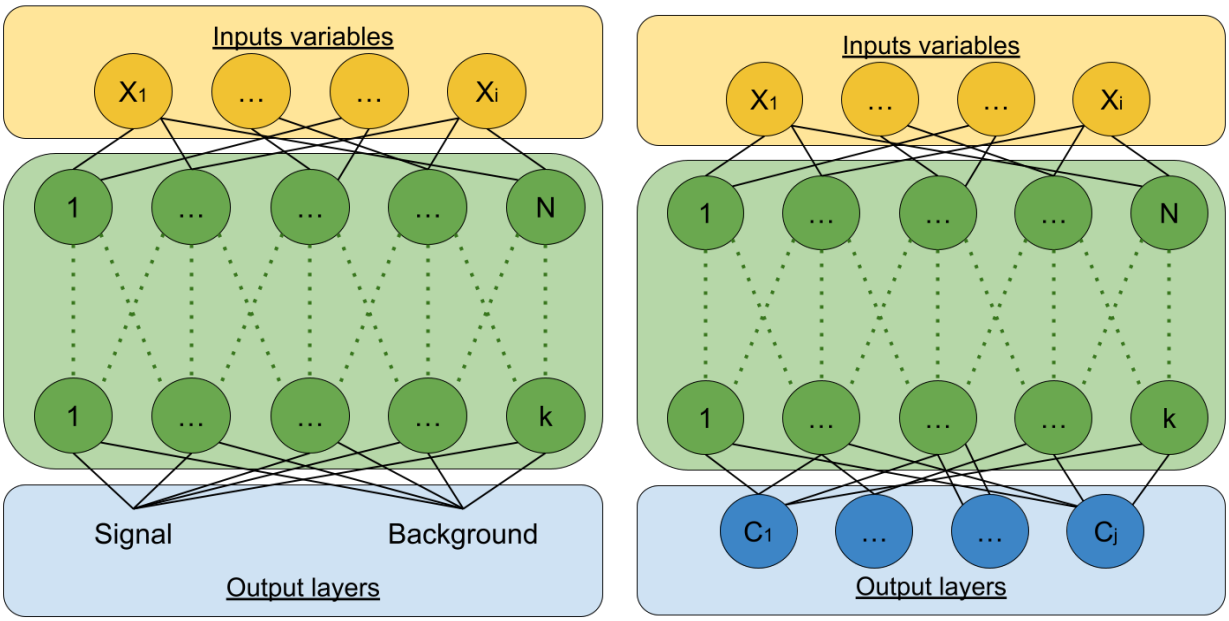

(a) Binary Classification.

(b) Multi-class classification.

Figure 7.22: Binary classification structure VS Multi-class classification structure.

It can be noticed that the structure of a multi-class is comparable with the strategy to have three specific BDTs, one per dominant background, which suggests that this method is promising. A multi-class has been trained, but despite achieving a comparable result with TMVA, no further study was conducted.

Deeper investigation in backgrounds and systematics

Various studies can be performed on backgrounds. For instance, the estimation of various backgrounds can be performed using the template fit method such as VV or ttH. As a consequence, a complete study for the definition of new control regions can be performed, decoupling each sample in VV for instance.
Finally, the systematic uncertainties have been added and the overall impact of the systematic has been studied. Yet, an individual systematic uncertainty study can be considered.

Study with additional κ_λ signal samples.

The test of the performance of the specific and combined BDT with signal simulated with additional values of κ_λ can be considered. At the time of writing this thesis, the samples for

κ_λ=10 are in production. Once these samples are produced, using the mass of the Higgs, it is possible to reproduce create and define a weight to generate a sample for all κ_λ values.

7.8 Combination with multileptons channels

The construction of the final discriminant variables for the rest of the channel is performed as for the 2ℓSS channel, with a multivariate, build from TMVA tool or XGBoost. On the contrary of the 2ℓSS strategy, the rest of the channel trains a unique BDT. The list of discriminant input variables differs as a function of the backgrounds. Finally, the non-prompt background estimate is performed using either the template fit method introduced in subsection 7.5.2 or either the fake factor method. Then, all channels are combined and the final sensitivity of the ML combined channels is estimated.

The combined sensitivity

The preliminary combination of the nine channels is performed in a blinded fit. The combined 95 % C.L. upper limit is computed using Asimov dataset. The table 7.9 summarizes 95 % C.L. upper limit for each channel and the combined limit. The expected limit equals to 8.93 with statistical uncertainties only, 9.29 when adding the MC systematics and 9.74 when considering the full systematic uncertainties. As the analysis is still blinded, the observed uncertainties remain unknown.
A recent result from CMS [100] obtained for HH→ (excluding $\gamma\gamma + ML$ channels) shows an expected (observed) 95 % upper limit at 19 (21) times the SM HH production cross-section. These results are obtained for both individual search categories and from a simultaneous fit of the seven following channels: 2ℓSS, 3ℓ, 4ℓ, 3ℓ1τ_{had}, 2ℓ2τ_{had}, 1ℓ3τ_{had} and 4τ_{had}. These results can be compared with a preliminary result of 14.84 times the SM HH production cross-section as the expected limit, obtained with the combined fit of ML channels (excluding $\gamma\gamma + ML$ and 4ℓ + 2b).

Finally, this channel should be combined with the other ATLAS di-Higgs searches. This combination is already performed considering only three channels, $bb\gamma\gamma$, bb$\tau\tau$ and bbbb. The latest public result [101], shows an expected (observed) 95 % CL upper limit on the signal strength of 2.9 (2.4). A preliminary combination of the three already quoted channels with the multilepton channel, supposedly decorrelated to the other channels, can provide an expected limit on the signal strength of 2.78. An equivalent study has been performed by the CMS collaboration, combining five channels, i.e. $bb\gamma\gamma$, bb$\tau\tau$, bbZZ, bbbb and multileptons, providing an expected upper limit on the signal strength of 2.5. Then, a recent study starts with the idea of combining the ATLAS and CMS results. The extrapolation of the expected limit shows a 34 % improvement in the expected upper limit up to 1.86 times the SM HH production cross-section. Even if the observation of the Higgs self-coupling is not possible

Channels	Stats. Only	Stats. + MC syst.	Stats.+ full syst.
2ℓSS	$30.70^{43.47}_{22.12}$	$31.62^{44.76}_{22.79}$	$34.81^{49.61}_{25.08}$
3ℓ	$23.82^{34.03}_{17.16}$	$25.58^{37.00}_{18.43}$	$28.13^{40.94}_{20.27}$
$b\bar{b}4\ell$	$27.24^{40.90}_{19.63}$	$27.62^{41.76}_{19.90}$	$28.71^{44.41}_{20.68}$
$1\ell + 2\tau_{had}$	$34.64^{49.51}_{24.96}$	$38.31^{54.33}_{27.60}$	$41.21^{58.92}_{29.70}$
$2\ell + 2\tau_{had}$	$32.82^{48.34}_{23.65}$	$33.46^{49.12}_{24.11}$	$33.99^{50.09}_{24.49}$
2ℓSS $+1\tau_{had}$	$50.50^{72.83}_{36.39}$	$62.37^{91.18}_{44.94}$	$63.52^{93.27}_{45.77}$
$\gamma\gamma + 1\ell 0\tau_{had}$	$25.43^{36.95}_{18.32}$	$25.43^{36.95}_{18.32}$	$26.68^{39.53}_{19.23}$
$\gamma\gamma + 0\ell 1\tau_{had}$	$52.58^{76.54}_{37.89}$	$52.50^{76.57}_{37.90}$	$54.50^{80.98}_{39.27}$
$\gamma\gamma + 2L$	$37.05^{54.86}_{26.70}$	$37.05^{54.86}_{26.70}$	$38.21^{57.76}_{27.53}$
Combined	$8.93^{12.69}_{6.44}$	$9.29^{13.22}_{6.70}$	$9.74^{13.91}_{7.02}$

Table 7.9: 95 % C.L. upper limit shown as Median $^{+1\sigma}_{-1\sigma}$ of each multilepton channel and the combination.

with the Run2 dataset, the combined upper limit of the di-Higgs production cross-sections by ATLAS, CMS or ATLAS+CMS, already provides strict constraints on the SM Higgs self-coupling value and would exclude $\kappa_\lambda = 0$.

7.9 Higgs self-coupling at HL-LHC

Projections studies of non-resonnant HH production at HL-LHC has been already presented. These projections include the three dominant channels, i.e. $bbbb$, $bb\tau\tau$ and $bb\gamma\gamma$. The results are extrapolated from the Run2 analyses, the distributions are scales by a multiplicative factor defined as the ration between the HL-LHC integrated luminosity and the Run2 integrated luminosity. Since the evolution of the systematic uncertainties from the Run2 to HL-LHC is not clear, various systematic uncertainties scenarios are considered:

- only statistical uncertainties (No syst. unc.).
- A baseline scenario where relevant systematic uncertainties are scaled down, following the improvements expected with the larger HL-LHC dataset available.

- A scenario where Run 2 experimental uncertainties are considered but theoretical uncertainties associated to HH signals are halved (Theoretical unc. halved).
- A scenario where Run 2 experimental uncertainties are left unchanged (Run 2 syst. unc).

The combined significance is estimated at 3.4σ for the baseline scenario. The result for the other scenarios are given in table 7.10. Figure 7.23 shows the evolution of this significance with the integrated luminosity and with the κ_λ value.

Uncertainty scenario	$b\bar{b}\gamma\gamma$	$b\bar{b}\tau\tau$	$b\bar{b}b\bar{b}$	Combination
No syst. unc.	2.3	4.0	1.8	4.9
Baseline	2.2	2.8	0.99	3.4
Theoretical unc. halved	1.1	1.7	0.65	2.1
Run 2 syst. unc	1.1	1.5	0.65	1.9

Table 7.10: Projected significance of the SM HH signal. This result includes a combinaison of the three following channels: $b\bar{b}\gamma\gamma$, $b\bar{b}\tau\tau$ and $b\bar{b}b\bar{b}$ [102].

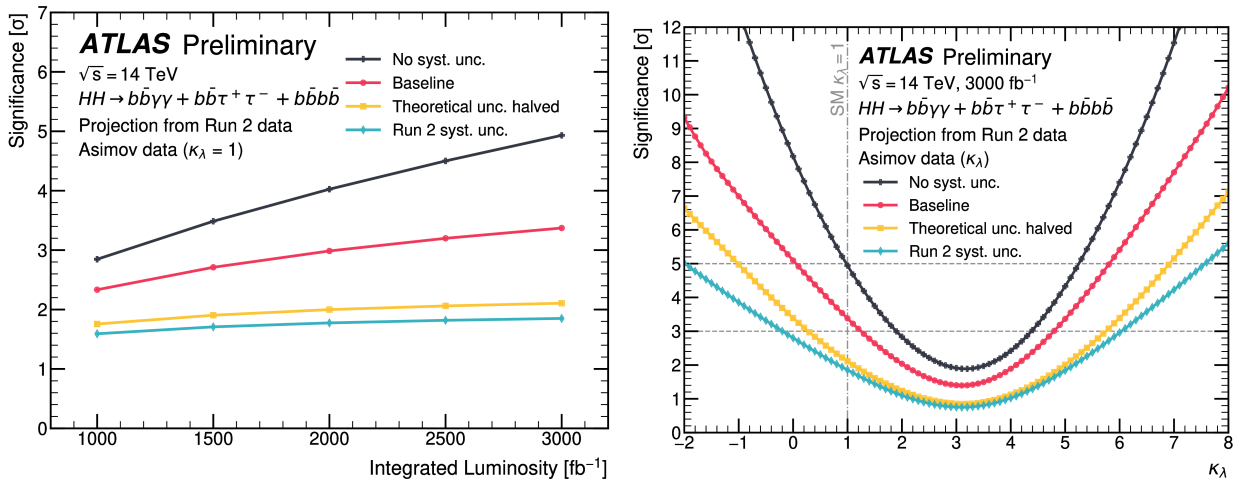

(a) (b)

Figure 7.23: Projected significance for SM HH production combining the $b\bar{b}\gamma\gamma$, $b\bar{b}\tau\tau$ and $b\bar{b}b\bar{b}$ channels at the HL-LHC assuming the four different uncertainty scenarios as a function of the integrated luminosity (on left) or the κ_λ value (on right) [102].

The projected confidence intervals for the κ_λ are given in table 7.11.

Uncertainty scenario	κ_λ at 95% confidence level
No syst. unc.	[0.3, 1.9]
Baseline	[0.0, 2.5]
Theoretical unc. halved	[-0.3, 5.5]
Run 2 syst. unc	[-0.6, 5.6]

Table 7.11: The projected confidence intervals for the κ_λ. This result includes a combinaison of the three following channels: $b\bar{b}\gamma\gamma$, $b\bar{b}\tau\tau$ and $b\bar{b}b\bar{b}$ [102].

Conclusions and outlook

Since the discovery of the Higgs boson in 2012, its characterization has become the main goal of the LHC program. In particular, the measurement of the Higgs self-interaction coupling appears as a crucial key for validating the electroweak symmetry-breaking mechanism. A potential deviation from the SM prediction could have considerable consequences on our understanding of nature or can reflect new physics phenomena. At LHC, the di-Higgs production provides direct access to this coupling but suffers from a very small SM cross-section, making it a very rare process with the current LHC luminosity.

This thesis presents the Run-2 search for non-resonant HH production in two light leptons with the same charge signature at $\sqrt{s}$ =13 TeV centre-of-mass energy. Various strategies and methods are developed for the events characterization and background estimate. The resulting expected limit at 95 % CL on SM production cross section is $31\times\sigma_{HH}^{SM}$ for 2ℓSS channel alone. The combination with other multilepton channels leads to an expected limit at 95 % CL $8\times\sigma_{HH}^{SM}$. At the time of writing this thesis, the unblinding is not granted, so the observed limit remains unknown. This result should be then combined with other di-Higgs analysis which includes up to now, $\bar{b}b\bar{b}b$, bb$\gamma\gamma$ and bb$\tau\tau$ channels.

The HL-LHC operation is expected to start in 2029 and operate for at least a decade, with an integrated luminosity up to 4000 fb^{-1}. Given the large expected dataset, this experiment will provide an ideal opportunity to measure the SM di-Higgs production and consequently the Higgs self-coupling. Recent projection of the combination of the three current channels indicates that the Higgs self-coupling can be measured with an expected significance of 3.2 standard deviations for ATLAS probing the evidence of HH production [102]. Assuming no deviation observed, this combination will provide an expected value of κ_λ in [0.6,1.5] without systematic uncertainties. This result will be surely better due to the improvement of experiment methods. This HL-LHC era presents a challenge to ATLAS collaboration in pileup mitigation and radiation hardness. The future tracker ITk is expected to maintain or improve the performance of the detector in spite of the increase of the luminosity. Yet, in the forward region, its performance will not be enough to disentangle the primary vertex from the pileup. To counterbalance, a timing sub-detector will be added in this region. This latest,

called HGTD, will provide a 30 ps to 50 ps time resolution per track. This thesis presented various tests of the front-end electronics prototypes, called ALTIROC2 and ALTIPIX. In addition, tests of the sensors and FE electronics during test beam sessions are presented. At the time of writing, the prototype ALTIROC3 is under test and the pre-production version ALTIROCA is under design. The installation is foreseen for 2026.

Finally, the exploitation of electron-positron colliders can be the key to explore the Higgs sector. The main advantage of these e^+e^- Higgs factories is to reach very low precision for many Higgs couplings. Four projects have been proposed already: ILC, CLIC, CEPC and FCC. The prospect of the next-generation collider projects is really promising, with an expected precision over the Higgs measurement lower than 1 %.

Bibliography

[1] Steven Weinberg. "A Model of Leptons". In: *Phys. Rev. Lett.* 19 (21 Nov. 1967), pp. 1264–1266. DOI: 10.1103/PhysRevLett.19.1264. URL: https://link.aps.org/doi/10.1103/PhysRevLett.19.1264.

[2] Abdus Salam. "Weak and electromagnetic interactions". In: *Selected Papers of Abdus Salam*, pp. 244–254. DOI: 10.1142/9789812795915_0034. eprint: https://www.worldscientific.com/doi/pdf/10.1142/9789812795915_0034. URL: https://www.worldscientific.com/doi/abs/10.1142/9789812795915_0034.

[3] R. L. Workman et al. "Review of Particle Physics". In: *PTEP* 2022 (2022), p. 083C01. DOI: 10.1093/ptep/ptac097.

[4] John Ellis, Mary K. Gaillard, and Graham G. Ross. "Search for gluons in e+e- annihilation". In: *Nuclear Physics B* 111.2 (1976), pp. 253–271. ISSN: 0550-3213. DOI: https://doi.org/10.1016/0550-3213(76)90542-3. URL: https://www.sciencedirect.com/science/article/pii/0550321376905423.

[5] W. Bartel et al. "Observation of Planar Three Jet Events in e+ e- Annihilation and Evidence for Gluon Bremsstrahlung". In: *Phys. Lett. B* 91 (1980), pp. 142–147. DOI: 10.1016/0370-2693(80)90680-2.

[6] F. Englert and R. Brout. "Broken Symmetry and the Mass of Gauge Vector Mesons". In: *Phys. Rev. Lett.* 13 (9 Aug. 1964), pp. 321–323. DOI: 10.1103/PhysRevLett.13.321. URL: https://link.aps.org/doi/10.1103/PhysRevLett.13.321.

[7] Peter W. Higgs. "Broken Symmetries and the Masses of Gauge Bosons". In: *Phys. Rev. Lett.* 13 (16 Oct. 1964), pp. 508–509. DOI: 10.1103/PhysRevLett.13.508. URL: https://link.aps.org/doi/10.1103/PhysRevLett.13.508.

[8] G. S. Guralnik, C. R. Hagen, and T. W. B. Kibble. "Global Conservation Laws and Massless Particles". In: *Phys. Rev. Lett.* 13 (20 Nov. 1964), pp. 585–587. DOI: 10.1103/PhysRevLett.13.585. URL: https://link.aps.org/doi/10.1103/PhysRevLett.13.585.

[9] Abdelhak Djouadi. "Le boson de Higgs: La quete de l'origine de la masse". In: *Images de la Physique, CNRS* (Mar. 2008).

[10] B. Hermberg. "Measuring hadronic jets at the ILC". PhD thesis. Universität Hamburg, 2015.

[11] Peisi Huang, Andrew J. Long, and Lian-Tao Wang. "Probing the electroweak phase transition with Higgs factories and gravitational waves". In: *Phys. Rev. D* 94 (7 Oct. 2016), p. 075008. DOI: 10.1103/PhysRevD.94.075008. URL: https://link.aps.org/doi/10.1103/PhysRevD.94.075008.

[12] John Ellis, Mary K. Gaillard, and D.V. Nanopoulos. "A phenomenological profile of the Higgs boson". In: *Nuclear Physics B* 106 (1976), pp. 292–340. ISSN: 0550-3213. DOI: https://doi.org/10.1016/0550-3213(76)90382-5. URL: https://www.sciencedirect.com/science/article/pii/0550321376903825.

[13] John Ellis, Mary K. Gaillard, and Dimitri V. Nanopoulos. "A Historical Profile of the Higgs Boson". In: *The standard theory of particle physics: Essays to celebrate CERN's 60th anniversary*. Ed. by Luciano Maiani and Luigi Rolandi. 2016, pp. 255–274. DOI: 10.1142/9789814733519_0014. arXiv: 1504.07217 [hep-ph].

[14] *SM Higgs Combination*. Tech. rep. Geneva: CERN, 2011. URL: http://cds.cern.ch/record/1370076.

[15] *Combination of the Searches for the Higgs Boson in 1 fb-1 of Data Taken with the ATLAS Detector at 7 TeV Center-of-Mass Energy*. Tech. rep. All figures including auxiliary figures are available at https://atlas.web.cern.ch/Atlas/GROUPS/PHYSICS/CONFNOTES/A
CONF-2011-112. Geneva: CERN, 2011. URL: https://cds.cern.ch/record/1375549.

[16] Georges Aad et al. "Observation of a new particle in the search for the Standard Model Higgs boson with the ATLAS detector at the LHC". In: *Phys. Lett. B* 716 (2012), pp. 1–29. DOI: 10.1016/j.physletb.2012.08.020. arXiv: 1207.7214 [hep-ex].

[17] S. Chatrchyan et al. "Observation of a new boson at a mass of 125 GeV with the CMS experiment at the LHC". In: *Physics Letters B* 716.1 (2012), pp. 30–61. ISSN: 0370-2693. DOI: https://doi.org/10.1016/j.physletb.2012.08.021. URL: https://www.sciencedirect.com/science/article/pii/S0370269312008581.

[18] G. Aad et al. "Measurement of the Higgs boson mass in the H$\to ZZ^* \to 4\ell$ decay channel using 139 fb^{-1} of $\sqrt{s}$=13 TeV pp collisions recorded by the ATLAS detector at the LHC". In: *Physics Letters B* 843 (2023), p. 137880. ISSN: 0370-2693. DOI: https://doi.org/10.1016/j.physletb.2023.137880. URL: https://www.sciencedirect.com/science/article/pii/S0370269323002149.

[19] B. Hermberg. "Measuring hadronic jets at the ILC". PhD thesis. Universität Hamburg, 2015.

[20] F. Bezrukov and M. Shaposhnikov. "Why should we care about the top quark Yukawa coupling?" In: *Journal of Experimental and Theoretical Physics* 120.3 (Mar. 2015), pp. 335–343. ISSN: 1090-6509. DOI: 10.1134/s1063776115030152. URL: http://dx.doi.org/10.1134/S1063776115030152.

[21] Y. Fukuda et al. "Evidence for Oscillation of Atmospheric Neutrinos". In: *Physical Review Letters* 81.8 (Aug. 1998), pp. 1562–1567. DOI: 10.1103/physrevlett.81.1562. URL: https://doi.org/10.1103/physrevlett.81.1562.

[22] V. Khachatryan et al. "Search for lepton-flavour-violating decays of the Higgs boson". In: *Physics Letters B* 749 (2015), pp. 337–362. ISSN: 0370-2693. DOI: https://doi.org/10.1016/j.physletb.2015.07.053. URL: https://www.sciencedirect.com/science/article/pii/S0370269315005638.

[23] R. Frederix et al. "Higgs pair production at the LHC with NLO and parton-shower effects. Higgs pair production at the LHC with NLO and parton-shower effects". In: *Phys. Lett. B* 732 (2014). Comments: 11 pages, 7 figures, version accepted for publication on PLB, pp. 142–149. DOI: 10.1016/j.physletb.2014.03.026. arXiv: 1401.7340. URL: https://cds.cern.ch/record/1645571.

[24] R. L. Workman et al. "Review of Particle Physics". In: *PTEP* 2022 (2022), p. 083C01. DOI: 10.1093/ptep/ptac097.

[25] Bo Andersson et al. "Parton Fragmentation and String Dynamics". In: *Phys. Rept.* 97 (1983), pp. 31–145. DOI: 10.1016/0370-1573(83)90080-7.

[26] G. Marchesini and B. R. Webber. "Monte Carlo Simulation of General Hard Processes with Coherent QCD Radiation". In: *Nucl. Phys. B* 310 (1988), pp. 461–526. DOI: 10.1016/0550-3213(88)90089-2.

[27] *Convention for the establishment of a European organization for nuclear research: Paris, 1st July, 1953 : as amended. Convention pour l'établissement d'une Organisation européenne pour la Recherche nucléaire. Paris, le 1er juillet 1953 : telle qu'elle a été modifiée*. Geneva: CERN, 1971. URL: https://cds.cern.ch/record/330625.

[28] Ewa Lopienska. "The CERN accelerator complex, layout in 2022. Complexe des accélérateurs du CERN en janvier 2022". In: (2022). General Photo. URL: https://cds.cern.ch/record/2800984.

[29] *The Phase-2 Upgrade of the CMS Muon Detectors*. Tech. rep. This is the final version, approved by the LHCC. Geneva: CERN, 2017. URL: https://cds.cern.ch/record/2283189.

[30] Matthias Schott and Monica Dunford. "Review of single vector boson production in pp collisions at $\sqrt{s} = 7$ TeV". In: *Eur. Phys. J. C* 74 (2014), p. 2916. DOI: 10.1140/epjc/s10052-014-2916-1. arXiv: 1405.1160 [hep-ex].

[31] *ATLAS magnet system: Technical Design Report, 1*. Technical design report. ATLAS. Geneva: CERN, 1997. DOI: 10.17181/CERN.9O5C.VDTM. URL: https://cds.cern.ch/record/338080.

[32] *ATLAS inner detector: Technical Design Report, 1*. Technical design report. ATLAS. Geneva: CERN, 1997. URL: https://cds.cern.ch/record/331063.

[33] ATLAS Collaboration. "Experiment Briefing: Keeping the ATLAS Inner Detector in perfect alignment". General Photo. 2020. URL: https://cds.cern.ch/record/2723878.

[34] Joao Pequenao. "Computer Generated image of the ATLAS calorimeter". 2008. URL: https://cds.cern.ch/record/1095927.

[35] *ATLAS liquid-argon calorimeter: Technical Design Report*. Technical design report. ATLAS. Geneva: CERN, 1996. DOI: 10.17181/CERN.FWRW.FOOQ. URL: https://cds.cern.ch/record/331061.

[36] *ATLAS tile calorimeter: Technical Design Report*. Technical design report. ATLAS. Geneva: CERN, 1996. DOI: 10.17181/CERN.JRBJ.7O28. URL: https://cds.cern.ch/record/331062.

[37] *ATLAS muon spectrometer: Technical Design Report*. Technical design report. ATLAS. Geneva: CERN, 1997. URL: https://cds.cern.ch/record/331068.

[38] *Technical Design Report for the Phase-II Upgrade of the ATLAS TDAQ System*. Tech. rep. Geneva: CERN, 2017. DOI: 10.17181/CERN.2LBB.4IAL. URL: https://cds.cern.ch/record/2285584.

[39] Tommaso Colombo and (on behalf of the ATLAS Collaboration). "Data-flow Performance Optimisation on Unreliable Networks: the ATLAS Data-Acquisition Case". In: *Journal of Physics: Conference Series* 608.1 (Apr. 2015), p. 012005. DOI: 10.1088/1742-6596/608/1/012005. URL: https://dx.doi.org/10.1088/1742-6596/608/1/012005.

[40] ATLAS Collaboration. *Luminosity determination in pp collisions at* $\sqrt{s} = 13$ *TeV using the ATLAS detector at the LHC*. 2022. arXiv: 2212.09379 [hep-ex].

[41] ATLAS collaboration. *Twiki*. URL: https://twiki.cern.ch/twiki/bin/view/AtlasPublic/LuminosityPublicResultsRun2 (visited on 09/07/2023).

[42] F. Zimmermann. "HL-LHC: parameter space, constraints, and possible options". In: *LHC Performance Workshop*. Apr. 2011.

[43] HL-LHC collaboration. *High Luminosity LHC Project*. URL: https://hilumilhc.web.cern.ch/ (visited on 09/08/2023).

[44] *The Phase-2 Upgrade of the CMS Endcap Calorimeter*. Tech. rep. Geneva: CERN, 2017. DOI: 10.17181/CERN.IV8M.1JY2. URL: https://cds.cern.ch/record/2293646.

[45] D Contardo et al. *Technical Proposal for the Phase-II Upgrade of the CMS Detector*. Tech. rep. Upgrade Project Leader Deputies: Lucia Silvestris (INFN-Bari), Jeremy Mans (University of Minnesota) Additional contacts: Lucia.Silvestris@cern.ch, Jeremy.Mans@cern.ch. Geneva, 2015. DOI: 10.17181/CERN.VU8I.D59J. URL: https://cds.cern.ch/record/2020886.

[46] *Technical Design Report for the ATLAS Inner Tracker Strip Detector*. Tech. rep. Geneva: CERN, 2017. URL: https://cds.cern.ch/record/2257755.

[47] *Technical Design Report for the ATLAS Inner Tracker Pixel Detector*. Tech. rep. Geneva: CERN, 2017. DOI: 10.17181/CERN.FOZZ.ZP3Q. URL: https://cds.cern.ch/record/2285585.

[48] ATLAS Collaboration. *Technical Design Report: A High-Granularity Timing Detector for the ATLAS Phase- II Upgrade*. June 2020.

[49] Allison Mccarn Deiana. *Development of the ATLAS Liquid Argon Calorimeter Readout Electronics for the HL-LHC*. Tech. rep. Geneva: CERN, 2023. DOI: 10.22323/1.414.0668. URL: http://cds.cern.ch/record/2841487.

[50] *Technical Design Report for the Phase-II Upgrade of the ATLAS Tile Calorimeter*. Tech. rep. Geneva: CERN, 2017. URL: https://cds.cern.ch/record/2285583.

[51] *Technical Design Report for the Phase-II Upgrade of the ATLAS Muon Spectrometer*. Tech. rep. Geneva: CERN, 2017. URL: https://cds.cern.ch/record/2285580.

[52] ATLAS Collaboration. "ATLAS Feature: A new ATLAS for the high-luminosity era". General Photo. 2023. URL: https://cds.cern.ch/record/2846341.

[53] Rudolf Frühwirth and Are Strandlie. "Secondary Vertex Reconstruction". In: *Pattern Recognition, Tracking and Vertex Reconstruction in Particle Detectors*. Cham: Springer International Publishing, 2021, pp. 159–165. ISBN: 978-3-030-65771-0. DOI: 10.1007/978-3-030-65771-0_9. URL: https://doi.org/10.1007/978-3-030-65771-0_9.

[54] ATLAS Collaboration. *Technical Design Report for the ATLAS Inner Tracker Strip Detector*. Apr. 2017.

[55] Verlaat, Ann Van Lysebetten, and Martinus van Beuzekom. "CO2 cooling for HEP experiments". In: 2008.

[56] G. Pellegrini et al. "Technology developments and first measurements of Low Gain Avalanche Detectors (LGAD) for high energy physics applications". In: *Nuclear Instruments and Methods in Physics Research Section A: Accelerators, Spectrometers, Detectors and Associated Equipment* 765 (2014). HSTD-9 2013 - Proceedings of the 9th International "Hiroshima" Symposium on Development and Application of Semiconductor Tracking Detectors, pp. 12–16. ISSN: 0168-9002. DOI: https://doi.org/10.1016/j.nima.2014.06.008. URL: https://www.sciencedirect.com/science/article/pii/S0168900214007128.

[57] Christophe de La Taille et al. "ALTIROC0, a 20 pico-second time resolution ASIC for the ATLAS High Granularity Timing Detector (HGTD)". In: *Topical Workshop on Electronics for Particle Physics*. Vol. TWEPP-17. Santa Cruz, United States, Sept. 2017, p. 006. DOI: 10.22323/1.313.0006. URL: https://hal.science/hal-02058308.

[58] D. Boumediene et al. "Measurement of single event effect cross section induced by monoenergetic protons on a 130 nm ASIC". In: *Journal of Instrumentation* 17.02 (Feb. 2022), P02007. DOI: 10.1088/1748-0221/17/02/P02007. URL: https://dx.doi.org/10.1088/1748-0221/17/02/P02007.

[59] Centre Antoine Lacassagne. *Institut Méditerranéen de protonthérapie*. URL: https://www.protontherapie.fr/presentation-de-limpt/.

[60] S. Kulis. "Single Event Effects mitigation with TMRG tool". In: *Journal of Instrumentation* 12.01 (Jan. 2017), p. C01082. DOI: 10.1088/1748-0221/12/01/C01082. URL: https://dx.doi.org/10.1088/1748-0221/12/01/C01082.

[61] G. Balbi et al. "Measurements of Single Event Upset in ATLAS IBL". In: *Journal of Instrumentation* 15.06 (June 2020), P06023. DOI: 10.1088/1748-0221/15/06/P06023. URL: https://dx.doi.org/10.1088/1748-0221/15/06/P06023.

[62] M Menouni et al. "SEU tolerant memory design for the ATLAS pixel readout chip". In: *Journal of Instrumentation* 8.02 (Feb. 2013), p. C02026. DOI: 10.1088/1748-0221/8/02/C02026. URL: https://dx.doi.org/10.1088/1748-0221/8/02/C02026.

[63] *X-RAD® iR-160 Biological X-ray Irradiator manual*. URL: https://www.accela.eu/files/products/192/brozura-160-series.pdf.

[64] ATLAS collaboration. *Twiki*. URL: https://twiki.cern.ch/twiki/bin/view/AtlasPublic/HGTDPublicPlots#ALTIROC2_MODULE_plots (visited on 10/29/2023).

[65] L.A. Beresford et al. "Destructive breakdown studies of irradiated LGADs at beam tests for the ATLAS HGTD". In: *Journal of Instrumentation* 18.07 (July 2023), P07030. DOI: 10.1088/1748-0221/18/07/P07030. URL: https://dx.doi.org/10.1088/1748-0221/18/07/P07030.

[66] *Improved electron reconstruction in ATLAS using the Gaussian Sum Filter-based model for bremsstrahlung*. Tech. rep. All figures including auxiliary figures are available at https://atlas.web.cern.ch/Atlas/GROUPS/PHYSICS/CONFNOTES/ATLAS-CONF-2012-047. Geneva: CERN, 2012. URL: https://cds.cern.ch/record/1449796.

[67] Morad Aaboud et al. "Electron reconstruction and identification in the ATLAS experiment using the 2015 and 2016 LHC proton-proton collision data at $\sqrt{s} = 13$ TeV". In: *Eur. Phys. J. C* 79.8 (2019), p. 639. DOI: 10.1140/epjc/s10052-019-7140-6. arXiv: 1902.04655 [physics.ins-det].

[68] *Identification of the Hadronic Decays of Tau Leptons in 2012 Data with the ATLAS Detector*. Tech. rep. All figures including auxiliary figures are available at https://atlas.web.cern.ch/A CONF-2013-064. Geneva: CERN, 2013. URL: https://cds.cern.ch/record/1562839.

[69] *Identification of hadronic tau lepton decays using neural networks in the ATLAS experiment*. Tech. rep. All figures including auxiliary figures are available at https://atlas.web.cern.ch/Atla PHYS-PUB-2019-033. Geneva: CERN, 2019. URL: https://cds.cern.ch/record/2688062.

[70] A. Tumasyan et al. "Identification of hadronic tau lepton decays using a deep neural network". In: *Journal of Instrumentation* 17.07 (July 2022), P07023. DOI: 10.1088/1748-0221/17/07/P07023. URL: https://dx.doi.org/10.1088/1748-0221/17/07/P07023.

[71] Ariel Schwartzman. "Jet energy calibration at the LHC". In: *Int. J. Mod. Phys. A* 30 (2015). Ed. by G. Dissertori. Article submitted to the International Journal of Modern Physics A (IJMPA) as part of the special issue on the Jet Measurements at the LHC, p. 1546002. DOI: 10.1142/S0217751X15460021. arXiv: 1509.05459. URL: https://cds.cern.ch/record/2053870.

[72] Connelly, Ian. "Performance and calibration of b-tagging with the ATLAS experiment at LHC Run-2". In: *EPJ Web Conf.* 164 (2017), p. 07025. DOI: 10.1051/epjconf/201716407025. URL: https://doi.org/10.1051/epjconf/201716407025.

[73] *Optimisation and performance studies of the ATLAS b-tagging algorithms for the 2017-18 LHC run*. Tech. rep. All figures including auxiliary figures are available at https://atlas.web.cern.ch/Atlas/GROUPS/PHYSICS/PUBNOTES/ATL-PHYS-PUB-2017-013. Geneva: CERN, 2017. URL: https://cds.cern.ch/record/2273281.

[74] *Secondary vertex finding for jet flavour identification with the ATLAS detector*. Tech. rep. All figures including auxiliary figures are available at https://atlas.web.cern.ch/Atlas/GROUPS/ PHYS-PUB-2017-011. Geneva: CERN, 2017. URL: https://cds.cern.ch/record/2270366.

[75] *Topological b-hadron decay reconstruction and identification of b-jets with the JetFitter package in the ATLAS experiment at the LHC*. Tech. rep. All figures including auxiliary figures are available at https://atlas.web.cern.ch/Atlas/GROUPS/PHYSICS/PUBNOTES/ATL PHYS-PUB-2018-025. Geneva: CERN, 2018. URL: https://cds.cern.ch/record/2645405.

[76] Georges Aad et al. "ATLAS b-jet identification performance and efficiency measurement with $t\bar{t}$ events in pp collisions at $\sqrt{s} = 13$ TeV". In: *Eur. Phys. J. C* 79.11 (2019), p. 970. DOI: 10.1140/epjc/s10052-019-7450-8. arXiv: 1907.05120 [hep-ex].

[77] ATLAS collaboration. *Twiki: Good Run Lists fro Analysis Run2*. URL: https://twiki.cern.ch/twiki/bin/view/AtlasProtected/GoodRunListsForAnalysisRun2 (visited on 10/03/2023).

[78] ATLAS collaboration. *Twiki: ExtendedPileupReweighting*. URL: https://twiki.cern.ch/twiki/bin/viewauth/AtlasProtected/ExtendedPileupReweighting (visited on 10/30/2023).

[79] *ATLAS Pythia 8 tunes to 7 TeV data*. Tech. rep. All figures including auxiliary figures are available at https://atlas.web.cern.ch/Atlas/GROUPS/PHYSICS/PUBNOTES/ATL-PHYS-PUB-2014-021. Geneva: CERN, 2014. URL: https://cds.cern.ch/record/1966419.

[80] Richard D. Ball et al. "Parton distributions for the LHC run II". In: *Journal of High Energy Physics* 4 (Apr. 2015). DOI: 10.1007/jhep04(2015)040. URL: https://doi.org/10.1007%2Fjhep04%282015%29040.

[81] David J. Lange. "The EvtGen particle decay simulation package". In: *Nuclear Instruments and Methods in Physics Research Section A: Accelerators, Spectrometers, Detectors and Associated Equipment* 462.1 (2001). BEAUTY2000, Proceedings of the 7th Int. Conf. on B-Physics at Hadron Machines, pp. 152–155. ISSN: 0168-9002. DOI: https://doi.org/10.1016/S0168-9002(01)00089-4. URL: https://www.sciencedirect.com/science/article/pii/S0168900201000894.

[82] Coll ATLAS et al. *The simulation principle and performance of the ATLAS fast calorimeter simulation FastCaloSim*. Tech. rep. All figures including auxiliary figures are available at https://atlas.web.cern.ch/Atlas/GROUPS/PHYSICS/PUBNOTES/ATL-PHYS-PUB-2010-013. Geneva: CERN, 2010. URL: https://cds.cern.ch/record/1300517.

[83] J. Alwall et al. "The automated computation of tree-level and next-to-leading order differential cross sections, and their matching to parton shower simulations". In: *Journal of High Energy Physics* 2014.7 (). DOI: 10.1007/jhep07(2014)079. URL: https://doi.org/10.1007%2Fjhep07%282014%29079.

[84] T Gleisberg et al. "Event generation with SHERPA 1.1". In: *Journal of High Energy Physics* 2009.02 (), pp. 007–007. DOI: 10.1088/1126-6708/2009/02/007. URL: https://doi.org/10.1088%2F1126-6708%2F2009%2F02%2F007.

[85] Stefano Frixione, Giovanni Ridolfi, and Paolo Nason. "A positive-weight next-to-leading-order Monte Carlo for heavy flavour hadroproduction". In: *Journal of High Energy Physics* 2007.09 (), pp. 126–126. DOI: 10.1088/1126-6708/2007/09/126. URL: https://doi.org/10.1088%2F1126-6708%2F2007%2F09%2F126.

[86] Torbjörn Sjöstrand, Stephen Mrenna, and Peter Skands. "A brief introduction to PYTHIA 8.1". In: *Computer Physics Communications* 178.11 (), pp. 852–867. DOI: 10.1016/j.cpc.2008.01.036. URL: https://doi.org/10.1016%2Fj.cpc.2008.01.036.

[87] ATLAS collaboration. *Twiki: Heavy Flavor Overlap Removal Tool in Run2*. URL: https://twiki.cern.ch/twiki/bin/view/Sandbox/HeavyFlavorOverlapRemovalinRun2 (visited on 10/30/2023).

[88] Stefano Catani et al. "QCD Matrix Elements + Parton Showers". In: *Journal of High Energy Physics* 11 (Nov. 2001), pp. 063–063. DOI: 10.1088/1126-6708/2001/11/063. URL: https://doi.org/10.1088%2F1126-6708%2F2001%2F11%2F063.

[89] Stefan Höche et al. "A critical appraisal of NLO+PS matching methods". In: *Journal of High Energy Physics* 2012.9 (). DOI: 10.1007/jhep09(2012)049. URL: https://doi.org/10.1007%2Fjhep09%282012%29049.

[90] Federico Buccioni et al. "OpenLoops 2". In: *The European Physical Journal C* 79.10 (). DOI: 10.1140/epjc/s10052-019-7306-2. URL: https://doi.org/10.1140%2Fepjc%2Fs10052-019-7306-2.

[91] Rustem Ospanov, Rhys Thomas Roberts, and Terry Richard Wyatt. *Tagging non-prompt electrons and muons*. Tech. rep. Geneva: CERN, 2016. URL: https://cds.cern.ch/record/2220954.

[92] ATLAS collaboration. *Twiki: SUSYSystematicUncertaintiesRun2*. URL: https://twiki.cern.ch/twiki/bin/viewauth/AtlasProtected/SUSYSystematicUncertaintiesRun2#Missing_Et (visited on 09/28/2023).

[93] ATLAS collaboration. *Twiki: Latest Run 2 Electron Recommendations*. URL: https://twiki.cern.ch/twiki/bin/view/AtlasProtected/LatestRecommendationsElectronIDRun2 (visited on 09/28/2023).

[94] ATLAS collaboration. *Twiki: JetEtMiss Recommendations for Release 21 MC16 (2015-2018)*. URL: https://twiki.cern.ch/twiki/bin/viewauth/AtlasProtected/JetEtmissRecommendationsR21 (visited on 09/28/2023).

[95] ATLAS collaboration. *Twiki: EtmissRecommendationsFullRun2*. URL: https://twiki.cern.ch/twiki/bin/view/AtlasProtected/EtmissRecommendationsFullRun2#Track_Soft_Term_Systematics (visited on 09/28/2023).

[96] ATLAS collaboration. *Twiki: Tau Recommendations for Release 21*. URL: https://twiki.cern.ch/twiki/bin/view/AtlasProtected/TauRecommendationsR21#Summer_2019_Recommendations (visited on 09/28/2023).

[97] *Luminosity determination in pp collisions at $\sqrt{s} = 13$ TeV using the ATLAS detector at the LHC*. Tech. rep. All figures including auxiliary figures are available at https://atlas.web.cern.ch/Atlas/GROUPS/PHYSICS/CONFNOTES/ATLAS-CONF-2019-021. Geneva: CERN, 2019. URL: https://cds.cern.ch/record/2677054.

[98] ATLAS collaboration. *Twiki: TriggerRecommendationsForAnalysisGroupsFullRun2*. URL: https://twiki.cern.ch/twiki/bin/view/Atlas/Trigger%5C%20Recommendations%5C%20ForAnalysis%5C%20GroupsFullRun2 (visited on 09/28/2023).

[99] ATLAS collaboration. *Twiki: LHC-HH sub group*. URL: https://twiki.cern.ch/twiki/bin/view/LHCPhysics/LHCHWGHH?redirectedfrom=LHCPhysics.LHCHXSWGHH (visited on 09/28/2023).

[100] Armen Tumasyan et al. "Search for Higgs boson pairs decaying to WW*WW*, WW*$\tau\tau$, and $\tau\tau\tau\tau$ in proton-proton collisions at $\sqrt{s} = 13$ TeV". In: *JHEP* 07 (2023), p. 095. DOI: 10.1007/JHEP07(2023)095. arXiv: 2206.10268 [hep-ex].

[101] G. Aad et al. "Constraints on the Higgs boson self-coupling from single- and double-Higgs production with the ATLAS detector using pp collisions at s=13 TeV". In: *Physics Letters B* 843 (2023), p. 137745. ISSN: 0370-2693. DOI: https://doi.org/10.1016/j.physletb.2023.137745. URL: https://www.sciencedirect.com/science/article/pii/S0370269323000795.

[102] *HL-LHC prospects for the measurement of Higgs boson pair production in the $b\bar{b}b\bar{b}$ final state and combination with the $b\bar{b}\gamma\gamma$ and $b\bar{b}\tau^+\tau^-$ final states at the ATLAS experiment*. Tech. rep. All figures including auxiliary figures are available at https://atlas.web.cern.ch/Atlas/GRO PHYS-PUB-2022-053. Geneva: CERN, 2022. URL: https://cds.cern.ch/record/2841244.

[103] S. Ali et al. "Performance in beam tests of carbon-enriched irradiated Low Gain Avalanche Detectors for the ATLAS High Granularity Timing Detector". In: *Journal of Instrumentation* 18.05 (May 2023), P05005. DOI: 10.1088/1748-0221/18/05/P05005. URL: https://dx.doi.org/10.1088/1748-0221/18/05/P05005.

Appendix

.1 Training of specific BDTs

.1.1 Variables distributions

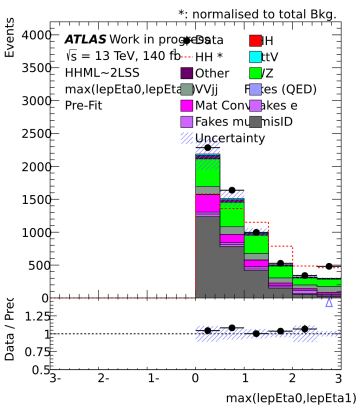

(a) $|\eta_0 - \eta_1|$

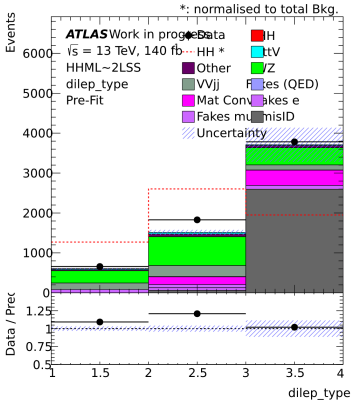

(b) Dilepton type

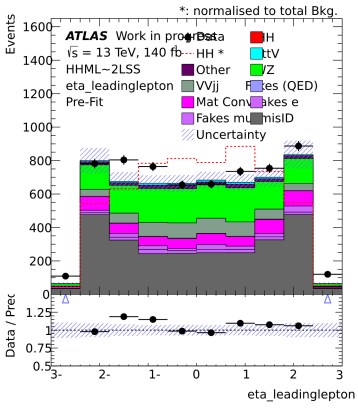

(c) $|\eta_0|$

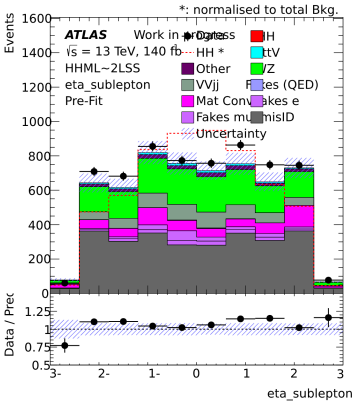

(d) $|\eta_1|$

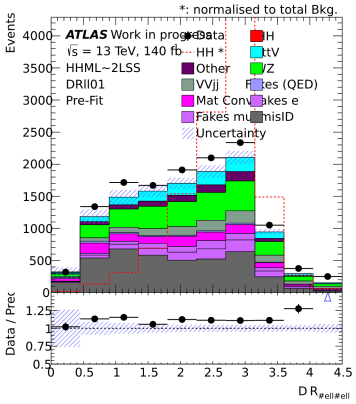

(e) Distance between the two leptons

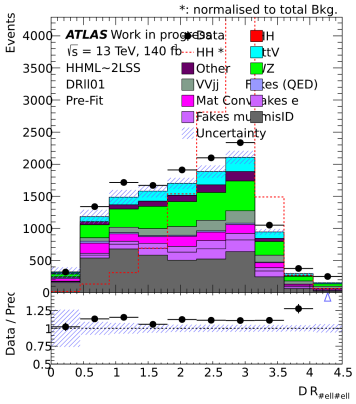

(f) Distance between the two leptons

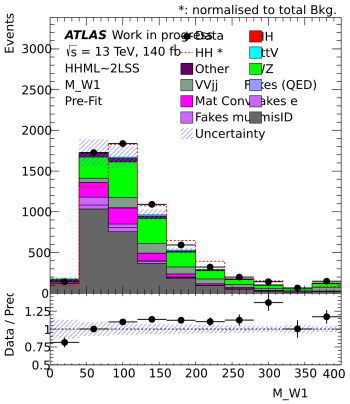

(g) The transverse mass of the leptonically decay W boson reconstructed by the MET with subleading lepton

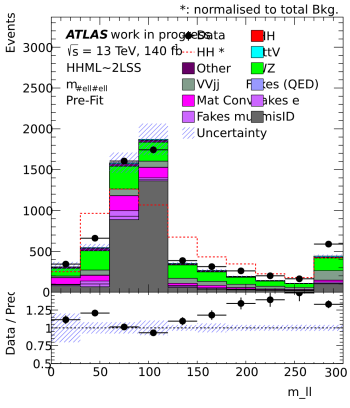

(h) Invariante mass of the two leptons

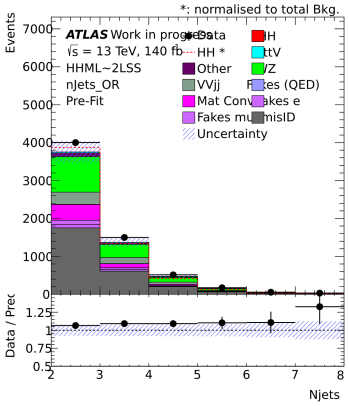

(i) Number of jets

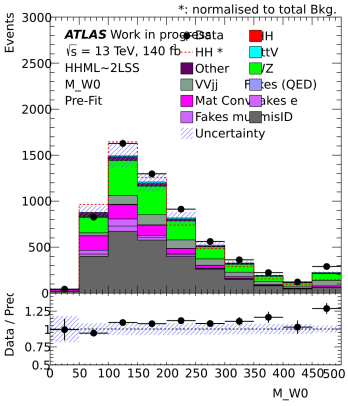

(j) The transverse mass of the leptonically decay W boson reconstructed by the MET with leading lepton

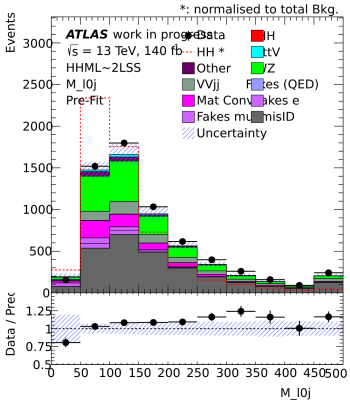

(k) Mass of the leading lepton and its closest jet

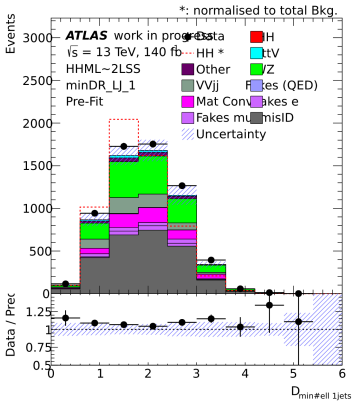

(l) Minimal distance of the subleading lepton and its closest jet

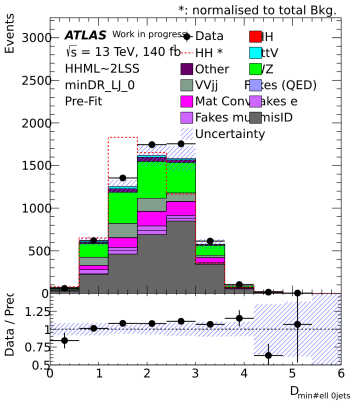

(m) Minimal distance of the leading lepton and its closest jet

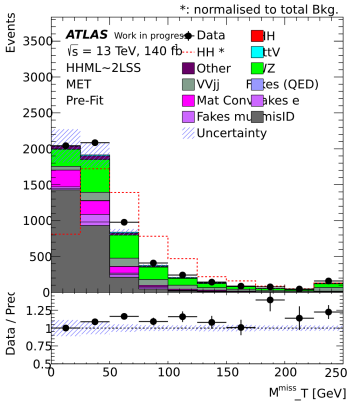

(n) Missing transverse energy

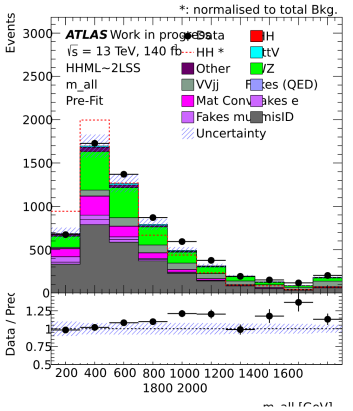

(o) Mass of all objects

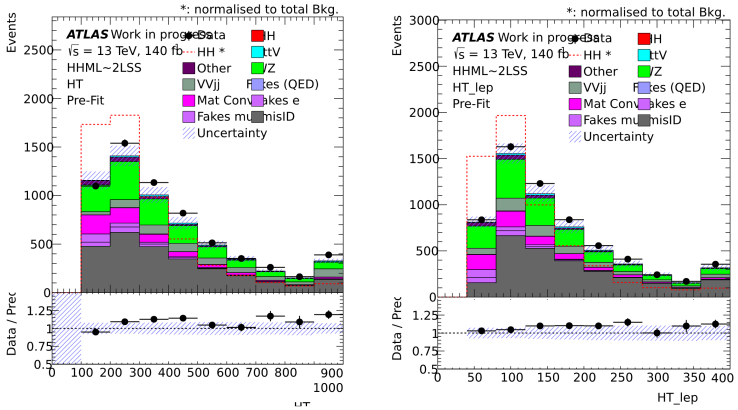

(p) HT (q) HT_{lep}

Figure 24: Distribution of each discriminating variable for all backgrounds, the signal and the data (black dots). The ratio Data VS prediction are shown below each distribution.

.1.2 Ranking and separation power

BDT	V+jets VS HH		$t\bar{t}$ VS HH		VV VS HH	
Variable	Separation power	Rank	Separation power	Rank	Separation power	Rank
$M_{l_1 j}$	3.553e-02	10	7.251e-02	4	5.666e-02	10
$M_{l_0 j}$	3.914e-02	9	6.595e-02	6	6.292e-02	5
$M_{\ell\ell}$	4.227e-02	8	5.908e-02	7	4.623e-02	14
M_{all}	/	/	4.916e-02	10	5.973e-02	7
M^T_{W0}	2.650e-02	15	5.158e-02	9	4.551e-02	15
M^T_{W1}	3.199e-02	12	4.732e-02	13	5.209e-02	11
HT_{lep}	3.523e-02	11	4.825e-02	11	4.294e-02	17
HT	7.779e-02	5	4.791e-02	12	5.857e-02	8
N_{jets}	4.727e-02	7	5.436e-02	8	6.008e-02	6
E_T^{miss}	2.712e-02	14	4.428e-02	14	4.646e-02	13
Dilep_type	6.357e-02	6	/	/	4.422e-02	16
$\|\eta_0\|$	1.001e-01	3	7.540e-02	2	8.182e-02	3
$\|\eta_1\|$	9.11e-02	4	6.766e-02	5	7.792e-02	4
$\Delta R_{min\ell jets}$	1.172e-01	2	8.928e-02	1	1.069e-01	1
$\Delta R_{min\ell 1 jets}$	2.610e-02	16	3.929e-02	15	5.672e-02	9
$\Delta R_{min\ell 0 jets}$	3.112e-02	13	2.978e-02	16	4.673e-02	12
$\Delta R_{\ell\ell}$	1.178e-01	1	7.296e-02	3	8.408e-02	2
Total_Charge	/	/	/	/	3.983e-02	18

Table 12: Variable ranking table obtained for the training of each specific BDT with their corresponding separation power

.2 Correlations matrix

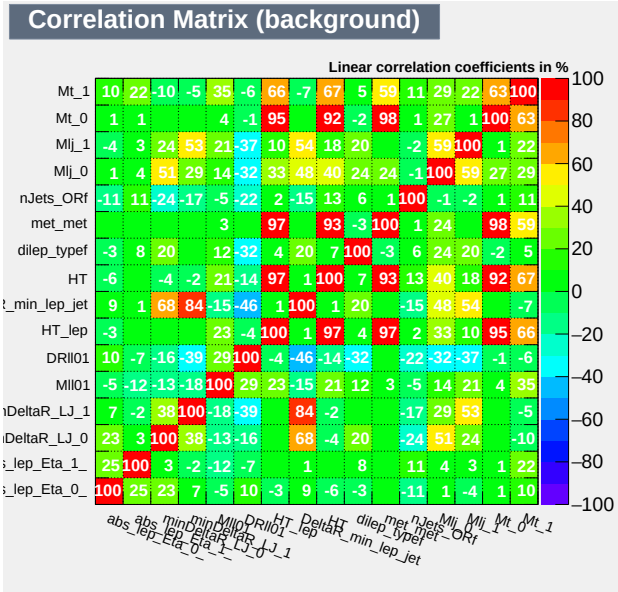

(a) V+jets specific BDT training - background

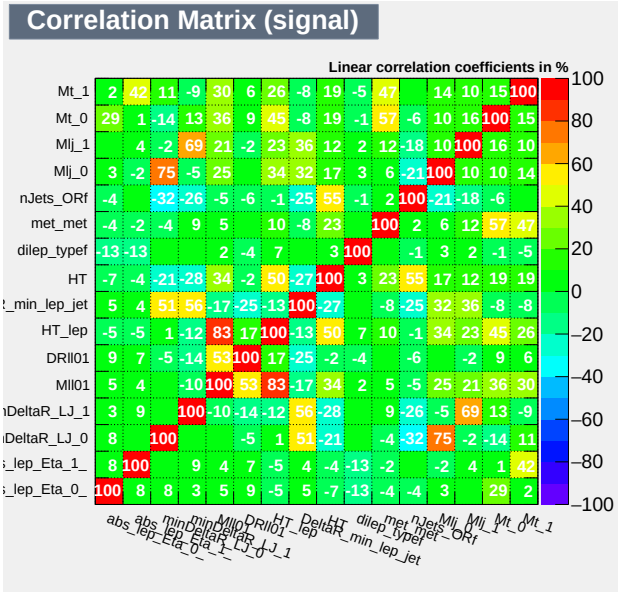

(b) V+jets specific BDT training - signal

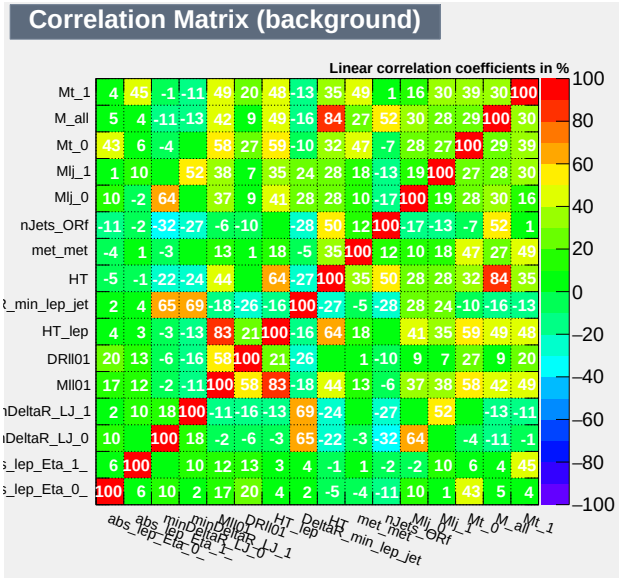

(c) tt specific BDT training - background

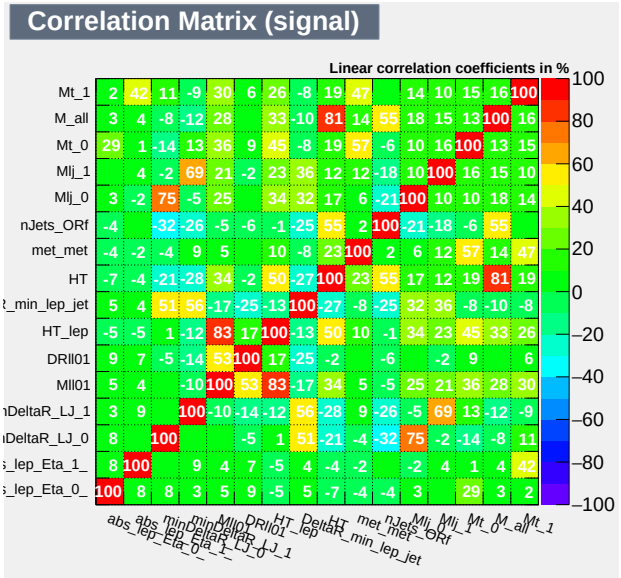

(d) tt specific BDT training - signal

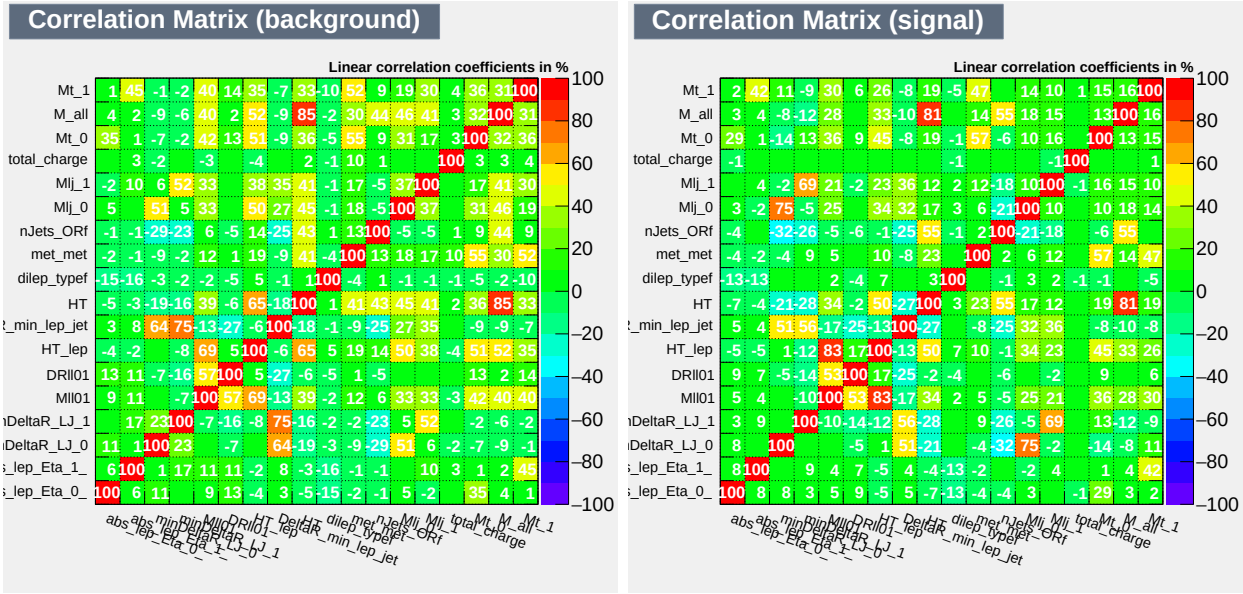

(e) VV specific BDT training - background

(f) VV specific BDT training - signal

Figure 25: Correlation matrices of the discriminating variables used as inputs for the training of the three specific BDTs. The impact over the background is shown or left, and on right for the signal.

.3 MC generators

Process	Generator	ME order	Parton shower	PDF	Tune
$t\bar{t}$ W	Sherpa 2.2.10	NLO	Sherpa	NNPDF3.0 NNLO	Sherpa default
	(MG5_aMC)	(NLO)	(Pythia 8)	(NNPDF3.0 NLO)	(A14)
$t\bar{t}t\bar{t}$	MG5_aMC	NLO	Pythia 8	NNPDF3.1 NLO	A14
	(Sherpa 2.2.10)	(NLO)	(Sherpa)	(NNPDF3.0 NNLO)	(Sherpa default)
$t\bar{t}$ H	Powheg-BOX	NLO	Pythia 8	NNPDF3.0 NLO	A14
	(Powheg-BOX)	(NLO)	(Herwig7)	(NNPDF3.0 NLO)	(H7-UE-MMHT)
	(MG5_aMC)	(NLO)	(Pythia 8)	(NNPDF3.0 NLO)	(A14)
$t\bar{t}$ ($Z/\gamma^* \to l^+l^-$)	Sherpa 2.2.11	NLO	Sherpa	NNPDF3.0 NNLO	Sherpa default
	(MG5_aMC)	(NLO)	(Pythia 8)	(NNPDF3.0 NLO)	(A14)
$t\bar{t} \to W^+bW^-\bar{b}l^+l^-$	MG5_aMC	LO	Pythia 8	NNPDF3.0 LO	A14
$t(Z/\gamma^*)$	MG5_aMC	NLO	Pythia 8	NNPDF2.3 LO	A14
$tW(Z/\gamma^*)$	MG5_aMC	NLO	Pythia 8	NNPDF2.3 LO	A14
$t\bar{t}$ W^+W^-	MG5_aMC	LO	Pythia 8	NNPDF2.3 LO	A14
$t\bar{t}$	Powheg-BOX	NLO	Pythia 8	NNPDF3.0 NLO	A14
	(Powheg-BOX)	NLO	(Herwig7.1.3)	(NNPDF3.0 NLO)	(H7-UE-MMHT)
$t\bar{t}$ t	MG5_aMC	LO	Pythia 8	NNPDF2.3 LO	A14
s-, t-channel, Wt single top	Powheg-BOX	NLO	Pythia 8	NNPDF3.0 NLO	A14
VV, $qqVV$, $lowm_{\ell\ell}$, VVV	Sherpa 2.2.2	NLO	Sherpa	NNPDF3.0 NNLO	Sherpa default
$Z \to l^+l^-$	Sherpa 2.2.1	NLO	Sherpa	NNPDF3.0 NLO	Sherpa default
$Z \to l^+l^-$ (matCO)	Powheg-BOX	NLO	Pythia 8	CTEQ6L1 NLO	A14
$Z \to l^+l^-$+(γ*)	Powheg-BOX	NLO	Pythia 8	CTEQ6L1 NLO	A14
W+jets	Sherpa 2.2.1	NLO	Sherpa	NNPDF3.0 NLO	Sherpa default
VH	Powheg-BOX	NLO	Pythia 8	NNPDF3.0 NLO	A14

.4 Experimental systematics

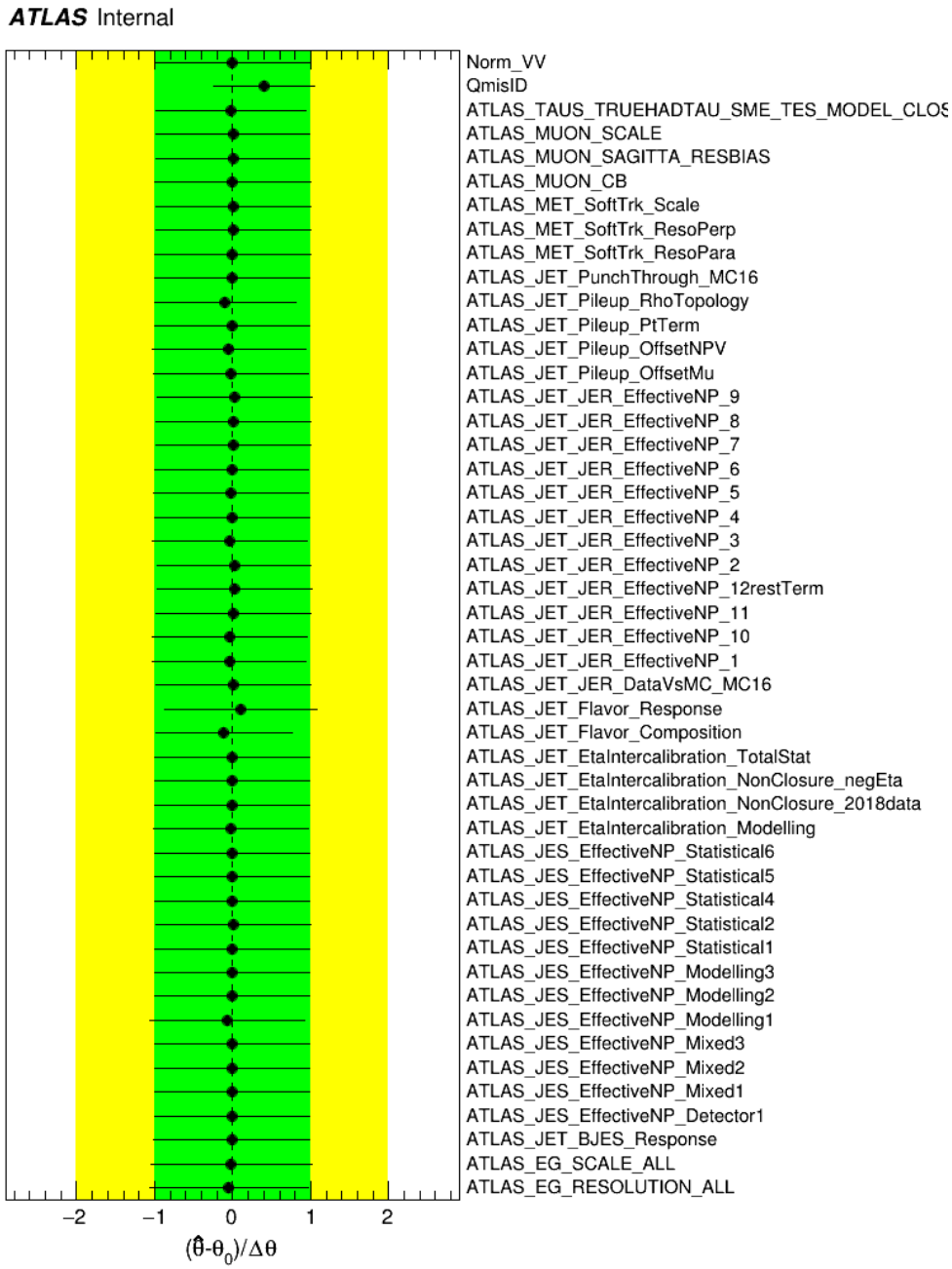

Figure 26: List and importance of the nuisance Parameters

Résumé en Francais

Dans la recherche de compréhension de notre univers, la question de la composition de la matière reste l'une des plus importantes. Sorti d'une vision primaire de la matière par les quatre éléments (feu, terre, eau, air), l'idée de composants fondamentaux apparaît au début du XIX^{e} siècle. À la fin de ce siècle, deux expériences majeures, respectivement réalisées par E. Goldstein et J.J Thomson, prouvent l'existence de deux particules chargées connues aujourd'hui comme étant le proton et l'électron. Suite à la Seconde Guerre mondiale, les physiciens ont construit les premiers accélérateurs à particules afin de caractériser le monde de l'infiniment petit. Dès lors, de multiples théories et découvertes se succèdent jusqu'en 1975, avec la présentation du Modèle Standard. Ce dernier reste, à ce jour la principale théorie de la composition de la matière, capable d'expliquer bon nombre de phénomènes physiques.

Résumé Chapitre 1: Le contexte théorique

Le Modèle Standard se compose de deux groupes de particules: les fermions et les bosons. Les fermions sont formés de trois générations de particules (up u, down d, electron e), (charm c, strange s, muon μ) et (top t, bottom b, tau τ) ayant les mêmes propriétés à l'exception de leur masse. Seul la première génération des fermions, la plus légère, est stable et compose la matière qui nous entoure. L'autre groupe, les bosons, se composent des bosons de gauges, i.e. les particules vecteurs des trois interactions fondamentales (électromagnétique, faible et forte), ainsi que de la particule responsable de la masse nommée le boson de Higgs. Cette dernière particule représente aujourd'hui un des sujets principaux de recherche en physique fondamentale et permet d'expliquer que certaines particules du Modèle Standard soient massives et d'autres non.
Postulé en 1964, le boson de Higgs ou boson BEH (Brout, Englert et Higgs) est le reflet de l'existence d'un champ dans lequel baigne l'ensemble de l'Univers. Ce dernier appelé champ

de Higgs donnerait une masse à toutes particules au travers d'un mécanisme: le mécanisme de Higgs, conséquence directe de la brisure spontanée de la symétrie électrofaible. Cette théorie fut confirmée par l'observation en 2012 d'une particule ayant une masse de 125 GeV, reconnue comme le boson de Higgs. Dès lors, les physiciens tentent de prouver les différentes propriétés que l'on confère à cette nouvelle particule.
Selon la théorie des champs, le champ de Higgs peut être décrit mathématiquement par le Lagrangian suivant:

$$L = (D_\mu \Phi)^\dagger D^\mu \Phi - V(\Phi)$$

Le premier terme correspond à l'énergie cinétique et le second correspond au potentiel du champs de Higgs. Une fois la brisure de symétrie électrofaible qui permet d'expliquer le problème de masse entre les bosons W, Z et le photon, le potentiel de ce champ de Higgs a une forme très particulière, dite en "chapeau mexicain" et peut s'exprimer de la façon suivante:

$$V = \frac{1}{2} m_h^2 h^2 + \frac{1}{6} \lambda_{hhh} h^3 + \frac{1}{24} \lambda_{hhhh} h^4 + \mathcal{O}(h)$$

avec ν la valeur moyenne du champs de Higgs dans le vide prédite à 246 GeV. Le premier terme correspond à la valeur de la masse du boson de Higgs. Le second terme et le troisième terme sont respectivement le couplage trilinéaire et le couplage quadrilinéaire. La mesure de l'autocouplage, c'est à dire du couplage trilinéaire, est le seul moyen expérimental connu et accessible de vérifier la valeur hypothétique du potentiel de Higgs dans le vide, par conséquent de la forme du potentiel de Higgs.

Résumé du chapitre 2: La phénoménologie

Au LHC, cet autocouplage est accessible au travers de la production d'une paire de Higgs, générée majoritairement par les deux modes de production suivants: la fusion de gluons et la fusion de bosons. La figure **??** présente les diagrammes de Feynman des deux modes de production majoritaires du di-Higgs au LHC.
La valeur de cet autocouplage est liée directement à la section efficace du di-Higgs au sein du LHC comme le démontre la figure 28.
Ainsi, connaissant cette relation, la mesure de l'autocouplage se fait grâce à la mesure de la section efficace du di-Higgs au LHC. Cependant, la production de di-Higgs est un phénomène très rare au LHC, en effet la section efficace attendue du di-Higgs par fusion de gluons est de 30 fb alors que la section efficace totale du Higgs est de 57 pb. Il y a une chance sur 2000 d'observer un Higgs avec un autocouplage.

(a) Gluon-gluon Fusion (b) Vector boson fusion

Figure 27: Les modes de production principaux du di-Higgs au LHC.

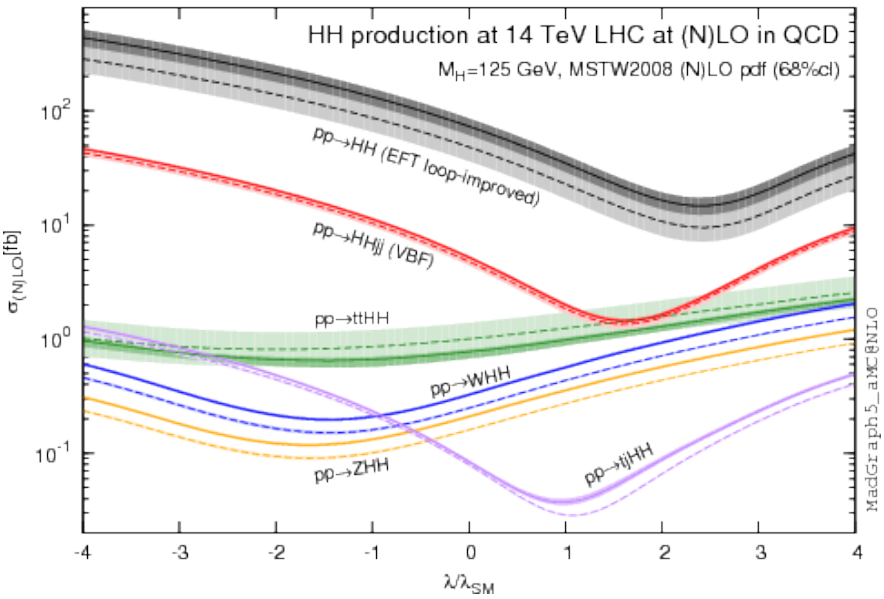

Figure 28: Évolution de la section efficace de chaque mode de production du di-Higgs en fonction de la valeur de l'autocouplage du Higgs λ comparée à sa valeur théorique dans le Modèle Standard λ_{SM}.

La désintégration du Di-Higgs

Considérant le temps de vie très court attendu pour le boson de Higgs, soit de 2.1×10^{22} s, seules les désintégrations du Higgs peut être observées dans les détecteurs du LHC. Les désintégrations les plus probables d'un boson de Higgs, soit avec les rapports d'embranchement les plus grands, sont la paire de quarks b (à 53 %), la paire de bosons W (à 25.7 %), la paire de gluons (à 8.2 %) et la paire de taux (à 6 %). Dans le contexte du di-Higgs, l'ensemble des désintégrations du di-Higgs est présenté dans le tableau 13.
La collaboration ATLAS exploite différentes états finaux pour l'étude de l'autocouplage.

	$b\bar{b}$	W^+W^-	gg	$\tau\bar{\tau}$	$c\bar{c}$
$b\bar{b}$	33.9				
W^+W^-	24.9	4.6			
gg	9.5	3.5	0.7		
$\tau\bar{\tau}$	7.3	2.7	1.0	0.4	
$c\bar{c}$	3.4	1.2	0.5	0.4	
Z^+Z^-	3.1	1.1	0.4	0.3	0.2
$\gamma\gamma$	0.3				

Table 13: Rapport d'embranchement de la désintégration du di-Higgs.

Trois canaux présentent un intérêt particulier car ont l'avantage d'avoir une statistique suffisante et/ou une contamination par les bruits de fond relativement basse, à savoir $b\bar{b}b\bar{b}$, $bb\tau\tau$ et $bb\gamma\gamma$. En parallèle, d'autres analyses moins sensibles sont utilisées, comme les multileptons pour affiner la mesure. Cette dernière inclut l'ensemble des désintégration du di-Higgs qui conclut à la production de plusieurs leptons associés ou non à une paire de photon notés respectivement par la suite HH$\rightarrow ML$ et HH$\rightarrow \gamma\gamma ML$. Cette thèse porte sur l'analyse du di-Higgs en deux leptons de même charge, noté 2ℓSS, signature inclue dans l'analyse HH$\rightarrow ML$.

Les simulations Monte-Carlo

Le but de chaque analyse est de venir comparer un modèle aux données réelles afin de confirmer ou d'invalider une hypothèse. Pour ce faire, les physiciens utilisent des données Monte-Carlo, qui consiste à générer des événements en fonction de leur probabilité. La collaboration ATLAS utilise plusieurs générateurs afin de proposer différents modèles (avec différents paramètres de simulation). Les simulations sont produites par une succession d'étapes représentée en figure 29. La simulation implique trois algorithmes:

- La génération des évènements issus de la collision proton-proton: Cela débute par le calcul de la section efficace de chaque processus pp$\rightarrow X$. Ensuite, on considère les interactions entre protons qui émettent des radiations en cascade.
- La simulation de la réponse du détecteur: La réponse de chaque sous-détecteur d'ATLAS est considérée. C'est à cette étape que l'effet de l'empilement est pris en compte.
- La numérisation des données.

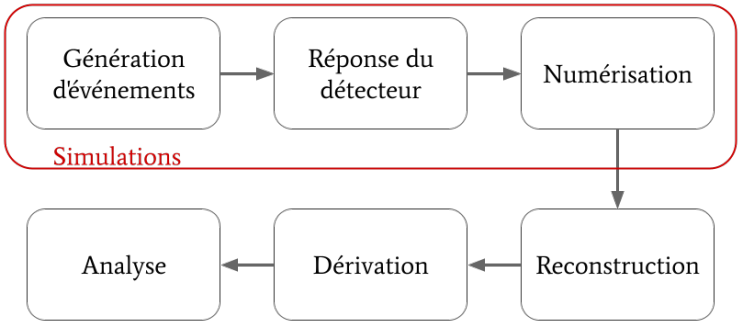

Figure 29: Chaine de production des simulations MC pour l'expérience ATLAS.

Résumé du chapitre 3: le contexte expérimental

Le Conseil Européen pour la Recherche Nucléaire (CERN) est une collaboration dédiée à la recherche fondamentale. Sa création en 1946 par douze pays européens a mené en 1954 à la construction du Grand collisionneur de hadrons (en anglais: Large Hadron Collider, LHC), situé à la frontière Franco-suisse, proche de Genève. Le LHC reste le plus grand collisionneur et le plus puissant construit à ce jour. Quatre grands détecteurs sont positionnés le long de ses 27 km de circonférence :

- ALICE: Ce détecteur est dédié à la physique des ions lourds et plus particulièrement à l'exploration du plasma quark-gluon. Le but de cet expérience est de reproduire des états de matière similaires à ceux présents juste après le Big-Bang.
- ATLAS: Ce grand détecteur polyvalent sonde un éventail de phénomènes physiques très large allant de la physique du Higgs à la recherche de matière noire. Ma thèse s'inscrit dans le cadre de l'expérience ATLAS.
- CMS: Second détecteur polyvalent du LHC, la physique sondée par ce détecteur est la même que celle d'ATLAS cependant les technologies utilisées sont différentes.
- LHCb: ce détecteur est dédié à sonder les désintégrations rares des hadrons B et les paramètres liés à la violation CP permettant de comprendre le déséquilibre matière/ antimatière.

Le détecteur ATLAS est composé d'une succession de sous-détecteurs. Le sous-détecteur le plus proche du point d'interaction est le détecteur interne (ID) qui permet de mesurer l'impulsion de chaque particule chargée. Vient ensuite le calorimètre électromagnétique puis le calorimètre hadronique, qui permettent de mesurer l'énergie des particules suivantes électron et photon puis des hadrons respectivement. Enfin, il y a le spectromètre à muons qui

permet l'identification et la mesure des impulsions des muons. Un système d'aimants ultra puissants permet de courber la trajectoire de chaque particule chargée, permettant ainsi de les identifier. La figure 30 représente une coupe transversale du détecteur ATLAS ainsi que les particules cibles de chaque détecteur.

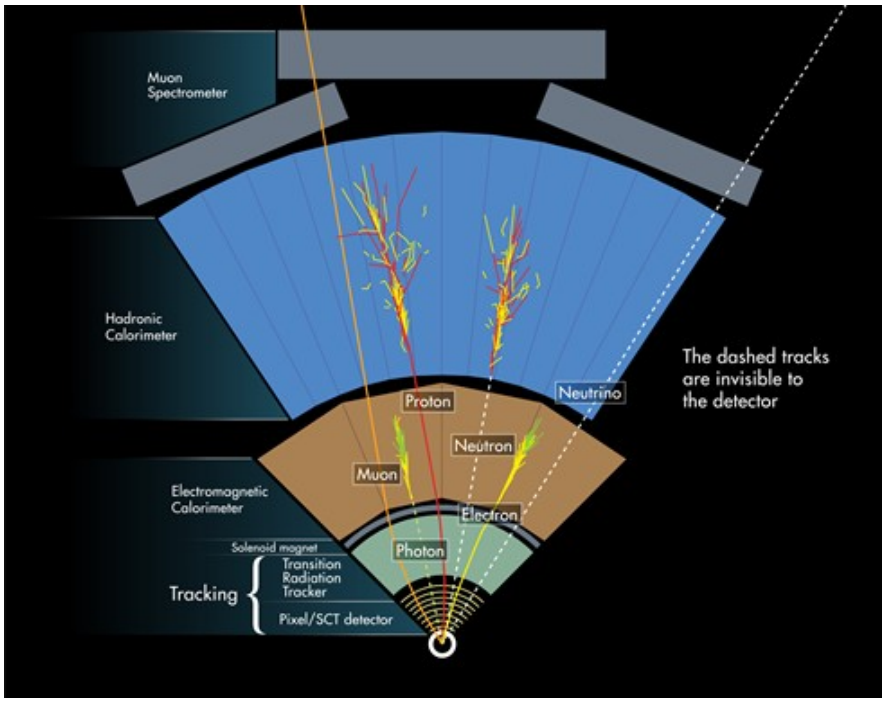

Figure 30: Coupe transversale du détecteur ATLAS avec identification des particules cibles pour chaque sous-détecteur.

Résumé du Chapitre 4: La phase de Haute Luminosité du LHC (HL-LHC)

Le Run-3 a débuté en juillet 2022 et devrait se terminer fin 2024. Dès lors, le LHC entrera dans sa dernière phase, la phase de Haute Luminosité du LHC (HL-LHC). Proposé en 2010 par Dr. Steve Myers, ce projet vise à étudier des phénomènes plus rares, non accessibles par le LHC actuellement. L'augmentation de la luminosité par un facteur 7, soit $4000\,\mathrm{fb}^{-1}$ de données obtenues en dix ans, pose un challenge en terme de gestion des effets de l'empilement et de résistance aux radiations. Le détecteur ATLAS sera mis à niveau afin de garantir au minima une résolution comparable à celle obtenue pour le Run-2, malgré l'augmentation de la luminosité.

Le HL-LHC devrait offrir des conditions idéales pour la réalisation de mesures très précises de paramètres physiques telles que l'autocouplage. En particulier, le HL-LHC servira a davantage explorer la force électrofaible et les propriétés du boson de Higgs, mais aussi investir davantage la physique du quark top avec l'observation de processus rares. Enfin, de manière générale, le HL-LHC permettra la réduction de plusieurs incertitudes systématiques (luminosité, calibration des jets...), qui sont aujourd'hui un frein dans les mesures.
Le projet HL-LHC inclut, entre autre, l'installation d'un détecteur en temps à haute granularité (HGTD) dans la région dite 'en avant' du détecteur ayant une pseudo-rapidité entre 2.4 et 4.0, voir figure 31.

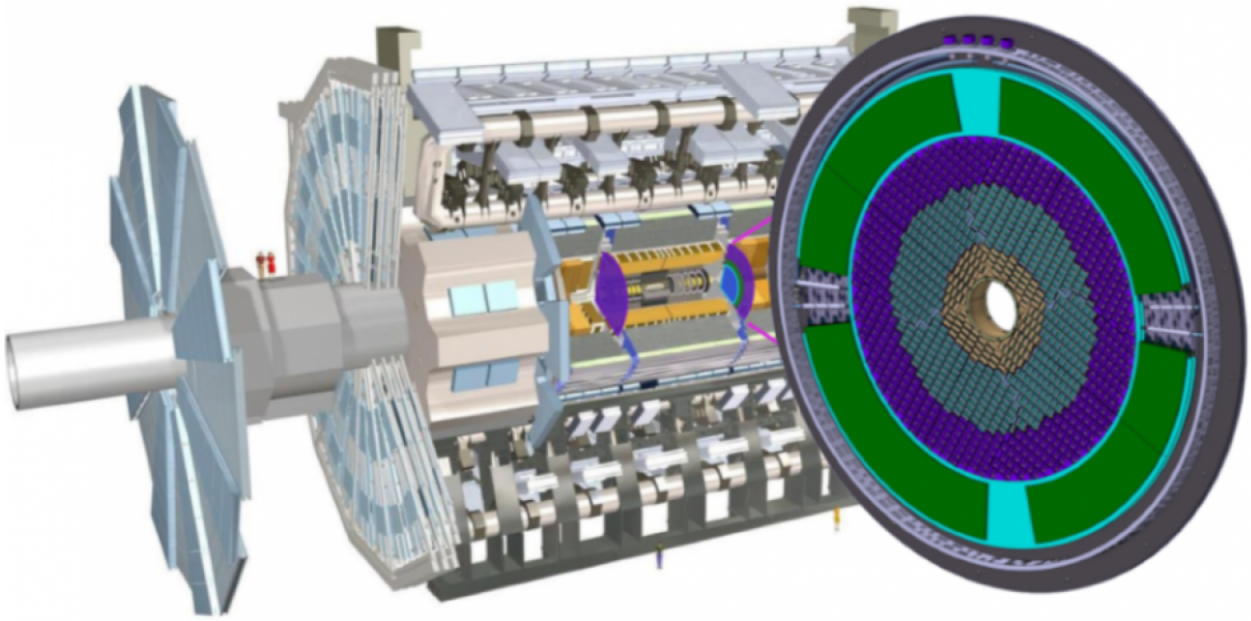

Figure 31: Détecteur ATLAS avec le future détecteur en temps HGTD, installé à $\pm 3.5\,\mathrm{m}$ du point d'interaction.

Le détecteur HGTD sera installé entre le nouveau trajectographe ITk et le calorimètre, dans un espace restreint de 12.5 cm dans l'axe longitudinal du faisceau, à $\pm 3.5\,\mathrm{m}$ du point d'interaction. Ce détecteur est un détecteur multi-couches, composé de deux couches instrumentales recto-verso, deux modérateurs et d'une structure hermétique et mécanique. La partie instrumentale est composée de trois anneaux, assurant différents recouvrements et efficacités par trace. Chaque anneau est formé de modules, c'est à dire d'un capteur appelé 'Low Gain Avalanche Detector' (LGAD) soudé par bille à un circuit intégré appelé ALTIROC.
Le capteur LGAD (pour Low Gain Avanlanche Detector) a été spécialement pensé pour convenir au détecteur HGTD. Il est basé sur une technologie de silicium dopé en n-p-n. Le

but est de générer une avalanche (un gain de 20) à chaque passage de particules dans une épaisseur très fine (50 µm). L'avantage premier de ce détecteur est l'excellente résolution en temps obtenue (25 ps), point essentiel dans la détermination des performances du détecteur en général.
Suite au passage d'une particule dans le détecteur HGTD, les capteurs produisent un signal directement transmis à ALTIROC. Le signal est d'abord amplifié par un pré-amplificateur, puis est transmis à un discriminant permettant de déterminer un seuil de détection et enfin à un convertisseur de temps en données digitales. Le but premier de ce détecteur est de mesurer deux temps, à savoir le temps d'arrivé de la particule (Time of Arrival - TOA) et le temps du signal passé au dessus d'un seuil choisi (Time Over Threshold - TOT), voir figure 32. Le TOT permet d'accéder à l'amplitude du signal. Les temps sont ensuite transmis à la partie digitale qui comprend un ensemble de mémoires tampon permettant la sauvegarde des données. La structure d'un canal montré en figure 33.

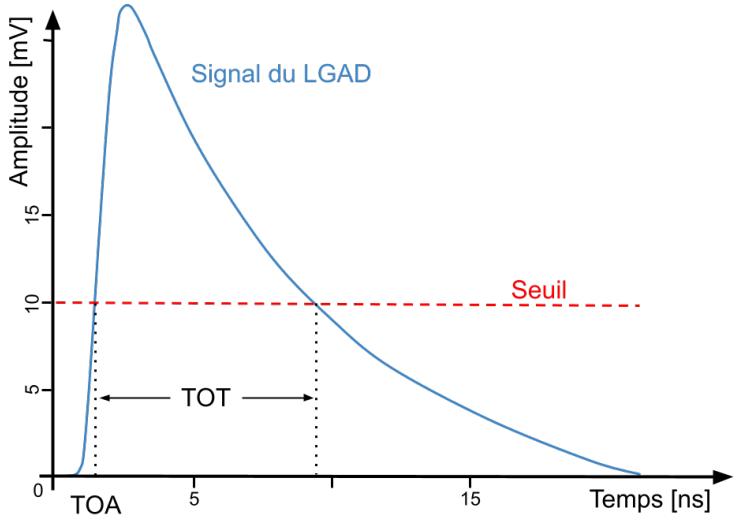

Figure 32: Définition du TOT et TOA. Le TOT correspond au temps du signal (généré par le capteur LGAD) passé au dessus du seuil choisi. Le TOA correspond au temps de passage au dessus du seuil.

Ma contribution dans le développement du future détecteur HGTD s'articule autour des tests de performance ainsi que les tests en radiation de deux prototypes du circuit intégré ALTIROC. Enfin j'ai contribué, de façon minoritaire, aux tests en faisceau des capteurs LGADs.

Résumé du Chapitre 5: Développement du future détecteur HGTD

Tests en performance des prototypes d'ASIC

Le prototype ALTIPIX est le premier prototype de carte intégrée ayant une partie digitale. Ce prototype d'ALTIROC à un seul canal a pour but de tester le bon fonctionnement de la partie digitale. La version ALTIROC2, est la première version d'ALTIROC avec une matrice complètement instrumentalisée de 225 canaux.

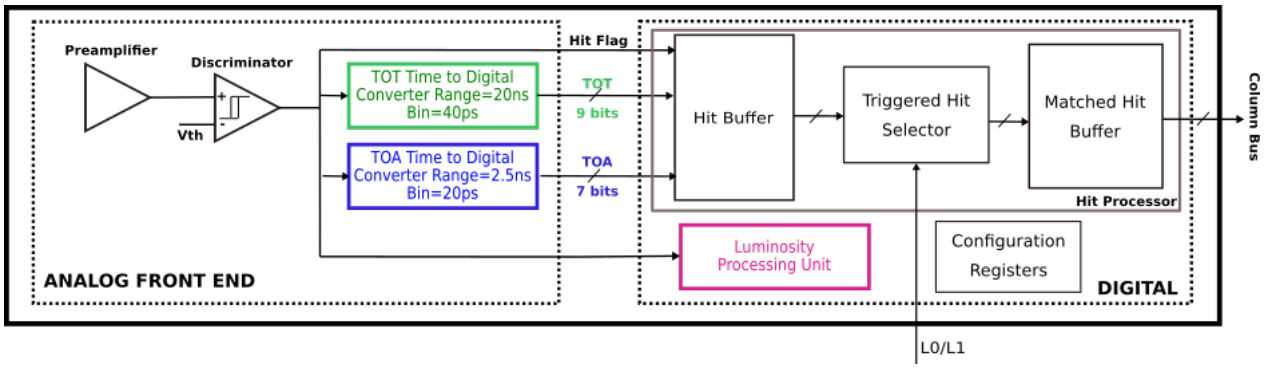

Figure 33: Structure interne de l'ASIC composée d'une partie analogique puis d'une partie digitale.

Le prototype ALTIPIX

Les tests se divisent en deux: les tests de configuration et les tests de performance. Les premiers tests incluent la validation des tensions de références, des courants générés et du bon fonctionnement de l'horloge. S'en suit ensuite le réglage du convertisseur de temps en numérique (TDC) et du seuil de détection. Le banc de test est composé de la carte électronique produite pour les tests d'ALTIPIX, d'une I2C externe et d'une Raspberry utile pour la communication avec l'I2C d'ALTIPIX, et d'une carte SLAC FPGA permettant la communication avec la carte de test.
Les TDCs sont utilisés dans la conversion des TOAs et des TOTs en sortie du discriminant en valeur numérique. Le LSB ou bit de poids faible est le pas de discrétisation de cette conversion et doit correspondre à 20 ps (160 ps) pour le TOA (TOT) sur une gamme dynamique de 2.5 ns (20 ns). Pour ajuster les LSBs, trois registres de contrôle, i.e. des potentiomètres, doivent être ajustés. Pour imiter les signaux reçus par le LGAD, un générateur de pulse interne est installé, avec la possibilité faire varier l'amplitude et le temps d'arrivé du pulse, ce qui revient à faire varier le TOT et le TOA du signal. Le résultat obtenu, voir figure 34, présente les

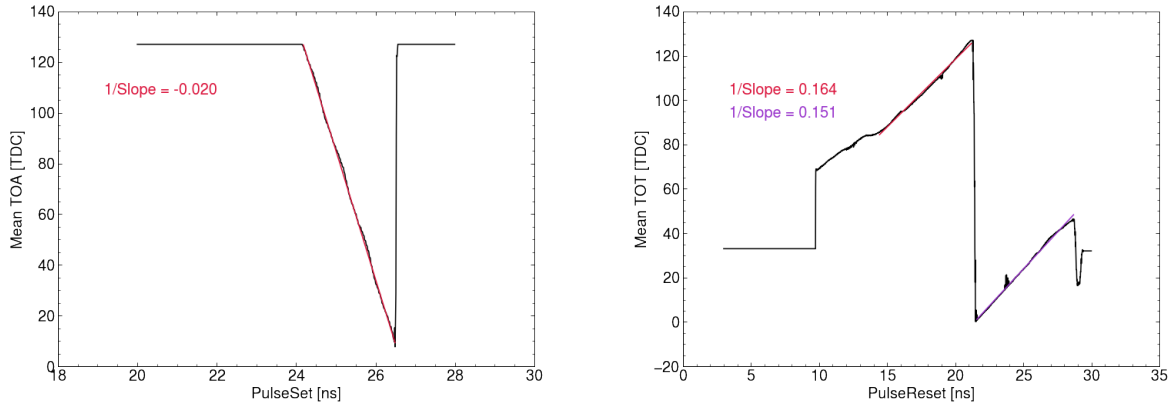

Figure 34: Linéarité du TOA (Time Of Arrival, à gauche)et du TOT (Time Over Threshold, à droite)en fonction des paramètres du pulse. Ces paramètres comprennent le retard (pulseSet) et l'amplitude du pulse (PulseReset).

linéarités du TOA et du TOT en fonction du pulse reçu, l'inverse de la pente donne la valeur du LSB.
Pour ALTIPIX, la détermination du seuil est liée au jitter, c'est à dire au bruit sur le signal du TOA. Le seuil est fixé comme la valeur minimale à partir de laquelle, le jitter est constant. La figure 35 démontre l'évolution du jitter en fonction de la tension de seuil du discriminant. La limite est fixée à 868 mV. Une fois ce seuil réglé, le jitter est mesuré de façon plus précise pour des charges croissantes de 4.92 fC à 10 fC. Suivant les recommandations du cahier des charges, ce jitter ne doit pas excédé les 25 ps. Le jitter est mesuré à 16 ps.
Lors des tests de la partie digitale, un bruit a été observé en sortie du pré-amplificateur. Ce bruit d'une amplitude de ± 100 mV a une fréquence de 80 MHz. L'origine de ce bruit n'est pas clairement définie cependant l'analyse de ce bruit à démontré une corrélation avec l'horloge interne et que son amplitude est corrélée avec la tension d'alimentation de la carte. Le bruit résulte donc d'un couplage en amont du pré-amplificateur. Comme la partie analogique d'ALTIROC2 diffère un peu de celle d'ALTIPIX et que les simulations d'ALTIROC2 n'ont révélé aucun bruit, la recherche s'est arrêté ici. De plus, aucun bruit n'a été observé avec ALTIROC2.

Le prototype ALTIROC2

Les tests réalisés avec le prototype ALTIPIX, ont été reproduits avec la versions ALTIROC2. Comme ALTIROC2 contient 225 canaux, le réglage du seuil est une étape plus importante que pour ALTIPIX. En effet, ALTIROC2 est composé d'une tension de seuil (nommé Vth) utilisable par l'ensemble des canaux et ajustée par une tension propre à chaque canal (nommé

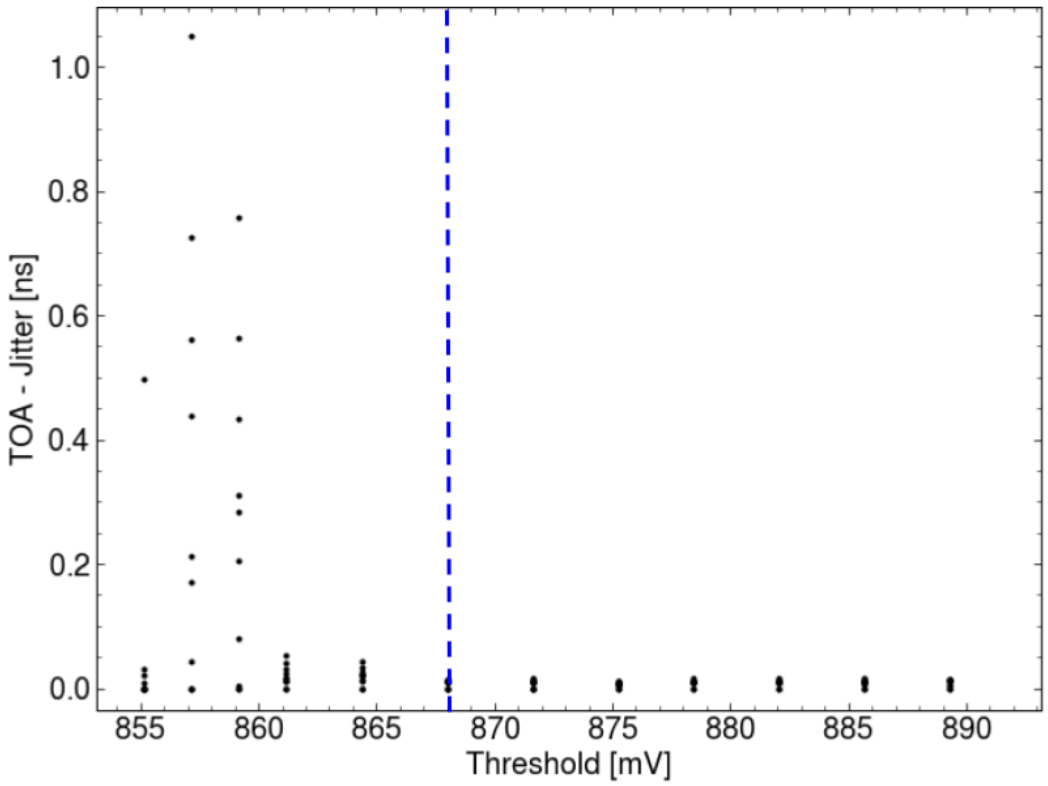

Figure 35: Évolution du bruit sur le TOA (en ns) en fonction du seuil (en mV). Le jitter devient stable à partir d'une charge supérieure à 868 mV.

Vthc). Ce Vthc vise à compenser le décalage en tension, ou offset, de chaque canal.
Ce test est réalisé en configurant l'ensemble des Vthc à zéro, et en injectant successivement N pulses dans chaque pixel, pour une amplitude de pulse donnée et pour un seuil donné. L'efficacité est calculé comme le ratio de pulses détectés par rapport au nombre de pulses injectés. On répète la mesure pour différents seuils. Le Vth est fixé pour avoir une réponse de 50 % sur l'ensemble de la matrice. Une fois le Vth fixé, l'ajustement des Vthc se fait de la même manière que celui du Vth. Le Vthc est fixé pour une efficacité de 50 % pour le canal considéré. Un fois la calibration faite, l'alignement des seuils peut se vérifier en injectant des charge croissante dans l'ensemble de la matrice, l'ensemble des pixels doit avoir une réponse équivalente pour une charge donnée, voir figure 36.

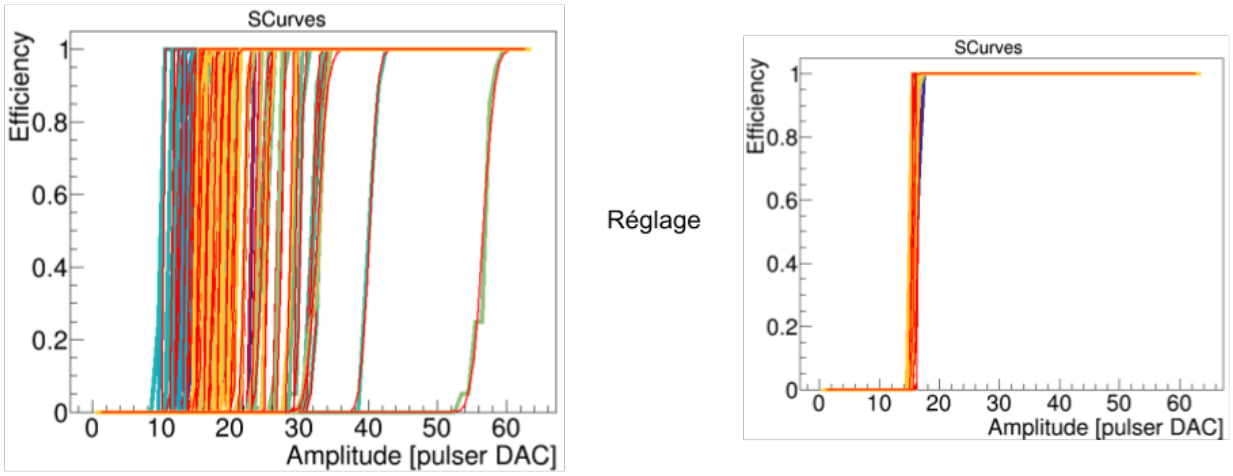

Figure 36: Efficacité de réponse de chaque canal par rapport à la charge. L'image de gauche correspond à la réponse d'une matrice non configurée, celle de droite correspond à une matrice calibrée pour une charge de 6 fC (15 DAC).

Les tests aux radiations et à froid

La résistance de l'ASIC aux radiations est un point essentiel pour le développement d'un sous-détecteur pour le HL-LHC. Deux types d'effets peuvent être observés, les effets cumulatifs et les évènements indépendants. Pour les effets cumulatifs, la dose total de ionisation (TID) à été testée avec le prototype ALTIROC2 avec une machine à rayon X X-RAD iR160 du CERN. Les tests de fonctionnement de base ont été réalisés au cours de l'irradiation, à savoir la vérification des LSBs des TDCs, le suivi des tensions de référence et mesure du jitter. Ces tests ont révélé que l'ASIC n'était pas sujet aux effets des TIDs pour une valeur allant jusqu'à 200 Mrad.

En ce qui concerne les effets indépendants liés aux radiations, les tests SEU (Single Event Upset) permettent de vérifier des évènements statiques issues d'une modification de valeur d'un bit (1→0 ou 0→1). Afin de préserver les données de ces effets, chaque registre considéré comme essentiel voit tous ses bits tripliqués. Cette méthode a pour but de protéger la valeur des bits des erreurs simples, i.e. une invertion de la valeur d'un bit dans une fenêtre de 25 ns. Cependant, cette méthode ne protège pas des erreurs doubles, soit deux erreurs sur un bit tripliqué dans une fenêtre de 25 ns. Ces phénomènes peuvent être quantifiés grâce à des compteurs et des registres dédiés avec le prototype ALTIPIX. Les compteurs s'incrémentent quand une erreur simple est observée puis corrigée dans l'un des 64 registres dédiés. Les erreurs doubles peuvent être estimées à partir de la fréquence d'apparition des erreurs simples ou directement observées dans les registres, par lecture simple. Les tests ont été reproduits avec le prototype ALTIROC2, cependant les résultats ont été moins précis

à cause de la boucle à verrouillage de phase ou PLL. Cette dernière n'étant pas tripliquée, elle est très sensible aux radiations, ce qui engendre un déphasage de l'horloge et donc une désynchronisation complète de la carte.
De la même manière que les tests aux TIDs ont été menés, des tests à froid de la carte ont étés réalisés. Il a été démontré que l'ASIC peut fonctionner jusqu'à $-30\,°C$, température de fonctionnement de la carte au HL-LHC.

Tests en performance des LGADs

Un test en faisceau en septembre 2020 sur les LGADs, a révélé une sensibilité des capteurs aux Single Event Burnout (SEB). Ce phénomène est le résultat d'un claquage induit par les radiations sur la structure NPN bipolaire du LGAD. Plusieurs versions de capteurs ont été produites issues de différents fournisseurs donc impliquant différentes technologies et avec différentes épaisseurs. Les tests en faisceaux auquels j'ai pu participer, ont eut le but de tester 64 versions de capteurs. Chaque capteur a été testé soit au CERN soit à DESY pour des gammes de tensions allant de $200\,V$ à $800\,V$ en fonction du fabriquant. Afin de réduire les effets des radiations, les capteurs sont refroidies à $-30\,°C$. L'état des capteurs est suivi par l'évolution de la résistance du capteur.
Ces tests ont permit d'identifier les technologies robustes aux radiations, c'est à dire une technologie basée sur un capteur enrichi en carbone. De plus, il est apparut qu'un champ limite de $12\,V/\mu m$ assure l'absence de SEB.

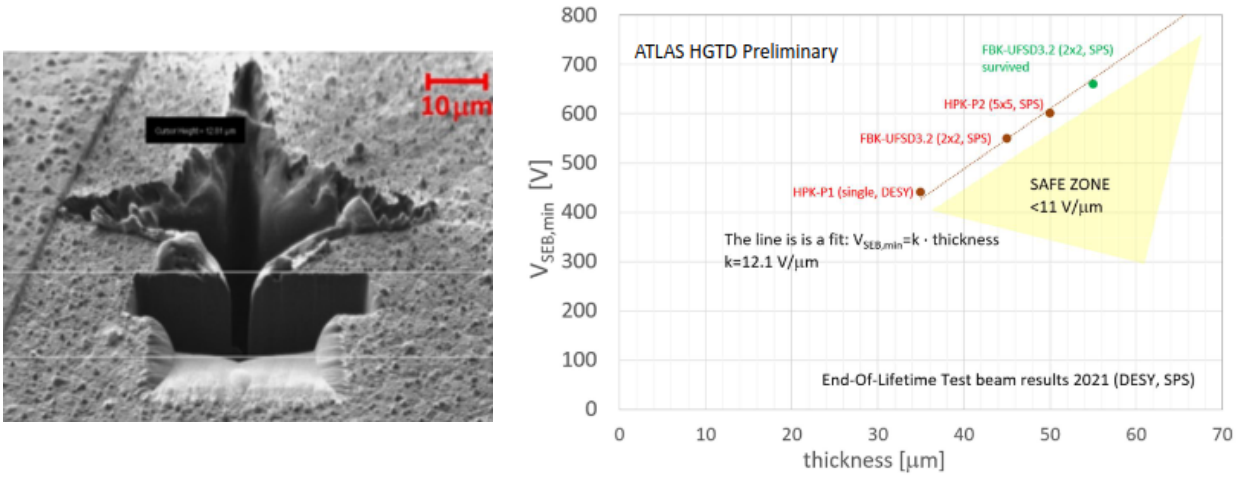

Figure 37: La figure de gauche est un single event burnout observé au microscope sur l'un des capteurs testé. La figure de droite représente l'évolution de la tension du capteur en fonction de son épaisseur. La ligne en pointillée représente le champ limite de $12.1\,V/mm$ en dessous duquel aucun SEB ne devrait être observé [65].

Une fois les capteurs résistants identifiés, des tests de performance ont été réalisés. Ces tests

ont pour but de vérifier le bon fonctionnement des capteurs ainsi que la validation du cahier des charges. En particulier, le capteur doit pouvoir détecter une charge minimale de 4 fC, avoir une efficacité au minimal de 95% et avoir une résolution en temps de 50 ps (70 ps) par coup au début (en fin) de vie du détecteur. Afin de reproduire l'usure des capteurs après les dix ans de fonctionnement du HL-LHC, les capteurs sont irradiés à une fluence entre $1.5 \times 10^{15}\,\mathrm{n_{eq}/cm^2}$ et $2.5 \times 10^{15}\,\mathrm{n_{eq}/cm^2}$. Les tests ont été réalisés sur sept types de capteurs différents à DESY avec un faisceau d'électron de 5 GeV et au CERN avec un faisceau de pion de 120 GeV. Les résultats obtenus, voir les figures 38, démontrent que les performances correspondent au cahier des charges.

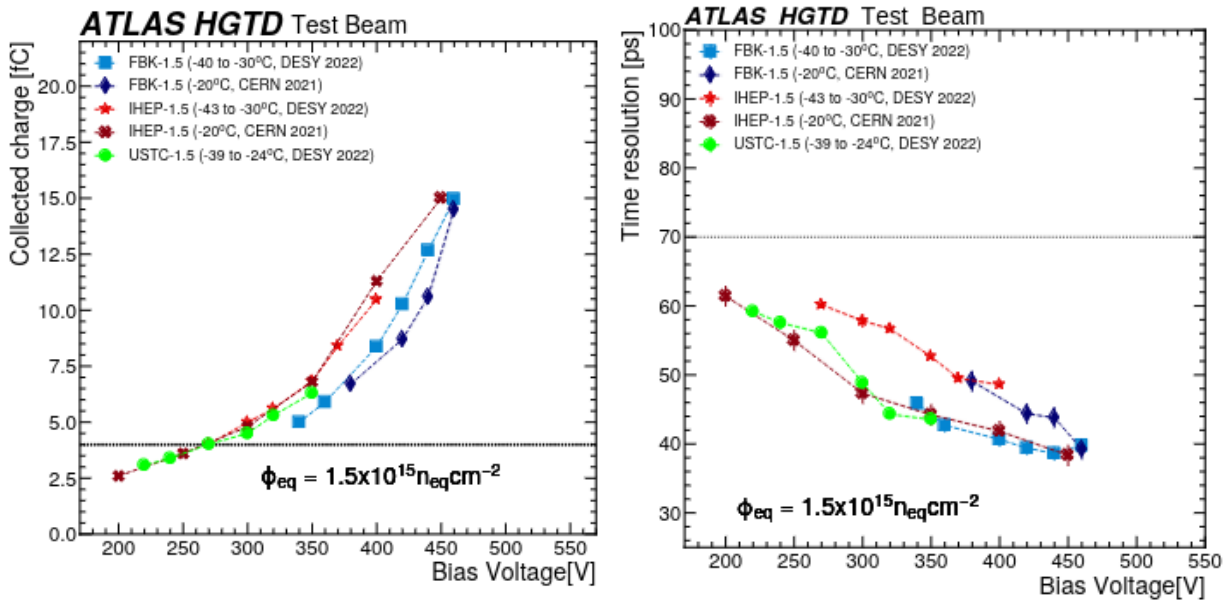

Figure 38: Charge collectée (gauche) et résolution en temps (droite) en fonction de la tension. Les lignes en pointillé noires représente les limites à atteindre pour satisfaire le cahier des charges des LGADs [103].

Les campagnes de tests réalisées sur les LGADs ont abouti à la publication des deux articles suivants [65] et [103].

Résumé du Chapitre 6: Reconstruction des objets dans le détecteur ATLAS

Chaque sous-détecteur d'ATLAS est sensible à un type de particules. Utilisant les informations reçues par chaque sous-détecteur, il est possible d'identifier les particules détectées, c'est

la reconstruction. La reconstruction est propre à chaque nature de particules et s'articule en deux étapes: l'identification et l'isolation.

- Électrons et Photons: Les méthodes de reconstruction des électrons et des photons sont similaires. La seule différence résulte du fait que le photon ne laisse aucune trace dans le détecteur interne, contrairement à l'électron. L'énergie déposée dans le calorimètre est reconstruit sous la forme d'un ensemble. En parallèle, les traces laissées dans le détecteur interne sont collectées puis on extrapole à partir de ces traces les ensembles possibles dans le calorimètre. Un électron est considéré comme reconstruit si au moins l'extrapolation correspond à un des ensembles reconstruits. L'identification des électrons se fait grâce à différents critères qui permettent de différentier l'origine de l'électron (vertex primaire ou secondaire). Enfin, des critères d'isolation sont définies afin de décrire l'activité entourant l'électron reconstruit et par conséquent de différentier l'origine des électrons issus de vertex secondaires. Dans le cadre de cette thèse, et afin de rejeté un maximum de bruit de fond, les électrons sont choisis avec des critères strictes en terme d'isolation et d'identification.

- Charge de l'électron: Identifiée par la courbure de la trace dans le détecteur interne, la charge peut être mal déduite, causant des conséquences importantes dans les analyses et notamment dans le 2ℓSS. La mauvaise identification de la charge peut avoir deux sources: la mauvaise mesure de la courbure ou l'émission d'un photon intermédiaire par Bremstrahlung. La probabilité de mauvaise identification de la charge est mesurée par comparaison du nombre d'évènements $e^{\pm}e^{\mp}$ et $e^{\pm}e^{\pm}$ dans le canal $Z \to ee$, en supposant que tous les évènements $e^{\pm}e^{\pm}$ proviennent d'une mauvaise identification de la charge.

- Muons: La reconstruction des muons se fait grâce à la trace laissée dans le spectromètre à muons et dans l'ID. Différents algorithmes de reconstruction sont utilisés afin d'associer les traces des sous-détecteurs du spectromètre à muon et de l'ID. La reconstruction est suivie par l'identification et l'isolation, avec plusieurs point de fonctionnement définies en fonction des besoins des analyses. Dans le cadre de l'analyse mené dans cette thèse, les muons sont choisies avec une identification dite médium et une isolation stricte afin de garantir un rejet important des muons dits non-prompts.

- Taus: Les taus sont des particules très massives avec un temps de vie extrêmement court (2.9×10^{-13} s), ainsi il se désintègre avant même d'avoir quitté la ligne de faisceau, en lepton (à 35 %) et en hadrons (à 65 %). Les taus sont ainsi reconstruits grâce aux traces de gerbe hadronique dans le calorimètre associées aux traces dans l'ID. La méthode de reconstruction est similaire à celle utilisée par les jets.

- Jets: Résultat de l'hadronisation des quarks et des gluons, les jets sont reconstruits comme des gerbes de hadrons. Ils sont reconstruits à partir des traces laissées dans les

calorimètres et dans l'ID. La reconstruction se base sur la reconstruction en 3D de la gerbe en fonction de la distance entre chaque trace observée. Une calibration des jets est nécessaire et permet, entre autre, de prendre en compte l'effet de l'empilement.

- Les jets b: Les jets b ont un temps de vie plus long que les autres jets, ce qui permet leur identification par un déplacement du vertex secondaire. Chaque jet (b ou autre) est reconstruit avec une efficacité choisie. Dans le cadre de ma thèse, cette efficacité est fixée à 77 % afin d'assurer l'orthogonalité avec les autres canaux.

- Énergie transverse manquante: Basé sur la conservation de la quantité de mouvement p_T, le calcul de l'énergie transverse manquante après collision est le reflet de l'émission de particules dites "invisibles". Cette catégorie inclut notamment les neutrinos ou les particules de matière noire.

Résumé du Chapitre 7: Désintégration d'une paire de Higgs en deux leptons légers de même charge

L'analyse portant sur la signature en deux leptons légers de même charge, noté 2ℓSS, est réalisée avec les données enregistrées avec le détecteur ATLAS pendant le Run-2, de 2015 à 2018, représentant une luminosité intégrée de $140\,\text{fb}^{-1}$. De plus, trois jeux de données Monte-Carlo ont été simulées correspondant respectivement aux données 2015 et 2016, 2017 et 2018. D'autres processus peuvent produire deux leptons légers de même charge et ainsi venir polluer l'observation des évènements issus de la désintégration du di-Higgs, appelé signal. Ces autres processus sont appelés bruits de fond.

Ma contribution dans l'analyse 2ℓSS a été de développer un stratégie efficace dans la construction de la variable discriminante finale et l'optimisation des hyper-paramètres associés à l'entraînement de la multivariable. J'ai aussi eut une contribution importante dans l'estimation des bruits de fond non-prompts. Enfin, j'ai eut une contribution mineure dans la génération des simulations Monte-Carlo.

Sélection des évènements

Les critères de sélection et d'identification des leptons est un point important de l'analyse. En effet, ils permettent d'augmenter la pureté en excluant un maximum de bruits de fonds, i.e. autres processus pouvant produire deux leptons légers de même charge. Ainsi l'analyse est mené avec les critères suivants:

- Le déclenchement: la sélection pour le déclenchement est basée sur des électrons et des muons avec des critères d'isolation et d'identification strictes (tight_SLTorDLT).

- Les leptons:
  - Deux leptons légers avec une même charge sont demandés
  - Les taus sont rejetés
  - Chaque lepton doit avoir une impulsion transverse supérieur à 20 GeV afin d'éliminer un domaine de la physique non souhaité
  - Les leptons sont choisis avec une isolation et une identification stricte afin de rejeter un maximum de bruits de fond, notamment les évènements issus de vertex secondaires.
  - La masse invariante des deux leptons doit être supérieure à 12 GeV afin de protéger la région signal de bruit de fond à basse résonance.
- Les jets: Les jets b sont rejetés (sauf pour les régions de contrôles), et au moins deux jets sont demandés.

Estimation des bruits de fond

Deux catégories de bruits de fond peuvent être distinguées: les bruits de fond irréductibles et réductibles. Les bruits de fond irréductibles proviennent majoritairement de la production de di-boson (VV), avec V pouvant être un boson Z ou un boson W. Le processus $WZ \to \ell\nu\ell\ell$ représente la contribution majoritaire. D'autres contributions moins importantes sont aussi considérées: VVV, VH, $t\bar{t}t\bar{t}$, $t\bar{t}$ +H.
Les bruits de fond réductibles incluent l'ensemble des processus issus d'erreurs de reconstruction ou d'identification des objets dans le détecteurs ATLAS. Ces bruits de fond sont majoritairement dues à la présence de matière sur la trajectoire des particules et donc proviennent de vertex secondaires. Ces bruits de fond sont en général très difficiles à modéliser dans les simulations MC et nécessitent de développer des méthodes dites "Data-driven", c'est à dire des méthodes d'estimation basées sur les données réelles. Deux bruits de fonds réductibles sont observées en 2ℓSS, à savoir les leptons non-prompts estimés par une méthode semi-data-driven appelée Template Fit (TF) et le bruits de fond issu de la mauvaise identification de la charge (QmisID) estimé par la méthode de vraisemblance.

Estimation de la QmisID

La mauvaise identification de la charge est un des bruits de fond particulièrement difficile à modéliser avec les générateurs. Ces évènements peuvent être estimés à l'aide d'une méthode data-driven. Le but de cette méthode est d'estimer la probabilité ϵ pour un électron de subir un Bremsstrahlung, soit une inversion de charge. Dans cette analyse, la mauvaise identification de la charge d'un muon est supposée négligeable. Considérant une paire d'électron de charge opposée e^+e^-, il y a trois manière possible de reconstruire ces évènements:

- e^+e^-: les deux leptons sont reconstruits correctement avec une probabilité de $(1-\epsilon_i)(1-\epsilon_j)$.
- $e^\pm e^\pm$: Seul un lepton voit sa charge mal reconstruite avec une probabilité de $\epsilon_i + \epsilon_j - 2\epsilon_i\epsilon_j$.
- e^+e^-: Les deux leptons ont leur charge mal reconstruite avec une probabilité $\epsilon_i\epsilon_j$.

Ainsi, en considérant N^{OS} le nombre de di-leptons reconstruits avec une charge opposée et N^{SS} le nombre de di-leptons reconstruits avec une même charge. La probabilité totale de mauvaise reconstruction de la charge peut s'écrire de la manière suivante:

$$N_{ee}^{SS} = \frac{(\epsilon_i + \epsilon_j - 2\epsilon_i\epsilon_j)}{(1-\epsilon_i-\epsilon_j+2\epsilon_i\epsilon_j)} N_{ee}^{OS} \quad \text{dans le cas d'une paire } ee$$
$$N_{e\mu}^{SS} = \frac{\epsilon_i}{(1-\epsilon_i)} N_{e\mu}^{OS} \quad \text{dans le cas d'une paire } e\mu$$

Les poids ϵ sont estimés dans le canal $Z \to ee$ dans une région particulière de la masse invariante des deux leptons appelée le pic du Z. Cela suggère de faire l'hypothèse que les évènements de même charge proviennent de faux leptons ou de la mauvaise identification de la charge. La probabilité d'observer une mauvaise identification de la charge augmente avec l'épaisseur de matière présent sur le trajet de la particule, donc dépend de la pseudorapidité η. De la même manière, cette probabilité augmente pour un faible rayon de courbure. La courbure de la particule est proportionnel à l'impulsion transversale p_T. Enfin, ces taux sont mesurés en fonction des critères de sélection de l'électron.
Cette méthode est basée sur la vraisemblance en supposant que la distribution des évènements suit une loi de poisson. La fonction de vraisemblance L s'écrit alors:

$$L(\vec{\epsilon}|N^{SS}) = \prod_{i,j} f(N_{ij}^{SS}|N^{SS}(\epsilon_i,\epsilon_j))$$

On minimise ensuite la fonction $-2ln(L)$ afin d'extraire les taux. La figure 39 présente la valeur des taux en fonction de l'impulsion et de la pseudorapidité.

Estimation des leptons non-prompts

Les leptons non-prompts proviennent de plusieurs sources reconnues: des leptons d'une désintégration semi-leptonique d'un hadron lourd (HF - heavy flavour) ou léger (LF - light flavour) ou encore d'une émission de photon intermédiaire par bremsstrahlung. Parmi les évènements provenant de la conversion de photon, il est nécessaire de distinguer les évènements issus de la électrodynamique quantique (QED) et les évènements provenant d'une conversion matériel (Mat Conv). La majorité des leptons non-prompts proviennent de la désintégration $t\bar{t}$ et V+jets. Chaque catégorie est définie en utilisant les informations dites 'truth':

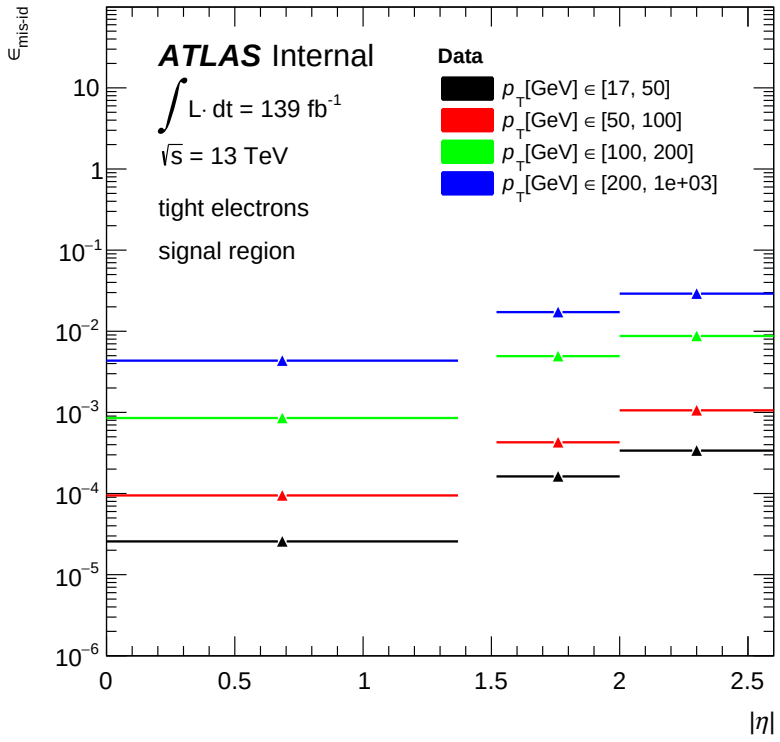

Figure 39: Taux de mauvaise identification de la charge obtenu en fonction de la pseudorapidité et du p_T

- Les leptons QmisID: Une information directement tirée des informations 'truth' permet d'exclure les évènements issus de QmisID. Ces évènements sont estimé par la méthode de vraisemblance.
- Les leptons de conversion matériel: évènements ayant un rayon de désintégration supérieur à 20 mm et une masse entre 0 et 100 MeV invariante de la trace associée à l'électron et sa trace la plus proche calculée au niveau du vertex de conversion.
- Les leptons de QED: Tous leptons issus de conversion matériel exclus et une masse entre 0 et 100 MeV invariante de la trace associée à l'électron et sa trace la plus proche calculée au niveau du vertex primaire.
- Les leptons issus de la désintégration d'hadrons: leptons ayant pour origine un hadron B ou hadron C en utilisant l'information 'truth' des parents des leptons.

La méthode des "templates" (ou template fit) permet de définir des régions enrichies, appelées régions de contrôle (CR), en chaque type de bruits de fond non-prompts et d'extraire quatre facteurs de normalisation (NF):

- $NF^{MatConv}$: NF a appliquer aux électrons issus d'une conversion matériel
- NF^{QED}: NF a appliquer aux électrons issus d'une conversion QED
- NF_e^{HF+LF}: NF a appliquer aux électrons issus d'une désintégration de hadrons
- NF_μ^{HF}: NF a appliquer aux muons issus d'une désintégration de hadrons

Les facteurs de normalisation sont extraits lors d'un ajustement simultané des MC simulation par rapport aux données, dans les cinq régions de contrôle ainsi que dans la région signal. Ils sont ensuite appliqués aux évènements correspondants.
Étant une méthode semi-data-driven, les résultats obtenus avec cette méthode dépend des simulations Monte-Carlo. De ce fait, des incertitudes systématiques sur le résultat est à prévoir. Les incertitudes des muons et des électrons provenant de la désintégration d'hadrons sont mesurées en relaxant le critère d'isolation du lepton secondaire, visant à enrichir les CR en cette catégorie de lepton. La comparaison entre les données et les simulations MC après pondération par les NFs permet d'extraire les incertitudes suivantes en fonction de l'intervalle: 1 % à 6 % pour les électrons et de 3 % à 9 % pour les muons.

Stratégie développée pour extraire le signal

Afin de maximiser l'identification des évènements signal, la construction d'une variable dite discriminante est essentiel. Dans le cas de l'analyse 2ℓSS, trois bruits de fond majoritaire sont considérés ($t\bar{t}$, V+jets, VV) ayant différentes origines ainsi une stratégie est mise en place afin de construire la variable discriminante optimale. Dans un premier temps trois variables sont construites, basées sur une méthode multivariée appelée arbre de décision boosté (BDT). Chaque variables dites spécifiques sont entraînées pour un bruit de fond versus le signal, soit $t\bar{t}$ VS HH, VV VS HH et V+jets VS HH. La figure 41 représente la distribution des trois BDTs spécifiques, avec le bruit de fond en rouge et le signal en bleu. Ensuite, les trois BDTs spécifiques sont combinées dans une dernière variable, un BDT entraîné en considérant l'ensemble des bruits de fond versus le signal. La figure 42 montre la distribution de la variable finale utilisée.
La région signal est ainsi définie par la sélection des évènements précédemment cité cumulé avec une coupure sur tous les évènements avec une valeur de BDT inférieure à 0.4. Cette sélection vise à rejeter un maximum de bruit de fond et donc avoir une région signal la plus riche possible.
Pour quantifier la capacité à observer le signal dans la région signal, les physiciens utilisent une méthode statistique permettant d'extraire une limite supérieure d'exclusion de la force

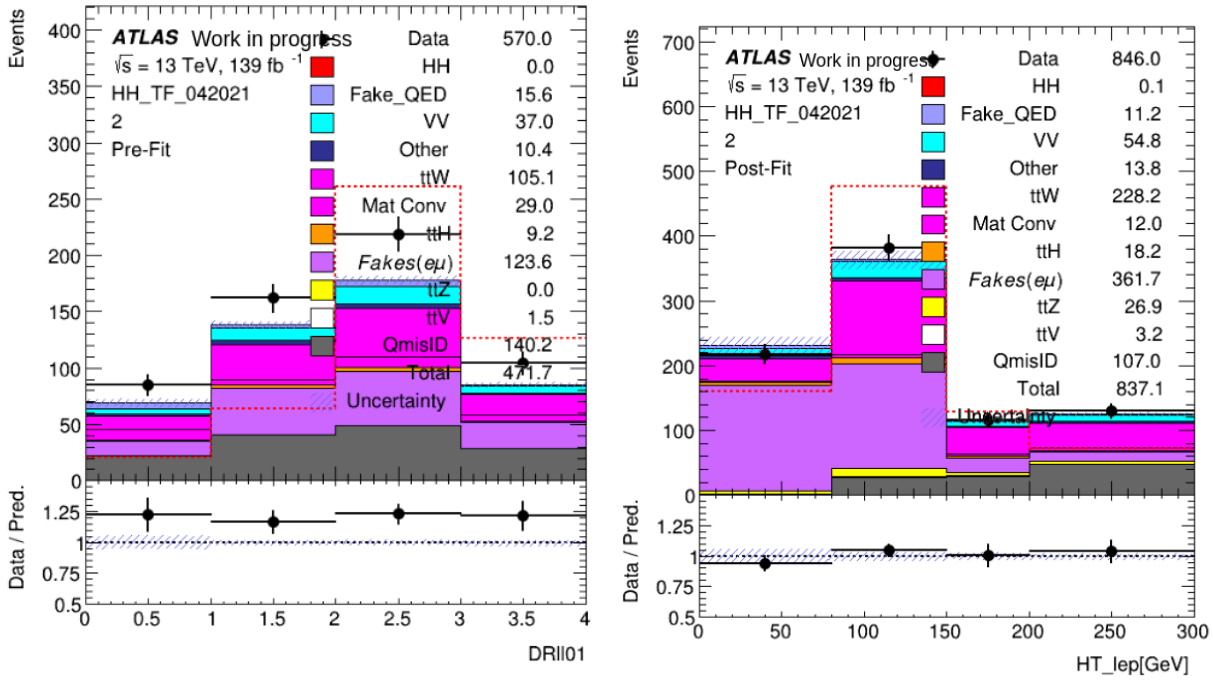

Figure 40: Région de contrôle spécifique à la désintégration de hadron avec un moins un électron. La figure de gauche correspond à la distribution avant l'ajustement. Celle de droite correspond à la distribution après ajustement.

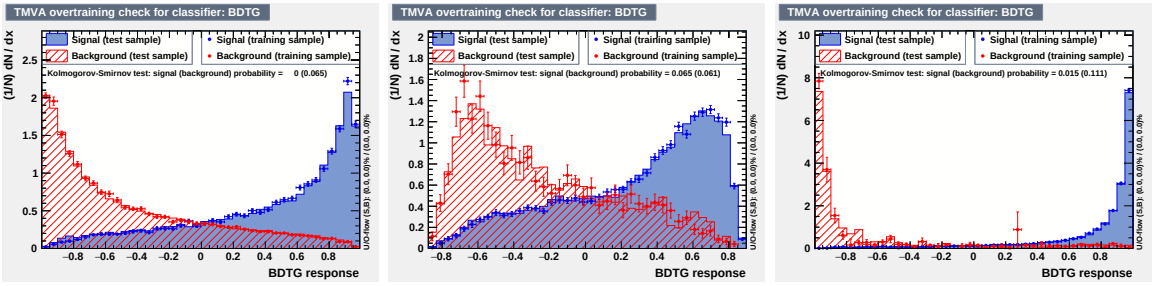

Figure 41: Distributions des BDT, de gauche à droite: HH VS di-boson, HH VS $t\bar{t}$ et HH VS V+jets. Le bruit de fond est en rouge, le signal est en bleu.

du signal, autrement dit de quantifier la compatibilité entre une hypothèse et les données collectées. Cette force de signal μ se définie comme le rapport entre la section efficace mesurée par rapport à la section efficace prédite dans le modèle standard, soit $\mu = \frac{\sigma}{\sigma_{SM}}$. Une déviation observée dans cette force de signal impliquerait une déviation dans la valeur de l'autocouplage du boson de Higgs et potentiellement une nouvelle physique. Dans le cas de la signature $\ell^{\pm}\ell^{\pm}$, cette force de signal est obtenu par un ajustement simultané des régions de contrôle ainsi

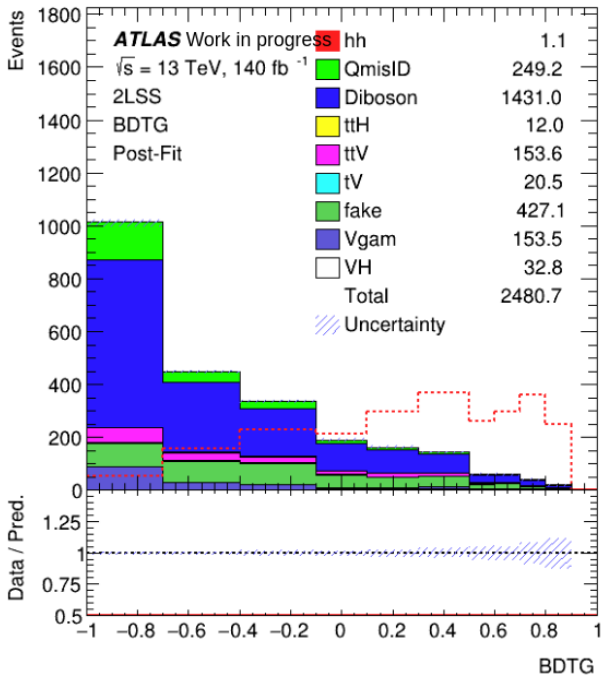

Figure 42: Distribution du BDt combiné avec estimation des bruits de fond par les méthodes data-driven.

que de la région signal. Le résultat obtenu en considérant l'ensemble des systématiques est de μ=34.8.
La recherche de la désintégration de la paire de Higgs en deux lepton leger de meme charge est intégré dans une étude plus globale à savoir la désintégration en multileptons. Au total, neuf signatures sont combinées. Les neuf canaux sont visibles sont visibles dans la figure 43. Les analyses du multileptons sont assez similaires: optimisation de la région signal en fonction de la signature, utilisation de techniques multivariées pour construire une variable finale optimale en utilisant la méthode BDT et l'estimation des différents bruits de fond. En fonction des signatures les bruits de fond majoritaires varient et donc nécessitent différentes techniques d'estimations (template fit, fake factor,...). La sensibilité de l'ensemble des canaux combinés mène à la une limite attendue de $8.93\sigma^{SM}$ en considérant des incertitudes statistiques uniquement et de $9.74\sigma^{SM}$ en considérant l'ensemble des incertitudes systématiques. L'analyse étant toujours faite à l'aveugle, la limite observée n'est pas encore dévoilée.

Un résultat récent du CMS obtenu dans le canaux multilepton (ne prenant pas en compte les désintégrations en photon) montre une limite attendue (observée) sur la force du signal de 19 (21). En considérant les même canaux que dans l'analyse de CMS, la limite attendue pour ATLAS est de $14.8\sigma^{SM}$.

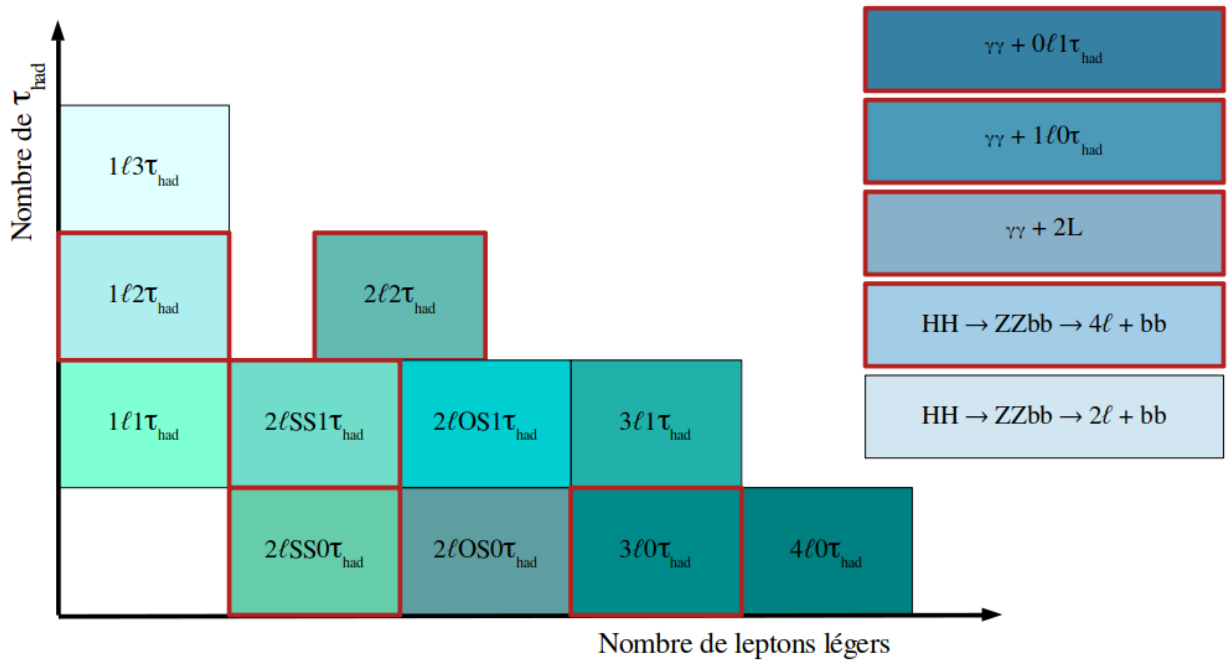

Figure 43: Liste des désintégrations du di-Higgs en leptons. Les canaux encadrés en rouge représentent les canaux considérés dans l'analyse multileptons. Les autres n'ont pas été considéré par manque de sensibilité.

Le résultat obtenu dans l'analyse multilepton sera par la suite combiné avec les canaux $bb\gamma\gamma$, $b\bar{b}b\bar{b}$ et $bb\tau\tau$. Pour le moment, la combinaison de ces trois canaux mène à une limite attendue (observée) de 2.9 (2.4)σ^{SM}. Une estimation de la combinaison des trois canaux avec le multilepton mène à une limite attendue de $2.38\sigma^{SM}$.

Conclusion

Avec la découverte du boson de Higgs en 2012, la caractérisation des paramètres qui lui sont associés est devenu un des programmes principal du LHC. Un des paramètres majeur est la mesure de l'autocouplage du Higgs qui permettrait de valider le mécanisme de brisure de symétrie électrofaible. Une déviation dans cet auto-couplage par rapport à sa valeur prédite dans le modèle standard, aurait des conséquences considérables sur notre compréhension de notre monde et serait le reflet d'une nouvelle physique. Cette thèse présente une analyse Run-2 du LHC d'une désintégration d'une paire de Higgs en deux leptons légers de même charge. Les méthodes d'estimations des bruits de fond ainsi que la stratégie mise en place dans la distinction du bruit de fond et du signal, permettent d'obtenir une limite attendue à

un intervalle de confiance de 95 % à $8\times\sigma_{HH}^{SM}$. L'observation directe de cet autocouplage n'est pas attendue avant la phase de haute luminosité du LHC. Cette phase de haute luminosité devrait débuter en 2029 et délivrera en 10 ans une luminosité intégrée de $4000\,\mathrm{fb}^{-1}$. Afin de contrebalancer avec l'augmentation du taux de radiation ainsi que de la quantité du empilement, le détecteur ATLAS nécessite d'être mis à jour, incluant l'installation d'un nouveau sous-détecteur en temps à haute granularité, nommé HGTD. Mon travail de thèse porte sur les tests en performance de l'électronique de lecture de ce détecteur. Les différents testes ont pu mettre en lumière que le prototype était en accord avec le cahier des charges en terme de performance et en terme de résistance aux conditions (radiation et basses température) du HL-LHC.